Controlling Area-Selective Growth Mechanisms of Nickel-based Nanostructures Through ALD and Surface pre-Patterning

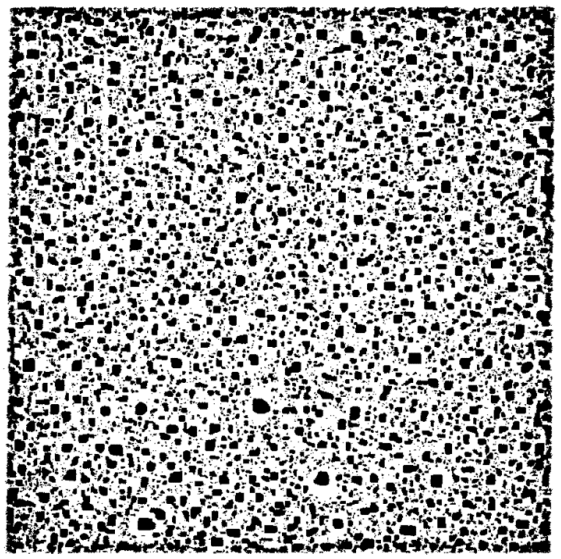

By:

Gabriele Botta

Supervised by Professor Mato Knez

2023

Resumen

A medida que la industria de semiconductores se esfuerza por producir sistemas altamente complejos y sin margen de error, la nanofabricación electrónica basada en la técnica de litografía con resina se enfrenta a limitaciones en términos de compatibilidad con sustratos y de precisión. De hecho, el uso de una resina, que es la capa sacrificial esencial utilizada para transferir patrones en la litografía convencional, tiende a dejar residuos en la superficie y causar desafíos experimentales al tratar con materiales frágiles y sensibles. Los desafíos actuales demandan la exploración de nuevas estrategias de fabricación para poder aprovechar al máximo los nuevos materiales.

Entre las diversas técnicas que han aportado novedad a la nanofabricación, la técnica de deposición de capas atómicas, en inglés Atomic Layer Deposition, ALD ha demostrado ser la solución tecnológica para muchas necesidades industriales gracias a su único mecanismo de crecimiento basado en la unión química entra la capa fina depositada y el substrato. Esta característica ha sido aprovechada principalmente hasta el dia de hoy para obtener recubrimientos incluso en nanoestructuras intrincadas, desafiando la manipulación de sistemas de baja dimensión. La alta conformidad de esta técnica, que determinó su éxito como técnica de recubrimiento en nanotecnologías, al mismo tiempo determinó su difícil incorporación en la nanoestructuración de materiales debido a la escasa compatibilidad entre los productos químicos de ALD, llamados precursores, y los pasos litográficos convencionales. En la actualidad, el concepto de que ALD no puede utilizarse como técnica de estructurado se ha visto desmentido. De hecho, una rama de ALD recién surgida, conocida como Area-Selectiva ALD (AS-ALD), demostró que, mediante el control avanzado de las reacciones específicas entre precursores y la superficie, se pueden depositar selectivamente materiales en áreas seleccionadas de un sustrato (áreas de crecimiento), dejando otras regiones sin afectar (áreas de no crecimiento) y sin necesidad de ninguna capa sacrificial o resina. Sin embargo, dado que la selectividad de estos procesos se deriva de propiedades particulares de la superficie, como la composición química diferente o la presencia de defectos, esta técnica todavía depende de alguna forma de la pre-estructuración de la superficie, que en muchos casos nos lleva de vuelta a la fabricación basada en en litografía. Para romper este ciclo, se esbozan métodos alternativos de estructuración por escritura directa capaces de producir modificaciones en la superficie sin depender del uso de ninguna capa sacrificial, siendo un complemento poderoso para el AS-ALD.

Este trabajo se centra en varios aspectos tecnológicos y experimentales relacionados con la selectividad del área, que se extiende desde el objetivo original del AS-ALD hasta otras formas de obtener nanoestructuras funcionales sin depender de pasos litográficos. Esta exploración se centra particularmente en un elemento, el níquel, debido a su alta abundancia junto con su relevancia tecnológica debida a su asombrosa lista de propiedades que pueden presentarse según su composición y estructura.

Después de presentar las principales técnicas experimentales y herramientas utilizadas durante esta tesis, el manuscrito comienza con un estudio de la ingeniería de la máquina necesaria para cumplir los propósitos tecnológicos avanzados deseados en este trabajo. El Capítulo III se centra en el desarrollo del reactor de ALD, que es la primera herramienta fundamental para explorar el campo de AS-ALD. Este proceso se realiza mediante la investigación experimental con herramientas de computación de dinámica de fluidos (del inglés, CFD). La optimización convencional de los procesos de ALD se basa en la iteración de experimentos con la optimización de parámetros individuales. Aplicar este enfoque a procesos que utilizan precursores sólidos, como los utilizados en esta tesis, puede generar un esfuerzo experimental masivo debido al gran número de variables que afectan a el transporte de los vapores de el precursor. Sin embargo, los métodos computacionales son lo suficientemente robustos en la actualidad como para permitir la simulación de condiciones experimentales y reducir drásticamente el número de procesos realizados físicamente. Además, para los propósitos avanzados de AS-ALD, la dinámica de fluidos puede tener un impacto profundo en el resultado del experimento y obstaculizar la ampliación de un proceso. El análisis mediante CFD de la velocidad de los vapores de precursores durante un experimento de ALD esclareció las limitaciones de la herramienta que son responsables de reducir la eficiencia de los procesos de ALD y, lo que es más importante, conducir a la captura de precursores, un factor que puede resultar perjudicial para los procesos de AS-ALD. Complementando las ejecuciones experimentales con simulaciones de CFD, se construyó un primer reactor de ALD (reactor 1) optimizando el uso de precursores para respaldar un estudio rentable de nuevas reacciones químicas de ALD. Las pruebas del reactor se realizaron optimizando el depósito por ALD de NiO utilizando $Ni(Cp)_2$ y ozono. Finalmente, la modelización de CFD del paso de pulsación de ozono reveló una correlación entre el reducido crecimiento de el material y las tasas de flujo de co-precursores aumentadas, mostrando que el CFD puede ser una herramienta poderosa no solo para la ingeniería de reactores, sino también como verdadera herramienta experimental.

En el Capítulo IV, se analiza un proceso térmico para obtener níquel metálico a partir de NiO. Se encontró que el recocido térmico utilizando un horno calentado por infrarrojos en presencia de un gas de conformación (mezcla 5% H_2 en N_2) era una configuración conveniente para lograr una reducción completa, obteniendo níquel metálico de alta calidad a partir de temperaturas de procesamiento de 400°C. Para probar la calidad del material, decidimos estudiar simultáneamente la aplicabilidad de la ALD con métodos litográficos convencionales. Recordamos que el propósito inicial de la tesis es desarrollar y proponer alternativas a la fabricación basada en litografía. Sin embargo, en esta etapa de la tesis, familiarizarse con las principales herramientas experimentales para la nanofabricación fue un paso necesario para experimentar las limitaciones tecnológicas de la ALD y poder ofrecer soluciones e innovación. En este

proceso de aprendizaje, se desarrolló un método optimizado que permite incorporar la técnica de ALD en la nanofabricación basada en la resina, donde generalmente se evitaría su uso debido a su menor compatibilidad en comparación con los métodos convencionales de deposición física de vapor (del inglés physical vapor deposition, PVD). Utilizando este enfoque, construimos matrices micrométricas de níquel, que son metasuperficies peculiares utilizadas en la actualidad para aplicaciones de detección en el campo de la magneto-plasmónica. Estas matrices están compuestas por nanodiscos de níquel, magnéticos por naturaleza y, gracias a su reducido tamaño y disposición geométrica en una red periódica, también adquieren de resonancias superficiales de red (en inglés surface lattice resonances, SLR) y de resonancias plasmónicas de superficie (surface plasmon resonances, SPR). Dada la amplia comprensión de la respuesta óptica de tales estructuras, este fue el dispositivo ideal para probar simultáneamente la calidad del material sintetizado y la precisión del método de fabricación (matrices micrométricas). Se produjeron y caracterizaron diferentes matrices de níquel a través de mediciones de extinción. Los espectros obtenidos fueron ajustados posteriormente con la respuesta teórica simulada numéricamente utilizando COMSOL. Con este enfoque, confirmamos que un método químico que consiste en la deposición de NiO por ALD seguido de un recocido térmico rápido (rapid thermal annealing, RTA) permite obtener metal de alta calidad que puede integrarse en nanoestructuras avanzadas. El conocimiento adquirido durante la ingeniería del reactor y la optimización del proceso condujo al desarrollo de un nuevo proceso compatible con la estructuración de escritura directa, que permite, a través del RTA, producir dominios de níquel estructurados en su matriz original de óxido de níquel. Esta metodología se etiquetó como recocido pulsado (pulsed annealing) porque se basa en la introducción del gas de conformación en pulsos cortos. Para conferir un tamaño y forma determinados al dominio magnético de níquel, utilizamos una capa fina de alúmina para evitar que el sustrato reaccione con el hidrógeno dejando expuestas al gas de conformación solo areas predeterminadas. Sin embargo, se propone que mediante el uso de una fuente de calor de escritura directa como podria ser un láser, el mismo proceso podría realizarse sin necesidad de litografía y con una resolución mejorada. Después de optimizar las condiciones del recocido pulsado y el grosor de la capa de alúmina, obtuvimos dos resultados tecnológicamente relevantes. El primero: pudimos crear fácilmente estructuras conductoras de níquel, completamente estructuradas en la capa de óxido de níquel. Esta forma de patrón no topográfico se puede incorporar en estructuras multicapa, ya que las nuevas propiedades son infundidas en el material a través de la modificacion local de su composición y no mediante la adición o eliminación de materiales. Destacamos que en el futuro, este método podría mejorarse y extenderse a una clase más amplia de materiales y, en el caso de Ni/NiO, podría aplicarse para estudiar si se pueden fabricar estructuras de níquel ferromagnético en contacto con dominios de NiO antiferromagnetico que presenten interacción de intercambio. El segundo descubrimiento de este capítulo está relacionado con la interacción entre el

óxido de níquel y la alúmina en presencia de hidrógeno. A través de un estudio en vacío de espectroscopia de fotoelectrones emitidos por rayos X, conocida en inglés como X-ray Photoelectron Spectroscopy, reproducimos las condiciones de RTA de experimentos anteriores, revelando que, bajo ciertas circunstancias, el recubrimiento de alúmina puede favorecer la reducción del óxido de níquel subyacente en lugar de desfavorecerla. El mecanismo que se propone concuerda con algunos estudios recientes y se basa en la captura reversible de hidrógeno en la capa de alúmina. Dada la amplia variedad de aplicaciones emergentes que involucran materiales a base de Ni y óxido de aluminio en el campo de la catálisis y el almacenamiento de energía, se concluye que se deben realizar estudios adicionales para comprender este fenómeno.

El Capítulo V se centra en la implementación de un paso de estructuración mediante escritura directa en la síntesis en estado sólido de siliciuro de níquel para promover el crecimiento selectivo de áreas deseadas únicamente. Recientemente, el interés en los siliciuros ha aumentado, gracias al descubrimiento de nuevas propiedades que surgen cuando los materiales se sintetizan en fases específicas o dimensionalidad reducida. Este estudio tiene como objetivo respaldar la investigación en este campo proponiendo una vía sintética que permite un control excepcional tanto sobre la morfología como sobre la ubicación del sustrato de nucleación de los cristales de siliciuro. Como se mencionó, esta clase de materiales se obtiene convenientemente mediante síntesis en estado sólido que consiste en el RTA de una capa delgada de metal sobre silicio. En este capítulo, se decide extender la química de ALD ya familiar del níquel, a esta síntesis en estado sólido con resultados sorprendentes. Se encontró que, durante el RTA, si se utiliza NiO de ALD en lugar de níquel metálico puro como fuente de metal, se favorece el crecimiento epitaxial de cristales de nanosiliciuro y, lo más importante, estos cristales se alinean automáticamente con características defectuosas del sustrato. En una superficie prístina, estos sitios son reconstrucciones de Si, defectos lineales y fallas de apilamiento, pero si la superficie se modifica con precisión a través de fresado iónico selectivo, la nucleación puede dirigirse a las áreas deseadas. Los descubrimientos de este capítulo sientan las bases de una nueva forma de extender el mecanismo de selectividad de área a reacciones en estado sólido. Nos referiremos a este proceso como AS-silicidation. Estos resultados, como se mostrará en el texto, se demuestran para el caso del siliciuro de níquel, pero se basan en mecanismos de crecimiento comunes a muchos otros siliciuros. Por lo tanto, predecimos que esta metodología podría producir resultados comparables en otros materiales de relevancia tecnológica.

Finalmente, el Capítulo VI se dedica a un proceso de ALD inherentemente selectivo. Para lograr tales resultados, cambiamos a una química de ALD diferente. El precursor metálico de elección es $Ni(DAD)_2$, que se utiliza en combinación con un agente reductor para obtener deposición directa de níquel. Recientemente se reportó que este proceso conduce al crecimiento de níquel en sustratos puramente metálicos, y crecimiento inhibido en superficies oxidadas. Dedicamos un esfuerzo considerable a la ingeniería de

un nuevo reactor (reactor 2) para facilitar el complicado suministro de vapores de precursor a los sustratos. Esta segunda fase de rediseño de la herramienta fue ayudada por el conocimiento adquirido anteriormente y permitió generar una gran cantidad de datos a partir de unos pocos experimentos de ALD. La selectividad del proceso se estudió en sustratos de diferente naturaleza química. Los resultados mostraron que los grupos -OH son responsables de destruir la selectividad del proceso. Según la literatura, este proceso AS-ALD debería dar lugar a la ausencia de crecimiento en SiO_2. Sin embargo, la composición superficial de este material se ve fuertemente afectada por su cristalinidad, y esto puede afectar la nucleación de níquel en la superficie. Para estudiar este fenómeno, comparamos el crecimiento en dos sustratos de SiO_2 con diferentes funcionalidades superficiales. Un sustrato de elección fue el silicio térmico, que presenta una alta concentración de grupos siloxano (Si-OH) en la superficie debido a su naturaleza amorfa. El segundo sustrato fue cuarzo fundido de alta pureza, que, por otro lado, presenta concentraciones de grupos OH muy reducida. El análisis de XPS después del procesamiento confirmó que el níquel puede nuclearse fácilmente en superficies altamente hidroxiladas, como el silicio térmico, pero no en cuarzo, destacando la importancia de eliminar los hidroxilos superficiales antes de la deposición para mantener una alta selectividad. El estudio también se centró en metales (Pt y Au) y óxidos metálicos (FeOx y CrOx), revelando que el crecimiento de níquel ocurre en todo el grupo de superficies. Mientras que en platino y oro, se esperaba la nucleación de níquel, en las superficies de óxidos metálicos no se esperaba. El análisis de espectroscopía de Energía Dispersiva de Rayos X" (EDX por sus siglas en inglés) y XPS reveló que el precursor $Ni(DAD)_2$ puede causar redeposición de hierro sugiriendo que el complejo o sus subproductos pueden reaccionar con el hierro. Identificamos este fenómeno como la posible causa del depósito de níquel tanto en las superficies de óxido de hierro como de óxido de cromo. Por lo tanto, proponemos que este compuesto presenta más de una vía de fisisorción y que se deben realizar experimentos adicionales para desentrañar su estabilidad térmica en presencia de diferentes superficies.

La combinación de AS-ALD y métodos de escritura directa está actualmente en las fases iniciales de investigación. A pesar de esto, este enfoque innovador presenta implicaciones significativas para el futuro de la nanotecnología. La intención de este trabajo de tesis doctoral es fortalecer y consolidar este enfoque innovador dentro del ámbito de las nanotecnologías enseñando las ventajas del procesamiento químico hacia la fabricación de dispositivos. Termino extendiéndole mis mejores deseos para una lectura provechosa. Espero que este trabajo pueda contribuir al campo de estudio y que pueda en alguna forma motivar a futuros scientific@s. ¡Buena lectura!

Abstract

Utilizing atoms as building blocks for bottom-up manufacturing has been a long-standing dream. However, the most pragmatic approach for generating patterns on various materials has utilized top-down manufacturing by means of lithography. [1] For centuries, this methodology has defined the standards of precision and reliability of manufacturing, leading us into the silicon era and supporting our ambition to produce ever smaller objects. However, as the semiconductor industry aims at producing highly complex systems with no room for mistake, conventional lithography encounters limitations, signaling the culmination of this race towards miniaturization. The current challenges demand a paradigm shift and the exploration of novel strategies and new physics. In this context, the success of future technologies hinges on the complementary integration of new methods in conventional device fabrication schemes. The development of new bottom-up techniques has gradually transformed from a mere dream into a pressing necessity. Among the plenty available techniques, atomic layer deposition (ALD) stands out for its capability to achieve highly controlled layer-by-layer thin film growth, a characteristic which stands up to the challenge of manipulating low dimensional and intricate systems. Moreover, a recently developed branch of ALD, known as Area Selective ALD (AS-ALD), is gaining momentum as a promising nanopatterning approach. This novel methodology leverages specific reactions between precursors and the surface to facilitate precise and controlled material deposition on selected areas of a substrate, leaving other regions unaffected. In contrast to lithography, the spatial control is achieved without relying on any sacrificial layer, but instead by exploiting unique chemical and physical properties of the surface to initiate or suppress localized reactions. The true potential of AS-ALD lies in its seamless integration with direct-write patterning methods, which can be used to modify the surfaces prior to deposition. In this context, the chemical/physical nature of the substrate, instead of a patterned resist, is the means for defining specific growth or non-growth areas, overcoming the limits such as surface damaging and contamination which can affect resist-based methods. Another consequence is that, during chemical deposition, the precision is dictated by nature, in this way eliminating experimental errors and misalignment which inherently affect resist-mediated deposition. The combination of direct writing and AS-ALD is in its nascent stages of exploration. Nonetheless, this innovative approach holds profound implications for the future of nanotechnology, supporting the extension of chemical processing advantages to device fabrication. Moreover, this transformation extends beyond technology, permeating various aspects of our lives. In the face of global crises and lack of

[1] Lithography from the Greek Lithos "stone" and Graphein "to write" stems for the ancient art of carving images on stone surfaces to reproduce patterns.

alternatives, the pursuit of innovative solutions and new resources across multiple fields becomes imperative.

This thesis, that was initially outlined to study exclusively area-selectivity involving ALD, rapidly branched into a wider study where unexpected means of achieving local modifications were unveiled and investigated.

"Bad times have a scientific value.

These are occasions a good learner would not miss."

Ralph Waldo Emerson

Table of Contents

1

Programmable molecules as building blocks

1.1 Beyond lithography

Photolithography and electron beam lithography (eBL) have led to exponentially increasing progress in the computer industry and nanoscience for more than three decades. These methodologies helped us producing ever smaller systems, and made us push the boundaries of Moore's Law [1] to the current 7 nm process node. Nowadays processors have been shrunk and packed into such highly dense systems that new limits, imposed by current leakage and heating effects, have been reached. [2] The understanding that miniaturization has a limit, made clear that new strategies need to be adopted. This technological revolution, labelled "More that Moore" (MtM), [2] is based on the integration of different nondigital functionalities into semiconductor technologies instead of further pushing miniaturization. The idea is that process scaling, as well as lithography, will still remain being important in the coming decades, but they will not be the sole drivers of the progress in electronics. [3]

In this scenario, it became essential to find ways to successfully incorporate new materials, such as fragile and sensitive two-dimensional materials (2DM), into functional devices. [4] New ways for controlling the shape and composition of these materials, together with the redesign of the device architecture, have become fundamental. In the past years, there have been many examples of new game changing "MtM" technologies such as MEMS (microelectromechanical systems), spintronics and spinorbitronics devices, which are supporting technological revolutions such as quantum computing and neuromorphic engineering. [5]

To support this progress, new lithographic methods, like extreme ultraviolet lithography (EUV) and Nanoimprint Lithography (NIL), have reached high resolution and reliability, [6] but are still negatively affected by the high costs and the requirement of a sacrificial layer (resist). [7] One widespread problem arises when lithography is combined with thin film deposition for the fabrication of structures with

[2] The strategic agenda and vision for More than Moore" (MtM) technology was formulated in 2005 by the European Technology Platform for Nanoelectronics (ENIAC).

high aspect ratios, because it tends to cause resist sidewall coating, resulting in the formation of undesired "*ears*" or causing undesired remains of the resin.

Another limit of lift-off-based fabrication is that conventional polymeric resists have molecular sizes which are comparable with the desired feature sizes and that energy transfer and proximity effects arising during the "writing" can lead to blurring of the designs, causing a significant loss of resolution. With these issues in mind, many new resist materials have been developed over the years for attaining higher resolution with smaller EBL writing time. [8] In parallel, experimental effort has led to a deeper understanding of all contributing factors that affect the exposure mechanism during eBL and the energy density distribution generated around the beam spot (point-spread function, PSF). [9] However, while some of the technological drawbacks can be overcome, other limitations of lithography on low dimensional systems are simply inevitable.

2D materials are crystalline solids composed of a single (or few) atomic layer(s). Compared to their bulk counterpart, the properties of these materials are very much related to the quality of their surface. In this sense, the use of resists during patterning can lead to surface contamination which deteriorate their performance (contaminants originating from the resist, solvents and nanoparticles). [10]

Another source of problems of lift-off-based methods is that a high patterning resolution is achieved, according to Abbe's diffraction limit, by increasing the energy of the source used for writing. The energy required for patterning the resist is dissipated into the substrate though scattering events, phonons, photons, plasmons and electron re-emission, that can introduce surface defects resulting in performance loss of the 2D materials. [11]

For these reasons, it became critical to develop fabrication methods capable of minimizing sources of defects and contamination. The success of many future technologies could be determined by the development of alternative fabrication pathways capable of overcoming the limits of conventional lithographic methods.

All the methodologies that enable the patterning of the substrate by using high energy sources and without relying on the intermediate step of resist patterning, are considered resist-free methodologies, and are grouped under the name of direct writing techniques.

The following paragraph overviews some promising technologies for direct-write patterning.

1.1.1 Resist-free nanopatterning

Recent years have witnessed the development of many technological answers to the challenge of manipulating matter at the nanoscale without relying on sacrificial layers such as resists or masks. Whenever patterning is required, a highly localized source of energy must be employed to induce controlled modification of the substrate.

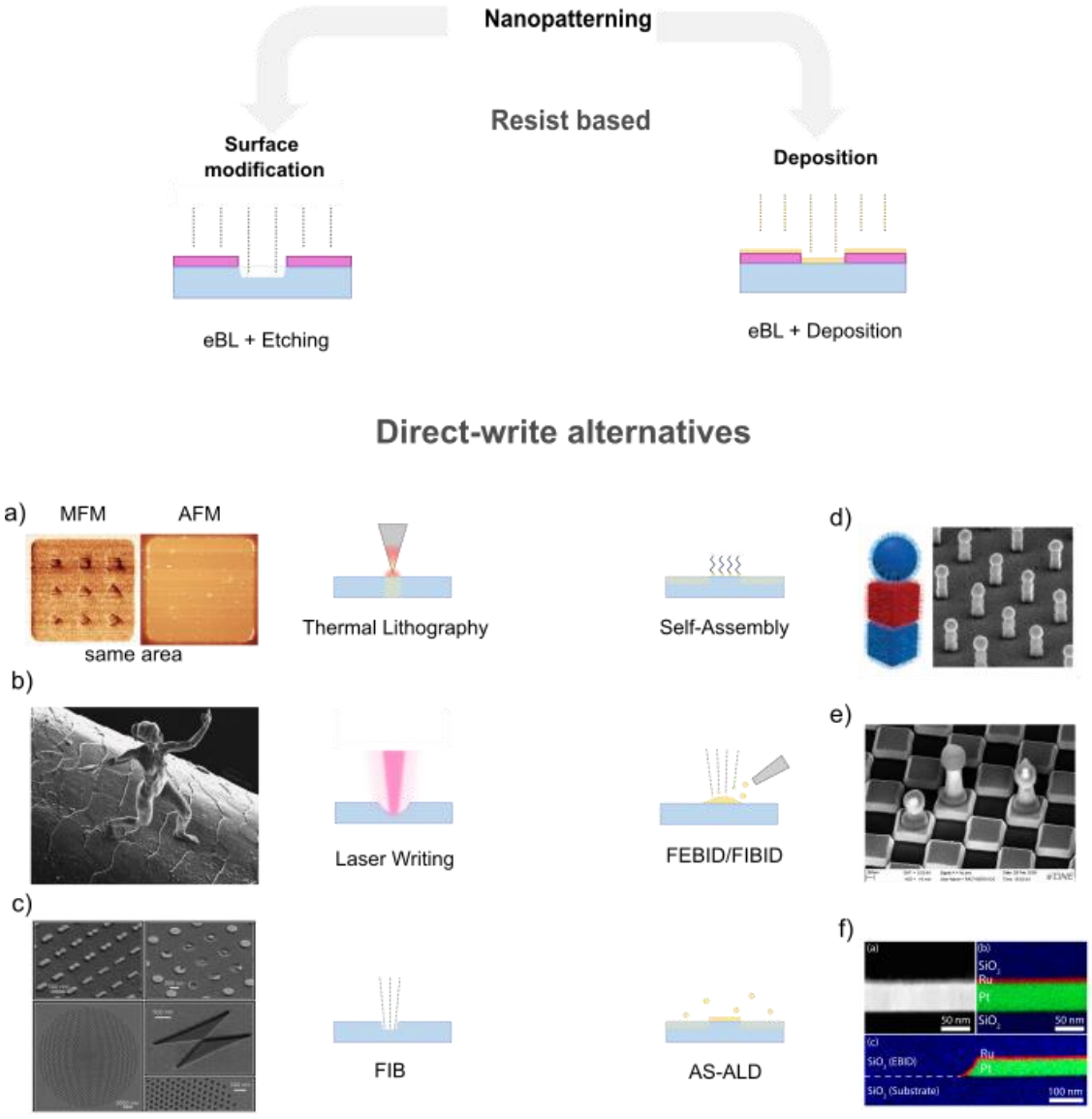

Figure 1: Direct-write patterning methodologies: a) Phase nanoengineering via thermal lithography. Image taken from Ref. [12]; b) micro sculpture titled "Trust" by Jonty Hurwitz, fabricated by two-photon direct laser writing on a human hair; [13] c) Nanostructures fabricated via direct write milling using a focused ion beam; [14] d) template-mediated self-assembled structured pillars; [15] e) Nano checkerboard, fabricated with FEBID on a Raith system; [16] f) Area-selective ALD of ruthenium on platinum. [17]

One possible approach is to directly manipulate matter with atomic scale resolution using a nano-sized object such as an atomic force microscopy (AFM) or scanning tunnelling microscopy (STM) probe. Such probes are employed to induce modifications to the surface by providing energy in a highly localized manner. One interesting example is *thermal scanning probe lithography*, where the tip is used to induce stable modifications to the substrate by point-by-point thermal irradiation, thereby completely preventing the contact between substrate and external materials. [18] A sophisticated way to use this approach is to perform the so called "*phase nanoengineering*", wherein new properties are infused into the target material without altering its topography, but by locally modifying its crystallinity and composition (**Figure 1**, a). [19] Techniques such as thermal lithography are methodologies which can offer a superior tunability and precision, but at the same time are limited in their use to very specific technological needs. Also, the mechanical scanning of the tip over the surface leads to extended processing times and limited up-scalability.

Other approaches of direct writing techniques rely on the use of ion beams (ion beam lithography, IBL) to modify the substrate properties via milling. [20] Writing using ion beams can offer high resolution and versatility but with the downside of inducing contaminations commonly caused by ion implantation. [14] Focused ion beams have also been used for phase nanoengineering by inducing layer intermixing into magnetically coupled multilayer structures. [21]

Processes can be sped-up by sacrificing resolution via direct laser writing techniques that have also demonstrated to be good tools for performing phase nanoengineering. [19] Recent progress in the field has demonstrated that, by using femtosecond laser irradiation, high resolution patterning (hundreds of nm feature size) of different 2D materials at a writing speed as high as 5 mm/s, can be achieved. [22] Direct laser writing can also be used for growing 3D objects but similarly to lithography, this requires a sacrificial photoresist and thus will not be discussed here.

Up to this point, whether with local heat, ions, or photons, all techniques are employed mainly for modifying a pre-deposited material or a substrate. They represent the resist-free alternative to the conventional lithography-based approach consisting in resist patterning, followed by an etching step to remove material from the desired areas (See eBL + etching in 2.5.1).

The other lithographic standard for nanofabrication relies on resist patterning, followed by thin film deposition and lift-off (See eBL + deposition 2.5.1). Two common alternative methods used for resist-free deposition of nanostructures are Focused Electron and Ion Beam Induced Deposition (FEBID) and (FIBID), respectively. These techniques are based on the local decomposition of a gaseous precursor via focused beams. They are established for micro/nano manipulation and fabrication of samples inside SEM/FIB systems since many years. Both fields demonstrated significant

progress in the recent years expanding the library of obtainable materials, reducing incorporation of contaminants during deposition, and showcasing the high potential for the fabrication of intricate 3D nanostructures. [23,24] Long-processing times are still an inevitable limiting factor that could relegate this technology to niche applications or to be used in conjunction with other methods. [25]

Among all the listed methods, one shared characteristic is that the modified area is always related to a physical magnitude such as the spot size (in the case of the high energy focused beams) or the size of the local field (for a heated AFM tip).

Another class of resist-free bottom-up patterning methods rely on chemistry to locally functionalize a substrate. This type of approach exploits different chemical affinities between dosed molecules and substrate functionalities of different nature to produce deposition on selected areas only. One characteristic of these methods is that, for achieving area selective deposition (ASD), they must be used on pre-patterned surfaces and thus present huge potential as complementary method to any previously described form of direct patterning. Among ASD strategies, examples of solution-based chemical patterning have been obtained using direct self-assembly (DSA) of block co-polymers, chemical assembly of organic electronic materials, and spin dewetting. [26] The combination of these techniques with lithographic methods led to interesting methodologies such as template-confined DNA-mediated assemblies of superlattices (**Figure 1**, d). [15]

Vapor phase methods, such as area selective atomic layer and chemical vapor deposition (AS-ALD and AS-CVD, respectively), are further approaches towards chemical patterning. Their high precision over large area processing, together with the reduced material waste and low energy consumption, make them promising candidates for the bottom-up fabrication of the devices of the future.

Given the important role the AS-ALD and ALD in general play for this thesis, they will be described in more detail in the following.

1.2 Area Selective atomic layer deposition

Area Selective Atomic Layer Deposition (AS-ALD) is a recently founded subsidy of ALD, a cyclic layer-by-layer thin film deposition technique based on self-limiting chemical surface reactions carried out by exposing a substrate to alternating doses of vaporized chemical reactants (See 2.1). [3]

[3] If not familiar with ALD, it is recommended to read 2.1 before continuing the reading.

In AS-ALD, all ALD processes which allow layered deposition on a desired region of the surface, are simultaneously maintaining adjacent regions unaltered. The growth and non-growth areas are defined by different characteristics of the surface such as chemical composition, surface group termination, topography and lattice structure that have different interaction qualities towards an ALD precursor (**Figure 2**). [26,27] This approach enables to completely re-think the processes of nanofabrication in the view of new resist-free direct patterning methodologies. At the same time, it inherits all the advantages of normal ALD such as, conformality over large areas and high aspect ratio structures, low manufacturing costs, and reduced environmental impact.

In AS-ALD two main strategies promote surface selectivity, as described in a review of Mackus et al. from 2018. [27] The first type exploits the different adsorption energies that the ALD precursor or co-precursor have with specific surfaces (**Figure 2**, III). The most studied system relies on chemical differences between hydroxyl-terminated (OH-terminated) and hydrogen-terminated (H-terminated) surfaces for promoting or inhibiting ALD growth. In a simple example, this enables ASD of metal oxides on OH-terminated Si substrates, while H-terminated Si surfaces exhibit a nucleation delay. [28] Variances in precursor adsorption on oxides versus metal surfaces have also been adopted for the growth of nickel and cobalt thin films. [29,30] Some examples of AS processes, based on selective adsorption of the co-precursor, are also present in literature. In this context, a paper from J. Singh et al. shows that catalytically active noble metals, such as platinum and ruthenium, can be used to promote dissociative chemisorption of oxygen which was used as co-precursor, enabling its reaction with the precursor in the catalyzed areas only. [31] Using this method, the authors were able to grow iron oxide and nickel oxide on Pt by using nickelocene and ferrocene as precursors and molecular oxygen as co-reactant. Although novel and ingenious, this approach has an intrinsic limit over the thickness that can be deposited, because the catalyst is rapidly passivated by the growing thin film.

The second approach is based on inducing a selective functionalization prior to ALD to promote or hinder the growth in some target areas. [32,33] Among the different strategies for selective functionalization, the use of self-assembled monolayers (SAMs) as growth inhibitors is one of the most studied systems. SAMs, applied before the ALD process, selectively bind to affine surface sites, inhibiting ALD precursor adsorption and rendering the surface unreactive. The group of S. Bent has devoted much attention to this topic, pushing forward novel ideas like the use of vapor phase processed small molecule inhibitors (SMI) for higher spatial resolution and easier processability. [34] This approach is optimal for passivating surfaces against highly reactive precursors that would otherwise cause uniform growth throughout the whole surface.

In summary, the first AS-ALD approach relies on inherently selective reactions between surface and precursor, while the second one requires a surface functionalization to extend selectivity to processes that otherwise would not be selective.

In the framework of this thesis, the second methodology is less appealing because it requires, like in lithography, the use of a sacrificial layer.

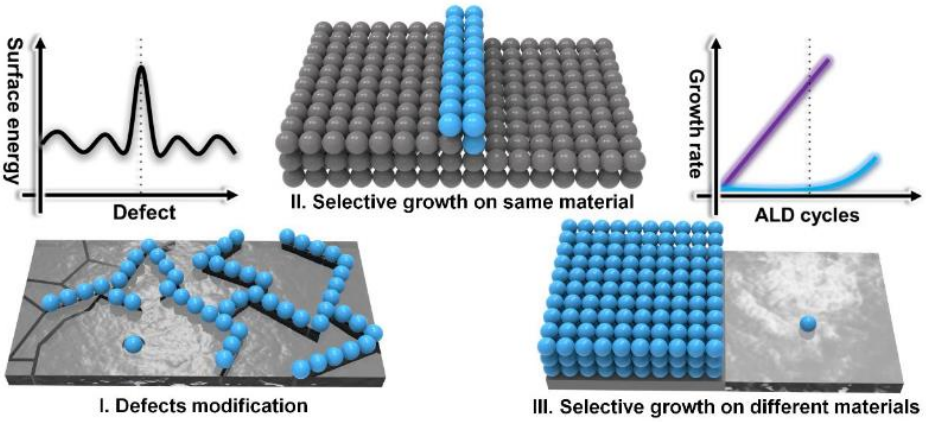

Figure 2: Mechanisms for achieving selective growth, either dictated by different types of surfaces or by the presence surface defects. Image taken from. [35]

As discussed before, AS-ALD always relies on surface pre-patterning and a common way to employ it is the combination with lift-off-based fabrication to produce perfect alignment between ALD-deposited coating and a pre-deposited structure, or to selectively coat high aspect ratio structures. [26] The advantage of AS-ALD in this context is the coating precision and convenience for large area samples where multiple lithographic steps would otherwise be needed.

The new challenge for ASD methods is the combination with direct-write patterning to completely remove any lithographic step. This combined approach can be used for inducing surface modification for promoting AS-ALD processes prior to the deposition. As a first demonstration, W.M.M. Kessels et al. performed a focused electron beam-induced deposition (FEBID) of a platinum seed layer, followed by AS-ALD of Pt to deposit thick contacts. [36,37]

Another mechanism of AS-ALD makes use of defect sites and edges of 2D materials (**Figure 2**, I-II). Examples in literature report selective growth of materials on graphene grain boundaries and point defects which have a relatively high free energy

compared to the unreactive basal plane of the surface. [38,39] This mechanism could be coupled with direct writing methods to modify the surface energy of 2D materials and define growth promoting and inhibiting areas. These last two examples outline the central role of this methodology in enabling the fabrication of devices based on low dimensional materials to which conventional lithographic methods are not applicable. [40]

During this thesis, different selective deposition processes involving nickel-based precursors will be discussed.

1.3 Nickel-based materials

Nickel is a hard and ductile transition metal with the atomic number 28, first isolated and classified as an element in 1751 by Axel Fredrik Cronstedt. [41] The name was tagged in the 1600s, when German miners called *Kupfernickel* ("copper demon") all ores which were resistant to refinement into copper, a phenomenon later assigned to the presence of nickel in the minerals. Nickel is the fifth most abundant element in Earth's crust, usually found in ultramafic rocks, and it is believed to be the second most abundant element in Earth's inner core. It is also greatly recyclable with current technologies, has low toxicity and is exceptionally valuable for a wide range of technological applications (**Figure 4**). [42] In the next section, the state-of-the-art of ALD-processed nickel-based materials will be presented, discussing aspects of their chemical synthesis and outlining current and future technological applications. Interest will be devoted to three different nickel-based compounds, namely nickel, nickel oxide and nickel silicide.

1.3.1 ALD synthesis

In ALD/CVD, metallic nickel and nickel oxide have been obtained using a variety of precursors (**Figure 3**).

The first ALD of NiO was reported in the late 90s and used Ni(II) acetylacetonate ($Ni(acac)_2$) or bis(2,2,6,6-tetramethylheptane-3,5-dionate)nickel(II) ($Ni(thd)_2$), in combination with oxygen, ozone or oxygen plasma as precursors (**Figure 3**, a). This first generation of precursors led to several technical publications suggesting application of this material mainly in catalysis. [43,44]

In the early 2000s, two new ALD precursors appeared in the ALD library: nickelocene ($Ni(Cp)_2$) and Nickel(II) 1-dimethylamino-2-methyl-2-butoxide $Ni(dmamb)_2$ (**Figure 3**, b), which, compared to the previous precursors, showed improved reactivity,

stability, and higher NiO growth per cycle (GPC). [45] Nowadays, these precursors offer an affordable way to produce nickel oxide films that can be converted into metallic nickel via hydrogen plasma or reductive thermal annealing.

Direct deposition of thin metallic nickel films has been achieved by either pyrolysis of $Ni(Cp)_2$ or $Ni(dmamp)_2$, or by ALD in presence of reducing co-precursors such as H_2, NH_3, or plasmas. The reported Ni growth rates from $Ni(dmamp)_2$-based plasma-enhanced ALD (PEALD) processes were 2.0 Å/cycle with NH_3 plasma and 0.8 Å/cycle with H_2 plasma at a process temperature of 250 °C. [46] Thermal ALD processes of metallic nickel have been achieved using $Ni(iPrNCMeNiPr)_2$ and H_2 at a deposition temperature of 250 °C. However, note that the precursor $Ni(iPrNCMeNiPr)_2$ has a decomposition temperature of 180 °C, which implies that the process is not fully compliant with ALD.

However, for the deposition of metallic nickel, almost all ALD processes required harsh processing conditions, involving strong reducing agents, such as hydrogen or ammonia, high temperatures, and/or plasmas. These factors are strongly limiting the implementation of such ALD synthesis into device fabrication because they can induce damages and unwanted modifications to other materials involved in the fabrication process.

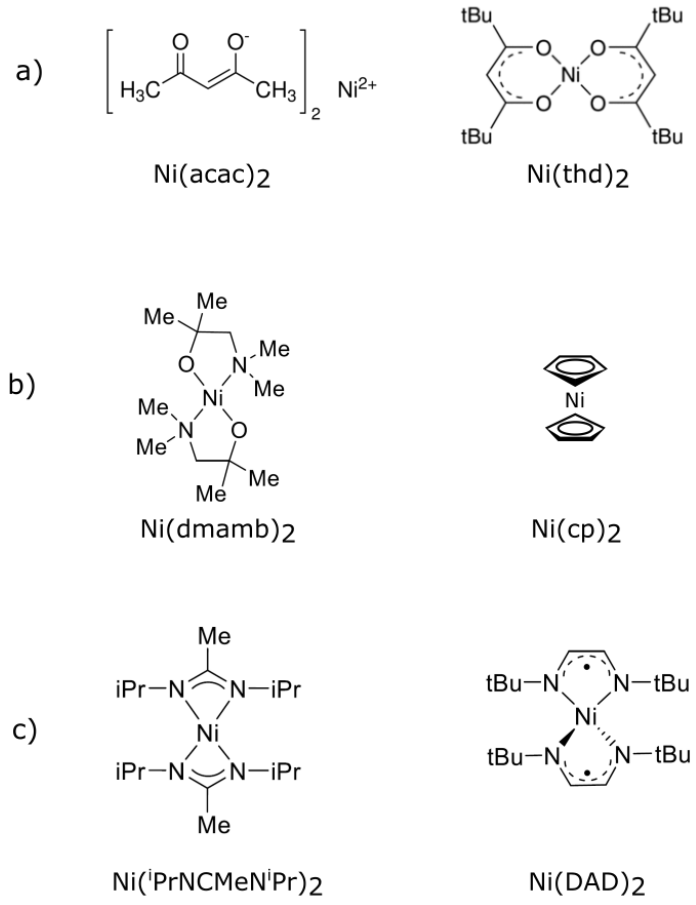

Figure 3: Common ALD precursors for nickel and nickel oxide depositions.

One exception to this trend was proposed in 2018 by Kerrigan et al. from the group of C. Winter, who showed direct nickel deposition using bis(1,4-di-tert-butyl-1,3-diazadienyl) nickel ($Ni(DAD)_2$) [4] (**Figure 3**, c) with tert-butylamine or formic acid. This process was not only performed at temperatures as low as 160 °C and in absence of strong reducing agents, but it was also found to be area-selective to metallic surfaces. Recently, $Ni(DAD)_2$ has also been used in conjunction with ozone to produce high quality p-type semiconducting nickel oxide thin films, [47] highlighting its great potential for various applications.

[4] Also referred to as $Ni(^{tbu}DAD)_2$

Motivated by the recent advances in Ni-precursors chemistry and AS-ALD processing, this thesis aims at providing a multidisciplinary study of nickel-based deposition processes and material systems that range from device and process engineering to chemistry and physics. In this work, $Ni(Cp)_2$ and $Ni(DAD)_2$ precursors have been used in conjunction with different co-precursors to investigate mechanisms and methods for advanced ASD and nanopatterning.

1.3.2 Technological applications

Nickel is a good conductor for both heat and electricity and is, together with cobalt, iron, and gadolinium, one of only four elements that are ferromagnetic at room temperature. Being a transition metal, nickel has valence electrons in two shells instead of one, allowing it to exist in different oxidation states. It is most commonly found in the oxidation state +2 in nickel oxide (NiO), which is a transparent p-type semiconductor with a wide band-gap (3.4-4 eV). Despite its simple composition and cubic rock salt structure, highly crystalline nickel oxide shows antiferromagnetic behavior and tunable optical and electrical properties. [48]

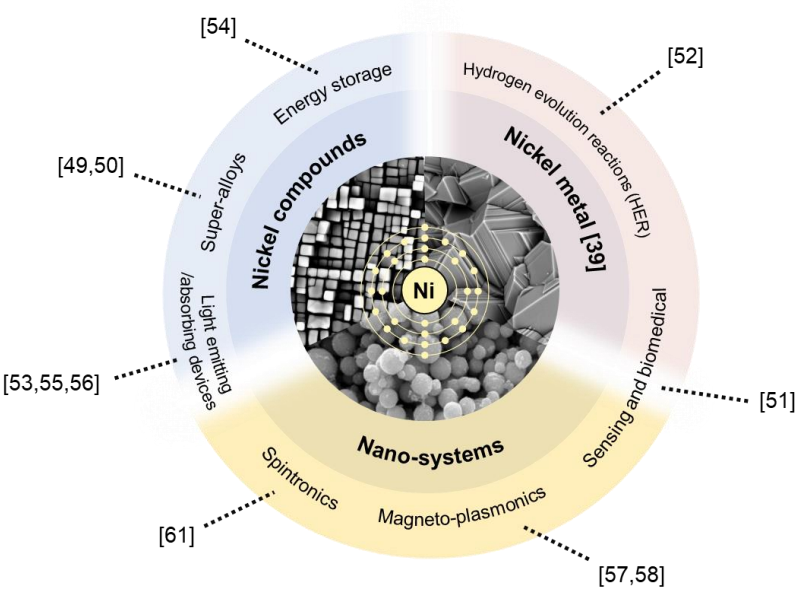

Figure 4: Graphical summary of technological applications of nickel-based materials with the related relevant literature.

In modern times, nickel is excessively used in the aerospace and metallurgical industry as essential component of (super)alloys. [49,50] The application of Ni/NiO nanoparticles is also under study in numerous biomedical applications such as MRI, cell segregation, and drug delivery. [51]

On a large scale, nickel is expected to play an important role as a catalyst for the hydrogen evolution reaction (HER) [52] and in further applications in the energy sector where it has been employed as oxide in next-generation solar cells and OLEDs. [53] Nickel is also a core element in rechargeable nickel-cadmium and nickel-metal hydride (NiMH) batteries. Nickel-containing compounds are also proposed as alternative or supplement to traditional carbon-based cathodes in next generation batteries. [54]

Recent publications show sophisticated ALD processes where the stoichiometry and composition of nickel oxides are finely tuned, enabling its application in photocatalysis as photoelectrode [55] and in photovoltaics as hole transport layer. [56]

Both nickel and nickel oxide are characterized by unique magnetic properties. As a metal, nickel finds application as a ferromagnet in magnetic data storage and various sensing applications (field modulated grating, optical switches, magneto plasmonic nanoarrays). As it will be shown in this thesis, one interesting characteristic that can be exploited is the evolution of plasmonic modes that can be coupled with magneto-optical modes when metallic nickel is shrunk to the nanoscale. This allows to create sensors capable of precisely detecting changes in the medium surrounding the nickel nanostructure. [57,58]

As an oxide, NiO is an antiferromagnet with a Néel temperature of 523 K for single crystalline bulk material, [59] which is lower for the corresponding nano-systems. [60] Its unique properties prompted investigations of applications in antiferromagnetic spintronics, [61] but ultra-high demands on stoichiometry, crystallinity, and dopant concentration pose challenges to its large scale production and commercialization. [62]

The examples of ALD-processed nickel-based materials in the field of magnetism are very limited and most of the publications are related to metallic nickel, typically obtained after a two-step synthesis involving ALD of NiO and its subsequent reduction to the metal by reductive annealing. [63,64]

The antiferromagnetic behavior of thin NiO ALD films has been observed only at temperatures as low as 2 K. [65] The main problem regarding the use of chemical deposition methods of NiO is that the material, without post synthesis treatments, [66] tends to show polycrystalline structure which destroys the antiferromagnetism.

Among the many further compounds that nickel forms, the silicides stand out and find use in silicon transistors, [67] especially if 1:1 stoichiometric. Their interest has risen thanks to the discovery of novel phenomena which arise when these materials are synthetized in specific stoichiometries [68] or in reduced dimensionalities, [69] underlying the lack of understanding of many mechanisms behind their formation and their high potential in future MtM technologies.

1.3.3 Recent trends and challenges

Many future technological applications of nickel-based materials rely on the precise modulation of the material properties through advanced control of composition and shape, while minimizing the processing steps required for its deposition. In the recent years, ALD processes capable of providing spatial control through ASD of both nickel [29] and nickel oxide [31] have been demonstrated, showcasing the enormous potential of these techniques for applications in future technologies.

Simultaneously, AS processes inherit all the intrinsic characteristics that make ALD valuable, such as easy upscaling and ensuring high precision, large volume processing and low cost. However, despite the increase of the number of publications every year, the application of these methodologies is slowed down by the limited reproducibility of the currently known processes and the high costs of the "trial and error"-based optimization of ALD.

One contributing factor is the existence of a large diversification between ALD reactors in industry and research, ranging from old tubular CVD-type reactors to modern industrial setups and custom-built machines. Such diversity is reflected in the broad span of processing parameters reported in literature and the overall tedious optimization compared to PVD methods. More specifically, many commercial reactors are designed for ALD operating at relatively high vapor pressure and with stable precursors which can be easily delivered to reactor even through the longest and most intricate manifolds. Today's new-generation precursors, instead, are designed to have unique and advanced growth properties such as the discussed surface-selectivity but with the trade-off of having thermodynamic limitations such as poor thermal stability and low vapor pressures. These aspects lead to poor precursor delivery in commercial setups, more wasted precursor, and accelerated machine ageing. Many successful depositions reported in literature are obtained through processes of optimization which can include ALD reactor modification or adopting unconventional processing schemes that relegate the reported growth parameters to the unique ALD system used by the authors. Without significant optimization of fluid dynamics, large-scale area-selective depositions remain unattainable. To address these challenges, engineering new ALD machines and reactors, capable of facilitating precursor delivery, reducing waste, increasing reaction yields, and prolonging the machine lifespan, is needed. This aspect could simultaneously be helpful for increasing the reproducibility of processes and accelerating the application of such methods in more device-oriented research.

Another essential pursuit is unveiling the chemical mechanisms underlying novel AS processes, such as growth on defects [38,39] and surface mobility of precursors during selective growth. [70] Unlike PVD, chemical methods heavily depend on the interplay between surfaces and reactants, significantly influencing the deposition outcomes and material properties. Although these interactions complicate the development of novel

ALD chemistries, they also offer unique advantages compared to the physical methods in fabricating new materials and structures. Understanding the surface-precursor interactions could enable direct patterning by controlling the surface chemistry. This can be achieved by creating controlled seeds for area-selective growth, e.g. by introducing surface defects or impurities. Combining direct patterning with ASD holds great potential for incorporating low-dimensional materials into next-generation devices. [40]

The study of gas-solid interactions occurring during ASD for different types of surfaces is certainly fundamental for the advancement of the field, but the investigation of the solid-state reactions that occur between the deposited ALD film and the substrate are equally important, leading to unforeseen AS reactions. In fact, it is very common that freshly deposited thin films are exposed to post deposition thermal treatments to increase the quality of the film. In some cases, even mild annealing conditions can lead to chemical modifications at the interfaces between materials. Due to the low-dimensional nature of these modifications, their impact on the device performance remained unnoticed for many years until more complicated devices, where interfacial effects prevail over bulk properties and determine the performance, were built. A consistent effort must thus be dedicated to the understanding of the solid-solid interfacial reactions that take place between the thin films and the substrates. In this context, extensive effort has been dedicated to study how substrate characteristics such as topography, composition and defect landscape, ALD film characteristics such as thickness and composition, and annealing conditions can be applied to nickel-based thin film systems to promote AS solid-state reactions.

1.4 Thesis motivation and structure of the manuscript

The objective of this thesis has been to study the selectivity mechanisms that can be triggered and controlled during different, industrially relevant, synthetic routes of nickel-based materials.

The primary motivation is to support the progress in the field of ASD by developing experimental and computational tools capable of facilitating ALD processing with different classes of materials. The importance of the ALD tool design and fluid dynamics of the vapors during ALD processing were extensively studied. Two custom-made ALD setups were designed, assembled and tested for the deposition of nickel-based thin films from the precursors $Ni(Cp)_2$ and $Ni(DAD)_2$.

The synthesized ALD materials were utilized for obtaining various nanostructured systems.

In detail, the chapters elaborate on following:

In **Chapter II** an overview of the experimental methods and setups is given.

Chapter III refers to the fluid dynamics studies performed with reactor I, which resulted in an optimization of the ALD process for nickel oxide deposition from $Ni(Cp)_2$ and ozone. The discussion focuses on the delivery of low vapor pressure precursors in ALD systems and the importance of the carrier gas flow. It further describes the effects of static processing conditions in ALD experiments on the precursor consumption.

Chapter IV describes the synthesis of metallic nickel through the reduction of pre-deposited nickel oxide. The study aimed at showcasing multiple applications of this chemical methods to produce structures and metasurfaces which are hardly attainable using other methods. Ultimately, intriguing phenomena involving research fields which were not initially in the scope of this thesis are presented.

Chapter V is dedicated to the development of a methodology that combines direct write patterning via FIB and thermal annealing of nickel-containing thin films to produce area-selective synthesis of nickel silicide nanostructures.

Chapter VI is devoted to the study of ASD of nickel thin films via $Ni(DAD)_2$ and tert-butylamine precursors. For this application, a customized ALD tool (reactor 2) was developed. The second part of the chapter elaborates on the precursor chemisorption mechanisms on different metals and types of substrates.

2

Experimental techniques

Materials can be obtained in form of thin films following many different techniques. During this thesis, Atomic Layer Deposition (ALD) has been the dominantly applied methodology for material synthesis. This chapter describes the technical and mechanistic aspects of this technique to facilitate comprehension of the results presented in the following chapters. A general introduction to the tools and methods used for both material fabrication and characterization will be provided in this chapter. The experimental details which are relevant for the comprehension of the results will instead be discussed in dedicated sections present in each chapter.

2.1 Atomic Layer Deposition (ALD)

ALD is a thin film deposition method which evolved as a modification of the processing scheme of CVD. [71,72] In analogy to CVD, thin film growth is carried out by exposing the target substrate to vaporized chemicals, called precursors. The term precursor, Latin for forerunner, implies that each chemical involved in the growth process is an "ancestor" of the final thin film and needs to participate in a specific chemical reaction to finally lead to the desired material. This aspect defines the key difference between chemical and physical deposition methods being the thin film, in the latter case, obtained by physically transferring atoms of a material from a source to the target substrate. Commonly two precursors are used in chemical vapor deposition methods. In the present work, thin film depositions were carried out using one organometallic precursor as metal source and reactive oxidants or reductants as co-precursors. Typical reactions between two ALD precursors yield volatile species as byproducts which are removed during the process, leaving the non-volatile products bound to the substrate composing the desired thin film. Both ALD and CVD are based on similar or even the same chemistry but adopt different processing schemes to carry out the reaction. Commonly, all precursors used in ALD can be also used in CVD, but not necessarily vice versa. In CVD often the two precursors are present simultaneously in the reactor and are "allowed" to interact in the gas phase, which leads to a time-dependent thin film growth. The growth rate in chemical deposition methods is influenced by two main factors, the precursor mass transport and its chemical reaction kinetics. [73] In PVD methods the thin film thickness is also controlled through a time dependent term (deposition rate).

ALD differs from all the listed thin film deposition techniques as the film growth is not time dependent. In ALD the two precursors are never dosed simultaneously, in this way limiting their interaction to the surface of the substrate only. The process (**Figure 5**, a) starts with the *"pulse"*, i.e., dosing of the first precursor into the reactor. The precursor molecules react with available functional groups at the surface, creating an adsorbed molecular layer. If the precursor dose is sufficiently high, all functional groups of the surface will be saturated and substituted by a layer of adsorbed molecules. Ideally, once the surface is saturated, no further adsorption is possible, independently of the amount of precursor still available in the gas phase or the applied exposure time. Once surface saturation is achieved, the excess precursor is *"purged"* from the reactor and the second precursor is dosed (co-precursor) with another "*pulse*". The co-precursor reacts with the functional groups of the adsorbed precursor forming a first layer of the desired material. Again, this reaction stops when all the reactive sites of the surface are saturated. The excess precursor is removed with a second purging step together with all the volatile reaction byproducts. After this so-called *"ALD cycle"*, the substrate is coated with a first atomic layer (**Figure 5**, a). After an ALD cycle the surface functionality is restored and the cycle can be repeated multiple times until, after a certain *number of cycles,* the thin film reaches the desired thickness. [74]

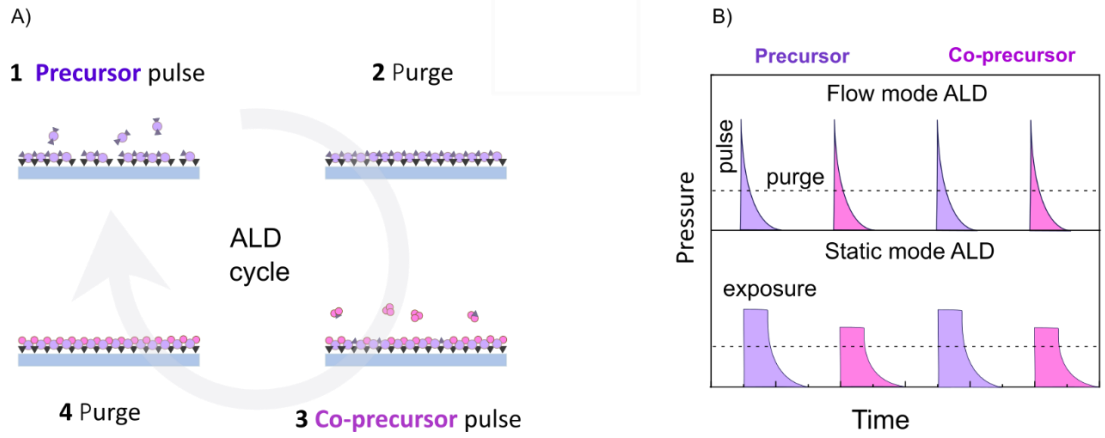

Figure 5: a) Schematic representation of an ALD cycle. b) Comparison of qualitative pressure diagrams of flow-mode and static ALD. The increase and decrease of pressure correspond to precursor pulse and purge, respectively. The presence of a plateau in the pressure curves corresponds to the exposure step during static ALD processing.

Thanks to this unique processing scheme, the growth becomes a function of the number of ALD cycles instead of time, which lowers the experimental error and leads to a superior control over the film thickness. [5] Growth through self-saturation also leads to increased conformality over high aspect ratio structures, making ALD an optimal

[5] In ALD, the rate at which the thin film grows is expressed as growth per cycle (GPC).

industrial solution for high-precision coatings on devices, for example as protective layers. [75]

One trade-off of ALD is that the composition of the thin film and its purity can be non-ideal because of the entrapment of contaminants and unreacted precursors during the growth. For this reason, it is common to apply post-processing steps for improving the material properties.

2.1.1 Process optimization: solid precursors

The coating conformality and thickness control achieved though ALD is the result of sequential saturation of the substrate during each precursor exposure. To work within this optimal conditions, a fine adjustment of the process parameters, namely pulsing time, purging time and temperature, is needed. [76]

The optimal temperature range for processing defines the so-called "ALD window" of a precursor combination. Ideal ALD precursors are highly reactive, thermally stable, and possess vapor pressures sufficiently high to evaporate without additional heating. With such precursors the ALD process optimization can be performed by simply studying the *precursor's saturation plots*, which relate pulsing and purging times to the GPC. Optimal precursor delivery to the surface is obtained by increasing the dosing (pulsing) times until constant GPC values are obtained (**Figure 6**, a). Parasitic CVD, in contrast, can occur if purging times are too short and cause that both precursors are simultaneously present in the reactor. This is corrected by increasing the purging times until the GPC reaches a value which is constant and time-independent (**Figure 6**, b). The simplicity of such optimization can be affected by the fluid dynamics of the reactor and the thermodynamic characteristics of the precursors in use, as it will be extensively discussed within this manuscript. For a traditional precursor, such as TMA, its high vapor pressure at room temperature ensures that, once the cylinder valve is opened during a pulse, its evaporation rate remains constant throughout the whole pulse duration. This ideal case stands in stark contrast to the solid-state, low-vapor pressure precursors used in this thesis.

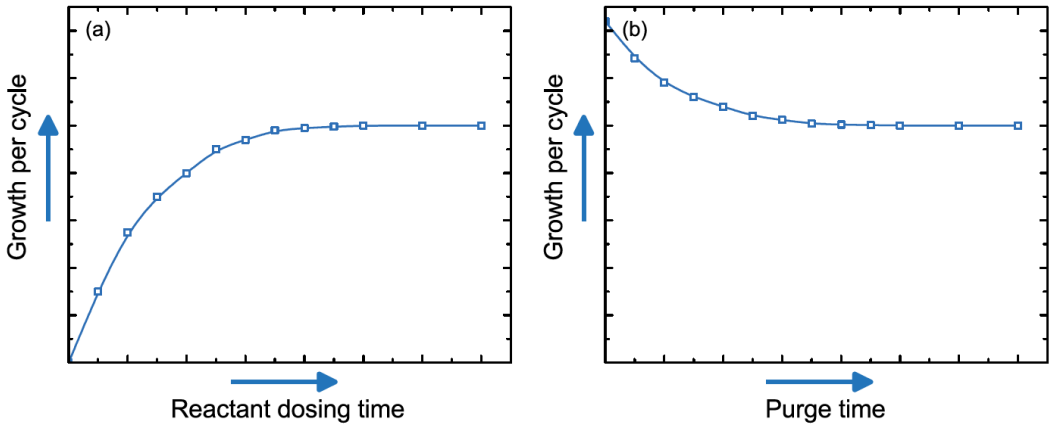

Figure 6: Optimal ALD conditions can be identified by reaching a plateau where the GPC becomes independent of the dosing and purging times. Figure from [76].

Low-vapor pressure precursors are typically solids or liquids that require heating to generate sufficient vapor for a use in ALD. Solid precursors are heated inside a closed container (vapor draw vessel, bubblers, ampoules) for a certain duration to accumulate enough vapor that is finally released into the reactor with a pulse. The time between two pulses, defined as *Idle Time*, should be long enough to saturate the vessel head space [6] with precursor vapor until reaching an equilibrium condition where the pressure built in the headspace (P_p^{HS}) is equal to the precursor vapor pressure (P_p^{VP}) at the chosen temperature.

When the dosing valve is opened and the gas is injected into the reactor, the pressure accumulated in the vessel rapidly drops until reaching the vacuum level ($P_p^{HS} = Pvac$). Once all the vapor phase has been drawn away, additional pulsing will not affect the GPC because at this stage the additional mass delivered to the reactor is negligible. [77]

Considering this, the optimization of processes involving solid precursors is different to standard ALD processes. The optimal pulsing time for saturation conditions cannot be achieved by simply extending the pulsing times, but it depends on multiple parameters such as the vessel temperature, vessel head space and reactor volume, precursor load in the vessel and precursors idle time between consecutive injections.

In an industrial process for high-volume production, optimization would involve high temperatures (slightly below the decomposition temperature of the chemical) to ensure highest sublimation rates (thus shorter idle times and overall processing times). Also, industrial systems are equipped with high volume sublimation vessels that require high precursor loads (tens to hundreds of grams) to ensure short idle times. This approach

[6] The vessel headspace refers to the free volume that can be occupied by the precursor's vapors during sublimation.

is reasonable for shortening the processing time, but it considerably increases the precursor usage.

The optimization of the ALD processes discussed in this thesis (R&D), instead, aims at reducing precursor consumption through designing compact ALD reactors and developing static deposition protocols (See 2.1.3).

2.1.2 ALD tool engineering

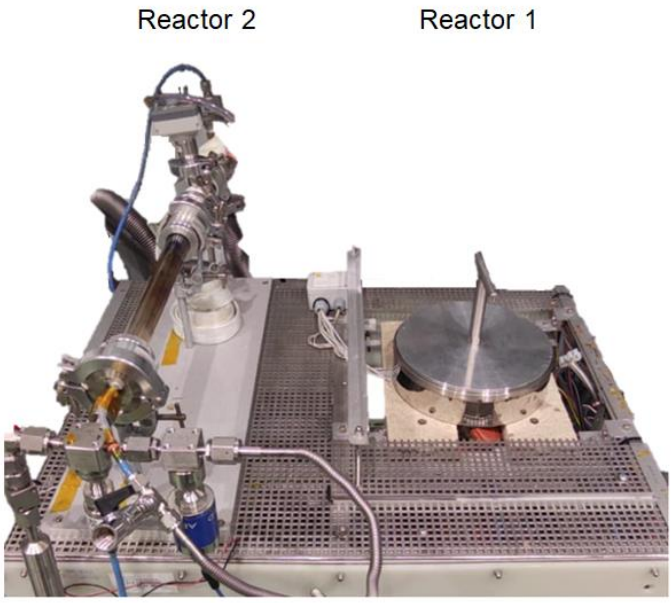

Figure 7: Image of the two reactors mounted on the original frame of the custom-made tool.

2.1.2.1 Reactor 1: *"Galina"*

This ALD system was built over an old platform assembled by Dr. Mato Knez between 2007 and 2009 at the *Max Plank institute* in Halle, Germany. The tool, informally baptized under the name of *Galina*, was originally designed with a high-volume reactor allowing the coating of larger 3D objects (**Figure 11**). During this PhD thesis, the deposition tool went through a complete rebuild including the re-design of the reactor, inlet and outlet lines, precursor's manifolds, and electronics. Even though only few parts of the frame remained unchanged, the main reactor (reactor 1, **Figure 8**) is still named Galina, a female name that was common during Soviet Union and that nicely links to the Russian origin of ALD [71] and to chemistry because it contains in its

spelling seven elements of the periodic table; gallium (Ga), aluminum (Al), lithium (Li), iodine (I), indium (In), sodium (Na), and nitrogen (N).

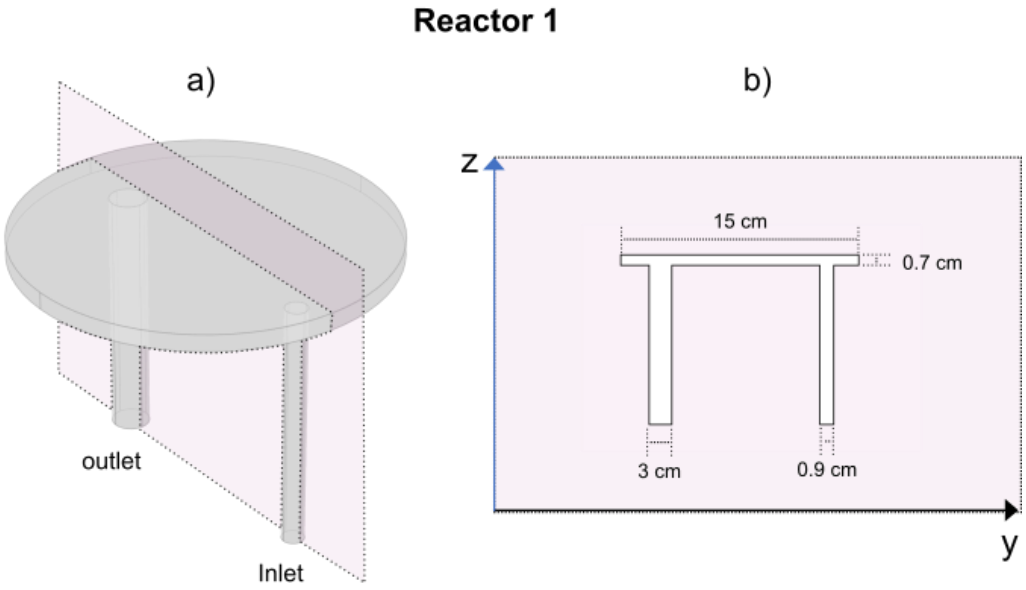

Figure 8: a) 3D graphical design of Galina´s redesigned reactor 1 and b) its geometrical characteristics.

The sketch of the ALD tubing system of the redesigned Galina is shown in **Figure 9**-b. The reactor's inlet is fed through a manifold which has three incoming precursor lines. The two lateral manifold channels are supplying high vapor-pressure liquid/gaseous precursors (line 1 and line 3), while the central channel is specifically designed for the delivery of low vapor-pressure solid precursors (line 2). Line 2 is designed to have a *constricted flow path* [7] to facilitate the delivery of the low vapor pressure precursors to the reactor by forcing the carrier gas through the precursor container before reaching the reactor. Nitrogen carrier gas flow is set with a mass flow controller (MFC) and split into two lines by a 3-way valve mounted downstream (maximum value of 1000 standard cubic centimeters per minute, sccm). One path is normally opened and is connected to the inlet valve of the vapor draw vessel mounted on the central line (line 2). On this line, a valve (V_2 *in*) stops the flow path of nitrogen to the vessel, unless it is opened during the pulsing step. The second nitrogen gas line is normally closed and connected to the two lateral channels of the manifold (line 1 and line 3). By adopting this simple configuration, it is possible to switch between having a constricted nitrogen path through line 2 during the pulsing step from the vessel and a normal steady flow of nitrogen through line 1 and line 3 during the purge.

[7] When referring to constricted flow path it means that during this precursor pulse, nitrogen flows only through the precursor's vessel favoring the precursor's vapor motion towards the reactor.

For depositions involving the use of the vessel, the flow sequence during a complete ALD cycle is shown in **Figure 9**-a.

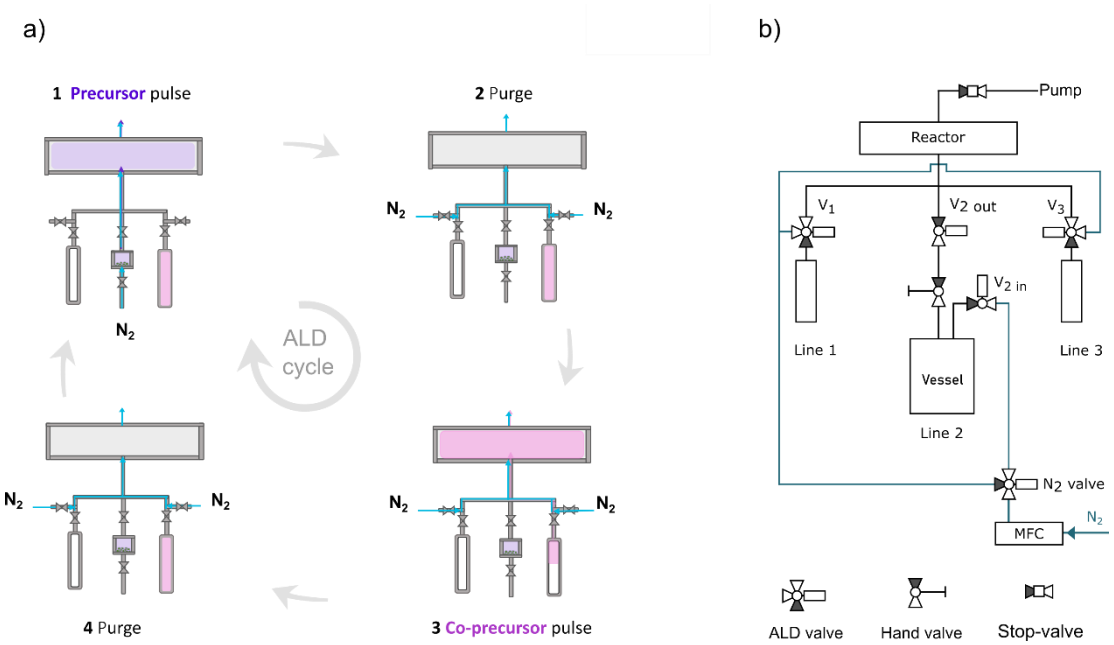

Figure 9: a) Schematic representation of the Reactor 1 gas line system during a complete ALD cycle. b) Detailed scheme of the gas line system of Reactor 1.

The precursor pulses are regulated by the ALD valves. The reactor's outlet has a Pirani gauge mounted upstream with respect to the stop-valve that separates the reactor from the vacuum line. The presence of a stop-valve enables to switch between flow-mode and exposure-mode, which will be discussed in the following section (See 2.1.3). The maximum achievable reactor temperature is 250 °C, while the manifold circuit and the vapor draw vessel can be heated to a maximum temperature of 150 °C. Uniform manifold heating has been maintained to avoid typical issues related to precursor recrystallization on cold spots.

2.1.2.2 Reactor 2: *"Archibugio"*

This ALD reactor was named after a fire weapon from the XVI century due to its tubular look that resembles the barrel of an archaic rifle. [8]

[8] The name was first used by PhD G. Ferrante during a lab visit in March 2023 to manifest his skepticism from an engineering point of view regarding the reactor reliability.

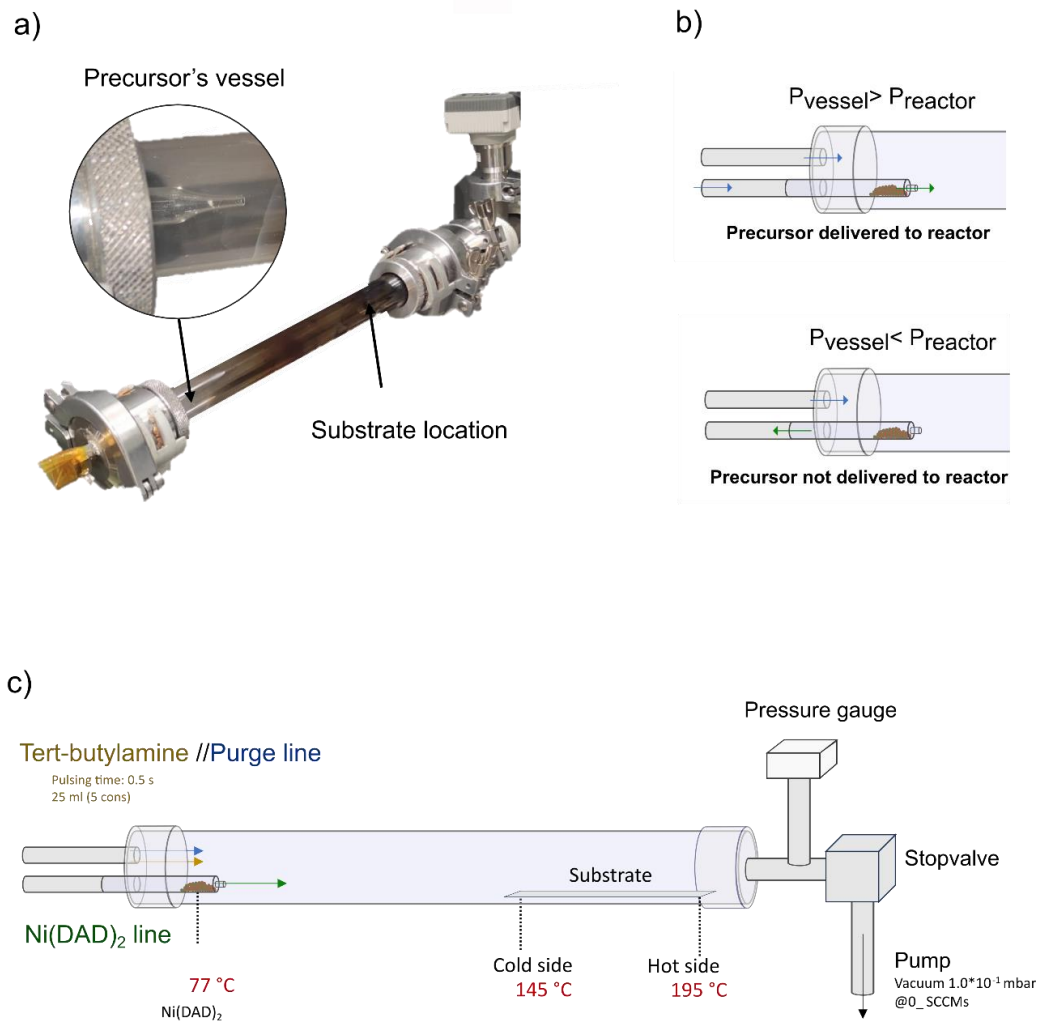

Figure 10: Schematic of reactor 2 showing the a) entire length of the tubular reactor (top) with pipette precursor vessel. b) representation of the nitrogen pressure valve used to suppress continuous precursor delivery. c) Representation of the entire reactor with processing temperature used during the experiments described in chapter VI.

The reactor was built on the frame of reactor 1 with which it shares the carrier gas line and the electronics control. This design was intended for reducing the distance between the solid precursor sublimation location and the substrate to limit precursor waste along the manifold line. The choice of quartz and glass for the parts allows for omitting contact between the $Ni(DAD)_2$ precursor vapors and metallic surfaces that could trigger irreversible adsorption and in this way would also contribute to delivery issues. A glass pipette was used as a vessel (**Figure 10**, a) and mounted inside a quartz tube which served as reactor. **Figure 10**-b shows that no ALD valve is separating the precursor vessel from the reactor. Any possible parasitic CVD contribution that could occur due to continuous dosing of the precursor vapors was suppressed through the carrier gas feed system which regulated the nitrogen carrier gas pressure inside the sublimation vessel, thereby functioning as a virtual valve. During the precursor pulse,

nitrogen flow was set to 20 sccm to reach Pvessel>Preactor, forcing the precursors vapors to exit the pipette towards the substrate. Between the pulses, the pressure condition is inverted to Pvessel<Preactor, causing a precursor motion into the opposite direction where can be crystallized and recovered.

The tubular reactor (220 mm in length and 25 mm of inner diameter) was heated with a temperature gradient increasing from the inlet to the outlet. On the side closer to the precursor the temperature was set to 77 °C, while on the opposite side it was set to 195 °C. One experimental advantage introduced by this approach is that, by placing the substrates in different positions of the reactor, the GPC in the whole applied temperature range can be obtained from a single experiment.

2.1.3 Static ALD mode VS flow ALD mode

Both reactor 1 and reactor 2 are equipped with a stop-valve positioned between the reactor outlet and the pump. This valve can be closed to momentarily disconnect the pump (Edwards Vacuum two stage RV12) to avoid continuous purging of the reaction environment. This adds a degree of flexibility to the tool that can be operated in two different processing schemes (**Figure 5**, b).

If the whole ALD cycle is performed with a stop-valve opened, the machine is operated in the so-called *"flow-mode"*, a condition where the stream of gases and transported precursors is continuously flowing through the reactor from the inlet to the outlet. This configuration helps to speed up processes and is convenient for performing chemical surface reactions with precursors with high vapor pressure and high reaction kinetics.

The second processing scheme is called *"static-mode"*. In contrast to the flow mode, it uses the stop-valve to disconnect the pump from the reactor before the pulses, impeding its evacuation. This allows to extend the exposure of the substrate to precursor vapors, in this way promoting reactions and mechanisms which in a flow-mode are kinetically hindered. Here, the precursor is allowed to fully react with the substrate surface groups or, for the case of porous materials, to infiltrate in the bulk and react with subsurface functionalities. The static-mode approach is commonly adopted for the modification of soft-materials´ properties via *Vapor Phase Infiltration (VPI),* [78] but in the frame of this thesis it was a convenient approach towards performing ALD from low vapor pressure and slow kinetics precursors, facilitating a surface saturation at small precursor doses. In the framework of this thesis, one drawback of this processing scheme is that it led to a higher accumulation of precursor inside the manifold line, causing the need of increasing the purging times.

2.1.4 ALD tool on COMSOL Multiphysics ®

The ALD experiments were complemented with Computational Fluid Dynamics (CFD) studies performed with COMSOL Multiphysics 5.4. [79] This software is based on the finite element method (FEM), consisting of solving partial differential equations for a finite number of points used to define the geometry of the system (here, the ALD reactor). [80] This numerical method requires building a 2D or 3D model of the object and subdivide it into a finite number of domains through construction of a *"mesh"*.

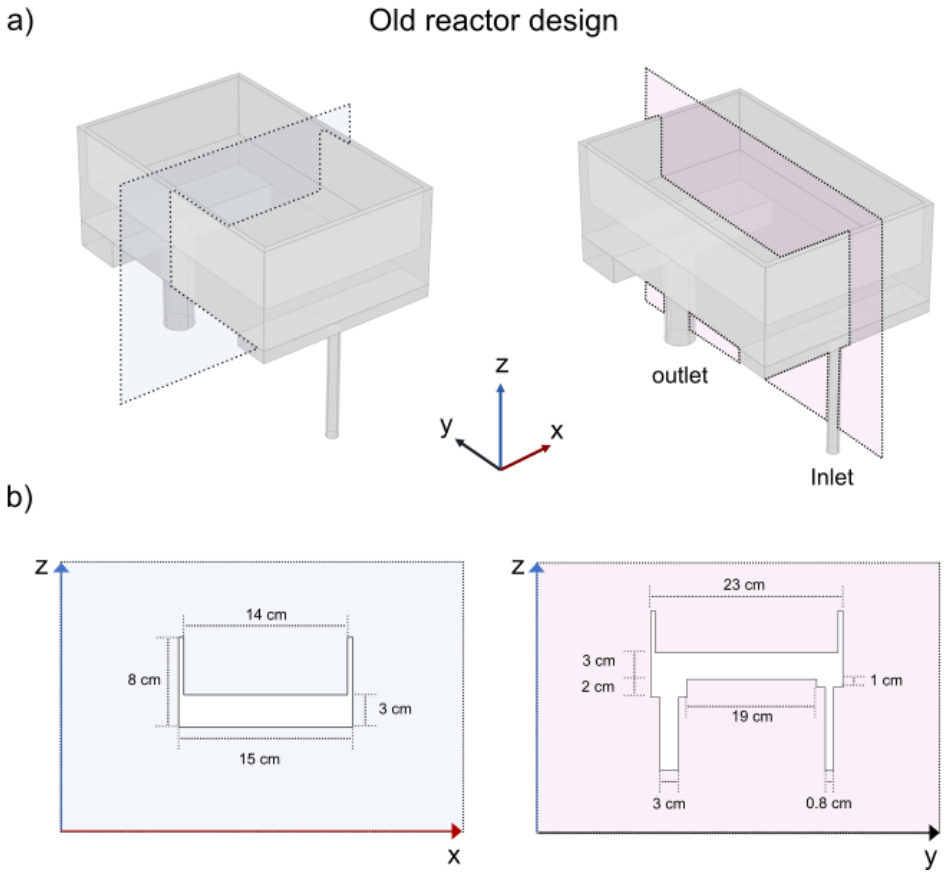

Figure 11: a) 3D design of the original square shaped reactor of Galina and b) its geometrical characteristics.

The geometries that have been constructed to simulate the experiments take into consideration the free volume inside the reactor with the gas inlet and outlet only, that is, all dimensions refer to parts in contact with the carrier gas.

The geometrical description of the original Galina reactor (**Figure 11**) and the re-designed reactor (**Figure 8**) have been used to construct the meshes for the numerical simulations.

Preliminary calculations, based on experimental dataset collected during ALD experiments, were performed to calculate the Reynolds number **Re=uL/v** (u gas velocity, L characteristic length, v Kinematic viscosity) and to determine the fluid flow type. These aspects, together with the results of the different numerical studies, will be discussed in the following chapter. However, for the whole experimental dataset of velocities, the calculated Re numbers were found to be below the critical value of transitional flow, suggesting that the fluid dynamics can be simulated with a laminar flow.

The *"Laminar flow model"* has been used to compute the velocity and pressure profile together with the carrier gas streamlines which characterize the flow of the single-phase fluid (N_2) during a typical purging step. This approach has been already used to describe fluid flow in flow-type ALD reactors. [81]

2.1.4.1 Laminar Flow model

The laminar flow model solves the Navier-Stokes equations for conservation of momentum (Eq. 1) and the continuity equation for the conservation of mass (Eq. 2). Navier-Stokes equations are partial differential equations which govern the motion of fluids. For the general case of a Newtonian compressible fluid, the definition is as follows:

$$\rho\left(\frac{\partial \mathbf{u}}{\partial t} + \mathbf{u} \cdot \nabla \mathbf{u}\right) = -\nabla p + \nabla \cdot (\mu(\nabla \mathbf{u} + (\nabla \mathbf{u})^T) - \frac{2}{3}\mu(\nabla \cdot \mathbf{u})\mathbf{I} + \mathbf{F} \qquad \text{(Eq. 1)}$$

Where $\mathbf{u}$, $\mathbf{p}$, ρ and μ are the velocity, pressure, density, and dynamic viscosity of the fluid, respectively. The four terms of the equation correspond to the forces acting on the fluid: inertial forces (1), pressure forces (2), viscous forces (3), and applied external forces (4).

For each point of the mesh, this set of equations is solved together with the continuity equation:

$$\frac{\partial \rho}{\partial t} + +\nabla \cdot (\rho \mathbf{u}) = 0 \qquad \text{(Eq. 2)}$$

The CFD simulations of the systems solve numerically these equations for each point of the mesh, starting from initial boundary conditions (BC) that were set over inlet and outlet (velocity or flow) together with the walls to impose geometrical constriction to the fluid flow.

2.2 Thermal annealing

The physical and chemical characteristics of thin films can be conveniently modified via post-deposition annealing. In this thesis, this approach has been used to explore processing conditions which were experimentally unreachable with ALD tools during the deposition process itself.

The annealing setup consisted of an infrared (IR) radiation-heated furnace (Mila-5000 from Ulvac-Riko, Inc.) that was used for post-deposition processing of the ALD-grown samples. In this furnace, small substrates are placed onto a quartz holder and inserted in a quartz reactor tube where they can be radiatively heated up to 1000 °C with a near infrared lamp (100V,1kW/pc) (**Figure 12**, a). The furnace is equipped with a water-cooling line and is designed to minimize IR absorption from the internal components of the tool, thereby enabling quick cooling and heating ramps (Max heating rate 50 °C/sec in vacuum). These specifications, together with VCR inlet and outlet ports, make this commercial equipment highly customizable. For the experiments carried out for this thesis, an ALD valve was mounted to the inlet port for dosing gaseous reactants such as oxygen or forming gas (5% H_2 in N_2) in a highly controlled manner. The outlet was equipped with a stop valve separating the chamber from a rotary oil pump (Edwards Vacuum two stage RV12). In this way, two different annealing schemes, conceptually analogous to static and flow ALD modes, were utilized (**Figure 12**, b). The first mode, "static annealing", consisted of evacuating the system, disconnecting it from the pumping line by closing the stop-valve, filling the volume with the desired gas, and heating. The second processing mode, named "pulsed annealing", consisted of supplying the gas to the reactor, once it has stabilized the desired temperature, under constant evacuation. This second processing mode enables an ALD-like processing, which will be extensively described in chapter V.

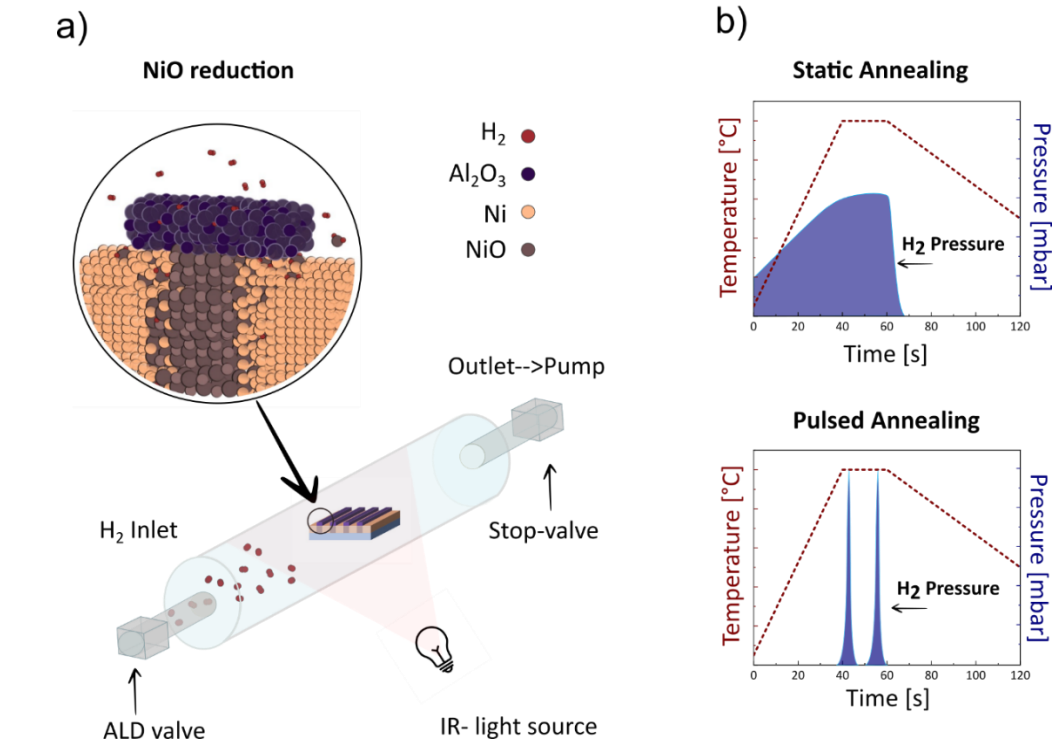

Figure 12: Illustration of the annealing setup for the post-deposition reductive annealing of NiO/Al_2O_3 structures. b) Schematic representation of static and pulsed annealing, the two processing modes used during this thesis.

2.3 Physical Vapor Deposition (PVD)

Physical Vapor Deposition (PVD) is a well-established family of thin film deposition techniques employed within the microelectronics industry for device manufacturing. The two most common methods, thermal or electron beam evaporation and sputtering, achieve deposition via the removal of atoms from a bulk source material through evaporation or high-energy particle bombardment, respectively.

Both methods differ from ALD in the fact that the thin film is physically deposited on the substrate at a time-dependent deposition rate which is influenced by the source-substrate distance and power of the energy source used for the sublimation or sputtering. This enables to achieve fast processing but limits the precision of the thickness control during the deposition. Another significant difference to chemical deposition methods is that, to sublimate or sputter the materials, PVD methods

usually require high vacuum and therefore virtually higher operation costs, with the advantage of depositing high quality materials with low level of contaminations. [82]

2.3.1 Thermal & e-Beam evaporation

Thermal evaporation is an established deposition method where the source material is sublimed through high-temperature heating. This facilitates the mobility of airborne particles, allowing them to directly reach the substrate and solidify. Typically, a crucible heater is used to heat up the source material.

For e-beam evaporation, the source material is sublimed using an intense beam of high-energy electrons. The thermionic emission of electrons is induced by a hot filament. These electrons provide the necessary energy for evaporating the source material.

In this thesis:

Au, Pt and Ni films were deposited via thermal/e-beam evaporation using the Kurt Lesker PVD 75 e-beam/thermal evaporator available at CIC nanoGUNE BRTA.

2.3.2 Sputter deposition

Thin film deposition by sputtering has been a common technique in the coating industry since the 70s. In this methodology, a stream of energetic particles, generated by plasma discharge, is directed onto a target (or cathode). The bombardment causes the liberation of atoms or clusters from the target into the vapor phase and their subsequent deposition onto a substrate producing a thin film. The particles or clusters are typically accelerated towards the substrate with an electric field. In the case of magnetron sputtering magnets are used to increase the probability of electron-atom collision on the target, increasing the deposition rate and reducing unwanted heating of the substrate.

Despite sputtering being a widely accepted quality standard for material deposition in the microelectronics industry, its directional nature (line-of-sight deposition) constrains the coating of high-aspect ratio features, particularly for feature sizes below 250 nm.

In this thesis:

Pt, FeO_x, Au, CrO_x were deposited using the AJA ACT 2200 UHV and Quorum Technologies (Q150 T ES) sputtering systems available in CIC nanoGUNE BRTA.

2.4 Scanning Electron Microscopy (SEM)

Scanning electron microscopy (SEM) is one of the most powerful characterization techniques in nanoscience. It can be used as imaging technique for surface examination or compositional characterization. It is also widely used in so called "dual beam" microscopes for nanoscale manipulation and advanced characterization of sub-surfaces and cross-sections. It is also extensively used for pattern writing in e-beam lithography. [83]

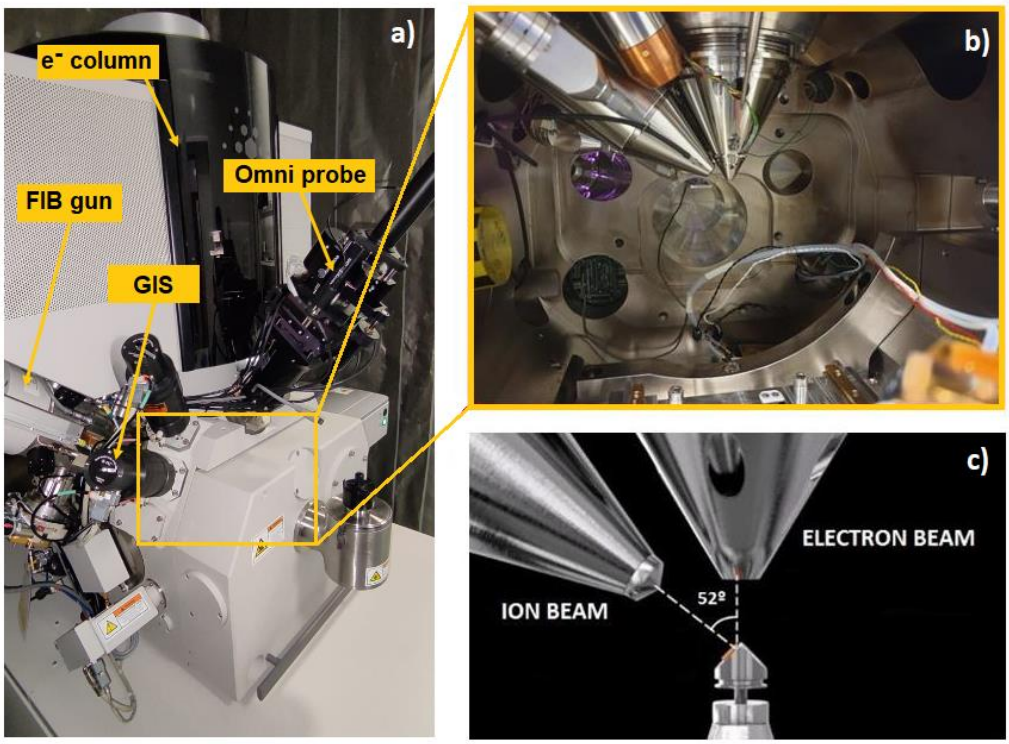

Figure 13: a) Photograph of the FEI Helios 450S, labelled with the main futures. b) Photograph of the microscope chamber; c) schematic view of the aligned ion and electron sources with a 52° angle between them.

2.4.1 SEM/FIB dual systems

A SEM/FIB dual beam system consists of an SEM microscope coupled with a focused ion beam (FIB) gun (**Figure 13**, a). The electron gun is positioned perpendicular to the sample stage, while the ion gun is generally tilted by 52° with reference to the electron gun enabling to simultaneously observe and manipulate the specimen from different angles (**Figure 13**, b-c).

The microscope is also equipped with microfabrication tools, such as probes, to manipulate nano/micro-sized objects, and Gas Injections Systems (GIS) to perform local electron and ion beam assisted material depositions (**Figure 13**, a). For compositional characterization, the microscope is also equipped with an energy-dispersive X-ray spectrometer (EDX detector).

In this thesis:

- The FEI Helios 450s microscope (Thermofisher, USA) was utilized for nanofabrication and characterization including morphology and compositional investigations, surface modification and patterning, three-dimensional characterization through cross-sectioning, and lamellae preparation for transmission electron microscopy (TEM). SEM measurements were conducted at different accelerating voltages, ranging from 1 to 20 keV, depending on the characteristics of the samples. The FEI Helios 450s is equipped with an EDAX Octane Pro detector which enables quantitative measurement of chemical composition and mapping of surfaces and cross-sections.

2.4.1.1 Topographic and compositional imaging

SEM employs condenser lenses to focus an electron beam onto the specimen surface, scanning it line by line with a spot diameter of 0.4-5 nm. At each spot, the electron bombardment causes electron emission from the specimen (**Figure 15**). The image of the surface is then constructed by re-collecting the electrons coming from the surface with various types of detectors. The interactions between the incident electron beam and the specimen electrons can be categorized as elastic or inelastic scattering. Inelastic scattering occurs through various interactions, potentially leading to ionization of the specimen matter and excitation of electrons. Upon relaxation of the excited electrons, secondary electrons (SE) are emitted. Although SE lack information about the elemental composition, they offer high spatial resolution and are valuable for investigating topography changes and for high-magnification imaging. Elastic scattering refers to interactions between the incident electron beam and atomic nuclei or outer shell electrons. The primary electron undergoes minimal energy loss but changes its direction significantly in a wide angle, producing backscattered electrons (BSE) with scattering angles exceeding 90°. The BSE signal intensity depends strongly on the mass of the nucleus, enabling display of the mass contrast on the specimen surface. The detection of backscattered electrons, performed with concentric backscatter (CBS) detector, can thus be advantageous for imaging domains of different composition which would be topographically indistinguishable (for example with 2D materials). However, the BSE signal originates from greater sample interaction volumes, resulting in a deteriorated spatial resolution.

2.4.1.2 Elemental characterization via EDX

Electron-atom interactions in SEM provide valuable spectroscopic information, enabling in-situ chemical characterization of specimens through EDX. Atoms possess discrete energy levels associated with their electrons. The incident primary electrons can excite and remove an electron from an inner shell, creating an electron void. Simultaneously, an electron from a higher valence shell fills this hole, emitting an X-ray photon.

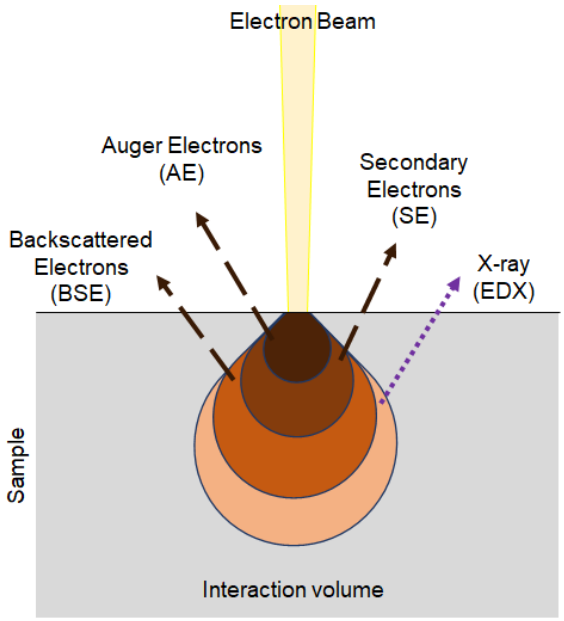

Figure 14: Representation of the various emissive phenomena occurring during electron bombardment in SEM imaging and EDX analysis and their sensitivity to the volume of the specimen.

An energy-dispersive spectrometer collects these X-rays whose energy is indicative of the energy difference between the shells and the atomic structure of the emitting element. Consequently, precise identification of the specimen's chemical composition is achievable.

2.4.1.3 Matter manipulation

The FIB technique, like SEM, enables surface imaging but most importantly, due to the high mass of accelerated ions hitting the surface, it enables matter manipulation and patterning. Focused ion and electron beams offer the capability of in-situ thin film deposition via focused ion/electron beam induced deposition (FIBID/FEBID). While electrons preserve the surface integrity during deposition, ions, thanks to higher

effective cross- section, lead to milling and ion implantation and allow local deposition of materials (FIBID) as well as selective milling of the surface.

On the Helios 450 instrument, Pt layers have been locally deposited using electron and ion beams through FEBID and FIBID. To achieve this, a precursor gas, trimethyl(methylcyclopentadienyl) platinum (IV) (MeCpPtMe3), is introduced into the SEM/FIB chamber using a gas injection system (GIS). Subsequently, the surface is scanned with electron or ion beams, causing the precursor to decompose and selectively form a film in the irradiated area. The in-situ deposition on Pt is commonly used for cross-section cutting and lamella fabrication (**Figure 15**). This process is performed with SEM/FIB microscopes by combining different steps of deposition and milling.

The first step consists of sputter-depositing a conductive carbon layer on the surface to enhance the contrast between surface and subsequent layers. For non-conductive specimens this layer helps to dissipate surface charges which occur upon beam exposure. A protective platinum layer is then deposited in selected areas. To preserve the specimen surface, a 15µm (X) x 1.5µm (Y) x 200nm (Z) Pt layer is first deposited via FEBID. Electron-assisted deposition is preferred to ion-assisted to not induce any physical damage of the surface during Pt deposition. A thicker Pt layer of 15µm (X) x 1.5µm (Y) x 1.5 µm (Z) is then deposited at a tilt angle of 52° using an ion beam (**Figure 15**, a). Subsequently, a staircase bulk-out etching is performed with ion currents of 1-2.5 nA until an etch depth of 6-8 µm is reached (**Figure 15**, b). The lamella is then extracted (**Figure 15**, c) and thinned down to less than 100 nm thickness, using low ion beam energies for the final polishing (**Figure 15**, d). A typical indication of an appropriate thickness for the TEM analysis is the occurrence of transparency of the lamella with an electron beam acceleration voltage of 3-5 kV.

The TEM analyses presented in this thesis were conducted in collaboration with the group of electron microscopy at CIC nanoGUNE, using a TEM FEI Co. Titan 60-300.

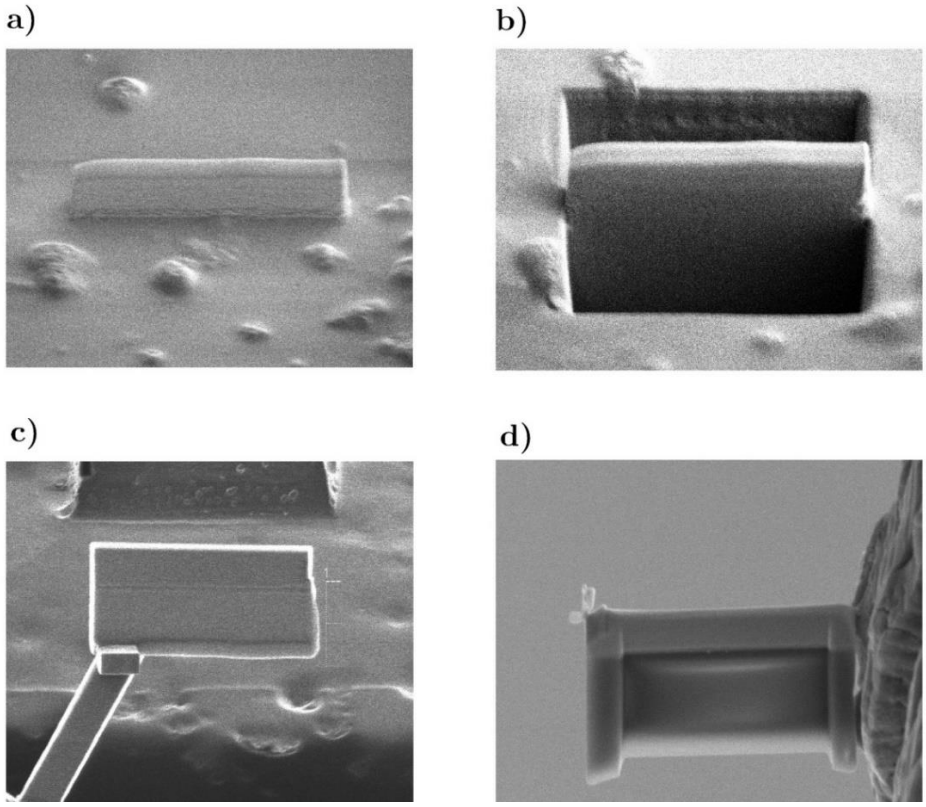

Figure 15: The four main steps of lamella fabrication, starting from a) Pt deposition via FEBID/FIBID; b) side excavation and cut with a FIB; c) lamella picking with a micromanipulator and Pt GIS for bonding; d) thinning and polishing of the lamella before TEM.

2.5 Resist-based fabrication

During this thesis, two main lithography-based fabrication pathways have been followed to fabricate the desired structure. The label *"eBL+ deposition"* will be applied whenever the resist deposition occurred before the "active material" deposition (**Figure 16**, a). In contrast, *"eBL + etching"* will be used for demarking the route of first depositing the active material thin film, followed by resist deposition and patterning, and ultimately subjected to argon ion milling to remove the active material from the exposed areas (**Figure 16**, b). These two pattern transfer methods constitute the core techniques in present day nanofabrication. [84]

2.5.1 Electron Beam Lithography (eBL)

One of the applications of scanning electron microscopes is the pattern generation in lithography. A focused e-beam is used to write a pattern on an electron-sensitive polymer that is then employed as a stencil for the pattern transfer via deposition or etching. [85]

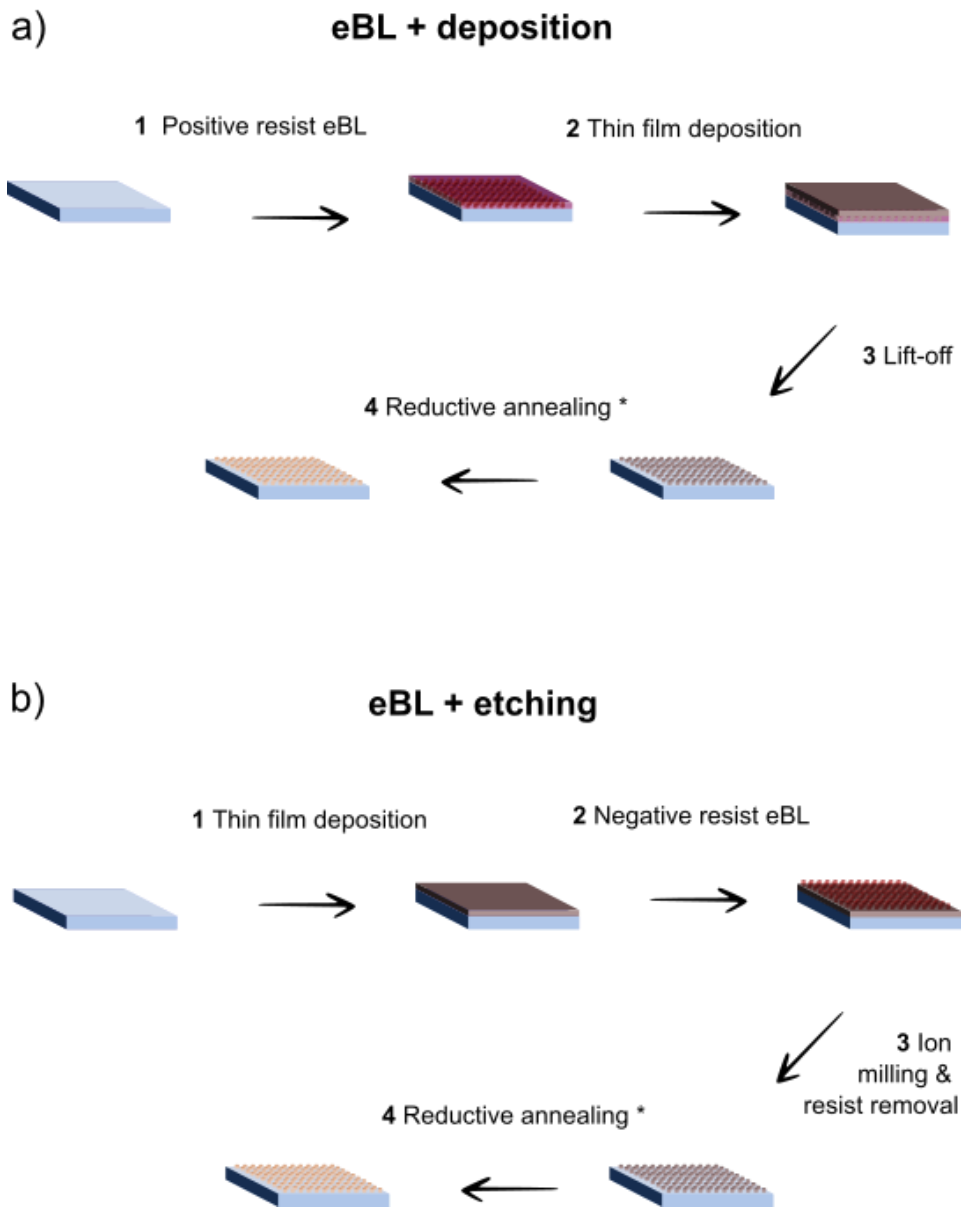

Figure 16: a) Lithography-based method consisting of resist spin coating and patterning, followed by thin film deposition and lift-off. b) Fabrication methodology based on thin film deposition, resist patterning, etching, resist removal. The last step of reductive annealing refers to NiO→Ni reduction, which is discussed in the following chapter.

First, the e-beam sensitive resin, technically called "resist", is deposited on the substrate via *spin coating*. This step consists of drop-casting the resin on the substrate and then spinning it to remove its excess and leave behind a homogenous thin film on the surface. After resin curing via baking, the e-beam is used to *"write"* the desired pattern locally onto the surface. A controlled dose of electrons changes the exposed resin chemically, altering its solubility in various solvents. In this way, during "*development*", it is possible to selectively remove either the exposed or unexposed resist by immersing the sample into a choice of solvents. We differentiate between two categories of resists: In positive tone resists the chemical bonds are broken when exposed to the e-beam, making them easily removed during the development, while negative tone resists are opposite. Here, the exposed areas remain on the surface after development. After the development, the patterned area is used as a stencil for pattern transfer by using subtractive or additive techniques (**Figure 16**). After pattern transfer the resist is removed in a step called *"lift-off"*. For both eBL+deposition and eBL+etching, the fourth step of reductive annealing is marked with a "*" because it was applied only for the case of nickel oxide reduction to metallic nickel.

In this thesis:

The electron-beam lithography (eBL) systems available at CIC nanoGUNE BRTA are the *e-line*$^{+}$ and the *150-two* from *Raith nanofabrication.*

❖ **Substrate cleaning before resist application**

To remove major contamination, the substrates were cleaned following these steps: 1) dip into acetone and sonication for 5 min., 2) dip into isopropanol (IPA) and sonication for 5 min., drying with nitrogen gas. Fine cleaning and improvement of resist adhesion was performed by plasma cleaning at a pressure of 1 mbar, using 10 sccm of oxygen flow at a power of 100 W for 5 min.

❖ **Resist selection**

For the devices made following eBL+deposition, double layer PMMA950A4/PMMA495A2 was used. Each of the two layers was spin-coated at 4000 rpms (1000 rpm acc) for 1 minute followed by a baking step of 90 s. An additional step of 2.4 nm of gold sputtering was used for all the samples requiring insulating substrates. eBL patterning was performed using 10 kV accelerating voltage, 30 μm aperture and doses of 110 $\mu C/\mu m^2$. Development was performed by immersion in MIBK/IPA 1:3 for 45 seconds, followed by in IPA for 45 seconds and drying using a

nitrogen gun. [Nickel nanoarrays (Chapter III) as well as the *sample c* used for AS-ALD of $Ni(DAD)_2$ and tert-butylamine (Chapter VI), were fabricated following this lithographic processes.]

Single layer PMMA950A2 was used only for samples fabricated following eBL+etching. The resist preparation and patterning are analogous to the ones described for double layer PMMA. [NiO/Al_2O_3 samples for pulsed annealing experiments (Chapter IV) as well as defective seed points on silicon for AS-silicidation (Chapter V) where fabricated using this process.]

Negative tone resist Ma-N-2401 was exclusively used for fabrication of the nickel nanoarrays used for plasmon resonance characterization (Chapter III) following the eBL+etching procedure described in **Figure 16**, b.

2.5.2 Argon ion milling

Ar-Ion milling is a common method used for precise material removal by highly energetic ions of an inert gas (Ar in this case). This process, if performed in a controlled way, enables to remove a target material at a precise rate.

In this thesis:

The system in use at CIC nanoGUNE BRTA is the ion-beam etcher by *4Wave inc.*

- **Low-incidence angle Ar-ion milling** has been used to facilitate the lift-off of ALD materials deposited on Au masks (Chapter III) or for removing sharp vertical edges after the lift-off. Such artifacts can form on the sidewalls of the resist. In both cases the experimental procedure is identical. The sample is rotating at 15 rpm, the Ar-ion beam is applied with an incidence angle of 80° relative to the normal of the surface, thereby milling the substrate from the side.
- **Ar-ion milling** has been used for pattern transfer from a resist (used as mechanical mask) to an underlying thin film or substrate (**Figure 16**, b). The sample is rotating at 15 rpm. The ion milling is performed with a 10° incidence angle with respect to the normal of the surface. The Ar-ion flow is set to 15 sccm.

The optimal beam parameters depend on the material to be etched and are summarized in Table 1.

Table 1: 4Wave Ar-ion miller etching parameters.

Material	Accelerating Voltage[V]	Beam current[mA]	Beam voltage[V]	Milling Rate
NiO	**300**	**50**	**300**	**5 nm/min**
Au	**300**	**50**	**50**	**14 nm /min**
Al_2O_3	**300**	**50**	**50**	**1.15 nm/min**

2.6 Materials/device characterization

2.6.1 X-ray spectroscopy

X-ray diffraction (XRD) is a technique used to determine various characteristics of a material such as, its crystallinity, phase composition, and crystallite size. When a material is exposed to an X-ray beam with the wavelength λ at different angles of incidence Θ, the electrons in the material scatter the beam. This scattering results in most of the waves experiencing destructive interference, unless the Bragg diffraction condition is fulfilled:

$$n\lambda = 2d\sin\Theta \quad \text{(Eq. 3)}$$

The diffraction pattern resulting from the interaction of the X-rays with a crystal provides information about the crystal's electron density, which can be analyzed through Fourier transformation.

Similarly, X-ray reflectivity (XRR) is a surface-sensitive technique that shares a similar setup with XRD. Here, X-rays reflected from a crystal are analyzed at an angle equal to the incident angle. By studying the reflected X-rays, characteristics like the thickness, density, and roughness of thin films can be estimated.

In this thesis:

XRD and XRR data have been collected with a PANanalytical X'Pert Pro diffractometer using Cu K$\boldsymbol{\alpha}$ radiation with a $\boldsymbol{\lambda}$ of=1.54 Å. The GPCs of the ALD

experiments were calculated by dividing the XRR-measured film thicknesses with the numbers of applied ALD cycles.

2.6.2 X-ray Photoelectron Spectroscopy (XPS)

X-ray Photoelectron Spectroscopy (XPS) is a technique employed to investigate the chemical composition and the overall electronic structure of a surface. Derived from Hertz's photoelectric effect, XPS involves the interaction between an electromagnetic incident radiation of known energy (X-ray) and material leading to electron emission. The energy of the emitted electrons ($E_{kinetic}$) can be measured using a hemispherical electron detector, enabling the calculation of the binding energy ($E_{binding}$) of the electrons in the sample using:

$$E_{binding} = E_{photon} - E_{kinetic} - \Phi_{sp} \quad \text{(Eq. 4)}$$

Here, Φ_{sp} represents the work function of the spectrometer and E_{photon} is the energy of the incident photon. XPS proves valuable for analyzing the chemical environment of specific atoms, as different elements produce characteristic peaks reflecting their electronic configuration. The intensity of these peaks depends on the element concentration in the analyzed volume, with relative sensitivity factors of each element being taken into consideration.

Electron scattering within the material determines that the electron signal reaching the detector is mainly coming from the very few atomic layers of the surface (up to few nanometers) as the number of electrons capable of escaping the material exponentially decays as we move into the bulk of the material.

When combined with a sputtering system, XPS becomes a potent tool for investigating the chemical state changes in a depth profile, as spectra can be recorded after each etching step. If equipped with dedicated antechambers or chamber configurations, *in vacuo* synthesis is also possible to reproduce some experimental conditions.

In this thesis:

- The XPS data discussed in this thesis result from a collaborative work with C. Rogero, M. Ilin and J.E. Barcelon at the Materials Physics Center (CFM) of the Spanish national research council (CSIC) in San Sebastian, Spain. XPS was performed with a SPECS instrument equipped with a source of monochromatic Al Kα X-rays (E_{photon}=1486.7 eV). Analysis of the XPS spectra was performed using the Casa XPS and the Origin 2018 software. Binding energy correction was

performed relative to the C 1s peak, located at a binding energy of 284.8 eV, originating from the organic carbon in the substrates. The spectra were fit with sets of Gaussian-Lorentzian functions with Shirley background subtraction.

2.6.3 Magneto Optical Kerr Effect (MOKE) microscopy

The interaction between electromagnetic radiation and magnetic fields within materials leads to the manifestation of magneto-optical (MO) effects capable of modifying both the polarization state and the intensity of light after interaction with the substrate. In instances where this magneto-optical interaction is studied by analyzing the light that is reflected from the sample, the phenomenon is defined as magneto-optical Kerr effect (MOKE). A prevalent methodology for studying this effect involves the utilization of a MOKE microscope, an instrument which integrates optical and electronic components required to produce and measure MO effects on a conventional optical microscope.

Along the incident light path of the microscope, additional features include an aperture diaphragm and a polarizer which manipulate the incident light to generate the characteristic "extinction cross" pattern in the back focal plane of the microscope. [86] By deliberate configuration of the extinction pattern and alignment of the sample magnetization axis, distinct variants of the Kerr effect can be selected (**Figure 17**). In the present research, the configuration enabling Longitudinal Kerr effect measurement, wherein the magnetization vector lies in the plane of the sample surface and is aligned with the incidence plane, was adopted.

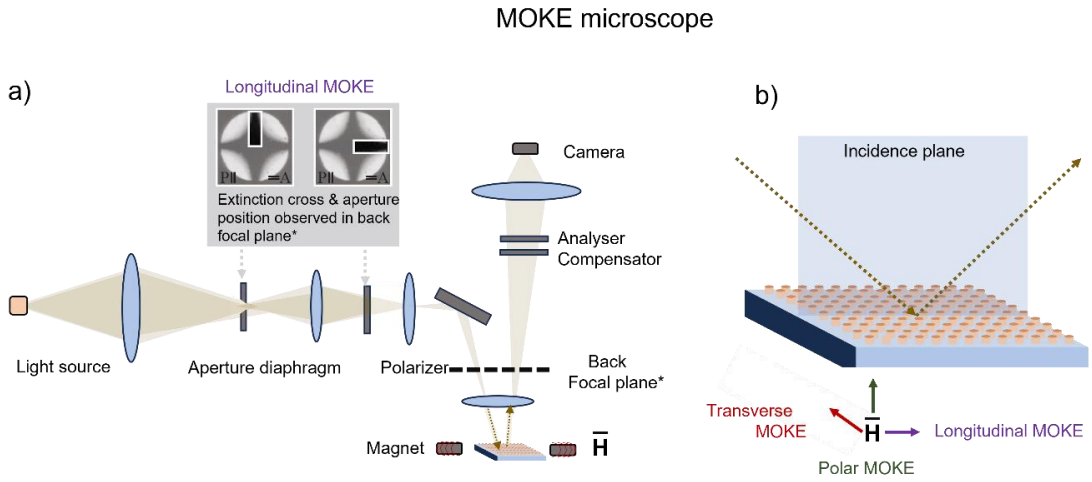

Figure 17: a) Schematic of the setup of a MOKE microscope (adapted from [86]). b) Different magnetization axis H respect to incidence plane determining different MOKE configurations.

Following the reflection from the magnetized sample, an analyzer in the outgoing light path assumes a pivotal role. Coupled with a compensator designed to rectify any ellipticity in the reflected light, this setup transmutes alterations in polarization, attributable to the Kerr effect, into corresponding light intensity changes. Such intensity fluctuation is readily detected and quantified through a detector placed at the terminal point of the optical pathway. [86]

In this thesis:

The MOKE microscope used for the MO characterization is a custom-made instrument by P. Vavassori available in BRTA CIC nanoGUNE.

- MOKE microscopy has been employed to measure hysteresis loops of ferromagnetic materials (Chapter III-IV). The measurements have been carried out by exposure of the samples to an increasing magnetic field ($\mathbf{H}$) until $\mathbf{H}_{max}$. Then, the field is gradually decreased to zero and increased again in the reverse direction until reaching again $\mathbf{H}_{max}$. The magnetization of the sample ($\mathbf{B}$) is recorded as a change in the MOKE intensity as function of the applied magnetic field. In NiO samples, the formation of a ferromagnetic nickel phase is detected through the appearance of a hysteresis loop. The ferromagnetism is associated with the presence of residual magnetization, defined *remanence* ($\mathbf{B_r}$), that can be removed only by applying a magnetic field, known as *coercive field* ($\mathbf{H_c}$), in the reverse direction. [87]

3

From vapors to solid thin films

This chapter evaluates the combination possibilities of ALD experiments and computational fluid dynamics (CFD) for facilitating ALD reactor design to improve its efficiency and lower the costs of research.

Conventional optimization of ALD processes bases on iteration of deposition runs with optimization of individual process parameters. Applying this approach to processes that utilize solids, such as the Ni-precursors used in this thesis, can generate massive experimental effort because of the large number of variables affecting precursor mass delivery (See 2.1.1). Computational methods are nowadays robust enough to allow simulation of experimental conditions and drastically reduce the number of physically performed processes.

The objective of the present study is the reduction of surplus precursor, which is otherwise wasted, and the development of cost-effective processing protocols that can facilitate the study of new ALD chemistries based on expensive precursors such as $Ni(DAD)_2$ (Chapter VI). Also, from an ecological perspective, this study points out that the industry-driven ALD optimization, involving fast processing and high precursor doses, can be advantageous to produce large area coatings but becomes counterproductive for AS depositions where the target thickness and surface coverage is low. [88]

3.1 ALD tool engineering: The role of CFD

The fluid dynamics of gases inside ALD reactors can influence the characteristics of the resulting thin films, including conformality and homogeneity, and affect ideal layer-by-layer growth through parasitic CVD contributions (inefficient purging) or desorption (high purging gas flows). When ALD is used as pure coating technique, these flow-deriving issues can produce minor effects that often are manifested as slight deviations from the ideal GPC. Instead, for advanced area-selective ALD purposes, such as the ones that will be discussed during this thesis, fluid dynamics can have a profound impact on the outcome of the experiment. For example, phenomena of parasitic CVD, occurring between precursors in the gas phase, can produce uniform coatings independent on the underlying substrate. If such growth type is not avoided during the deposition, the growth resulting from the actual substrate selectivity can

be concealed. Similarly, high fluid velocities during the dosing and purging steps can hinder absorption or increase desorption, suppressing the mechanism of selective growth.

The different fluid dynamics of reactors can in fact have strong implications on material synthesis and, as it will be discussed during this thesis, leads to different outcomes even for virtually identical processes. [89,90]

Since the early 2000s, numerical studies related to ALD mainly involved modelling surface-precursor interactions by Molecular Dynamics (MD) and Density functional Theory (DFT) simulations, [91] while approaches utilizing computational fluid dynamics (CFD) are scarce. CFD is a crucial tool for engineering machines, while MD and DFT are common routes for modelling chemical reactions of molecules with their environment. Each approach provides a distinct insight into the same problem. The fluid motion inside a constricted path, defined by the machine architecture, determines temperature and velocity fields of gases inside the reactor as well as precursor concentrations interacting with the surfaces during film growth. For these reasons, fluid dynamics intrinsically impact the surface chemistry during the experiments and should be considered when defining the conditions of DFT and MD models. [89]

The implementation of a simple CFD model which allows us to understand some stages of an ALD experiment can significantly lower the experimental load and provide information that would otherwise be inaccessible. ALD reactors commonly acquire pressure and temperature data, unless specific *in-situ* monitoring systems, such as a quartz crystal microbalance (QCM) or FTIR, are installed. This lack of information leads to trial-and-error process development by addressing individual parameters to finally optimize the whole parameter space. This type of optimization can become tedious and expensive, especially when dealing with non-ideal ALD precursors. Here, optimization of the tool design through fluid dynamics studies can be helpful. Each ALD reactor type has its individual design regarding volume and shape, precursor supply lines, etc., which impact the carrier gas volumetric flowrate, pump vacuum level and ultimately the temperature distribution. All these factors can contribute to deviations from the optimal growth rate and without knowledge about the flow inside the reactor, these contributors are difficult to identify.

One common contributor to this deviation is insufficient purging of the system. If the flow of the purging gas is not optimized for efficient removal of the excess precursor from the reactor, this can lead to an increment of the film growth due to parasitic CVD. Commonly, a solution is the increase of the purging time, but sometimes, as it will be discussed, these contributions are simply inherent to the reactor design and cannot be completely suppressed by adapting the processing parameters.

3.1.1 Modelling the reactors shape and carrier gas flow

To study the purging step of the "Galina" ALD reactor, a simple CFD model of the laminar flow of the carrier gas inside two different reactors, i.e., the original square-shaped and the newly developed cylindrical reactor, has been developed, according to previous studies on flow-type reactors. [81] The results of these simulations have been considered for re-designing the reactor and the gas lines (described in experimental section) to facilitate precursor delivery during the pulses and suppress CVD-type of growth.

The results of the simulations depict a precise timeframe of the purging step where, after pulsing and purging the reactor to a steady pressure state, the rotary pump does not generate any fluid flow anymore and higher vacuum can only be achieved with stronger pumps, like molecular pumps. The flow in this stage is still not molecular because the reactor is supplied with a carrier gas (N_2) whose flowrate entirely determines the velocity field inside the reactor.

The 3D geometries of the free space of the original square shaped reactor of Galina (**Figure 11**), as well as the re-designed cylindrical low volume reactor (**Figure 8**), were used to construct the mesh for the numerical simulations. Calculations based on the experimental operating boundary conditions and geometrical characteristics of the machine and the two reactors were made to aid determining the Reynolds number *(Re).* [92]

In fluid dynamics, the Reynolds number is a quantity that is used to predict the type of fluid flow. Below a certain *Re*, known as the transitional value, the flow can be described as a laminar flow, while above this value it becomes turbulent. The following calculations of the quantity *Re* were performed to corroborate that the flow inside the reactor can be modelled as laminar in the entire range of studied velocities. The *Re* is a dimensionless number obtained by calculating the ratio between inertial forces and viscous forces of the system.

The first term can be represented with the *dynamic pressure*: $\rho \boldsymbol{u}^2$, resulting from inertial forces. High fluid velocities $\boldsymbol{u}$ or high fluid density ρ will result in an increased momentum. The free mobility of the fluid expressed by this term is hampered by the friction resulting from the action of viscous forces. This term can be expressed as the *shear stress* resulting from viscous forces: $\mu \boldsymbol{u}/\mathrm{L}$, where μ is the viscosity and $\boldsymbol{u}/\mathrm{L}$ represents the average velocity $\boldsymbol{u}$ over a characteristic length L. The Re number can be expressed as:

$$Re = \frac{\rho \boldsymbol{u}^2}{\frac{\mu \boldsymbol{u}}{\mathrm{L}}} \qquad \text{(Eq. 5)}$$

By substituting the kinematic viscosity $\nu = \mu/\rho$, equation 5 can be rewritten as.

$$Re = \frac{\boldsymbol{u}L}{\nu} \quad \text{(Eq. 6)}$$

In this model, ν is the kinematic viscosity of nitrogen at room temperature ($\nu = 1.57 * 10^{-5}\, m^2/s$) and L=5 mm corresponds to the inner diameter of the inlet tube.

The average gas velocity in the inlet tube $\boldsymbol{u}$ is calculated from:

$$\boldsymbol{u} = Q/A \quad \text{(Eq. 7)}$$

Where Q is the flowrate and A is the cross-sectional area of the channel, here 0.196 cm^2. The cross-sectional area was calculated with:

$$A = \pi(r)^2 \quad \text{(Eq. 8)}$$

Where r=2.5 mm is the radius of the channel. To generalize the results of these calculations to the whole group of numerical simulations that will be discussed in this thesis, a high volumetric flowrate of 5 LPM (5000 sccm) was chosen. This value was measured at the inlet with a flowmeter during various ALD processes when pulsing high vapor pressure co-precursors (such as ozone). The highest experimentally observed velocity was **u**=4.24 m/s. For this **u** the corresponding *Re* is 1350, which is below the transitional value for pipes of *Re*=2000 which would determine transition to turbulent flow. [93] The *Re* in the reactor's domain is calculated as a fluid flow over a flat plate. According to this rule, the characteristic length L corresponds to the length of the plate, in this case, the bottom surface of the reactor. This corresponds to L=23 cm for the square shaped reactor and L=15 cm for the circular reactor. Even using the maximum **u**=4.24 m/s, corresponding to the inlet tube, the calculated *Re* values for the square shaped and the circular reactors are 6.2 x 10^4 and 40432 x 10^4, respectively, both below the transitional value of 3.2 x 10^5 for a flow over a flat plate. [93]

It is confirmed that, for the complete set of boundary conditions, the numerical model can be computed using the laminar flow model.

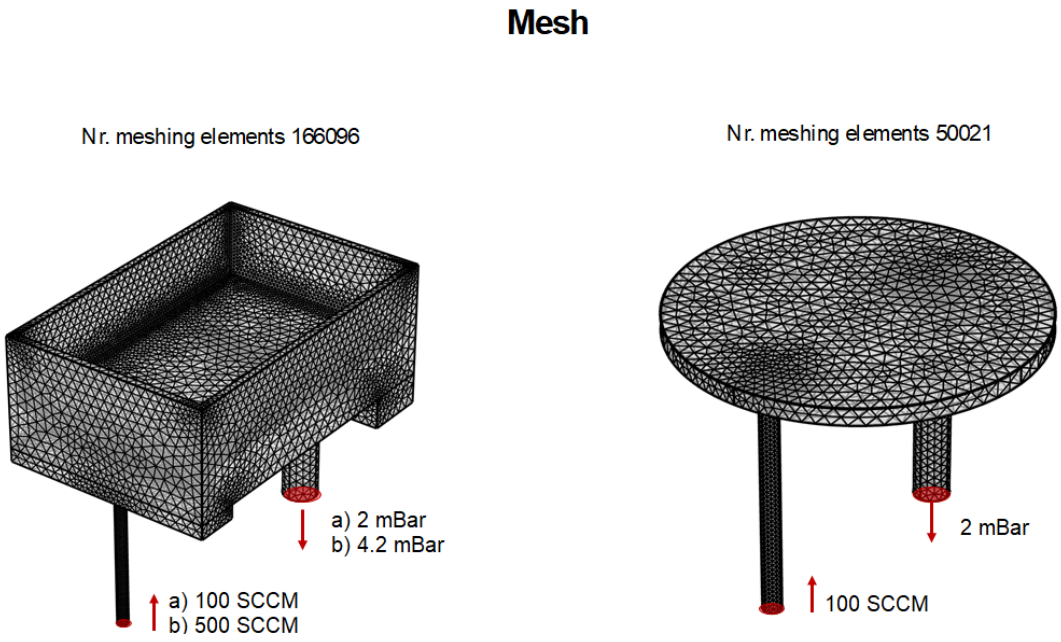

Figure 18: Meshes used for COMSOL simulations of the two reactor types. The inlet flow boundary conditions and outlet pressure boundary conditions are indicated in the respective sketch.

The mesh of these two reactor domains (**Figure 18**) is composed of 166'000 elements for the high-volume square shaped reactor and of 50'000 elements for the cylindrical reactor with a reduced volume. The boundary conditions chosen to simulate a stationary nitrogen flow inside each reactor are: As *inlet boundary condition,* the *volumetric flowrate* of N_2 was set to 100-500 sccm. For the *outlet*, a pressure boundary condition was set to static pressure at no flow (vacuum baseline pressure). This pressure value is 2 mbar for 100 sccm carrier-gas flow and 4.2 mbar for 500 sccm. The *no-slip* walls condition was used to simulate the flow constriction given by the domain walls.

3.2 CFD Results

The computed velocity fields inside these two reactors have been used to simulate the flow lines of the carrier gas during an extended purge. The graphical representation of the results is shown in figures 19 to 24.

Square shaped reactor (100 sccm)

As it can be extrapolated from the nitrogen velocity field (**Figure 19**, a-b), the average nitrogen velocity in the inlet tube is 8.48 cm/s. As the gas enters the reactor, the sudden volume expansion causes the fluid velocity to drop. A cylindric free-volume domain (10 cm in diameter and 3 cm in height) located in the middle of the reactor's chamber, has been defined to simulate the region above the substrate corresponding to a 4-inch wafer, which is commonly used as reference sample in laboratory scale ALD processes. In this region, the average gas velocity ranges between 0.041 and 0.072 cm/s. This shows that the velocity of the carrier gas in an evacuated high-volume reactor is excessively low. The carrier gas streamlines visualize how the laminar nitrogen flow upon entering the reactor splits into two main components after generating a minor turbulence in proximity of the lid's edge, located above the inlet (**Figure 19**, c-d). The main region ("Reactor region" in **Figure 19**, c) is the free-volume area where a presence of gaseous precursors is desired because it represents the substrate location during ALD. The second region ("Sidewall gap region") is the 5 mm gap between lid and sidewalls of the reactor. This reactor was designed to allow to modify its volume by exchanging the lid. The reactor thus presents high lateral walls and enables, by using a sloping lid that protrudes inside the reactor's walls, alteration of the free volume (**Figure 11**). However, this architecture leaves a 5 mm gap between the reactor walls and the portion of the lid which reduces the free space. These narrow gaps are found to be the strong contributors to precursor entrapment because of their high surface area and the almost negligible purging effect by the carrier gas flow.

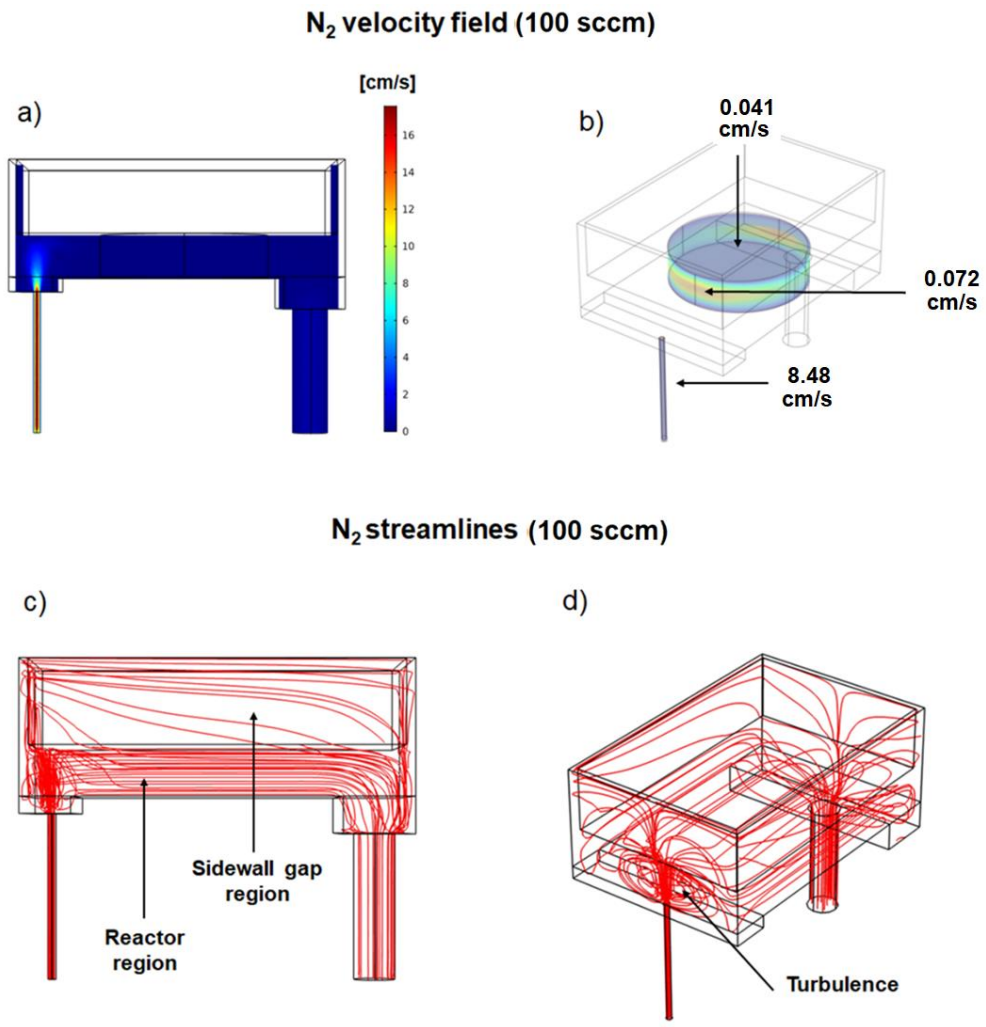

Figure 19: a) Carrier gas velocity field for an inlet flow of 100 sccm; b) average N_2 velocities sampled from two different regions of the reactor; c,d) streamlines in the reactor generated by the constricted flow path through the domain.

As will be shown, flow lines in this region result in fluid dynamic conditions which are not ideal for ALD. To highlight these flow limitations, low velocity field plots are shown in **Figure 20**. In these figures the "high velocity stream" (1 mm/s and above) is presented in dark red, while the areas with very low nitrogen flow are blue.

To better visualize this issue, the magnitude **u** is plotted over two representative xz-planes of the reactor domain (**Figure 20**, a). One plane cuts the reactor along inlet and outlet tubes axis. Along this plane the nitrogen stream has higher velocities. Two small low-velocity areas, presented in blue, can be seen on top of the outlet. The second xz-plane is placed in the side gaps between walls and lid. In this area the fluid velocities

are nearly zero and thus negligible. From **Figure 20**-b, the velocity field is homogenous along the reactor basal plane and low velocity pockets are only present in the squared corners of the reactor.

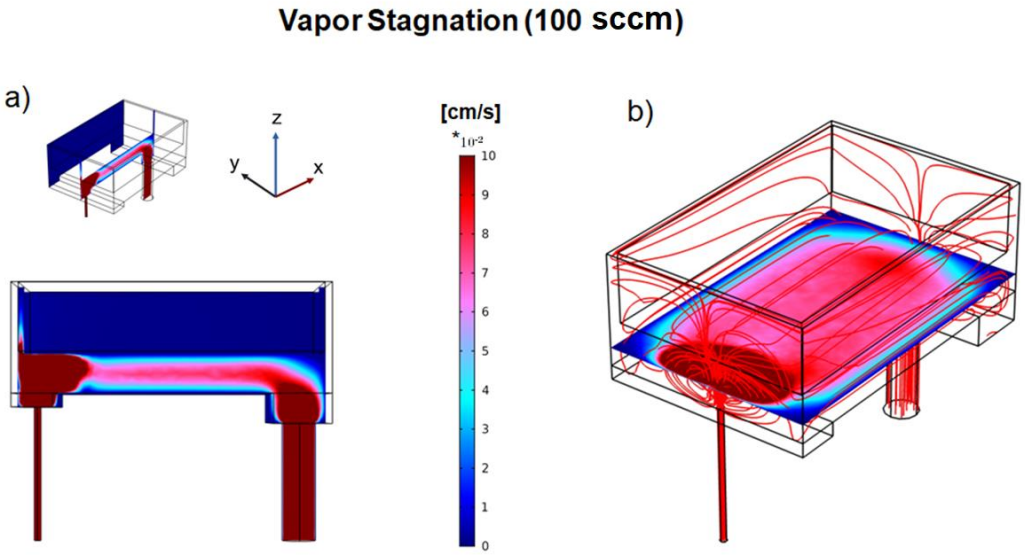

Figure 20: Representation of the area with stagnated vapor inside the reactor (dark blue), resulting from low carrier gas velocities (below 1.0 $^{-2}$ cm/s).

From these results it can be concluded that during an ALD experiment the blue areas of the reactor will be affected by poor gas flow (velocities around 1.0^{-2} cm/s) and therefore will contribute to precursor trapping and CVD-like growth.

Square shaped reactor (500 sccm)

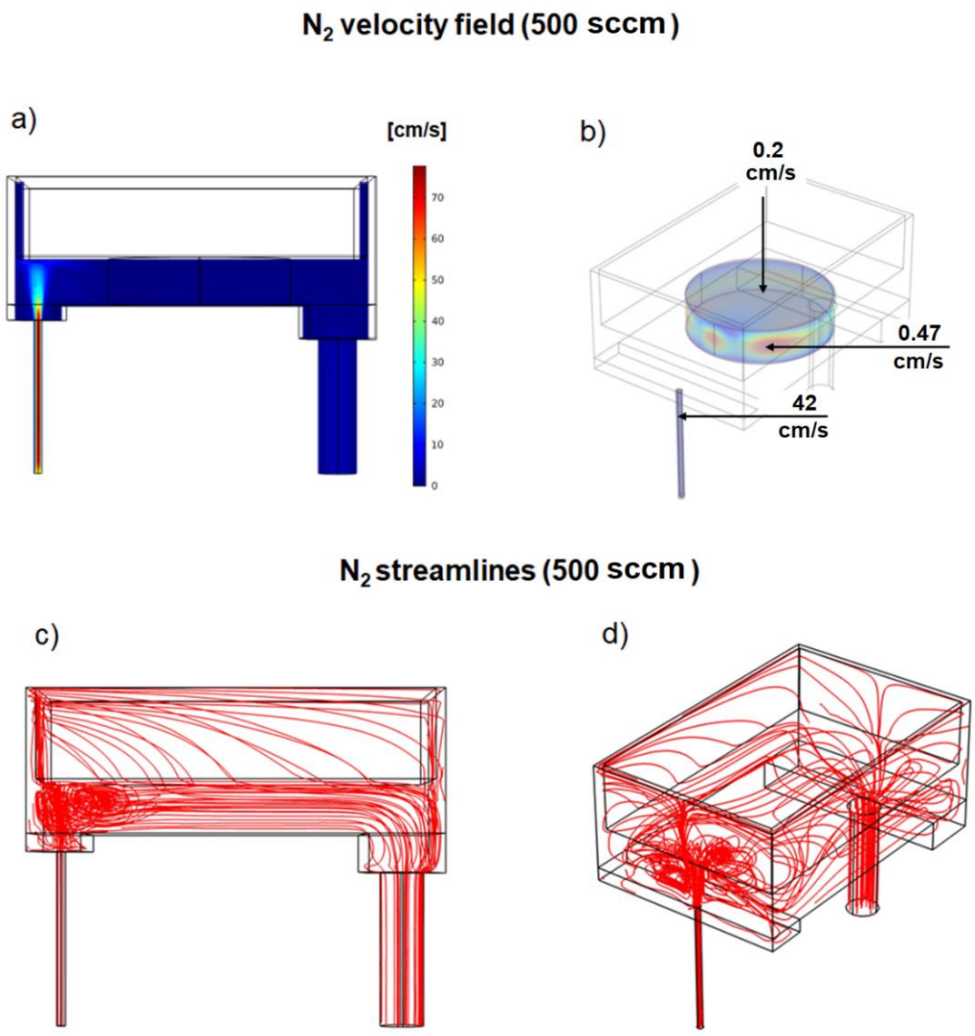

Figure 21: a) Carrier gas velocity field upon 500 sccm flow at the inlet; b) average N_2 velocities sampled from two different regions of the reactor; c,d) streamlines generated by the constricted flow path through the domain.

Given the non-ideal carrier gas flow in the reactor when operated at 100 sccm, a simulation at a higher nitrogen flowrate of 500 sccm was performed for testing whether the square shaped reactor might be optimized for ALD. The fivefold increase of the flowrate causes an increase of the average inlet velocity to 42 cm/s and up to a maximum of 0.48 cm/s in the reactor (**Figure 21**, a-b). Although the average carrier gas velocity inside the reactor is significantly increased, the velocity field distribution is negatively affected by the geometry of the tool. Streamline plots (**Figure 21**, c-d)

show that the gas entering the reactor with high velocity generates a severe turbulence, which, in contrast, was very modest in the 100 sccm model. The velocity distribution can be better seen in **Figure 22**, a-b: The turbulence leads to a highly inhomogeneous velocity field in the substrate area and low velocity areas along the sidewalls (in blue).

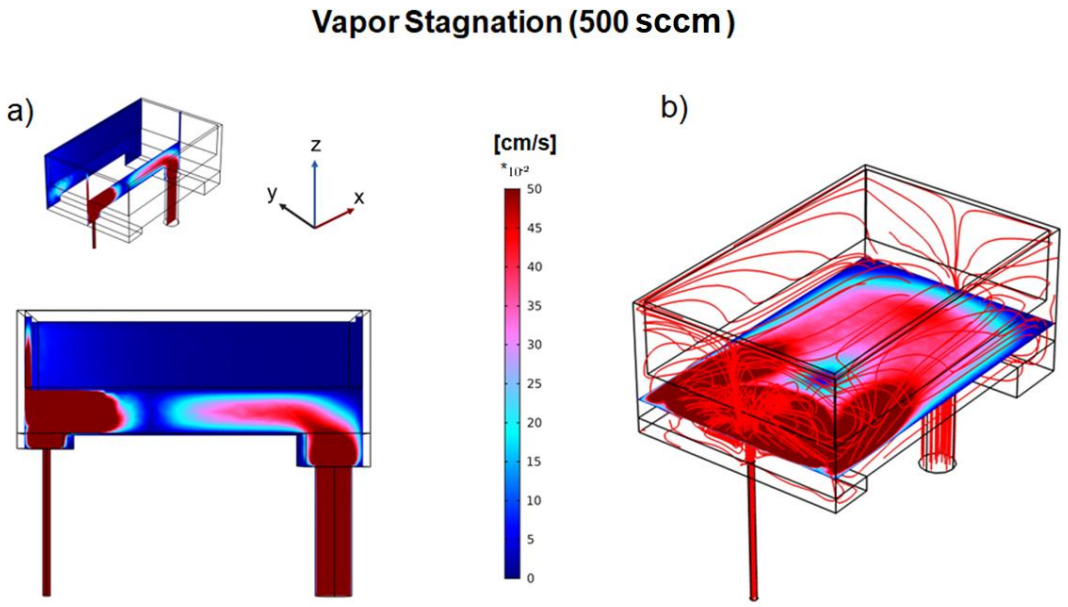

Figure 22: Representation of vapor trapping inside the reactor (dark blue) as a consequence of low carrier gas velocities (below 1.0 $^{-2}$ cm/s).

These results show that the reactor geometry plays a crucial role over the fluid flow and, most importantly, that precursor trapping could be inherently related to the reactor design and be hardly omitted by changing the processing parameters. Under these circumstances, the increase of the carrier gas flowrate does not necessarily lead to an increase of purging efficiency and is found to produce the opposite effect, which is detrimental for the tool performance. Specifically, the increased flowrates are found to destroy the laminarity of the flow, generating inhomogeneous velocities in the deposition area that would negatively affect the uniformity of the coating.

Re-designed reactor (100 sccm)

These aspects were taken into consideration when re-designing the reactor by adopting a flat cylindrical geometry with a considerably reduced wall surface. The smaller reactor volume leads to higher carrier gas velocities in the deposition area. The average **u,** calculated in cylindrical substrate region, is 2.1 mm/s with a maximum velocity of 8 mm/s (**Figure 23**, a-b).

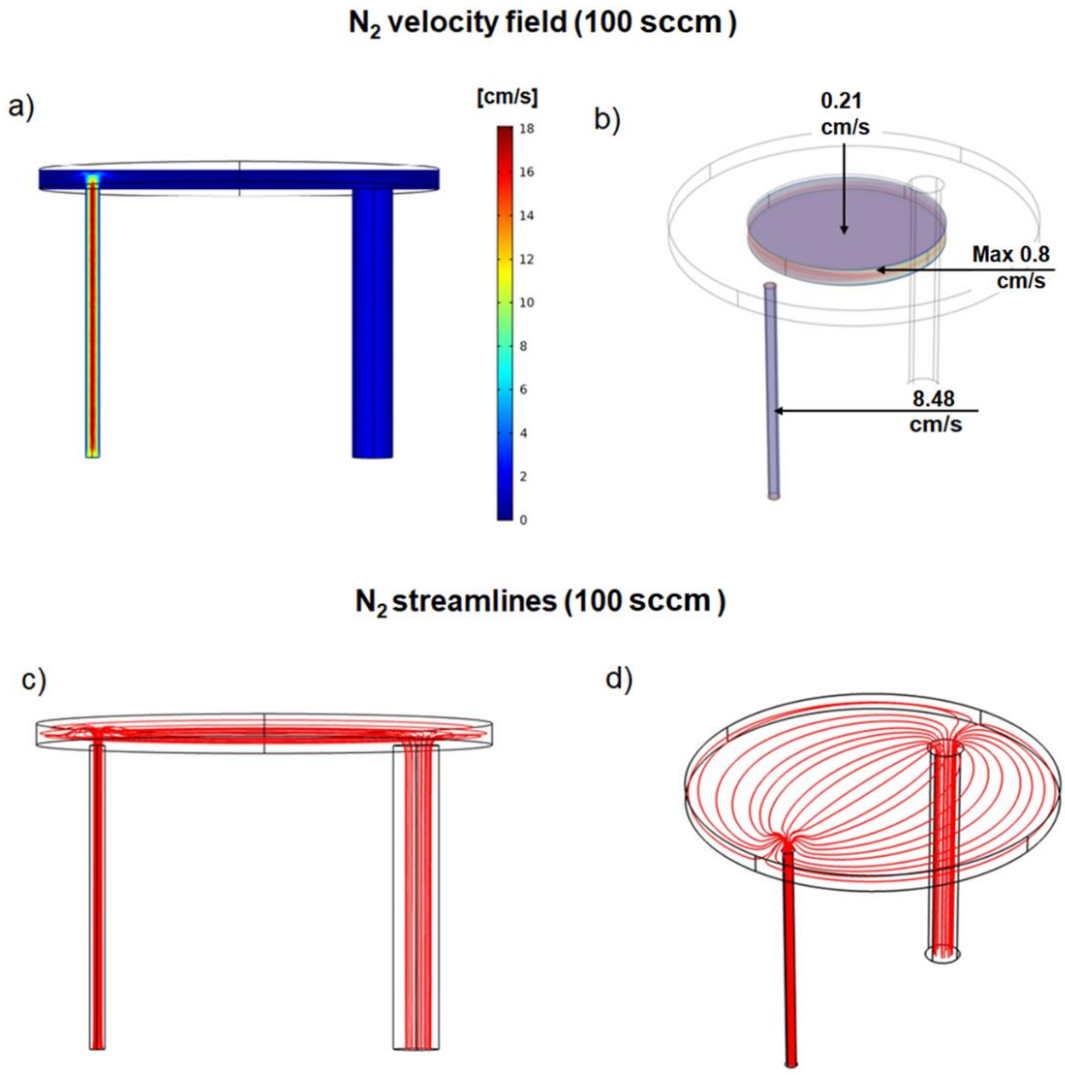

Figure 23: a) Carrier gas velocity field for an inlet flow of 100 sccm; b) average N_2 velocities sampled from two different regions of the reactor; c,d) streamlines generated by the constricted flow path through the domain.

Figure 23, c-d shows that the streamlines of nitrogen at an inlet flow of 100 sccm are evenly distributed along the reactor free volume and the flow is fully laminar thanks to the circular reactor design that reduces turbulences. This new reactor design almost entirely suppresses precursor trapping and ensures optimal purging of the entire volume. Areas with velocities below 0.2 mm/s are only found close to the inlet and

the outlet (**Figure 24**, a-b). This design facilitates efficient precursor removal during the purging step, shortening the overall processing times.

The fluid dynamics of this reactor is ideal for achieving high quality, homogenous coatings. As it will be shown, these aspects also allow for lowering the precursor dose, thereby reducing the precursor consumption.

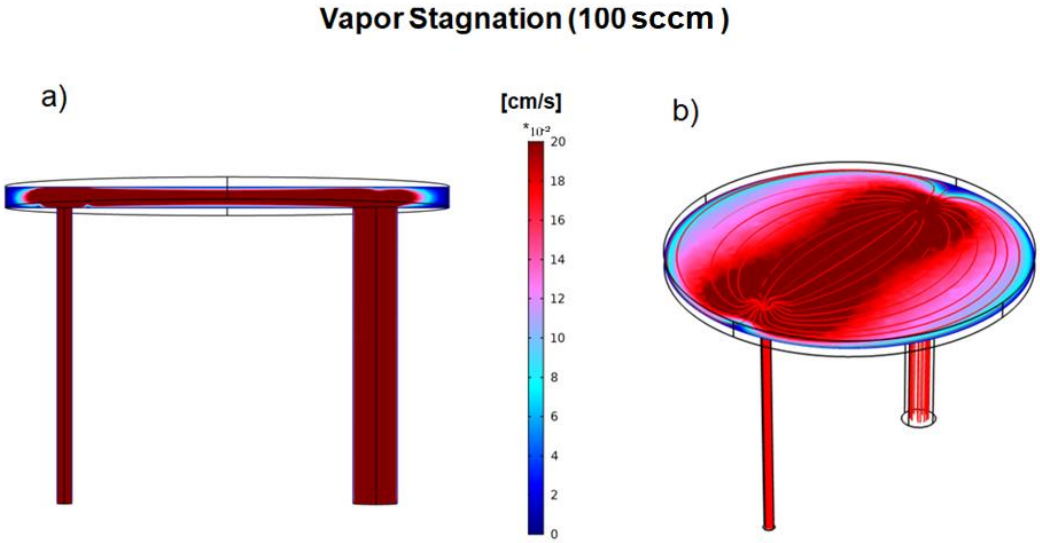

Figure 24: Representation of vapor trapping inside the reactor (dark blue) as a consequence of low carrier gas velocities (below 1.0 $^{-2}$ cm/s).

After observing the improvement of reactor re-designing using this simple CFD model, we have proceeded to the characterization of the actual ALD process involving $Ni(Cp)_2$ and ozone.

3.3 Two-step nickel synthesis

The ALD-synthesis of metallic nickel involving $Ni(Cp)_2$ as metal-containing precursor can been performed in two steps by:

(1) ALD of nickel oxide using $Ni(Cp)_2$ and ozone as precursors.

(2) reduction of the deposited NiO to metallic nickel by annealing in H_2/N_2 gas mixture.

In this chapter, which entirely focuses on ALD, only the first step will be presented, while the second step will be discussed in the fourth chapter.

3.3.1 Inherent chemical limitations

This chemical synthesis, which is representative for a vast variety of similar ALD processes, presents some inherent issues due to the thermodynamic characteristics of nickelocene and in particular its limited stability.

1st half-reaction: $Ni(Cp)_2$ pulse

Bis(cyclopentadienyl)nickel (Nickelocene, $Ni(Cp)_2$), was first synthesized in 1953 by E.O. Fischer and it is an organometallic compound belonging to the class of metallocenes. [94] This chemical has been subject of numerous studies and became a versatile precursor in ALD thanks to its unique, and yet not fully understood, mechanism of absorption. From the vast literature, it is well established that its absorption on silicon occurs through Van der Waals interactions and that this absorption is self-limiting. Once the first molecular layer is adsorbed, the excess precursor should not lead to multimolecular nickelocene stackings. [95] However, this precursor characteristic, which is highly desired in ALD, could not be conserved throughout the entire process. In fact, many of the studies related to the absorption of nickelocene are performed in highly controlled environments (low temperature, pristine substrates, controlled atmosphere) and are not fully representative of the dynamic nature of an ALD experiment. During ALD the substrate composition is continuously changing, and the reactant molecules are subjected to different forces (vapor flows), temperature gradients and can also participate to multiple reactions.

However, at room temperature, physisorbed metallocenes are known to possess high mobility through translational modes and, for the case of nickelocene, it is still not clear whether at increased temperatures chemisorption is favored or it can desorb from the surface. There is evidence of chemisorption for other metallocenes, such as chromocene, which are found to favorably react with hydroxylated groups forming CpCr(III) bound to the surface through a siloxide anion, but similar behavior has not been observed for nickelocene. [96]

Ideally, physisorbed nickelocene is reported to be stable until 200 °C, thanks to the high activation energy required for breaking the Ni-Cp bonds (385 kJ/mol). [97] Its decomposition temperature, as isolated physisorbed molecule, is lowered only on catalytic surfaces such as Ag(100) and Cu(100) or in presence of other chemicals. [98] A favorable mechanism to initiate $Ni(Cp)_2$ decomposition is the hydrogenation of the Cp ligands (9.6 kJ/mol) with gaseous hydrogen, [99] following the reaction:

$$Ni(C_5H_5)_2(ads) + 1/2\ H_2\ (g) \rightarrow Ni(C_5H_5)(ads) + C_5H_6(g) \qquad \text{(Eq. 9)}$$

This reaction mechanism is not occurring in the ALD processes performed during this thesis, although a similar hydrogenation pathway can still occur. It has been experimentally observed that, even at comparatively low temperatures (80 °C) and in absence of other gaseous reactants, the hydrogenated by-product C_5H_6 is produced during nickelocene absorption.

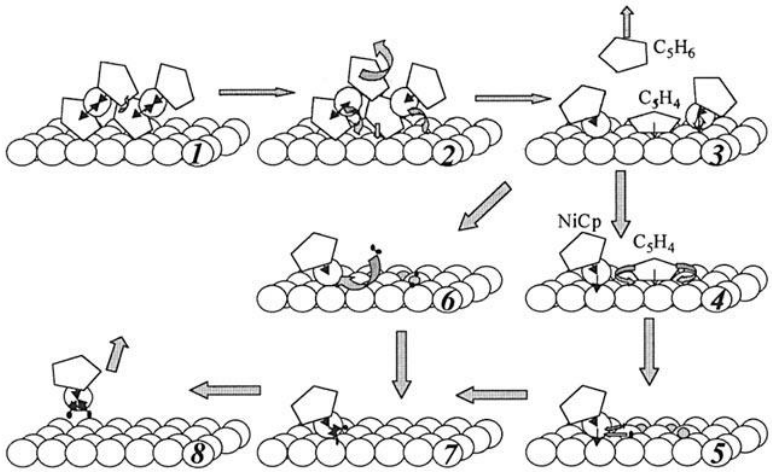

Figure 25: $Ni(Cp)_2$ decomposition mechanism initiated by two physisorbed molecules , image taken from [97].

The accepted mechanism is a decomposition involving two neighbouring $Ni(Cp)_2$ molecules adsorbed on the surface which exchange a hydrogen atom between Cp ligands and initiate decomposition (**Figure 25**). The mechanism of the hydrogenation is proposed to occur following the reaction: [97]

$$2Ni(C_5H_5)_2(ads) \rightarrow Ni(C_5H_5)(ads) + (C_5H_4)Ni(C_5H_5)(ads) + C_5H_6(g) \qquad \text{(Eq.10)}$$

Further studies have underlined that free cyclopentadiene ligands, released upon $Ni(Cp)_2$ decomposition, can adsorb on the surface and further decompose through a mechanism of disproportionation initiated by Cp dehydrogenation, leading to accumulation of carbonaceous contaminants. This mechanism is reported to start at 125°C (depending on the surface) and proceeds as the temperature is increased to 225 °C. [100]

2nd half-reaction: O_3 pulse

The second half reaction consists of pulsing a mixture of oxygen and ozone into the reactor that targets the removal of the Cp ligands, resulting in the formation of a complete NiO layer.

The activation energy for the reaction between O_3 and Cp ligands is estimated to be on the order of 8 kJ/mol and occurs through carbon-carbon double bond breaking by O_3, followed by Cp ring opening. In contrast to thermal decomposition, which produces non-volatile carbon by-products, ozonolysis proceeds through CO_2 or O_2 elimination, leading to minor carbon contamination as the film grows. [101]

Lowering the processing temperature below 200 °C is minimizing the nickelocene decomposition, but it also negatively impacts the process kinetics. The low thermal energy of the system slows down the reactions between the surface-absorbed species and the precursors. As will be discussed in more detail throughout the thesis, the low reactor temperature may suppress the chemisorption of nickelocene on the surface and hinder the ozonolysis of the Cp ligands during ozone exposure, resulting in incomplete half-reactions.

Thus, it is evident that "pure ALD" of nickel oxide from nickelocene and ozone is hardly attainable. $Ni(Cp)_2$ chemisorption can also occur through decomposition mechanisms which are not driven by the surface functional groups. These aspects are not ideal for ALD processing as they hinder self-limiting growth and lower the quality of the thin film. However, by optimizing reactor design and processing conditions, these undesired mechanisms can be minimized.

3.4 ALD process

Thermal ALD of nickel oxide has been performed using $Ni(Cp)_2$ and ozone as precursors, utilizing Reactor 1 (See 2.1.2.1). For each process the manifold was heated at 150°C. The sublimation vessel was heated at 60 °C to minimize the decomposition $Ni(Cp)_2$ upon prolonged heating. [102] The delivered mass per pulse is calculated from the surplus precursor at the end of the process [9] divided by the number of cycles. The mass per pulse from each individual experiment is then used to calculate the average mass per injection (weighted average). The average mass per pulse for idle times above

[9] The average mass injected per pulse is calculated from the vessel precursor load before and after deposition: (initial $Ni(Cp)_2$ mass – Residual $Ni(Cp)_2$ mass)

80 seconds, loads of 250 mg and vessel temperature of 60 °C is 0.55 ± 0.5 mg. For precise in situ reading of the delivered mass, a QCM [103] or a residual gas analyzer with mass spectrometer or a non-dispersive infrared analyzer [104] are required. It is worth noting that the initial ALD experiments were performed in "flow-mode" (See 2.1.3, **Figure 5**, b) and did not yield deposition. Considering these initial results, the "static-mode" was preferred for both nickelocene and ozone pulses (**Figure 26** and **Figure 27**).

The characterization of nickel oxide has been performed by single parameter sweep; the tested parameters are reported in the chart.

Table 2: Processing parameters used for ALD of NiO using $Ni(Cp)_2$ and O_3.

Deposition parameter	Studied interval	Optimal value
Reactor temperature [°C]	**150, 175, 200, 225, 250**	**225**
Nickelocene pulsing time [s]	**1, 3, 5, 7, 9**	**5**
Nickelocene exposure time [s]	**2.5, 5, 10, 20**	**5**
Nickelocene purging time [s]	**10, 20, 40, 80, 120**	**80**
Ozone pulsing time [s]	**0.05, 0.1, 0.5, 1, 2**	**0.5**
Ozone exposure time [s]	**2.5, 5, 10, 20**	**10**

The characterization of the GPC vs. T (**Figure 26**, a) was carried out using idle times of 200 seconds and 250 mg of precursors loads of $Ni(Cp)_2$ (reloaded at each experiment).

Given the reactor temperature limitation imposed by the thermal stability of the FKM fluorocarbon O-ring (230 °C), the maximum processing temperature was set to 225 °C, except for one experiment that was performed at 250 °C only to collect one datapoint for GPC (**Figure 26**, a). The GPC at 225 °C was 1.49 Å and it was linear throughout the whole investigated cycle number range (**Figure 26**, b). The GPC as function of nickelocene pulsing time (**Figure 26**, c) shows that a minimum of 5 s pulsing time is necessary to achieve constancy. Extended pulsing times of 7 or 9 seconds did not notably increase the GPC. To investigate whether the flattening of the GPC curve is

due to a true self-limiting behavior and not an artifact related to head space emptying, the characterization was repeated with a fourfold increased vessel load. The first consideration from the difference between the two GPC curves is that, for short pulsing times, higher load leads to a quicker saturation. With 1 g precursor load the GPC after 1 s pulses is almost double of that with a 250 mg load. This confirms that the idle time of 200 s used before each $Ni(Cp)_2$ pulse is not sufficient to reach the processing condition of P_{HS}=Pv_{ap}, as otherwise the higher load would not affect the GPC. Although the undersaturation in the vessel is not ideal for ALD processing, it can still be observed that the GPC is stable at 1.5 Å, meaning that operating in a static mode enables to reach self-limited growth even in undersaturation conditions.

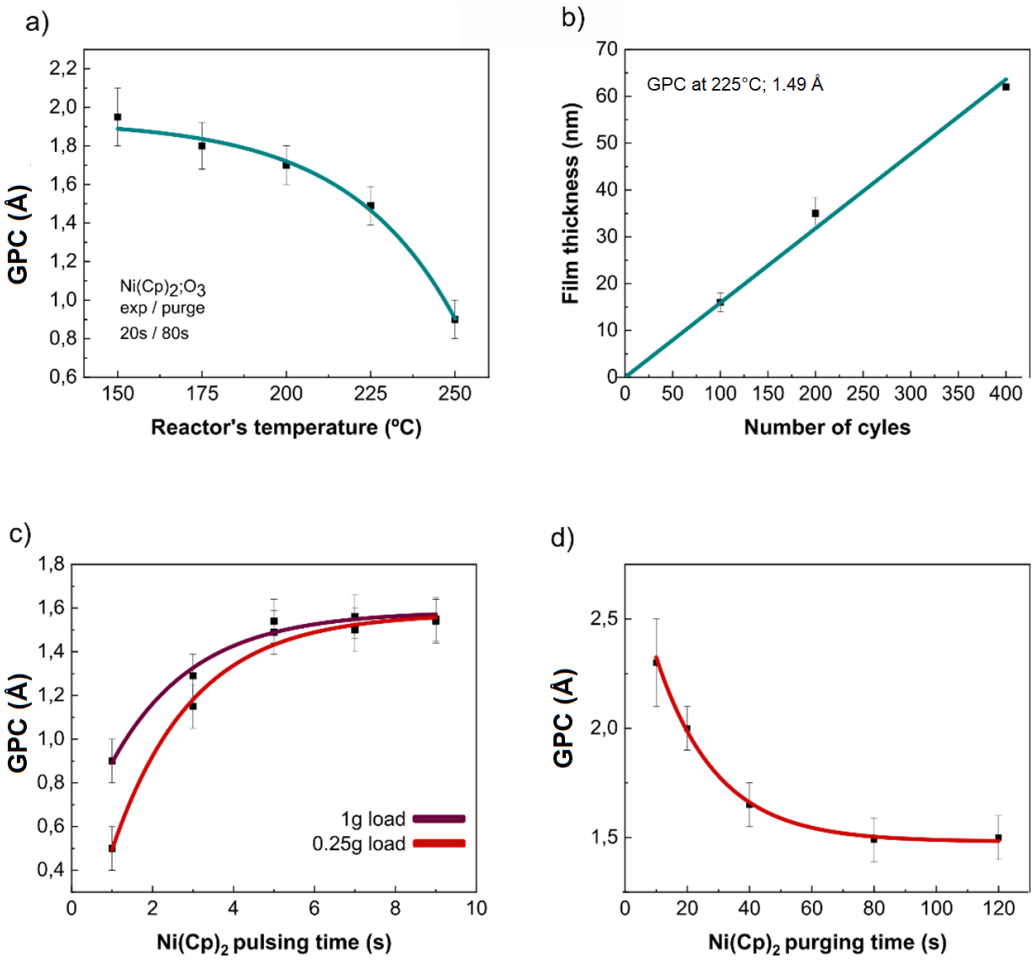

Figure 26: Optimal parameter space evaluation for the nickel oxide ALD process: a) temperature dependence of the GPC; b) linearity of the growth with the cycle number; c) Dependence of the GPC on the $Ni(Cp)_2$ pulse time; d) Dependence of the GPC on the purge time.

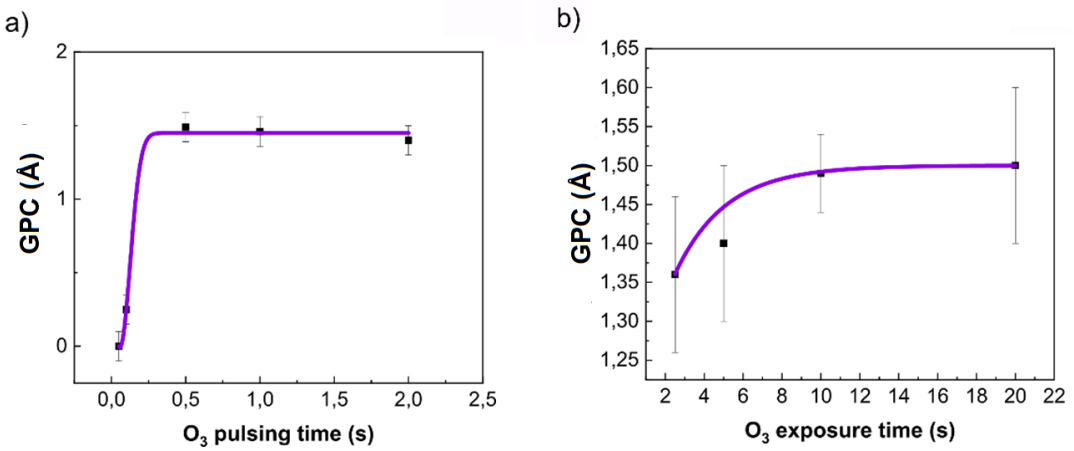

Figure 27: Dependence of the GPC on a) the ozone pulsing time, and f) ozone exposure time.

For $Ni(Cp)_2$, the GPC stabilizes at a value of approximately 1.5 Å when the purging times exceeds 80 seconds. The reason behind such long purging times can be related to precursor trapping along the manifold due to low temperatures (150 °C) accentuated by the split nitrogen paths and the operation in static mode (See 2.1.3).

For the co-precursor (**Figure 27**), the growth has been characterized by changing the pulsing time from 0.5 seconds to a maximum of 2 seconds. After pulse, the reactor was kept in static mode (stop-valve closed) for a total of 10 seconds. A short pulse of 0.5 seconds was found to be sufficient for reaching the plateau of the GPC curve (**Figure 27**, a). The effect of ozone exposure on the GPC was tested by maintaining 0.5 s of pulsing time and changing the exposure time from 2 s up to 20 s (**Figure 27**, b). It was found that a minimum of 10 s of exposure time is required for reaching a constant GPC.

The GPC of 1.49 Å, obtained in static mode at 225 °C, lowered to 0.35 Å if the co-precursor was dosed in flow-mode (**Figure 29**, red star). Under this condition the only processing difference was that the O_3 half-cycle was performed without disconnecting the pump. In this way ozone was flown into the reactor for 10 s instead of being kept in the reactor for 10 s with the stop-valve closed. [10]

Interestingly, the GPC reduction to 0.35 Å is attributable only to some specific areas of the reactor. A reduced growth was found in the substrate area and close to the reactor walls, but it did not affect the remaining surface of the reactor.

[10] In static mode, the ozone half-cycle consists in 1) closing stopvalve, 2) pulsing 0.5 s ozone, 3) waiting for 9.5 (total of 10 s exposure in no flow conditions) 4) opening stopvalve (purging).

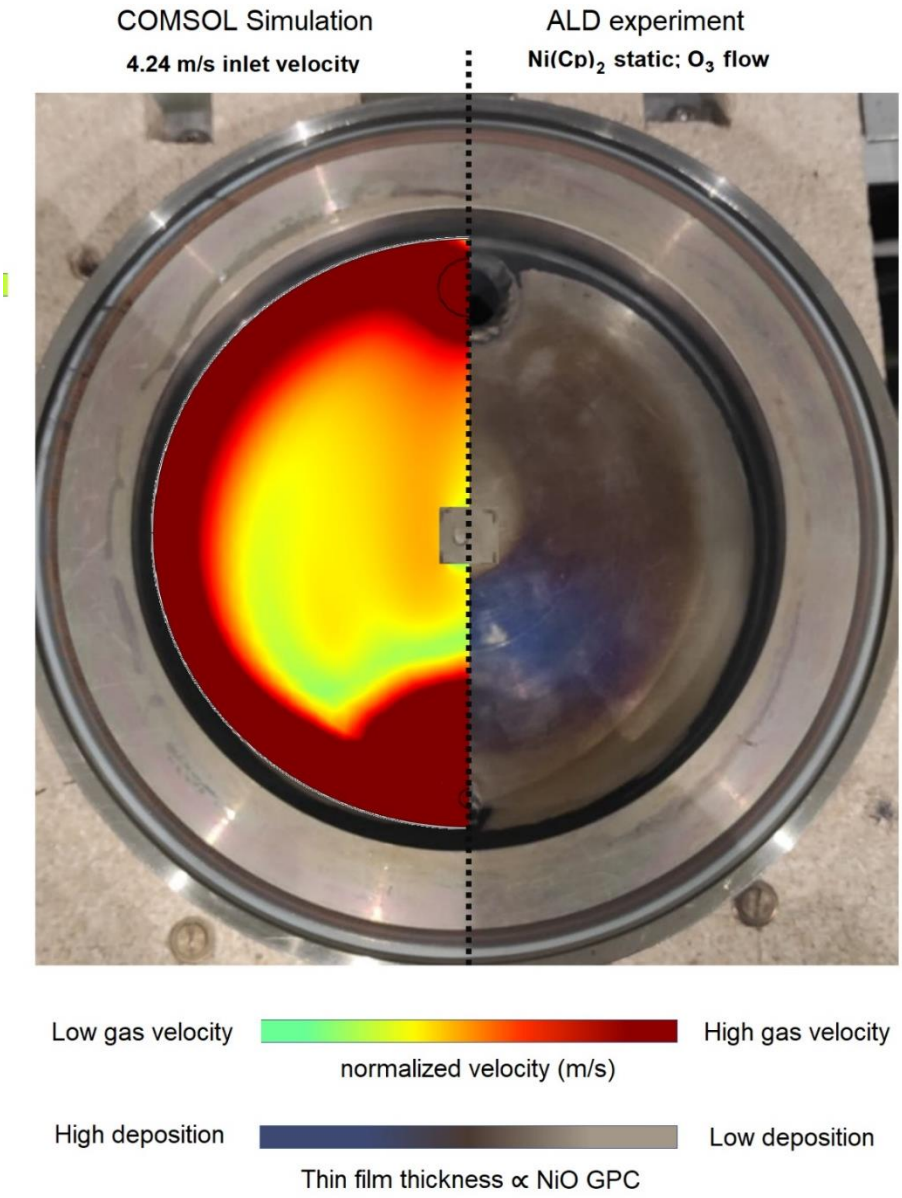

Figure 28: Fluid velocity ($\boldsymbol{u}$) map, computed using COMSOL multiphysics (left), overlapped with an image of the reactor base plate after 600 cycles of NiO ALD performed pulsing ozone in flow-mode.

To better visualize the inhomogeneous coating, which derives from the ozone injection mode, the reactor stainless steel base was polished to remove the coloration resulting from previous depositions, and an ALD process with 600 cycles was performed. In this way, thin film deposition was detected through a color change from metallic (steel of the reactor) to brown (40 nm NiO) and blue (80 nm NiO) (**Figure 28**, right).

A noticeable color change, indicating a high GPC, was observed on the bottom of the reactor (blue/brown areas) and a low GPC (0.35 Å) close to the reactor walls (**Figure**

28, right). The shape and symmetrical distribution of these regions (high and low deposition) suggests that this phenomenon arises from the interaction between the fluid flow (O_3 stream) and the boundaries represented by the reactor walls and the substrate height profile.

To investigate correlation with fluid dynamics during pulsing and inhomogeneity during deposition, the previously described numerical model of the cylindrical reactor was re-used and slightly modified. A 10x10 mm, 1 mm thick squared slab was added to the mesh of the cylindrical reactor (**Figure 18**) to simulate the sample. In addition, the ozone velocity during pulse in flow-mode was measured experimentally using a mass flow controller mounted at the inlet. The obtained value of 4.2 m/s was used as inlet boundary condition for the simulation. The computed velocity field map of the reactor surface is overlayed with the image of the reactor base to facilitate the discussion of results (**Figure 28**, left).

The highest fluid velocities (red) are localized along the reactor walls. This uneven distribution of velocities over the reactor base arises from a phenomenon that was precedingly observed in the CFD results relative to increased carrier gas flows (**Figure 22**) in the square shaped reactor. For high fluid velocities, the highly constricted laminar flow of ozone entering the reactor from the inlet tube generates turbulence as it encounters the lid boundary. This interface causes part of the fluid stream to be deflected along the walls leading to the formation of high and low velocity domains in different areas of the reactor. In the center the fluid velocities are low, especially in the area in close contact with the turbulent interface. The fluid velocity along the central part of the reactor base is then increased as the laminarity is re-established. The fluid velocity is ulteriorly increased in correspondence of the substrate interface where, according to the continuity equation, [11] the narrowing of the reactor cross section due to the presence of the wafer, causes an increase of the ozone velocity.

By comparing the color change deriving from 600 ALD cycles and the CFD results, a correlation between computed ozone velocities and the deposition thickness can be found. Increased O_3 velocity results in a decrease of the GPC, while lower O_3 velocity promotes higher GPC.

The reason behind this could be related to non-uniform O_3 pressure distribution in the reactor deriving from the non-uniform O_3 velocities. The ozone pressure is expected to be lower in the areas of higher fluid flow. Another hypothesis is that the nickelocene surface adsorption is not fully irreversible and increased flows lead to desorption. To better understand this mechanism further ALD experiments coupled with refined numerical runs are envisioned.

[11] The continuity equation for an incompressible fluid flow of constant density states that $A_1u_1=A_2u_2$ where A and u are the cross-sectional area and the velocity respectively.

3.4.1 Scattering of GPC data in literature

To better understand the experimental results relative to NiO deposition, literature data of analogous processes is discussed in the following.

As it can be observed in **Figure 29**, the GPC data of this ALD process significantly differs between the results collected during this thesis (red) and from the results of other authors (yellow, blue).

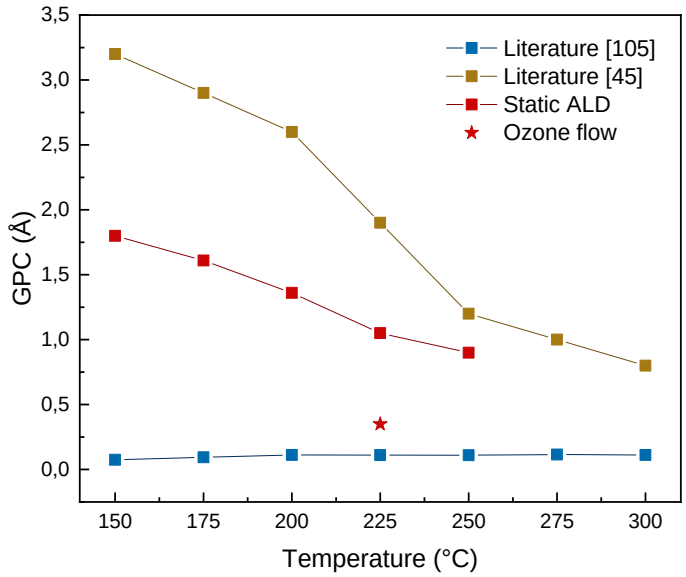

Figure 29: Overview of GPC vs. T data of NiO ALD depositions using $Ni(Cp)_2$ and ozone. Data points in red refer to the experimental results of this thesis; yellow: literature data taken from Lu, H. L., et al. [45]; blue: literature data taken from Koshtyal, Y., et al. [105]

If we compare the GPC of 1.49 Å at 200 °C, it significantly differs from the value of 2.6 Å measured by Lu, H. L., et al., [45] and the GPC of 0.12 Å. Reported Koshtyal, Y., et al. [105]

Lu, H. L., et al. used a tubular quartz ALD reactor from ASM microchemistry ltd and sublimed nickelocene from an open boat at 40 °C, [71] while Koshtyal, Y., et al. used a disk-shaped steel reactor, dosing the precursor from a container heated at 80 °C. The origin of the differences regarding this reaction can thus be linked to the considerable differences between the experimental setups used by the different authors and the consequently different precursor delivery, adsorption, and desorption mechanisms.

The precursor delivery, as previously discussed, can be the main source of poor surface coverage and incomplete half-reactions. The co-precursor exposure time can also strongly impact the growth. Recent studies show that, to achieve self-limiting ALD

growth using nickelocene and ozone, the ideal co-precursor dose is achieved through hundreds of seconds of ozone exposure. [106] With this statement the authors proposed that at 200°C the low GPC of 0.3 Å to 1 Å is related to insufficient ozone exposure. However, when observing the enormous differences between the growth data referring to very similar processes (similar pulsing times and concentrations of ozone) [12], it is hardly imaginable that the ozone exposure is the only factor influencing the growth.

Another credible reason for the differences in the GPC is the undersaturation during nickelocene exposure. The consistent delivery of low-vapor pressure precursors through an entire ALD process requires extensive process optimization (See 2.1.1) and, for the case of nickelocene, can be further accentuated by issues related to poor adsorption or enhanced desorption deriving from the machine design and fluid dynamics.

To explain the data, we subdivide the growth data into two temperature ranges, below and above 200 °C.

Resulting from the literature, if the reactor temperature is set **below 200 °C**, self-decomposition of $Ni(Cp)_2$ through equation 10 is not favorable and removal of Cp-ligands should occur through oxidation of nickelocene during the ozone pulse. However, at such temperatures (150-200 °C) ozonolysis is kinetically hindered and long co-precursor exposure times or higher pressures are required. [106] Also, at lower temperatures nickelocene physisorption is favored.

The high GPC at low temperatures (yellow curve, **Figure 29**) observed in literature can be attributed to higher doses of both ozone and nickelocene and reduced flow velocities. Under these conditions, the nickelocene delivery is sufficient for saturating the surface and the Cp removal. In contrast, a small GPC at low temperatures (blue curve, **Figure 29**) is attributable to smaller precursors doses. In this case poor surface saturation during the $Ni(Cp)_2$ supply, followed by partial ozonation reactions, will lead to a significant decrease of the GPC. The undersaturation of the half reactions can be due to small doses, deriving from increased desorption, or reduced adsorption (high vacuum level for example).

As the temperature is increased **above 200 °C,** the two described mechanisms of nickelocene decomposition are favored and the kinetics of the ozonolysis reaction is increased. In the case of high doses (yellow curve, **Figure 29**) of both precursors, the presence of many neighboring $Ni(Cp)_2$ molecules will favor decomposition through equation 10. The GPC decreases because increased decomposition hinders successive

[12] Ozone generators use an electric discharge to dissociate O_2 into atomic oxygen which rapidly reacts with oxygen molecules producing ozone

precursor chemisorption. [107] Another possible explanation could be that the surface coverage after the nickelocene pulses and high doses is not entirely chemisorptive. A percentage of the mass increase at each pulse comes from nickelocene molecules physisorbed through van der Waals interactions that, contrary to chemisorption (favored by increasing temperatures) decreases as the temperature increases, thereby favoring their removal. [108] When low temperatures and flows are used, the adsorption is facilitated but as the temperatures are increased, desorption also increases, causing a reduction of the GPC.

For the opposite case (blue curve, **Figure 29**), the GPC slightly increases with low precursor doses. This trend could be explained by considering that the surface saturation is poor, and the phenomena of decomposition through hydrogenation between neighboring molecules is hindered. Simultaneously, higher temperatures favor the ozone half-reaction causing an increase of the GPC. [109]

3.5 Conclusions

This chapter has shown that ALD reactor development can be facilitated using a simple computational model that provides insight into fluid dynamic limitations that otherwise would negatively affect the performance of the reactor. The analysis of the velocity field, generated during the ozone pulse in flow-mode, unveiled correlation between reduced growth rates and increased co-precursor velocity. These results underline that nickelocene adsorption/growth mechanisms in ALD are still not fully understood and further research is required.

Regarding the poor stability of nickelocene, it is shown that, for R&D purposes, the use of a static processing mode during the $Ni(Cp)_2$ half cycle allows to achieve stable ALD growth with minimum precursor usage (250 mg). For research purposes, reloading the vessel at each experiment guarantees to fully consume the precursor, thereby limiting waste. However, for large batch production, timesaving protocols require the load of hundreds of grams of precursor and avoiding repeated vessel refilling. In this way the precursors necessarily undergo several heating cycles, causing formation of non-volatile decomposition products. These products, present in the vessel as a thin brown dust, do not participate in any reaction and can accumulate in valves and delivery lines causing quick ageing of the reactor. The present work points out that, for future improvement of ALD machines, the designing of vessels which enable rapid/automatized reloading without being disassembled could be a key aspect for reducing precursor waste and maintenance requirements in large batch ALD processing.

4

From thin films to structures

4.1 Ni(II) to metallic nickel

One frequently applied strategy for obtaining nickel coatings and powders is the reductive annealing of NiO with hydrogen, [110] CO/CO_2, [111] or methane. [112] In the present thesis annealing experiments have been carried out in an IR lamp-heated furnace in presence of forming gas (5% of H_2 in N_2), as described in section 2.2.

The reaction proceeds as follows:

$$NiO(s) + H_2(g) = Ni(s) + H_2O(g) \qquad \text{(Eq. 11)}$$

This reaction requires an activation energy on the order of 20-30 kJ/mol, [113] and can therefore be initiated at temperatures as low as 400 °C. [114]

At the beginning of this work based, we had outlined as one appealing application for pulsed annealing, the fabrication of exchange-biased Ni/NiO structures through the local reduction of NiO films. This phenomenon arises at the interface between ferromagnets (Ni) and antiferromagnets (NiO). [115] While ferromagnetism, as it will be shown, is easily achievable through post-processing reductive annealing, the antiferromagnetism of nickel oxide requires highly controlled epitaxial growth, as it easily undergoes to phase transition into a paramagnetic state as the crystallinity is reduced. Envisioning these future applications, we thus decided to characterize also sputtering deposited NiO thin films. The film used in this preliminary stage of the study were not epitaxially grown, but future experiments on antiferromagnetic nickel oxide epitaxially grown on MgO are envisioned.

The choice of the thickness of 40 nm for the NiO films results from considerations that subsequent reductive annealing will cause film shrinkage and therefore sufficiently thick films are needed to remain above the detection limit of MOKE and XRD.

The first reduction experiments were performed by evacuating the annealing furnace to $5*10^{-2}$ mbar, flooding with forming gas until 0.5 bar of pressure were achieved and heating for 20 minutes. Temperatures of 700 °C were required for complete conversion

of the cubic Fm3m nickel oxide (**Figure 30**, a) into FCC nickel (**Figure 30**, c). Below 700 °C, the XRD spectra confirmed the coexistence of both metallic and oxide phases (**Figure 30**, b).

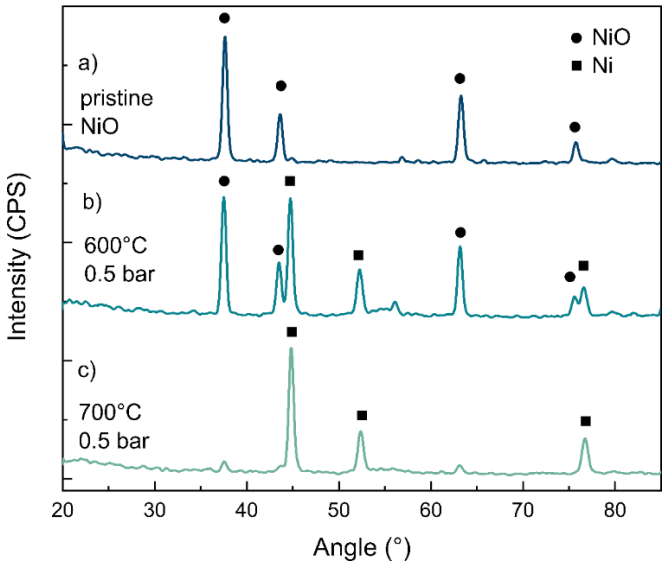

Figure 30: XRD spectra of a) a 40 nm thick nickel oxide thin film after sputter deposition; b) the same thin film after partial reduction at 600 °C; c) the same film after complete reduction at 700 °C.

For the following experiments, the H_2/N_2 pressure was increased to 1.25 bar to speed up the reduction process. Under these conditions, complete conversion of nickel oxide to nickel is found to be attainable at temperatures as low as 400 °C within 10 minutes.

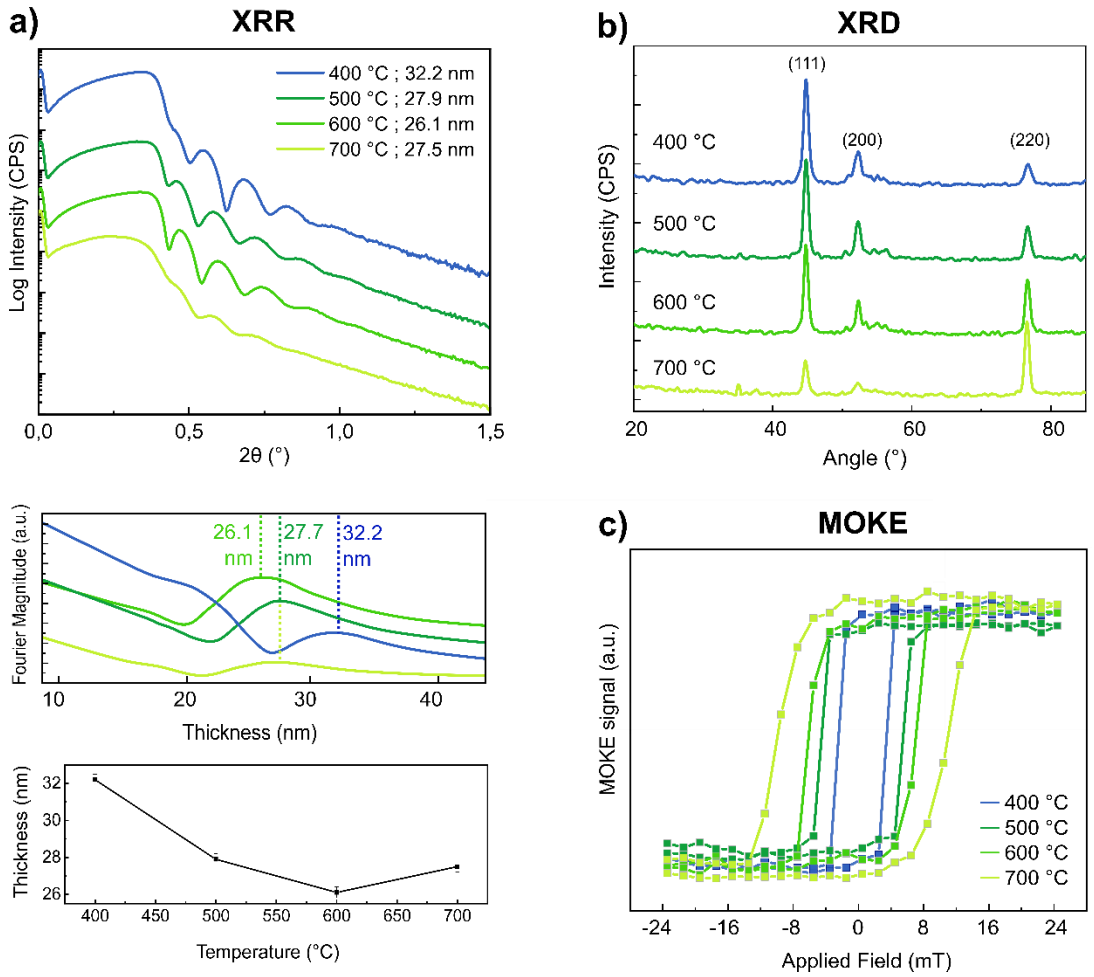

Figure 31: XRR; XRD and MOKE characterization of 40 nm thick NiO thin films, reduced in 1.25 bar of forming gas atmosphere for 10 minutes at temperatures varying from 400 °C to 700 °C.

The samples were reduced in static annealing conditions (See 2.2; **Figure 12**, b) in a forming gas [$H_2(5\%)/N_2$] atmosphere at 1.25 bar for 10 minutes. The temperature range was varied between 400 and 800 °C.

The samples processed at 700 °C and 800 °C showed considerable roughness causing light scattering that impeded the characterization via XRR and MOKE, techniques that both rely on the collection of reflected light at specific angles. While the 700°C sample was still measurable in some flatter areas of the surface, the 800 °C sample was not suitable for characterization with the listed methods and was thus discarded. The stronger scattering of both x-ray and laser (MOKE) incident beams is associated with the observed porosities that the thin films develop at high temperatures and high reductant concentration that cause rapid degassing of water from the surface, thereby creating voids. This can be suppressed with lower reducing temperatures (600°C) or lower forming gas concentration and longer reduction time. As it can be extrapolated

from the X-ray reflectivity measurements, the film shrinkage increases from 7.8 nm for the sample annealed at 400 °C to 12.1 nm for that annealed at 500 °C, and finally to 13.9 nm for the sample annealed at 600 °C (**Figure 31**, a). For the sample annealed at 700 °C, an increase of the roughness leads to an overestimation of the thin film thickness due to the evolution of higher terraces. [116] The increase of the film shrinkage at higher annealing temperatures (below 700 °C) could be linked to the presence of residual nickel oxide in the thin film. In fact, studies on nickel oxide reduction with hydrogen demonstrated that the reaction proceeds with a pseudo first-order kinetics when the nickel oxide clusters are close to each other, and finally slows down when the conversion of the oxide into nickel has reached the 80%, hindering the complete removal of the oxide phase. [117] XRD data further show that increased temperature causes a significant increase of the intensity of the (200) plane signal (**Figure 31**, b), a phenomenon that can occur in textured thin films, when the crystallites are preferentially oriented along certain lattice planes. [118]

The MOKE measurements of the samples show that each thermal treatment in the studied temperature range leads to a different magnetic response (**Figure 31**, c). From the comparison of the different hysteresis loops it can be observed that the increase of the annealing temperature leads to a progressive increase of the coercive field (Hc), but no significant change in the MOKE signal intensity. Several factors can influence the coercive field of the thin film such as material composition, microstructure, and magnetic domain structure. As the most visible changes in the thin films are crystallographic and not compositional (no NiO phase detected), the microstructure should play a dominant role in changing the magnetization behavior of the thin films. The development of the preferential (200) crystallographic orientation and the formation of well-defined magnetic domains due to high temperature re-crystallization [119] are the two most likely explanations behind the increase of coercive field Hc.

4.1.1 Constructing metamaterials

After characterizing the reduction parameters through the observation of the magneto-optical response and crystallography, we have dedicated the remaining chapter to the study of the additional functionalities that nickel acquires when structured into a confined object and interfaced with other materials. The resulting metasurfaces can appear transparent when observed with the bare eye, but are indeed intricated systems that have unique electromagnetic features. [120]

The first case of study is a magneto plasmonic nickel nanodisk array whose functionality derives from the displacement of nickel nanostructures into an artificial lattice. The fabrication of these kind of nanostructured surfaces is conveniently performed using lift-off-based patterning methods. This section will showcase how ALD

can be used in conjunction with resist-based fabrication to structure matter at the nanoscale with high precision. Also, the collective lattice and plasmon resonances arising from high quality nickel nanostructures will be characterized.

The second case of study is a multilayered system composed of a nickel oxide thin film containing nickel metallic domains and coated with aluminum oxide (Section 4.3). The interest for investigating such systems evolves from recently found evidence for an interplay between nickel oxide and alumina and their interaction with small molecules such as ozone and hydrogen. It will be shown that various phenomena such as gas diffusion or entrapment can be exploited during reductive annealing in presence of hydrogen to achieve local reduction of nickel oxide which leads to the formation of metallic domains. These nickel structures, different from those described in the previous part, are not topographical but, instead, they are embedded in the nickel oxide medium. Thus, the obtained object can be considered a flat surface whose properties (magnetics, electric, etc.) change depending on the location. This study unveils that the synergistic interplay of Ni/NiO and alumina may find applications in fundamental studies related to catalysis (HER; hydrogen storage) or engineering of magnetic interfaces.

4.2 Plasmonic nanoarrays

Theoretical and experimental works related to plasmonic nickel-based nanoarrays have already been extensively discussed in literature. [121,122,123] The motivation behind choosing this system is related to two aspects: First, the combination of fabrication methods needed for creating such nanostructures served as the starting point for studying the applicability of ALD methods to nanofabrication. Second, the plasmonic nanoarrays can be finely characterized by optical methods (extinction measurements) and computational tools (Numerical simulations). Given that the overall performance of such structures is affected by the composition and the nanostructure of the material, this characterization provides a simultaneous quality-test for both material synthesis and fabrication.

4.2.1 Fabrication

The nanostructured system of choice is a nanoarray composed by nickel nanodisks of different diameters and heights, positioned on a 10x10 mm sapphire/SiO_2 substrate in a square lattice with a 555 nm pitch for a total lattice area of 500 x 500 μm.

Such structures are typically obtained by eBL, followed by PVD deposition of nickel thin films on top of a patterned resist and subsequent lift-off (See steps 1-2-3 **Figure 16**, a). When using ALD for thin film deposition, such methodology can require

modification of the surface to avoid direct contact between precursors and resists. In the present work, the contact between the co-precursor ozone and the resist polymethylmethacrylate (PMMA950A2) is avoided by using a metallic mask of gold as a template instead of the polymeric resist, which is known to react with strong oxidants. [124] The step-by-step scheme resuming this methodology is shown in **Figure 32** and consists of depositing a thin gold film (80 nm) before spin-coating and curing the PMMA. The resist is then deposited via spin coating and patterned via eBL (step 1); the pattern is transferred to the gold metallic mask via Ar-ion milling (step 2). This step permits a quick removal of the gold from the exposed areas at a rate of 13.15 nm/min while leaving the PMMA-coated areas unaltered. The optimal milling time for mask patterning is 365 s using a conventional ion milling setup with 90° of angle of incidence with the surface described in the experimental section. PMMA is then removed from the gold surface with acetone (step 3) and ALD of NiO is performed (step 4).

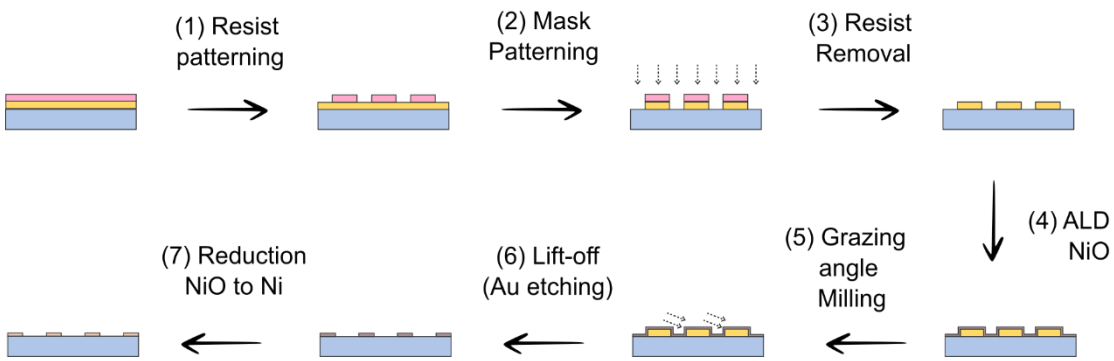

Figure 32: Modified lithography-based fabrication compatible with ALD of NiO.

After NiO deposition, SEM cross-sectional analysis of the nanoarrays showed that a conformal thin film coated both the substrate and mask (**Figure 33**).

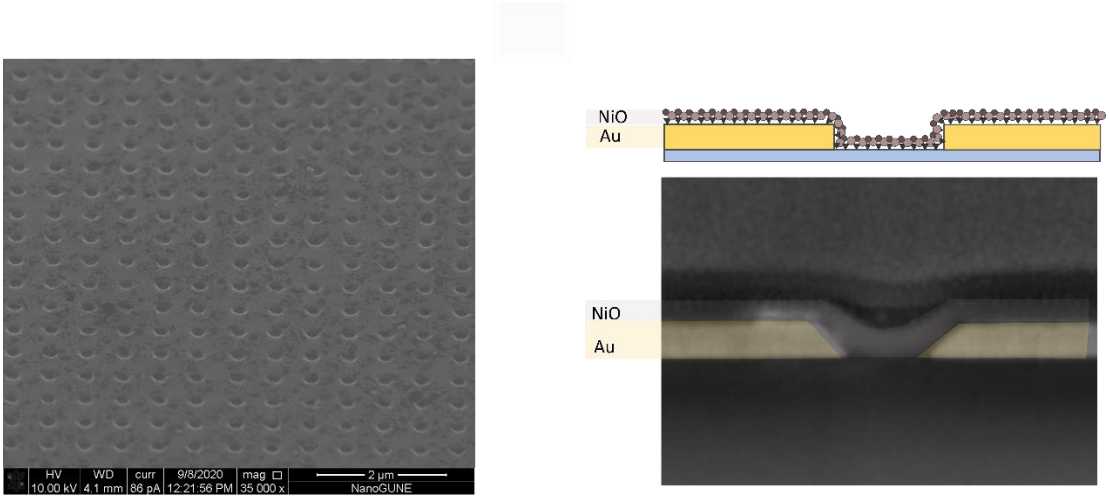

Figure 33: (Left) NiO (40 nm) deposition on a patterned gold mask; (right) simplified schematic and FIB cross-section of the structure, showing conformal coating on the sidewalls of the Au mask.

If the sidewalls of the gold mask were uncoated, its dissolution with Au etchant effectively lift-off the nickel oxide from its surface, leaving behind the desired structures on the substrate. However, gold etching does not result in NiO lift-off, but a continuous thin film is left on the surface, even after gold mask removal (**Figure 34**, a). In this case, the presence of porosities in the NiO microstructure are found to still enable gold dissolution, leaving behind a partially suspended and yet structurally stable nickel oxide thin film.

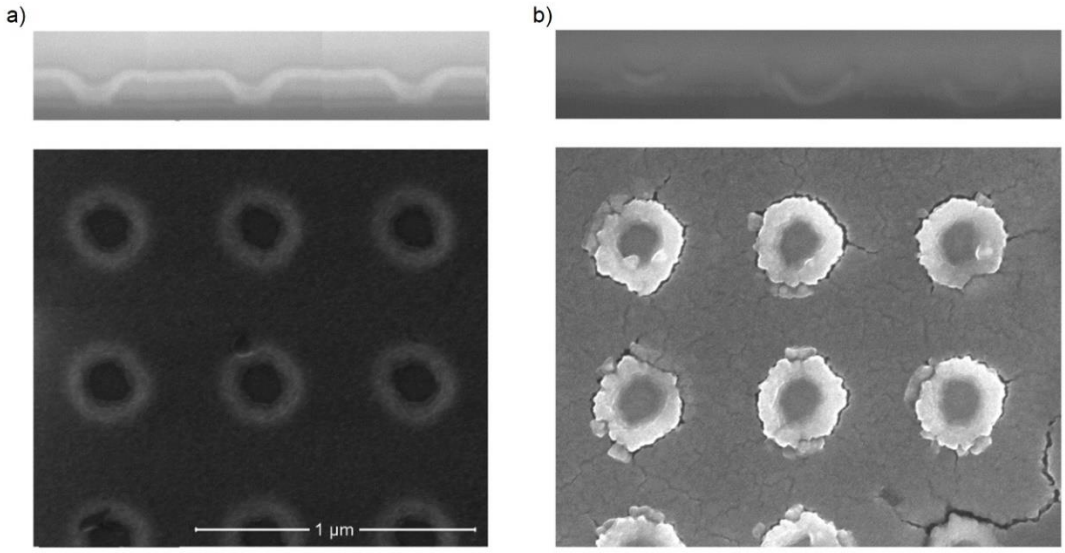

Figure 34: Cross section (top) and top view (bottom) SEM image of a 40 nm thick nickel oxide thin film after (a) Au mask removal or (b) vertical FIB milling, followed by mask removal.

If the film is vertically milled by short exposure to a focused ion beam, the induced damage and resulting surface stress causes its breaking in those areas where, after the gold mask removal, the thin film is unsupported (**Figure 34**, b). The residual thin film, although disconnected from the structures, remains on the substrate and is hardly removed (**Figure 35**).

In both cases the remainder of material between the structures after gold removal makes these pathways not suitable for nanofabrication.

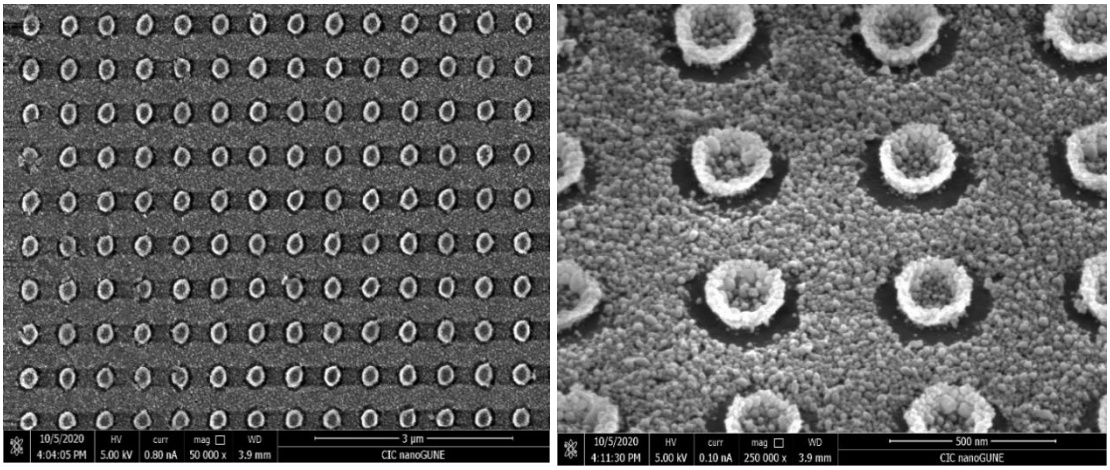

Figure 35: SEM top and birds' eye view of nanoarrays on surfaces and undesired residual film between the discs.

The optimized methodology for ALD-compatible nanofabrication is reported in **Figure 32** and utilizes a step of ion milling at a low angle of incidence prior to lift-off (Step 5), to facilitate the thin film removal. This is a common procedure in lift-off-based fabrication, which is conventionally applied after resist removal to eliminate defects arising from material accumulation (deriving from PVD) on the sidewalls of the resists. This step, when ALD is used for thin film deposition, must be anticipated in the sequence, and performed before lift-off.

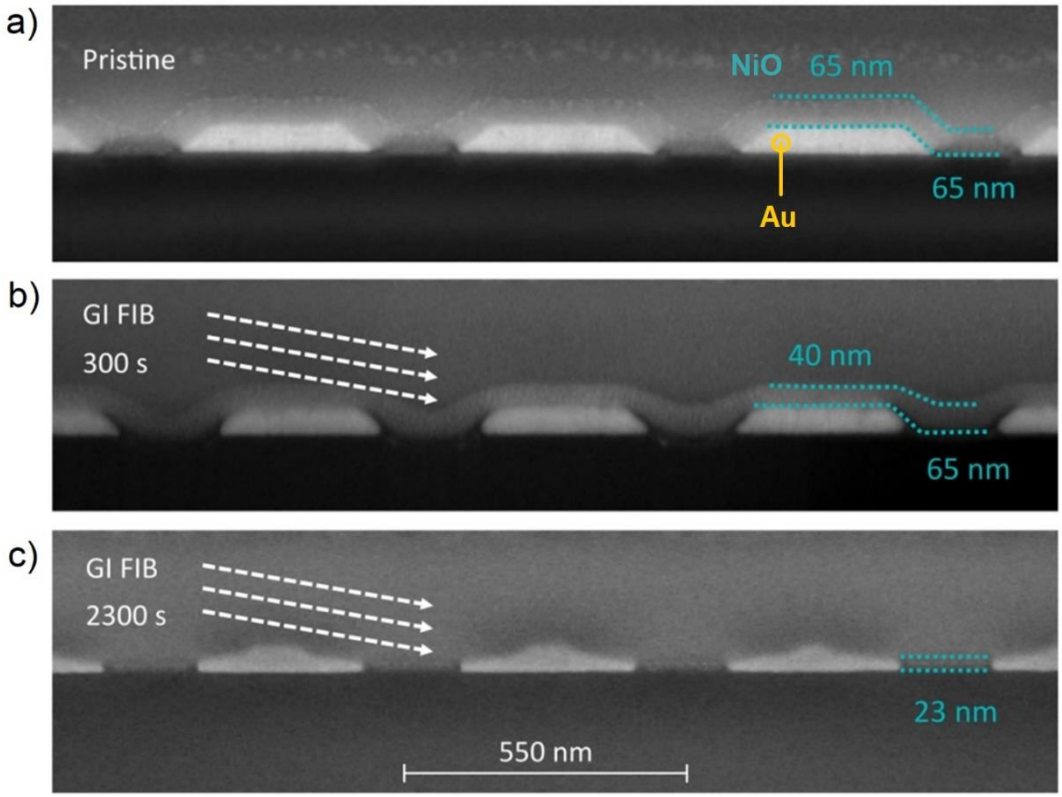

Figure 36: Cross-sectional SEM images of the Au (bright grey)/NiO interface a) after ALD deposition, b) after 300 s, and c) after 2300 s of low angle of incidence milling.

The ion milling conditions were optimized on a sample with 65 nm of NiO deposited atop an 80 nm Au mask. The beam parameters are reported in section 2.5.2.

To calculate the NiO milling rate, the sample is exposed to an argon ion beam for 300 s and transferred to the SEM. The cross-section analysis (**Figure 36**) shows that the milling of the NiO thin film occurs on features with higher topography. No NiO removal is observed in areas where the oxide is in direct contact with the substrate thanks to the shadowing by surrounding elevations (**Figure 36**, b). Using this configuration, the thin film is removed at a rate of approximately 5 nm/min from the top of the hard mask. Upon milling for 2300 s, which should correspond to the removal of three times the thickness of nickel oxide thin film, the gold mask is thinned to half of its original thickness (approximately 40 nm at the highest point) (**Figure 36**, c). Still, a residual NiO thin film of 23 nm thickness remained, demonstrating that even after excessive milling the mask is screening the thin film on the surface, avoiding its complete removal. This implies that, when implementing this step, the milling time does not necessarily need to be exact. Slight over-milling will not destroy the desired structures.

The optimal milling time for facilitating lift-off was found to be 480 s. Under this condition, the desired thin film is left unmodified, and the residual thin film is easily removed during mask etching.

Using this scheme, nickel oxide nanostructures have been successfully fabricated. In **Figure 37** an array, composed of 40 nm thick nickel nanodisks of 260 nm diameter, is shown. The surface was analyzed and EDX showed that after lift-off the silicon surface is clean from NiO residuals. The inset in the middle figure shows the overlay of 3 different EDX signals, Ni-L (orange); O-K (yellow) and Si-K (purple). The obtained NiO disc array reflects the original design of the pattern on the resist.

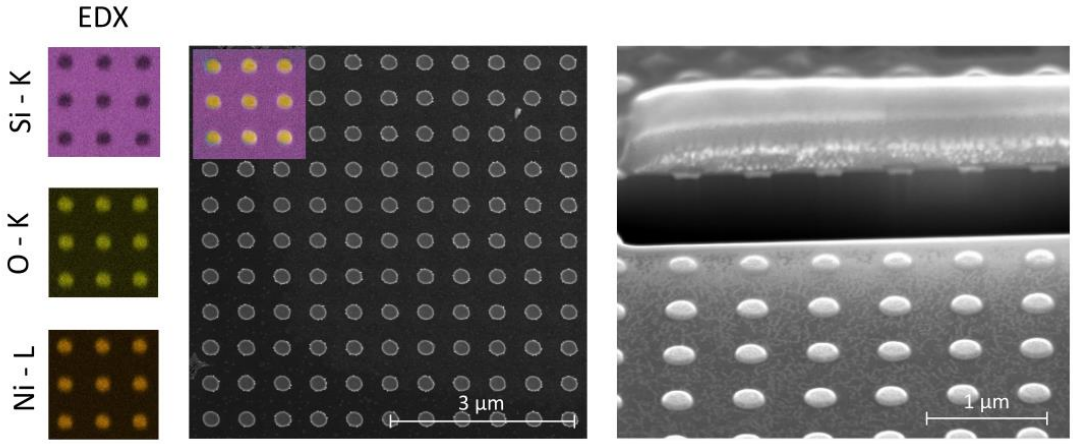

Figure 37: SEM figure of the array surface and the cross-section. EDX micrographs to the left show a clean silicon surface (purple), decorated with NiO (yellow,orange) nanodisks. The cross-section image to the right shows 40 nm high NiO nanodisks.

4.2.2 Surface and plasmon resonances

Nanostructured nickel metasurfaces are advanced functional surfaces which enable to exploit light-matter interaction for technologically relevant effects. [58] As previously discussed, nickel nanostructures, just as thin films, are magneto-optically (MO) active, a characteristic which derives from their composition and domain structure. In our case those factors are controllable by the synthesis parameters (ALD + reduction). When confined into small structures, the magnetic properties can be tailored through magnetostatic contributions deriving from shape and edges. In this thesis, the effect of the reduced dimensionality will not be investigated from the magnetism perspective, as it is already extensively studied for these systems, [58] but from the perspective of light-matter interactions.

When light irradiates nickel structures with dimensions comparable to the incident wavelength, localized plasmon resonances (LPR) can be excited. When excited particles are aligned in an array, collective lattice excitations, known as *Surface Lattice*

Resonances (SLR), can simultaneously be excited with the incident light. The synergistic interaction of these resonances, in coexistence with the inherent magnetism, lead to an enhancement of both MO and plasmonic response of the system. [123]

Nickel nanodisk arrays have proven to be efficient nanoantennas for molecular detection where the interplay of the mentioned phenomena enhances the sensitivity and adds tunability through the application of external fields. [57] The working principle of these systems is analogous to all the other plasmon-based sensors where small local perturbations are detected as shifts in the LPR peak position deriving from the changes of the sensor's surrounding medium. [125] The accuracy of such detectors thus relies on the precision of peak tracking relative to the change of the refractive index of the surrounding environment. This means that LPR-characteristic magnitudes, such as the full width at half maximum (FWHM), are key performance-defining parameters.

4.2.2.1 Sensitivity enhancement

Compared to metals such as gold and silver, which show sharp and narrow LPR absorption peaks, the nickel peak is wide and rounded. Without any enhancement, the added MO functionality, introduced by a ferromagnet instead of a prototypical plasmonic metal, would come with the tradeoff of having a lossy plasmonic response which does not enable any technological application.

One way to narrow the LPRs peaks is to arrange nickel particles into ordinate arrays which, similarly to crystalline materials, produce collective resonances. In a crystal, atoms are arranged in a specific periodic pattern which determines distinctive vibrational modes (phonons) that can be excited by monochromatic light whose frequency matches the natural frequency of these vibrations. [122,126] These light-matter interactions, occurring at a specific wavelength determined by the lattice, are so-called "lattice resonances" which cause a collective excitation of the lattice structure leading to an enhancement of optical effects (absorption, scattering or reflection).

Through the design of an "artificial crystal" such as a nanoarray, the frequency of these resonances is modified to match LPR absorption, producing absorption enhancement and ultimately increasing the overall accuracy of the sensor. In analogy to normal crystals in which the resonance frequency is determined by the atom spacing, in nanoarrays they are determined by the so-called "lattice constants" of the periodical displacement of nanostructures composing the array. An array with the lattice constant (W) in contact with a medium with refractive index "n" generates a lattice resonance at the wavelengths $\lambda_L(m,n)$ at different refractive orders (m,n):

$$\lambda_{\mathrm{L(m,n)}} = n\frac{W}{\sqrt{m^2+n^2}} \qquad \text{(Eq. 12)}$$

In the case of the present study, all neighboring nickel nano-discs in the array are positioned in a square lattice with the constant W= 555 nm. The interfaces between structures and the surrounding medium are on the one hand with the sapphire substrate (n= 1.73) and on the other hand with air (n=1).

4.2.3 Optical Characterization

The optical characterization of four different nanoarray structures were performed by Dr. Paolo Vavassori (Nanomagnetism group) at CIC nanoGUNE. The measurement consisted of irradiating the samples with monochromatic light in the wavelength range between 400 nm and 1600 nm and acquiring the transmittance $T=I/I_0$. I and I_0 are the intensity of transmitted and incident light, respectively. The excitation of the plasmon and lattice resonances is detected by means of increased light absorption by the sample. It is represented by the quantity 1-T (proportional to extinction) [13]. The measured absorption curve is fitted with the numerical absorption spectra of an ideal infinite nickel nanoarray which has the same geometrical characteristics as the fabricated samples. The theoretical response of the arrays was simulated by Dr. Mario Zapata from the Materials physics center (CFM) using the RF (radio-frequency) module on COMSOL Multiphysics, [79] with the same experimental approach that he adopted already in previous studies. [127,128] The computed (1-T) of the arrays are presented together with the experimental spectra.

The relationship between the optical response and the array design has been studied by correlating shape and positioning of the resonance peaks to the change of one single dimensional parameter, namely the diameter of the nanodisk "*D*". Each array was composed of discs with following diameters: D=215 nm, D=235 nm, D=285 nm, D=315 nm (**Figure 38**).

[13] We will refer to the quantity 1-T as extinction.

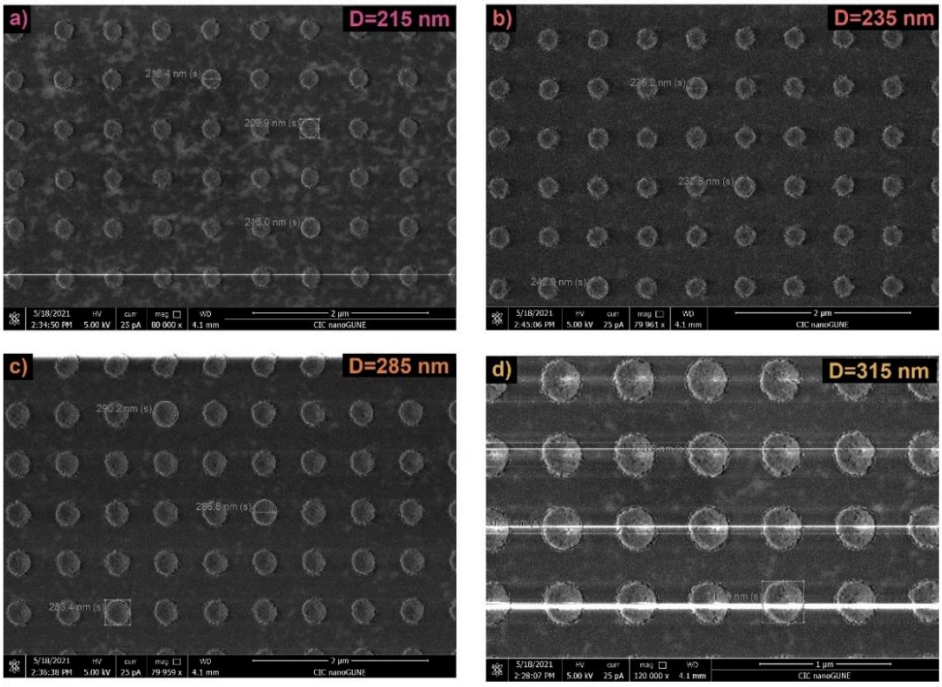

Figure 38: SEM images of the 4 fabricated nanoarrays with the disc diameters having been varied: a) 215nm, b) 235 nm, c) 285 nm, d) 315 nm.

The fabrication consisted of thin film deposition, eBL patterning, and Ar-ion beam etching, following the sequence depicted in **Figure 16**, b. The reductive annealing (See 2.2) was performed at 600°C for 1hr with 1.25 bar of forming gas.

The remaining characteristic dimensions of the arrays were kept constant. Ni disc height: 50 nm ± 2 nm, square lattice with 555 nm of center to center spacing between nearest neighbors.

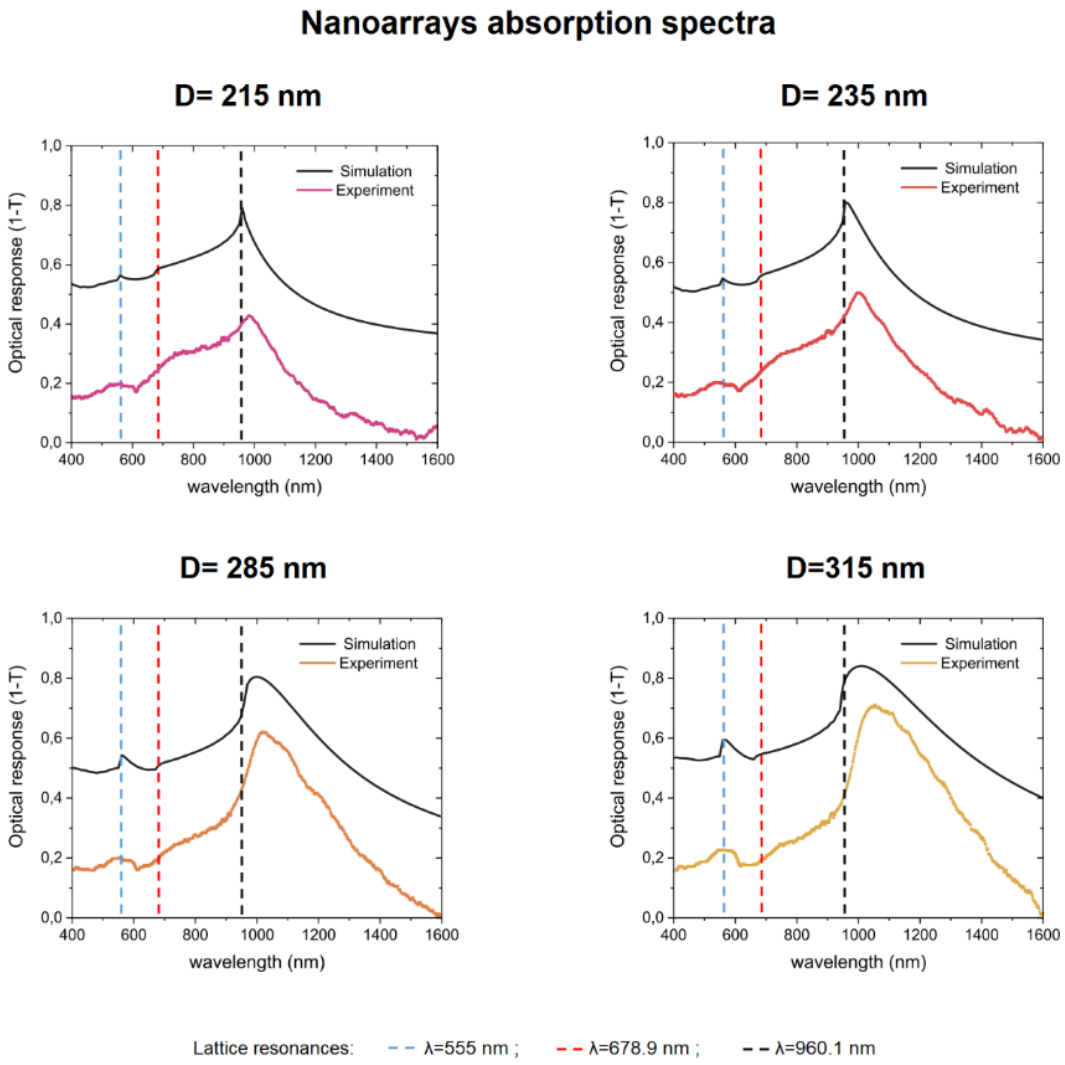

Figure 39: Optical response (1-T) of the nanoarrays with D = 215 nm, 235 nm, 285 nm, 315 nm in the λ region between 400 nm and 1600 nm.

The spectra of the 4 different arrays (**Figure 39**) contain both numerical and experimental extinctions of the four array systems. The black curves show the calculated 1-T of the respective nanoarray, while the colored curves are experimental data. The dashed lines represent the 3 different lattice resonances which satisfy **Equation 12**. The first SLR for λ=555 nm (blue) is obtained for refractive index n=1 (air) and m,n=1,0 (m,n are degenerate therefore m,n=1,0=0,1). The second lattice resonance is positioned at λ=678,9 nm (red) for the same m=n=1 refractive orders at the interface between discs and the underlying sapphire crystal (n=1.73). The last lattice resonance appears at λ=960.15 nm (black) for m,n=1,0=0,1. In this spectral region the nickel LPR is also present as a broad peak.

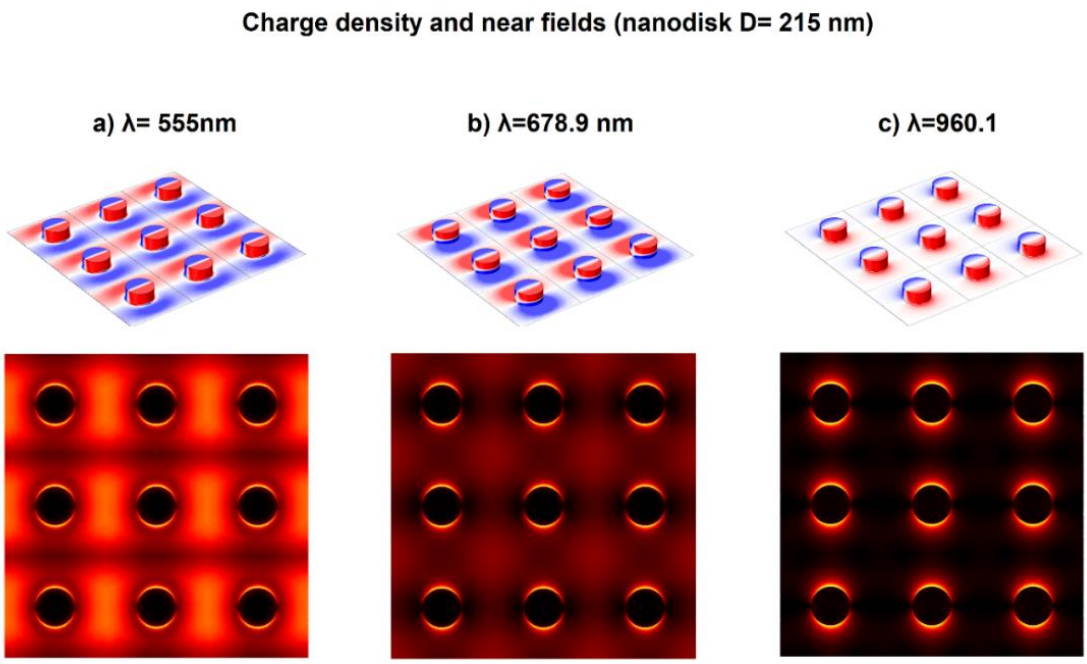

Figure 40: Modelled charge densities and near fields of nanodisk arrays with D=215 nm at the three lattice resonance wavelengths: a) 555 nm; b) 678.9 nm; c) 960.1 nm.

For all samples the experimental curves are in good agreement with the model of the structures. However, the theoretical values are systematically shifted to higher 1-T values due to the underestimation of the transmittance in the infinite array model. The overestimation of the 1-T, as well as a widening of the absorption peaks, is not surprising given that the theoretical model is based on an ideal infinitely large array, that, compared to the actual array of finite area, presents higher 1-T.

Figure 40 shows the charge densities and near fields of the infinite arrays at the resonance frequencies. The charge density maps of a single resonant nanodisk have been simulated and are shown. These images, even though composed of Ni discs with 215 nm diameter, are representative for the whole group of samples.

The first lattice resonance (λ = 555 nm) is generated at the interface between metal and air and leads to an increased charge density in the shortest gap between two neighboring discs (**Figure 40**, a). The radiation pattern of a single nanodisk antenna is represented by the directivity [14] (**Errore. L'origine riferimento non è stata trovata.**, a). Here, the emitted power is lowest in the plane of the substrate and the radiation is mainly located in two lobes extending along the x and y axes. By

[14] In electromagnetism, the directivity is a quantity which defines the spatial distribution of the radiation intensity emitted by the nanoantenna, in this case a single nanodisk.

considering the simulated extinction curves of the arrays (black curve in **Figure 39**), it can be observed that the increase of disc diameter leads to an enhancement of the resonance intensity. The height of the predicted $\lambda_{555\ \mathrm{nm}}$ resonance (dashed blue line) gradually increases as the disc diameter is increased from 215 nm to 315 nm as a consequence of the narrowing of the gap between two resonating structures as the diameter is increased but the W is kept constant. This enhancement, which is considerable in the numerical prediction and leads to a pronounced peak narrowing, is less evident in the fabricated arrays. In contrast to the theoretical prediction, showing a peak with small intensity for D=215 nm and an increased intensity as D is increased, each fabricated sample showed a broader absorption peak in this region and the intensity is visibly enhanced only for D=315. In the experimental dataset this absorption peak is still centered at $\lambda = 555$ nm, but it extends into a wider spectral range (wider peak). The widening of the experimentally observed resonance peak compared to the computational model is related to the mismatch between the sample's inter-disc spacing to the ideal 555 nm. When fabricating these arrays, misalignment during eBL writing can lead to the presence of different spacings at the boundaries of different write fields. Contrary to the ideal case, the samples present a gaussian distribution of longer and shorter spacings centered at 555 nm, contributing to the widening of the peak.

The second lattice resonance ($\lambda = 678.9$ nm) mainly propagates into the substrate (**Errore. L'origine riferimento non è stata trovata.**, b) and has 4 small lobes in the near surface region which extend along the vector connecting the closest discs. When multiple discs interact in the array (**Figure 40**, b), the resulting charge density is homogenously distributed throughout the whole substrate due to the strong overlap between the generated fields. For both experimental and theoretical data, the disc diameter does not affect the intensity of this absorption. In the experimental data, this SLR peak position is shifted at higher wavelengths, and it can be observed as a flex point in the extinction curve located around $\lambda = 730$ nm. The fact that this experimental SLR peak position, as well as the highest λ SLR peak position, are both shifted compared to predictions, can be related to a deviation of the refractive index n of sapphire compared to its nominal value of 1.73 used for the simulations.

The third lattice resonance ($\lambda = 960.1$ nm) also shifts upon increasing the diameter of the disc in both simulations and experiments. In the simulation, the resonance of the D = 215 nm sample is centered at $\lambda = 960.1$ nm, which coincides with the pure lattice resonance frequency. Here, it can be observed that in the experimental results the peak position for D=215 nm shows a small offset with the theoretical prediction, a result that, as explained before, can be related to a deviation of the refractive index of the substrate. However, in both cases the SLR peak noticeably shifts to higher wavelengths when D is increased. This demonstrates that the lattice resonance, which

should be independent of the disc size, is hybridized with a LPR mode, whose spectral position instead depends on the disc size. Along with the shift, the shape of the resonance peak also changes from sharp to rounded. The same behavior is found in the experimental dataset. From the charge density and near field maps of the arrays (**Figure 40**, c) it can be observed that the fields resulting from such hybridization are highly localized around the particles.

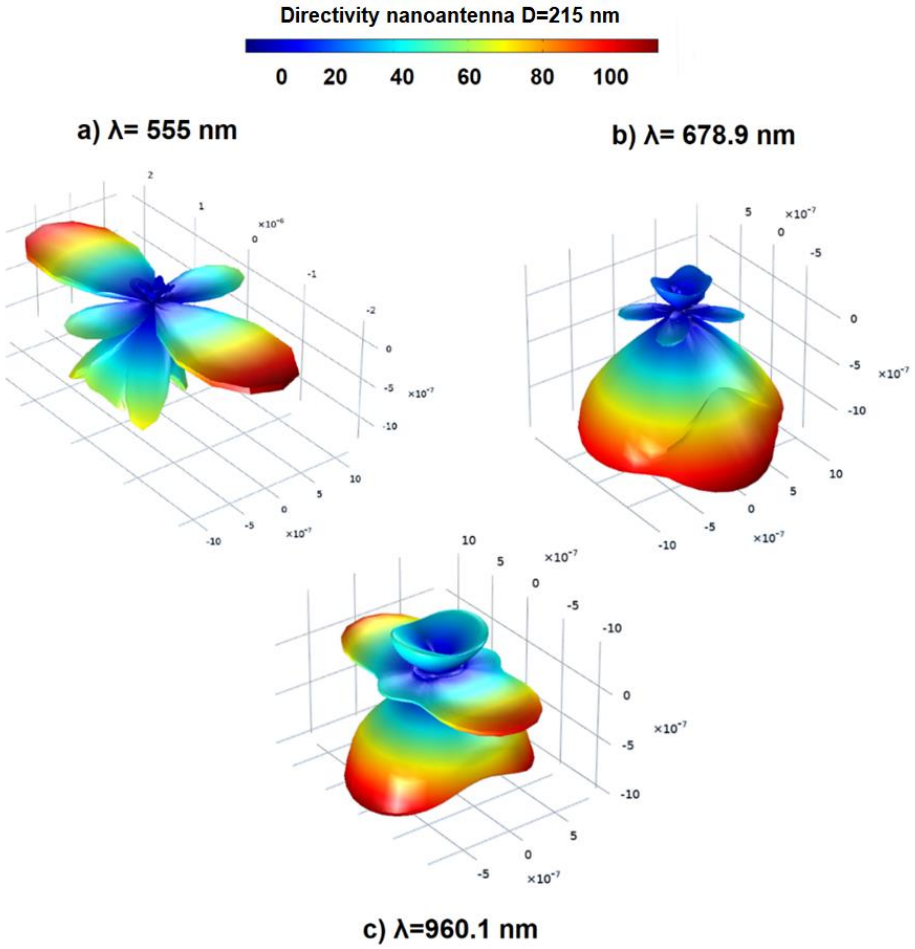

Figure 41: Modelled directivity of a single nickel nanoantenna with D=215 nm at the three lattice resonance wavelengths: a) 555 nm; b) 678.9 nm; c) 960.1 nm.

The good agreement between theoretical and experimental data reveals that ALD-deposited metallic nickel films are fully functional and suitable for future technological applications. Moreover, the fact that such material characterization could be performed on intricate systems, such as the described arrays, shows that ALD can also be implemented in fabrication schemes for such nanostructures.

4.3 Embedded magnetic domains

In this chapter, we discussed how nickel oxide can be reduced to metallic nickel and structured into nano-sized objects to achieve new functionalities arising from the material confinement. Up to now, such confinement has been achieved by adding or removing material in some desired areas through conventional lithographic techniques.

However, the topographical structuring of matter (defined by either the presence or absence of the material on the surface) is not the only way to achieve new functionalities. This section focuses on a newly developed method to achieve spatially controlled reduction of a nickel oxide layer to produce conductive and magnetic patterns embedded into the original oxide film. Like in phase nanoengineering, we introduce new properties into the thin film by locally changing its composition instead of directly structuring it into a small object.

The method uses an ultra-thin alumina capping layer to passivate nickel oxide from reduction by suppressing gas exchange with the environment during annealing (**Figure 42**). Some openings (windows) are patterned into the alumina exposing the underlying film. The annealing step is then optimized in a way that the reduction occurs only in exposed areas.

4.3.1 Fabrication

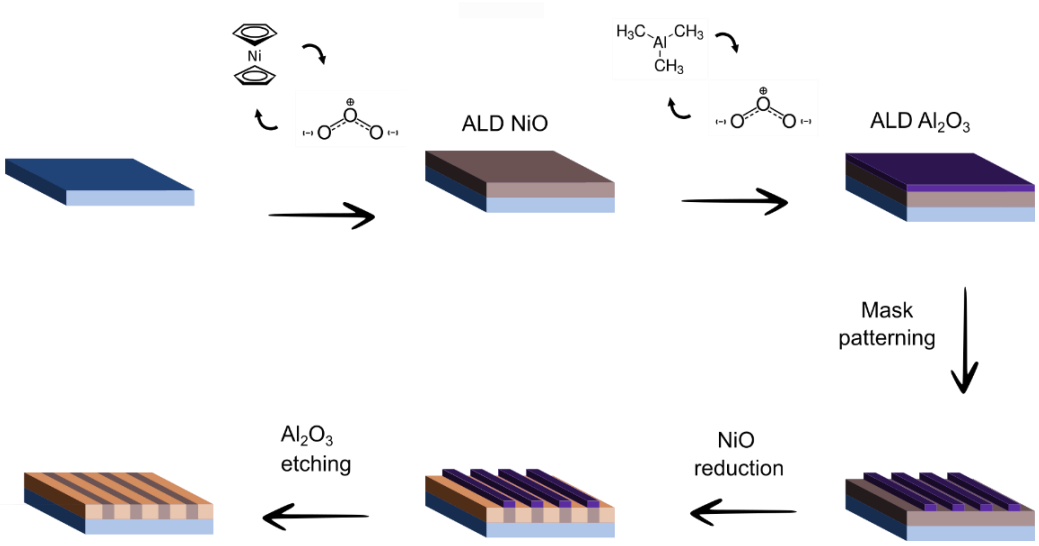

Figure 42: Processing steps for fabricating nickel domains embedded in nickel oxide thin films.

The samples discussed in this section consist of silicon (100) wafers coated with nickel oxide and capped with aluminium oxide. Al_2O_3 has been deposited by ALD using Trimethylaluminium (TMA) and ozone as precursors (GPC=1.1 Å). The alumina film thickness ranged from 5 to 40 nanometres, depending on the experiment. The exact experimental details of the annealing step will be described at the beginning of each section before discussing the results.

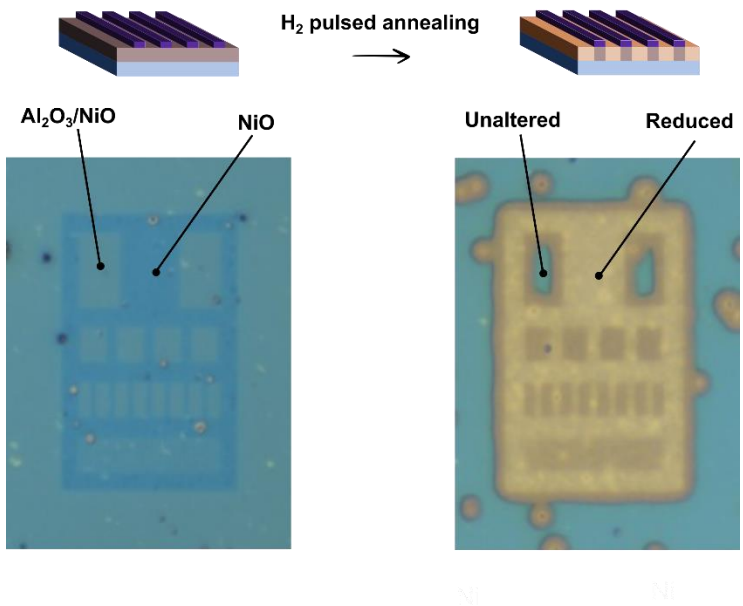

Figure 43: Sample coated with a 16 nm thick Al_2O_3 mask that has been patterned to expose the underlying NiO. To the left, the darker areas demark selectively removed alumina. To the right, the color change shows the domains of reduced NiO to Ni after pulsed annealing with H_2.

After deposition the alumina was selectively removed from some areas, creating some windows using eBL+etching (See 2.5.1,2.5.2). Reductive annealing experiments were carried out using the IR-heated furnace (See 2.2) in static and pulsed annealing mode (**Figure 12**, b). After reduction, the alumina can be easily removed with various etchants. In this thesis 50 wt.% KOH solution has been used to remove Al_2O_3 while leaving the Ni/NiO domains unmodified.

The complete step-by-step fabrication scheme is shown in **Figure 42**.

4.3.2 Characterization of domain broadening

As it can be observed in **Figure 43**, the shape of the nickel domain obtained after reduction appears blurred with reference to the originally milled window. This "broadening" is a consequence of the lateral gas diffusion occurring at the interface between masked and unmasked areas (**Figure 44**, a,b) and cannot be completely avoided. However, it can be strongly suppressed by adjusting the processing parameters of the reduction (such as temperature and reductant pressure) and the alumina mask thickness.

To quantify the broadening, the mismatch between one arbitrary edge [15] of the alumina mask and the boundary of the corresponding ferromagnetic domain obtained after reduction, has been measured. Domain broadening can be easily observed with an optical microscope because the reduction from nickel oxide to nickel is associated with a noticeable colour change (**Figure 43**).

Defining this quantity is useful to determine the precision of the process of pattern transfer during reduction and the resolution of the technique (smallest feature achievable).

[15] Every edge is equally valid for characterizing the broadening because of its anisotropy in the x-y plane,

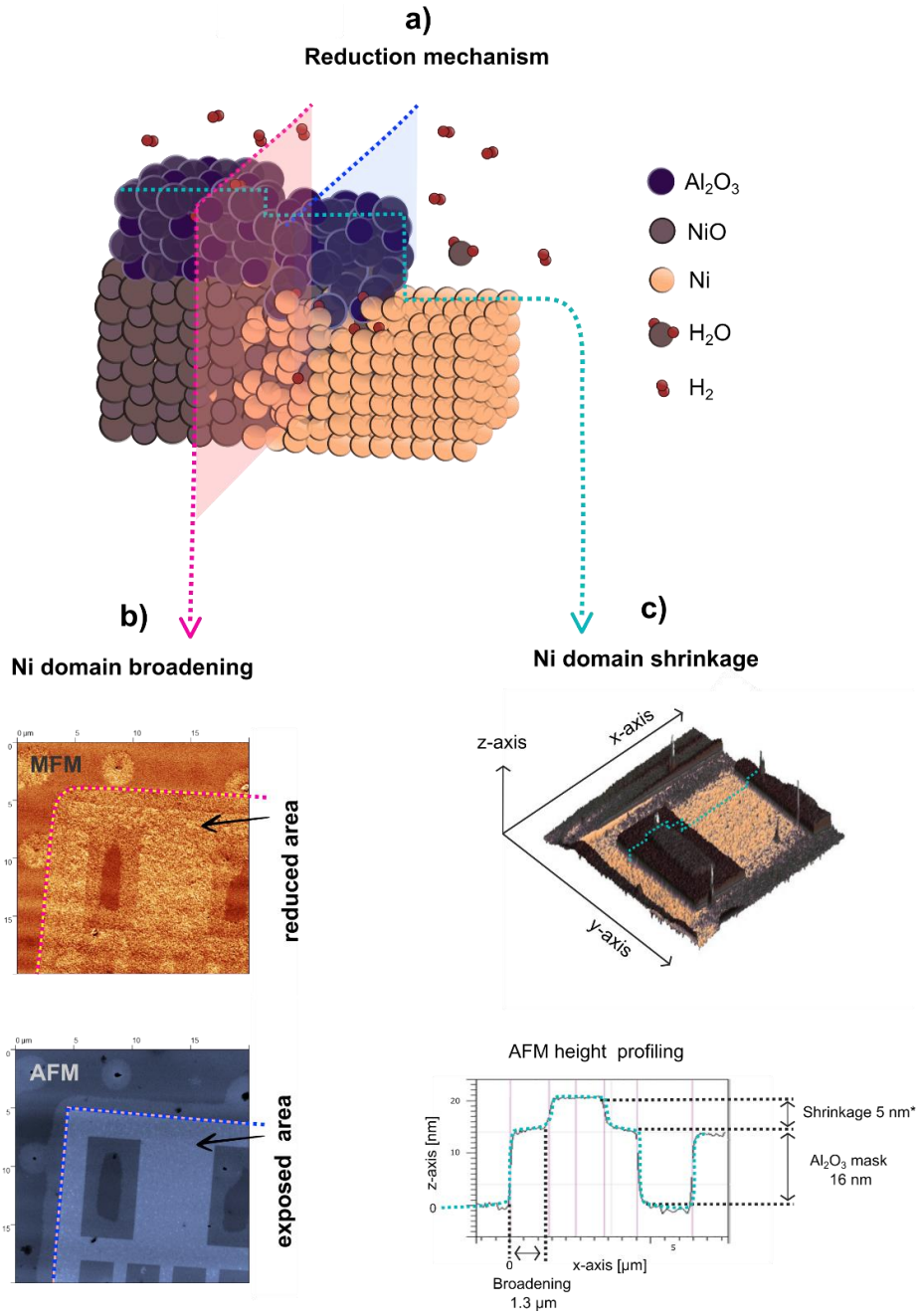

Figure 44: a) Diffusion-mediated reduction of nickel oxide. The three dashed lines represent the edge of alumina mask (blue), the edge of a magnetic domain (red) and the line profile traced with AFM (aquamarine); b) MFM and AFM images of the magnetic domain where the magnetic domain edge (dashed red line) and the mask edge (dashed blue line) have been highlighted. c) AFM 3D map and resulting line profile where both shrinkage and pattern broadening can be observed.

A combined AFM/MFM [16] (**Figure 44**) analysis of a test sample [80nm NiO/15 nm Al_2O_3] was performed after its reduction to confirm that the edge of the modified area (identified by the color change on the optical microscope) corresponds to the actual edge where ferromagnetism is detectable.

To create the domains the sample was rapidly heated to 500 °C under vacuum. After 40 seconds of thermal stabilization, 10 s of H_2/N_2 (at 0.5 LPM) were applied to reduce the NiO. The surface topography and magnetic response of the reduced area at the interface with the alumina mask (**Figure 44**, b,c) was studied with AFM/MFM. The AFM height profile (**Figure 44**, c) shows that the extent of the broadening is approximately 1.3 μm and the NiO shrinkage is about 5 nm. A comparison between surface topography (AFM) and magnetic response (MFM) of the same area (**Figure 44**, b) highlights the mismatch between the magnetic domain and the size of the window in the alumina mask. From the MFM data of the surface (**Figure 44**, b) the size of the magnetic domain correlates with the 5 nm shrunk film (**Figure 44**, c) and thus with the color change associated to the reduction. Thanks to this consideration, future characterization has been performed through observation of the color change with an optical microscope which is a time efficient procedure to determine the lateral broadening of the magnetic domains.

Regarding the surface planarity, it is found that the reduction causes a loss of the 6.25% of the initial film thickness. It can be expected that the shrinkage induced by this fast reduction is always close to this value. For thin nickel oxide films (40 nm), the height difference between reduced and oxidized domains is expected to be 2-3 nm.

4.3.2.1 Temperature dependency

The effect of the temperature on both broadening and extent of magnetization has been analyzed by performing 60 seconds of static annealing in presence of 200 mbar of forming gas in the temperature range between 600 °C and 750 °C (**Figure 45**).

To quantify the extent of the reduction, hysteresis loops have been collected using the MOKE microscope (2.6.3).

In the studied temperature range rapid annealing causes a change of the magnetic properties of the surface from paramagnetic (NiO) to ferromagnetic. At 600 °C the

[16] AFM/MFM analysis was performed by Matteo Menniti of nanomagnetism group under the supervision of Paolo Vavassori.

hysteresis loop shows no coercivity and remanence. Between 650-700 °C, the magnetic response shown by the metallic domains is very similar. They present a higher coercivity and remanence due to the higher conversion rate of nickel oxide into nickel as the temperature is increased. A further increase to 750 °C causes an extra increase of the coercivity. The analysis of the pattern broadening shows an expected increase of the domain size as the temperature is increased which correlates with the increase in coercivity. This result emphasizes that the extent of the reduction and the lateral diffusion causing the broadening are both enhanced as the temperature is increased.

In analogy to the temperature increment, increased reductant pressure also accelerates the NiO reduction, but is also detrimental for the resolution (enhanced broadening). For this reason, low temperatures and pressures are preferred.

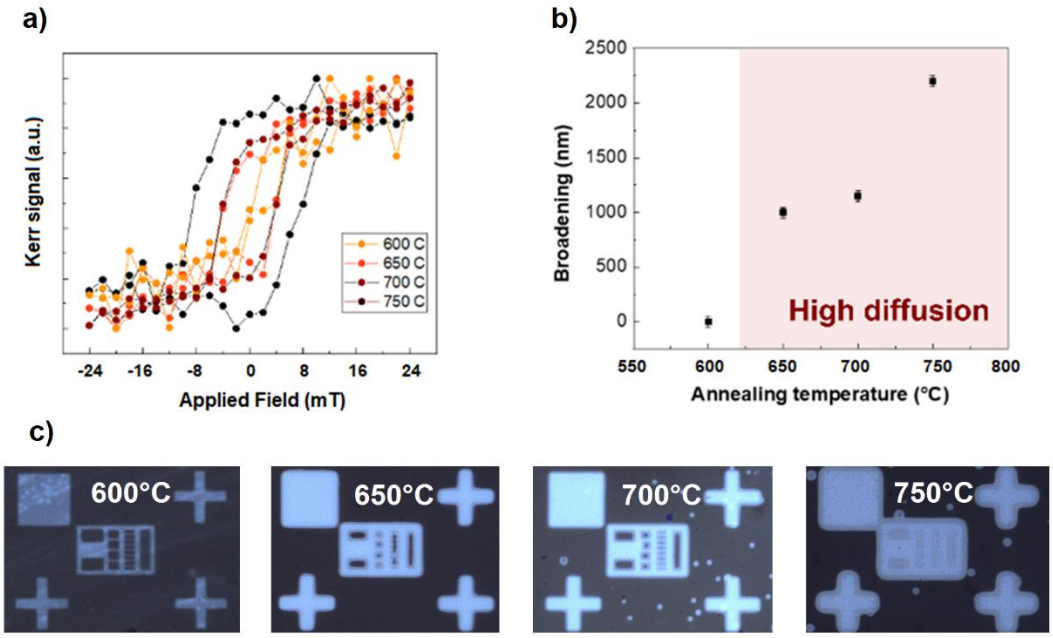

Figure 45: A broadening of the pattern is observed as the annealing temperature is increased. a) hysteresis loops collected from the reduced areas for the four different annealing temperatures. b) Broadening as a function of the temperature. c) Optical images of the magnetic domains.

4.3.3 Conductivity measurement

In this section we show one possible application for this newly developed method and the studied group of materials. Through time-efficient processing (approximately 5

minutes), which could be easily upscaled to wafer size production, we produce a conductive nickel Hall-bar embedded in an insulating nickel oxide thin film.

To fabricate a conductive nickel structure, we transferred the design from the patterned Al_2O_3 mask (5 nm) to NiO (40 nm) through pulsed annealing performed at 600 °C with 6 s exposure to H_2/N_2 with 0.5 LPM), under these conditions, the lateral broadening is approximately 700 nm and does not affect the functioning of the device which is hundreds of micrometres in size.

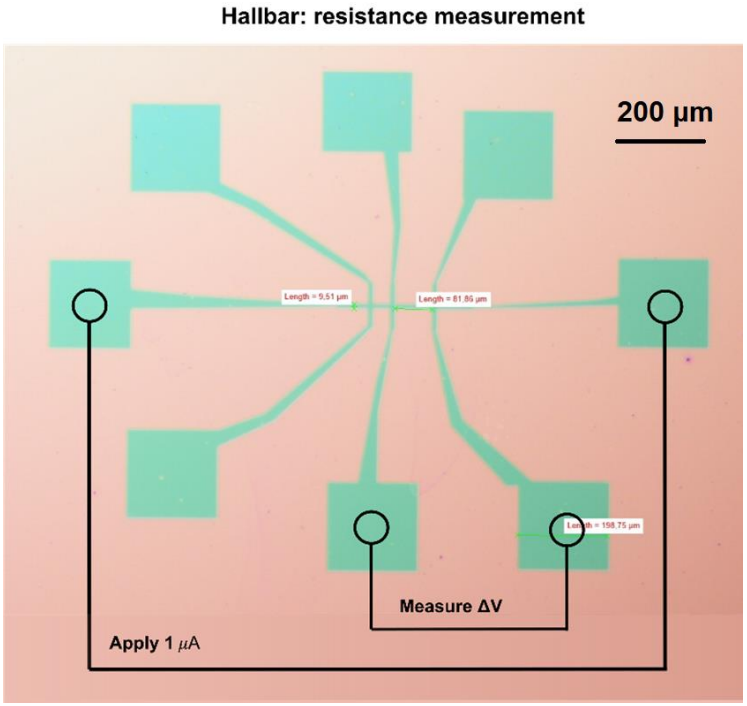

Figure 46: Pulsed reduction process used to a) quantify the hysteresis of the reduced domain and its broadening by 690 nm and b) fabricate a functional nickel structure for the IV measurement.

The device is characterized through 4-point probe method, [17] by applying 1 μA and by measuring the resulting voltage as depicted in **Figure 46**. From Ohm's law (R=I/V), the resistance (R) corresponds to 264.4 Ω. To calculate the resistivity, the dimensions of the channel have been measured from an image of the surface captured with an optical microscope.

For the fabricated sample, the resistivity $\rho = 1.28$ $\mu\Omega$m is calculated from:

[17] This measurement was performed by F. Calavalle from the group on Nanodevices at CIC nanoGUNE.

$$\rho = \frac{RA}{l} \qquad \text{(Eq. 13)}$$

Where A=0.4 μm and l = 82 μm are the cross section and the length of the conductive channel, respectively.

The resistivity of the metallic domain obtained in this experiment is expectedly higher than the resistivity of bulk crystalline nickel (0.07 $\mu\Omega$m) [129] or chemically deposited nickel thin films (0.2-0.3 $\mu\Omega$m) [130] due to its partially oxidised nature, but it is still useful for technological applications.

We suggest that this simple experimental approach to nanofabrication could unlock new device architectures which integrate, in a single thin film, many functionalities.

Using this method, topographically flat nickel contacts could be used to characterize 2D materials in a fast and efficient way. Thanks to it planarity, the flakes under investigation could be simply stamped on the surface avoiding tedious liftoff-based fabrication.

4.3.4 The role of Alumina

The pulsed annealing procedure was optimized to allow reduction of NiO at lower temperatures and reductant pressures, limiting the undesired lateral growth of the domains.

4.3.4.1 Hydrogen trapping in alumina thin films

The choice of using alumina is based on its high performance as capping layer [131] and for surface passivation. [132] For the specific case of hydrogen, Al_2O_3 coatings have been extensively studied as permeation barrier and their performance strongly varies depending on the deposition method and the final composition of the material. [133] Outstanding conformality, high density and low deposition temperature make ALD-deposited alumina an efficient capping material. [134] Another advantage of ALD is that, by adjusting the deposition temperature or switching co-precursors, the material properties can be tailored for a desired application. The most used precursor for ALD-Al_2O_3 is Trimethylaluminium (TMA), which can be combined with various oxygen sources such as H_2O, H_2O_2, O_3, or oxygen plasma. [135] TMA-H_2O deposited alumina, for example, is non-stoichiometric and hydrogen-rich. Its composition is more

accurately represented by the formula $Al_2O_x(OH)_{6-2x}$, where the OH concentration can be increased by decreasing the deposition temperature. [136]

For the desired application as hydrogen barrier, high deposition temperatures [137] and reduced OH concentration [138] are reported to improve the material performance. By using ozone instead of H_2O as co-precursor, the thin film composition changes from -OH rich to -CO rich. Higher carbon is found to contribute to hydrogen diffusion blocking in the thin films through a trapping mechanism. [139] When the film takes up hydrogen, it can react with the C-O bonds and form C-OH bonds following the reaction:

$$C\text{-}O + H \rightarrow C\text{-}OH \qquad \text{(Eq. 12)}$$

For the desired application of hydrogen-trapping, ozone-deposited alumina is expected to outperform water-deposited Al_2O_3 and is therefore chosen for the experiments in this thesis.

4.3.4.2 Varying Al_2O_3 thickness

The samples used for this characterization are 40 nm thick NiO films coated with alumina with thicknesses of 5, 20, 30, and 40 nm. All samples have been reduced simultaneously in a single experiment to ensure identical conditions. The samples were loaded into the furnace which was connected to vacuum reaching a baseline pressure of 0.5 mbar. The samples were heated to 500°C and stabilized for 5 min. The forming gas was introduced into the chamber in a short pulse of 6 s at a flowrate of about 0.5 LPM. After the pulse, the chamber was rapidly cooled down to room temperature before venting.

After pulsed annealing, each pattern showed a color change (see **Figure 47**) and a magnetic hysteresis. From the MOKE data, the magnetic response of the four samples in the reduced area was totally invariant on the alumina thickness. However, the area of the magnetic domain notably increases as the alumina layer thickness is increased. Also, an increased alumina thickness leads to the development of defective circular areas (blisters) where the capping layer is damaged, exposing the thin film below. This phenomenon of blistering has been previously observed in alumina coatings and it is related to a local entrapment of gaseous molecules that leads to pressure buildup and consecutive breaking of the film. Molecular hydrogen and water are reported to cause such effect on alumina thin films. [140,141] Possibly, for thinner Al_2O_3 films, effusion

is still possible through smaller channels and does not lead to any breaking of the capping layer.

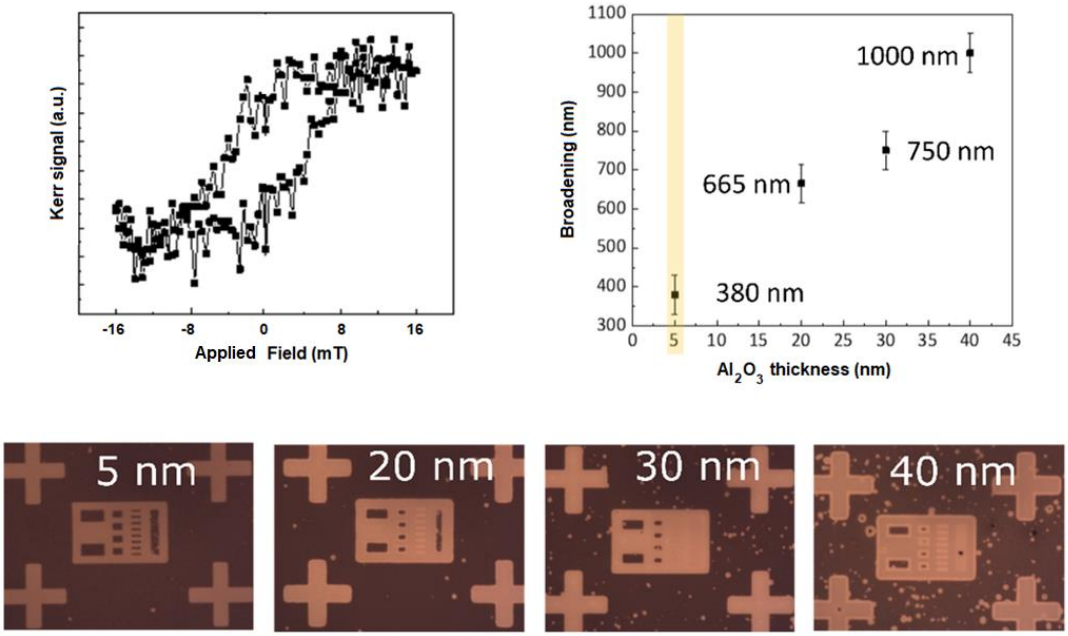

Figure 47: Broadening and MOKE response of four different samples in which the alumina mask thicknesses were 5, 20, 30, or 40 nanometers, respectively.

The fact that this phenomenon of blistering, together with domain broadening, intensifies as the capping layer thickness increases reveals that the effective dose of reductant reaching the NiO substrate is enhanced by Al_2O_3 rather than diminished. Similar blistering is not observed in absence of reductant, excluding that this effect could be related to simple degassing of contaminants from the alumina film due to the increased temperatures.

This indicates that the mechanism of passivation by alumina is likely based on chemical entrapment of hydrogen and not on sole impermeability. In this case, when hydrogen is supplied, a small amount of it gets incorporated into Al_2O_3 and released towards the substrate during the annealing step. This would explain why thicker alumina films promote reduction. A similar mechanism of hydrogen storage has been recently proposed for ozone-deposited Al_2O_3 films and it is based on chemical reactions between atomic hydrogen and carbonaceous species present in the alumina matrix. [139] As it was explained in the previous section, the mechanism of chemical trapping is reported to improve the efficiency of the surface passivation by alumina. However, in this thesis the increased temperature possibly causes the release of hydrogen, leading to detrimental effects as the alumina layer thickness is increased.

An alternative mechanism may be that nickel oxide participates in the gas storage. It has been recently reported that NiO can reversibly incorporate oxygen species after being exposed to ozone during ALD. [142] With molecular hydrogen being smaller than oxygen, nickel oxide should be permeable to hydrogen. In this scenario, the hydrogen, that is incorporated into nickel oxide, can effuse more efficiently when thinner capping layers are used.

4.3.4.3 A XPS study

For this experiment, a 10x10 mm silicon wafer, coated with 40 nm of NiO, was fabricated (**Figure 48**, a). One half of the coating (5x10 mm) was kept as it was, while the other half was further coated with a structured film with 5 nm thick 100x100 μm squares of alumina in a checkerboard pattern. The idea of this design is based on maximizing the interfacial area between alumina and NiO for enhancing the chemical reduction, while simultaneously leaving some portions of the NiO surface uncoated for XPS characterization.

The sample was loaded in the chamber, degassed at 120°C for 5 minutes and measured on both halves. The Ni2p spectra, collected between 890 eV and 845 eV show no difference between the two sides (**Figure 48**, b). At 855 eV and 872.8 eV the two peaks relative to NiO (purple), with possible contributions of $Ni(OH)_2$, were found. [143] For discussion of the results, advanced peak deconvolution using a multiplet envelope, as well as a study of the satellite regions (blue peaks), will be neglected.

After collecting the spectra, the sample was moved to an antechamber where it was heated to 510°C in vacuum and exposed to 500 mbar of H_2/N_2 mixture for 60 seconds to reproduce the annealing conditions of the previous experiments. After cooling down, the sample was loaded in the chamber and measured again in the two different regions.

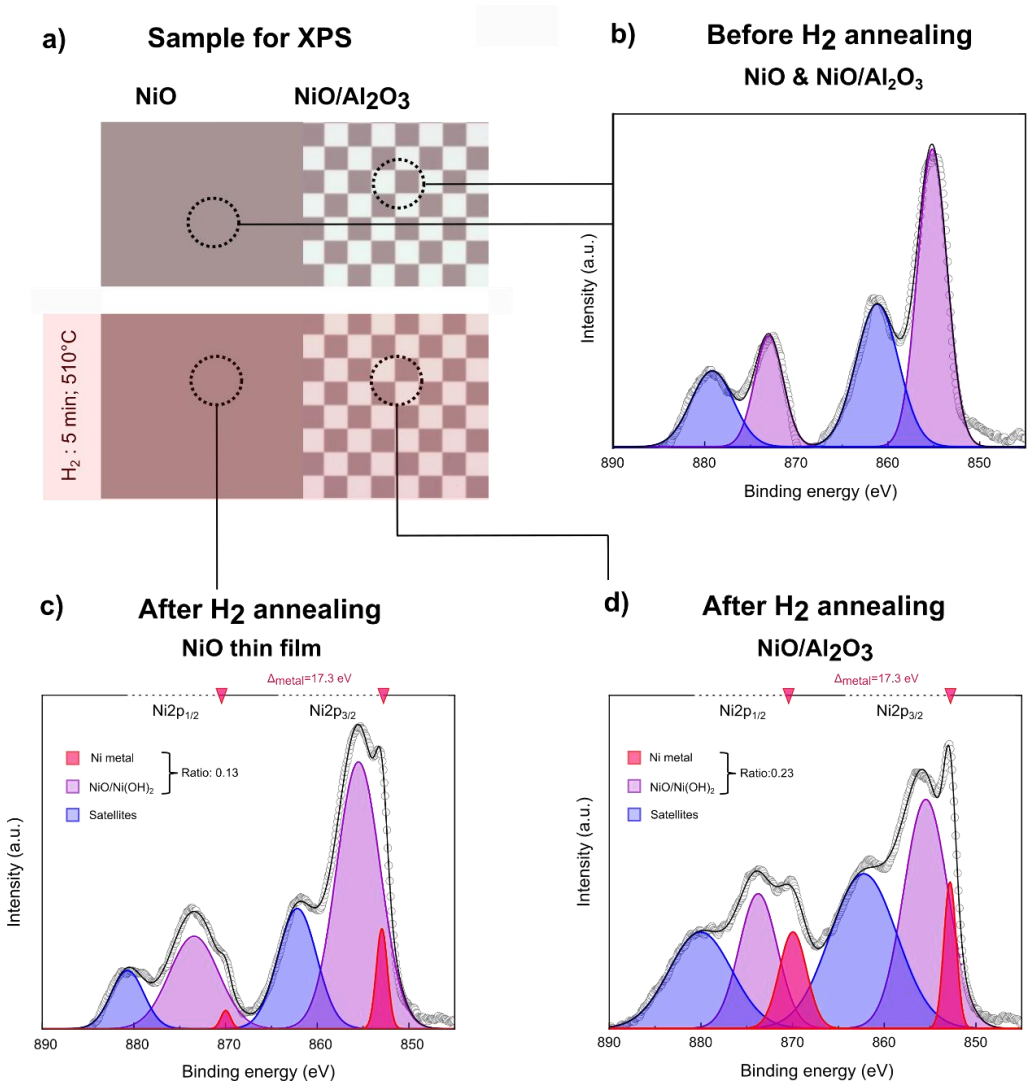

Figure 48: a) Sample fabricated for the XPS analysis of the reduction promotion by alumina. b) Ni2p region of the substrate before annealing, the spectra collected from the two regions before annealing were identical. c) Nickel oxide region and d) NiO/AL_2O_3 structured surface after reduction.

The results of this experiment (**Figure 48**, c-d) cement the hypothesis that the presence of alumina leads to an enhanced reduction efficiency. On both the uncoated and alumina-coated side, peaks corresponding to $Ni2p_{3/2}$ and Ni2p½ appear at 852.9 eV and 870.2 eV, respectively. The peak positions and their separation by 17.3 eV confirm that this signal stems from metallic nickel. After deconvolution, the area of the peak corresponding the $2p_{3/2}$ Ni-metal (red) has been divided by the area of the $2p_{3/2}$ peak, corresponding to the Ni-oxide (purple), to give a quantification of the ratio between the two phases. For the uncoated side, this ratio is 0.135, while for the area in contact with alumina it is 0.230. This significant increase of the metallic phase in

the second sample (**Figure 48**, d) confirms that the alumina interface enhances the reduction efficiency.

Further experiments performed on the IR-furnace showed that hydrogen incorporation is reversible when the structure is exposed to environmental conditions. We compared 2 samples of 40 nm NiO, one was uncoated, and the other one was coated with 40 nm of alumina (TMA-O_3). Both samples were loaded into the annealing furnace and exposed to 1.25 bar of $H_2(5\%)/N_2$ for 3 minutes at room temperature. After exposure, the annealing oven was vented, and the sample holder exposed to air for 30 seconds. After this step, the samples were reinserted into the furnace and rapidly heated, this time, in absence of any reductant, at 600 °C for 10 minutes.

Upon this treatment only the alumina-coated sample was reduced.

Longer exposure to air leads to no reduction on both alumina coated and uncoated sample, suggesting that hydrogen incorporation in the NiO/Al_2O_3 structure is reversible under ambient conditions. From this experiment it is not clear whether hydrogen is physically stored into NiO and cannot effuse because of the presence of alumina, or if there is an actual chemical entrapment of the reductant as suggested by previous studies. [139] Given, its low formation enthalpy and its metastability, AlH_3 could be one chemical species responsible for solid-state hydrogen incorporation. [144]

4.3.4.4 Outlook on applications for hydrogen storage

From a fundamental point of view, the results relative to reactant entrapment are emphasizing that substrate-vapor interactions occurring during ALD are conventionally oversimplified and do not consider the reactions which occur in the subsurface. Understanding such mechanism is not only crucial for guaranteeing reproducibility and high control during chemical processing, but also to unlock alternative area-selective pathways which could rely on the incorporation of reactive species in some regions of the substrate that promote local chemisorption of the desired co-reactants.

Further studies of this mechanism are out of the scope of this thesis. However, from a technological point of view, the evidence of incorporation of hydrogen in alumina/NiO bilayers and the reduction enhancement is an appealing mechanism which could have relevant implications in the field of hydrogen production, [145] storage, [146] and catalysis.

In the area of environmental catalysis, nickel and nickel oxide/nickel systems already find many applications. They are studied for photocatalytic hydrogen production

[147,148] and outlined to be a valid alternative to platinum for hydrogen evolution reaction (HER) [149] as well as a material for carbon sequestration [150] and CO oxidation. [151]

Future studies should thus be addressed at detecting compositional changes in the alumina layer upon exposure to forming gas further elucidating the mechanism of hydrogen entrapment and further defining the role of nickel oxide in this context. In vacuo XPS analysis and FTIR could be valid methodologies to study this problem, but the reversibility of this entrapment mechanism and the timescale of such reversibility (tens of seconds) poses experimental challenges to this characterization.

4.4 Conclusions

The first part of this chapter demonstrated that ALD can be applied to synthesize high quality thin metallic Ni films with potential for incorporation into advanced device applications. We showed that lift-off compatible ALD methods can be implemented and that fully metallic nickel can be obtained at 400°C. Also, the magnetic response can be modulated from soft-magnetic to harder-magnetic, depending on processing parameters. When structured into nano-sized Ni disks, localized plasmon resonances can be excited and modulated by hybridizing them with surface lattice resonances.

In the second part of this chapter, we set the base for a new, direct write compatible methodology that can be used to fabricate novel composite materials that incorporate ferromagnetic-conductive nickel domains and insulating nickel oxide domains in the same surface.

We demonstrated that functional conductive patterns can be easily obtained. In future, one potential application would be to fabricate exchange biased NiO-Ni interfaces by applying pulsed reductive annealing to antiferromagnetic epitaxial NiO thin films. Research in this field would have high technological relevance.

This method is easily up-scalable, cost-effective and can be applied to different systems in terms of both functional materials (such nickel and nickel oxide in the present work) and substrates. If ultra-thin films are employed, this methodology could be used to fabricate semi-transparent metasurfaces that are compatible with flexible substrates.

To achieve high patterning resolution (at the cost of increasing processing times) a localized heat source could be used to scan the surface in a reductive environment,

promoting the reduction of the irradiated areas only. In this way this methodology could be simplified by removing the need of the Al_2O_3 barrier. This would minimize the broadening of the modified areas. Thermal lithography or laser writing are highlighted as advantageous techniques for the improvement of the resolution limits of this methodology. Both these techniques allow adjusting patterning speed and temperature of the energy source. This approach could be used to achieve phase nanoengineering, creating a system where the properties are not abruptly changed from pure nickel to pure nickel oxide domains but where the extent of reduction as well as the crystalline structure can be gradually modified from one area to another, creating a more intricate and spatially varying property landscape.

5

Area-selective silicidation

In the previous chapter, the reduction of nickel oxide to metallic nickel was discussed. Most of the experiments were carried out on quartz or sapphire substrates mainly for following reasons: i) to have transparent devices to be characterized in transmission, and ii) to screen out reactions between nickel and the substrate. In this chapter, the focus is on the silicidation reaction that occurs when nickel oxide, deposited on a silicon substrate, is exposed to heat. We study the relationship between substrate characteristics (such as topography, defective areas, crystal plane of the surface) and ALD based processing, to promote area-selective mechanism during nickel silicide formation.

5.1 Renewed interest for silicides

Since their discovery in the 60s, nickel silicides have been investigated mainly for the sake of understanding the thermodynamics behind the phase transitions. The intention was to find pathways to produce high-quality, stable interfaces for contacts in silicon based transistors. [67]

The most appealing phase for such applications was outlined to be NiSi thanks to its low resistivity. The promise of its application in CMOS technologies, that in early 2000 were already in the era of nanotechnologies, led to interest in the synthesis of silicides that could fit into smaller devices. Since then, literature got enriched by many silicides of controlled morphology, reduced size and different compositions such as nickel silicides, [152] iron silicides, [153] and manganese silicides. [154]

The increased attention for low-dimensional systems unveiled unique mechanisms which affect composition and performance of the nanosized-silicides. For the case of nickel monosilicide it was found that the decrease of dimensionality reduces the resistivity to 10.5-18 $\mu\Omega$-cm. [155] Also, it has been shown that the nickel silicide phase formation sequence can be altered by modifying the Si-Ni interface and synthesis. [156] During the first phases of nickel silicide formation, it has been shown that the shape of a $NiSi_2$ nanocrystal is determined by the underlying dislocation arrays and lattice stress of the silicon substrate. [157] Similarly, it has been shown that nanosheets of NiSi crystals grow along preferential crystallographic planes. [158,159,160]

In the past years, new exotic properties have been discovered or predicted for different types of silicides. [161] For example, it was found that by finely tuning the manganese silicide ratio during the synthesis, altermagnetic Mn_3Si_5 phase can be selected. [68] By reducing the material dimensionality to few atomic layers, $FeSi_2$ nanorods acquire a ferromagnetic behaviour due to uncompensated spins. [69] By controlling the cobalt silicide/silicon interface in heterostructured nanoparticles, enhancement of ferromagnetism and catalytic activity have also been demonstrated. [162]

The most convenient synthetic route for silicide formation consists in the deposition of a thin metallic nickel film on a silicon surface, followed by rapid thermal annealing (RTA) to promote silicidation. It is evident that, in order to achieve such advanced applications, a great control over thickness and composition of the metal-silicon interface is key. In this chapter we investigate the manifold advantages brought by using ALD for thin film deposition prior silicidation and unveil a unique reaction mechanism that is promoted by the use of this technique.

We demonstrate that, by introducing surface defects via direct patterning of the silicon wafer prior to silicidation, the silicide growth can be routed to the desired areas, creating nanostructures of controlled morphology and surface location with a degree of control that has never been reported before. This approach, here demonstrated for the case of $NiSi_2$, has great technological value and can be potentially extended to further silicides. In fact, the surface and bulk diffusion and self-alignment mechanisms, which are exploited to achieve area selectivity, are not exclusively observed during nickel silicidation, but are common to other metal-silicides (gold,[163,164] cobalt,[165] iron,[166] copper,[167] germanium[168] and others) where the transition metal has similar diffusivity into silicon. [169,170]

5.1.1 Phase formation sequence

According to literature, nickel silicides (Ni_xSi_y) exist in 14 different phases. The most common are Ni_2Si, NiSi, and $NiSi_2$. The thermodynamic sequence of nickel silicide phase formation starts from the formation of a nickel rich phase Niδ-Ni_2Si forming at 250°C, which is converted into NiSi at approximately 350°C and ultimately into $NiSi_2$ at 750-800 °C. [171]

However, multiple studies have shown that the thermodynamic equilibrium between these phases can strongly differ, depending on two main factors: [172]

The first factor is the amount of nickel present on the silicon surface. As previously stated, we recall that the silicidation is obtained by simply annealing a thin metallic film pre-deposited on the silicon substrate. During the annealing, the silicidation is found to be a supply-controlled reaction and not bulk-diffusion-controlled. [173] With

bulk diffusion we refer to the interstitial diffusion of nickel atoms into silicon. This magnitude, during thermal annealing, is high enough to not hinder the kinetics of silicidation that instead, is found to be affected by the amount of nickel present on the surface that can be supplied as the silicide nucleates. In literature, it is outlined that for nickel thin film thicknesses below 5 nm, increased temperature leads to the rapid consumption of the metal supply, favoring the formation of silicon rich phases ($NiSi_2$). Under these conditions, the formation temperature of $NiSi_2$ can drop from 750-800 °C (for normal case of thick nickel films) down to 320-600 °C. [171,174,157]

The second factor altering phase formation dynamic is the presence of an already formed Ni_xSi_y on the surface prior the annealing. It is found that as-deposited thin films can lead to the formation of an interfacial nickel-rich phase even before any thermal treatment is applied. [175,176,177] This condition can occur if, for example, the metal deposition is performed at temperatures approaching the formation temperature of the first silicide phase. In this case, the presence of a silicide on the surface is found to pin the subsequent silicidation that occurs during RTA, resulting, similarly to the first case, in the reduction of the $NiSi_2$ formation temperature. In this case, however, the formation of the silicon rich phase is favored by a mechanism that is not determined by the supply limitation (found for thick films up to 25 nm). [156,178,179,180]

5.1.2 Bulk diffusion

Recently it has been formalized that the diffusion mechanism which regulates the growth nickel silicide crystals, leads to interstitial diffusion of nickel atoms against a concentration gradient. This phenomenon, named "*uphill diffusion*" [173] determines that the silicide nucleation can occur far away from the interface with the metal. The mechanism can be pictured as follows: at the interface with the metal film, as the temperature is increased, nickel starts diffusing interstitially into silicon. The concentration of nickel into silicon is determined by its solubility at the chosen annealing temperature, and it decreases as we move away from the metal source. Several studies showed that silicide nucleation requires *supersaturation*, a condition where the silicon lattice contains more metal than the equilibrium solubility allows. [181] This condition is not fulfilled in close contact with the metal source where the interstitial nickel cannot lead to silicide formation. However, the presence of these additional atoms in the silicon lattice creates a strain potential that pushes nickel atoms away from the source and accumulate in favorable lattice locations, where the strain potential is lower. This diffusion, defined uphill because it works against the concentration gradient, is the mechanism responsible for the achievement of nickel supersaturation and consequent silicide nucleation.[173]

5.2 Experimental section

Silicon (100) and (111) substrates were cleaned following the procedure described in the general experimental section (See 2.5.1)

Surface defects were introduced via FIB using both Ga^+ and Ar^+ ions. In most of the cases Ga^+ bombardment using the FIB gun on the Helios 450S, being a direct writing technique, was preferred. The patterning was performed with a beam accelerating voltage of 30 kV and a current of 0.43 pA. With these parameters, ion bombardment causes fast milling of the silicon surface and implantation of gallium ions into the subsurface area. The depth of milling was varied by changing the total area dose.

To avoid Ga implantation, Ar-ion milling was performed following eBL+etching, using ion milling for the removal of 6–10 nm of Si/SiO2 (Parameters in Table 1; SiO_2).

Nickel silicidation was achieved by annealing silicon substrates, previously coated with 4-9 nm of ALD NiO (deposited at 225°C) for 15-30 minutes at temperatures of 600-650 °C under a continuous flow (0.5 LPM) of forming gas (5% H_2; 95% N_2). This annealing procedure differs from the static and pulsed annealing described in the previous chapter, because it was performed at ambient pressure.

The sample surface after annealing is imaged using a Circular Back Scattered (CBS) electron detector for an improved contrast (2.4.1.1), with an accelerating voltage of 5-10 kV and a beam current of 0.1-0.4 nA.

5.3 Results

5.3.1 Silicidation on Si(100) and Si(111)

When few atomic layers of nickel are deposited onto silicon substrates and annealed, they can rapidly react with the underlying silicon atoms and form nickel silicide. [67]

If the metal film is thin enough (few nanometers), upon annealing it can lose its structural integrity and form clusters through a process of dewetting. [167]

Under these conditions, surface diffusion (and not only bulk diffusion) contribute to the accumulation of nickel atoms in energetically favorable locations such as surface reconstructions, steps, kinks or stacking faults. [182,183]

When ALD nickel oxide is used as metal source for silicidation, this phenomenon becomes particularly evident resulting in the formation of silicide islands, whose

morphology and position on the surface is determined, to a large extent, by the epitaxy of the substrate.

In **Figure 49**, we report Ni_xSi_y nanostructures obtained by reductive thermal annealing of 9 nm thick ALD NiO on Si(110) and Si(111).

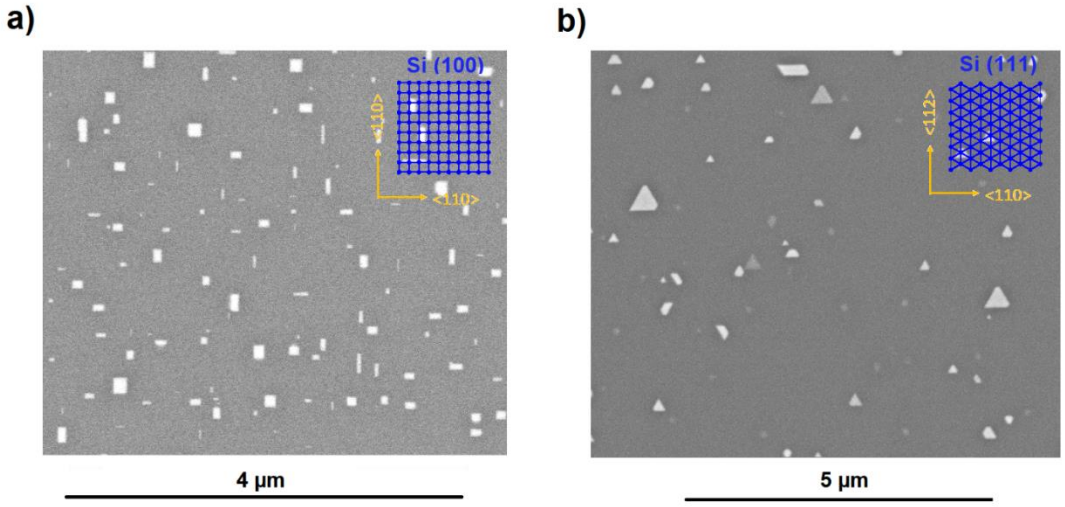

Figure 49: Nickel silicide crystals grown on a) Si(100), and b) Si(111).

The morphology of the silicide crystals and their orientation relative to the substrate crystallographic planes vary depending on the silicon facet. If Si(100) is used as substrate, the nickel silicide´s lateral growth is oriented along the <110> direction (**Figure 49**, a), giving rise to thin rods or square shaped crystals. As it will be shown later in this chapter, when Si(100) is used, nickel silicides grow inside the bulk of the substrate along the <111> directions. In contrast, if Si(111) is used, the silicides grow parallel to the surface as triangles (**Figure 49**, b).

5.3.2 Area selectivity in solid-state synthesis

This method takes advantage of the high lateral diffusivity of nickel atoms on the silicon surface during annealing, together with the "guiding effect" of the surface symmetry, to modify the natural self-organization of nickel during silicidation.

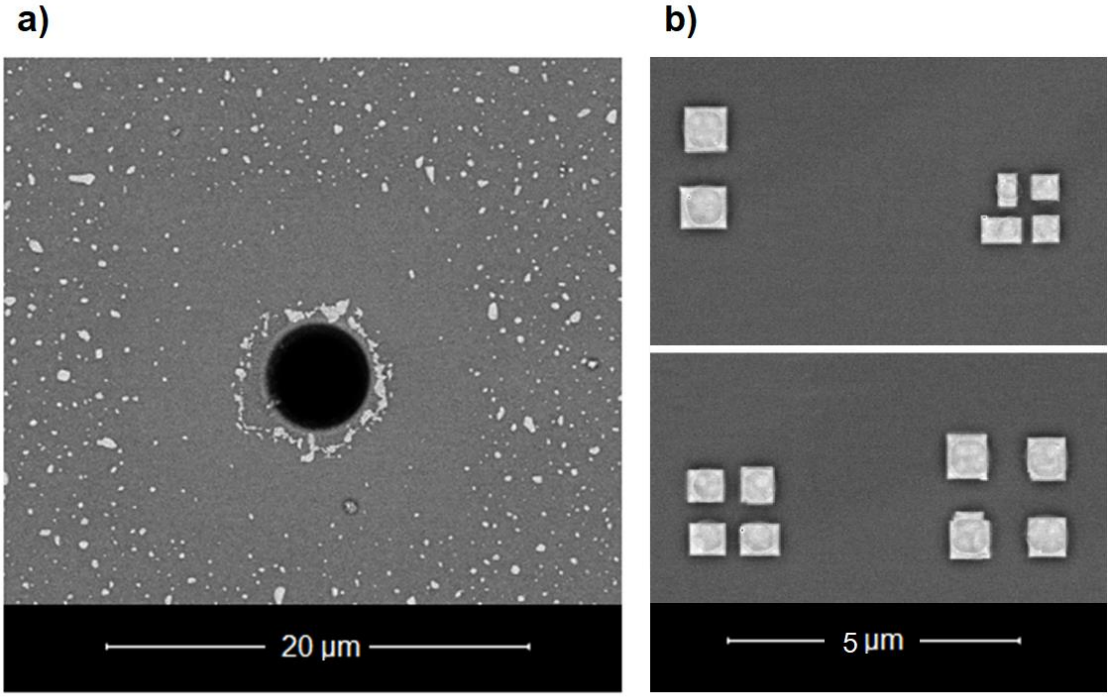

Figure 50: a) Depletion area around a defective site showing few micrometers of displacement on the surface upon reductive RTA. b) Formation of highly ordered silicide crystals on Si(100) by using Ar-FIB to fabricate circular seeding points.

The method consists of introducing surface defects to create favourable nucleation sites. As we will show throughout this chapter, by accurately designing the shape and depth of such defects, high selectivity can be achieved. As anticipated in the previous section, the long-range mobility that nickel atoms acquire during thermal annealing is very marked. This fact is highlighted in **Figure 50**-a, where a substrate of Si(100), containing a well of 8 µm of diameter, was coated with a 8 nm thick nickel oxide film and annealed for 2 minutes at 600°C.

An extended depletion area around the defect can be observed, showing that during the annealing nickel atoms possess a high surface mobility. In this example the short annealing time leads to the formation of nickel clusters and is not sufficiently extended to allow epitaxial silicide formation. In the second example, Si(100) is patterned with a shallow well of 1 µm of diameter, coated with a 4 nm thick nickel oxide film and annealed for 15 minutes at 600°C (**Figure 50**, b). Under these conditions, small square shaped silicide crystals are found to grow in the desired areas aligning with <110> directions.

Interestingly, as it will be shown in the next paragraph, similar results cannot be obtained if PVD is used instead of ALD as deposition method for the nickel thin films.

5.3.3 Comparison between ALD and PVD on FIB trenches

The effect of different nickel oxide deposition methods (ALD vs PVD), as well as the fabrication sequence for the silicidation, were evaluated by producing three different samples (a,b,c) on silicon (100). The FIB-patterned areas [size: 20 µm x 0.5 µm] were exposed to an ion dose of 120 µC/µm^2, which corresponds to a nominal milling depth of 12 nm.

Sample **a** was fabricated by first coating pristine silicon with 4 nm of NiO via ALD, followed by FIB patterning. In sample **b** the steps were identical, but the sequence was inverted. The substrate was first patterned and then coated with 4 nm of NiO via ALD. Sample **c**, instead, was processed with the same sequence as sample b, but used a PVD method for depositing the metal. After patterning, the substrate was coated with 1 nm metallic nickel via thermal evaporation.

The three samples were annealed at 600°C for 15 minutes.

The SEM micrographs of the three samples after annealing are shown in **Figure 51**.

The bright grey areas demark the FIB-fabricated trenches where Ni_xSi_y nucleates and grows. The strong contrast of these areas is not only due to nickel, but also due to the presence of gallium ions implanted into the subsurface during patterning (**Figure 51**, d).

One evidence is that, when ALD of NiO is used (sample **a** and **b**), no presence of residual nickel is found on the silicon surface with the exception of small nickel silicide crystals which, consistently with the epitaxial growth on pristine Si(100) (**Figure 49**, a), align with the 110 planes. Vice versa, after silicidation, the PVD-fabricated surface (sample **c**) is covered with nickel clusters and no epitaxial growth is observed on the surface. Instead, the substrate is covered by metallic nickel clusters. Another noticeable difference between the samples is related to the morphology of the clusters found on the trenches. In samples **a** and **c** nickel silicide does not show any long-range order or epitaxy with the substrate.

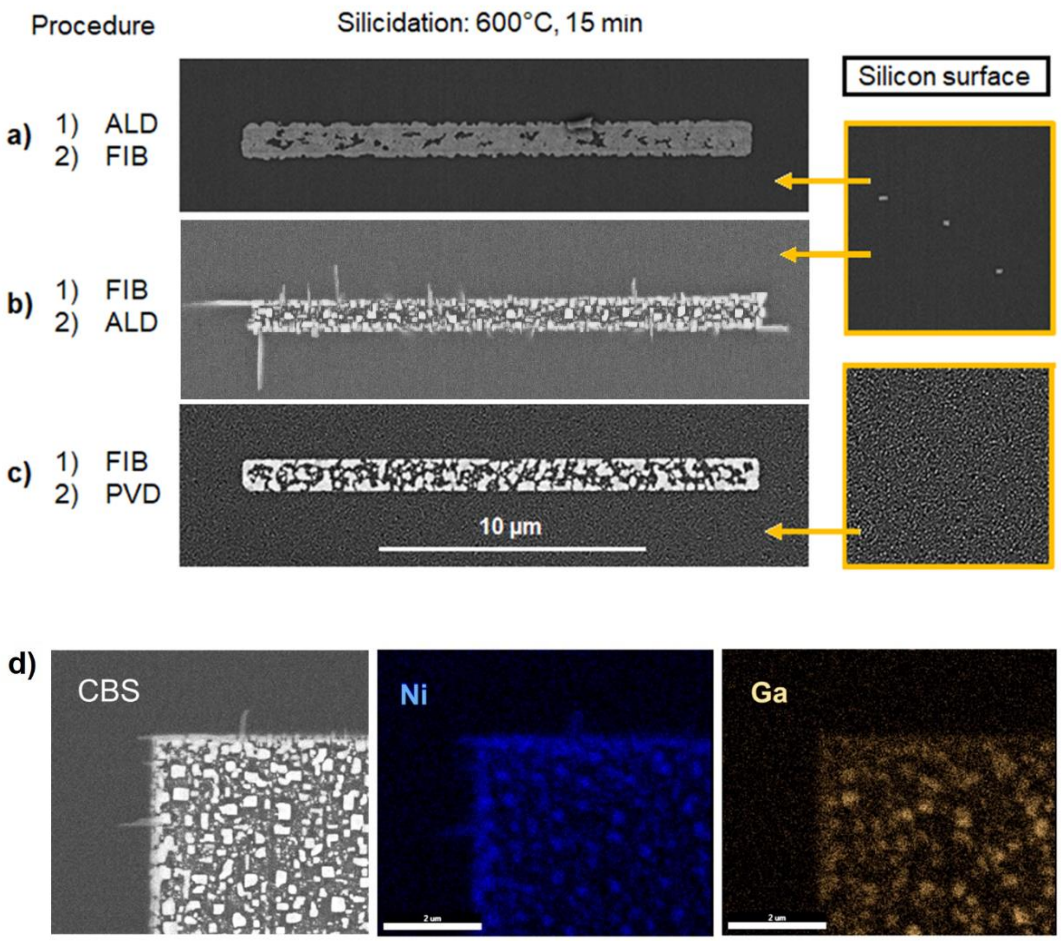

Figure 51: Images of the surface of Si(100) after silicidation using different metal sources and fabrication sequence: a) 4 nm of NiO deposited via ALD, followed by patterning; b) patterning, followed by 4 nm of NiO ALD; c) patterning, followed by 1 nm nickel sputtering. All images were collected using a CBS detector and an accelerating voltage of 5 kV and currents between 0.2 and 0.4 nA. d) EDX analysis of structure b showing gallium implantation.

From the SEM analysis it cannot be verified whether it develops a polycrystalline structure, is amorphous, or mainly composed of gallium. In fact, the ion dose used for creating the trench causes a high concentration of gallium.

Sample **b** strongly differs to **a** and **c** in its morphology. Ni_xSi_y grows epitaxially around and inside the trench. Elongated thin nickel silicide crystals extend from the growth-area towards pristine silicon along the <110> directions. In the middle of the trench, instead, thicker square shaped nickel silicide crystals are also growing epitaxially. The processing conditions used for sample **b** have been also used to produce a larger area for EDX mapping (**Figure 51**, d). From this analysis it can be observed that gallium is present in high concentrations and affects to some extent

the epitaxy of the silicide. For the following studies Ar^+ ion beams or Ga^+ doses lower than 120 µC/µm² were used. The chosen sequence is 1) FIB 2) ALD of NiO, followed by RTA.

5.3.4 Patterns with Ar-ion beam

In order to screen out the impact of gallium implantation over the silicide growth, another Si(100) substrate, patterned with ebl+Argon ion milling (500 s), was fabricated. The ALD and annealing steps were kept unaltered (4 nm, 600°C, 15 min).

AS-growth in the patterned areas was observed in this sample as well (**Figure 52**). In contrast to Ga^+ FIB, the Ar^+ milling does not generate any compositional change (no argon implantation), but still leads to silicidation in the patterned areas, proving that nucleation in the defective areas is topographically driven. The presence of implanted gallium affects the composition of the silicide, but not the mechanism of nickel segregation on the defects. Therefore, Ar-ion milling was preferred as patterning technique to avoid contamination.

Another fundamental difference between the patterns obtained with Ga^+ and Ar^+ beams is that in the latter case nickel silicide crystal growth occurs on the edges of the pattern, while with gallium the growth seems to occur in the whole exposed area. This difference might be related to the fact that when the Ar-FIB is used, the absence of surface contaminations at the end of the process allows the formation of a new native silicon oxide layer after exposing the sample to air. Instead, when the Ga-FIB is used, the sputtering of carbon contaminants resulting from SEM/FIB processing together with gallium implantation, hinders oxide formation, thus enabling the silicidation to take place in the whole patterned area.

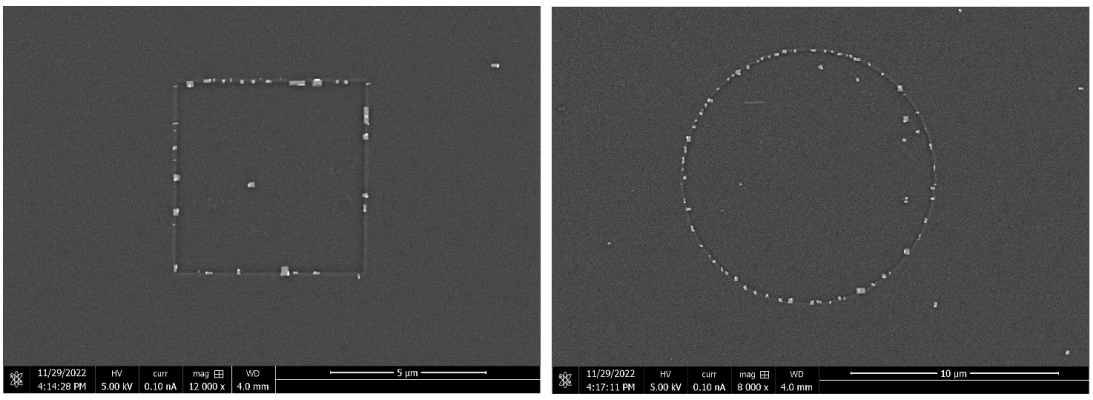

Figure 52: Ni_xSi_y formation on the edges of a Ar-FIB produced terraces on Si(100).

The fact, that in neither of the ALD cases the silicon surface shows clustering is likely related to the use of NiO as metal supply instead of nickel metal (as in PVD). During

the step of reduction, Ostwald ripening [184] is also contributing to the displacement of nickel atoms further increasing the long-range diffusivity. The presence of native oxide on the surface might also play a role on the area selectivity of the process. We propose that when metallic nickel is formed during the RTA, it's affinity to the silicon dioxide surface is reduced. Therefore, the most favorable sites for its accumulation prior silicidation are those areas (growth areas) where the surface oxide has been selectively removed from the surface. Further experiments should be carried out to clarify the role of native oxide on promoting AS mechanism during RTA.

5.3.4.1 Programmable growth on Si(100) surface

In this section, we evaluate which types of topographic defects can promote controlled nickel silicide formation.

As we saw in the previous section, nucleation occurs dominantly on defect edges. Thus, we studied the interplay between the amount of defect edges and the crystal formation. The process parameters are unchanged from the previous section.

We compare the effect of single edged defects (Type I) and multi-edged defects (Type II) on the nickel silicide crystal growth (**Figure 53**, a).

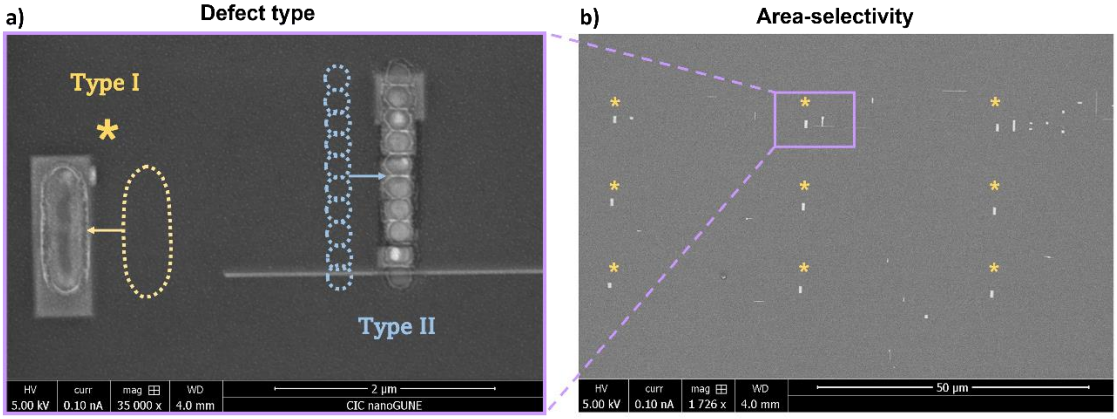

Figure 53: a) Study of the shape/morphology control of nickel silicide crystals attainable through defect engineering of Type I and Type II defects. b) Large area reproducibility of Area-selective growth.

With the previous observation it is evident that nucleation is favored with an increased number of defects (defect edges). If the defect presents a single edge (Type I), a single crystal is obtained (**Figure 53**, a). In contrast, if the defect presents several edges (Type II), simultaneous crystal nucleation at different edges lead to the formation of

a polycrystalline entity (composed of different grains). Accordingly, to favor the growth of single crystals, the number of edges must be reduced.

The area-selectivity of the process is demonstrated in **Figure 53**-b, where the nickel silicide crystal deriving from type I defect, highlighted with the asterisk, is growing with a well-defined shape in all designated locations of the substrate.

Even though the morphology of the nickel silicide crystals and their positioning on Si(100) can be accurately programmed by designing the surface defects, we recall that the crystal growth is based on nickel interdiffusion into silicon. On Si(100) the Ni_xSi_y crystals that result from this process growing hundreds of nanometers into the bulk of silicon.

5.3.4.2 Uncontrollable growth in Si(100) bulk

As outlined at the beginning of this chapter, the intricate mechanism of silicidation is affected the strain potential of the lattice that is capable of guiding nickel atoms that dissolve into silicon towards favorable locations. While this diffusive mechanism is controllable on the surface through the designing of nucleation sites through FIB, the bulk diffusion is hardly controllable. Considering Si(100), we observed that the silicide crystals grow epitaxially on the 110 planes of silicon, directions that, being located on the surface plane, are accessible to modification through patterning. However, although a high degree of control over the growth has been demonstrated on the (100) surface plane, uncontrolled growth in the subsurface cannot be avoided. In fact, (111) planes, due to their highest interplane distance, are the most energetically favorable lattice locations which inevitably lead to nickel accumulation, supersaturation and ultimately silicide nucleation. [160,158]

We compare the cross-sections of nickel silicide crystallites with comparable morphology (size and shape on the surface), such as two rod like silicides (**Figure 54**, a) and two rectangular crystals (**Figure 54**, b) formed on Si(100).

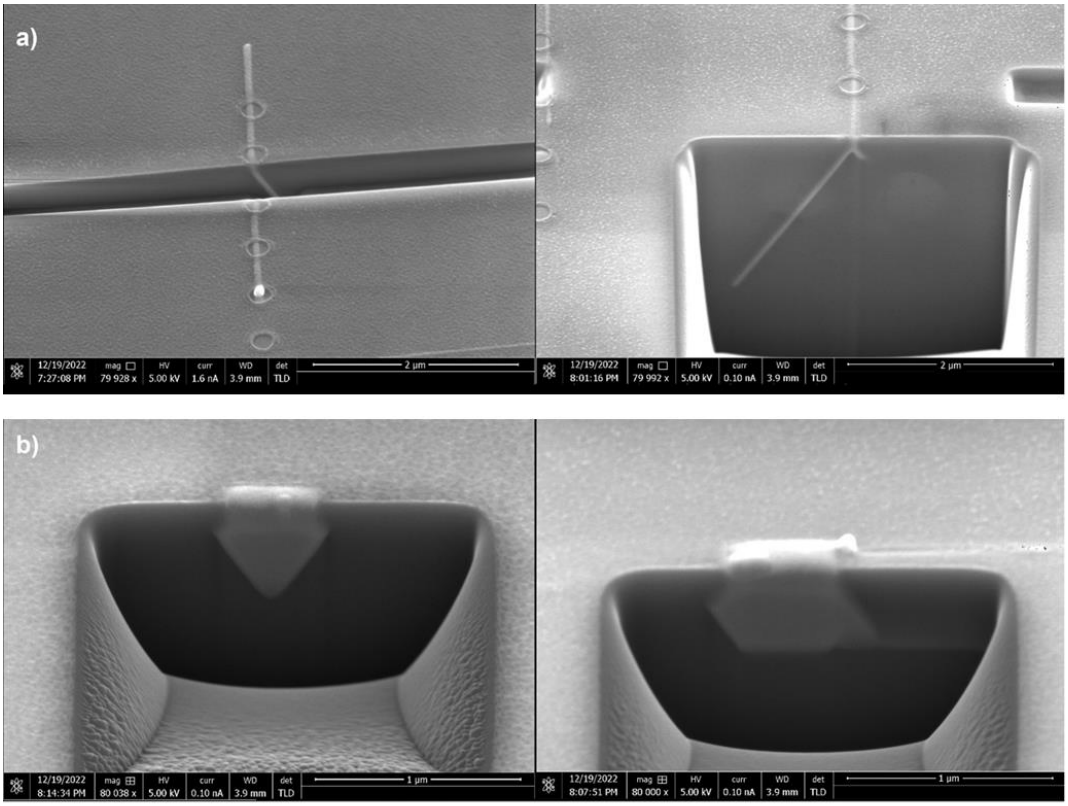

Figure 54: Study of two different structures of nickel silicides formed on FIB defects on Si(100). Cross-section shows high diversification of morphologies found in the subsurface for a) nanorods and b) square-shaped crystals.

Although the Ni_xSi_y look alike on the surface, they strongly differ in the subsurface area. The crystals are found to grow several hundreds of nanometres to micrometres deep into silicon, forming nanosheets or more intricate structures. From the morphology [159,178] of these nanocrystals and the similarity of the processing conditions with those reported in literature, [158] the phase is identified as NiSi or $NiSi_2$.

From these results we learned that, in order to limit the bulk-diffusion, Si(111) substrates are required. [159] With this substrate, area selectivity can still be achieved (**Figure 55**), with preferential crystallization along the <101>, <011> and <110> directions as previously described.

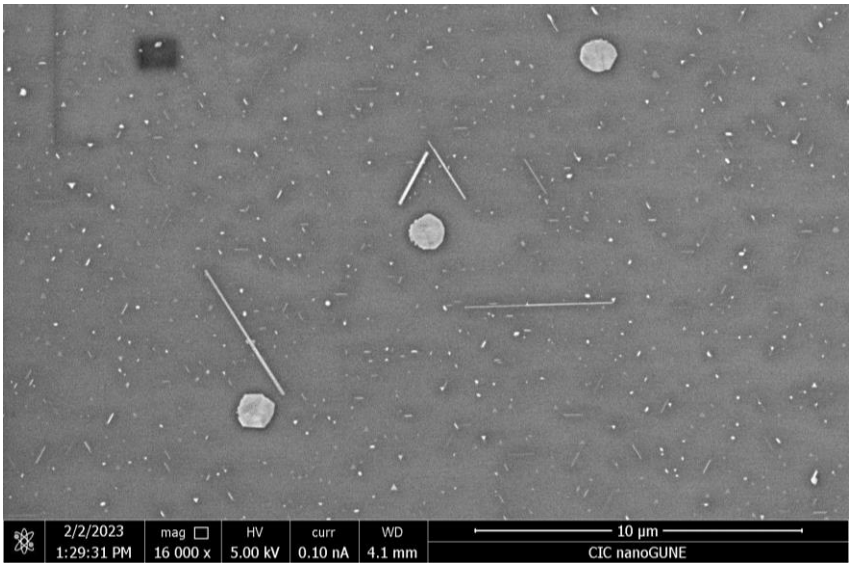

Figure 55: Ni_xSi_y on Si(111) showing growth of small crystallites on the pristine surface and an enhanced growth in three circular FIB-exposed areas.

5.3.5 I/V measurement

A common method to measure the resistance of a material is through 2-point probe measurements. [18] This method permits to calculate the resistance from the I/V curve obtained from supplying a current and measuring the voltage drop between two points, which is caused by the current flow. Analogously it can be performed by applying a voltage between two contacts and measuring the generated current. The characterization of a small nanostructure thus requires two electrical contacts which enable connecting the probes used for the measurement of the nanomaterial. Contact fabrication is conventionally performed via eBL and thin film deposition on top of the studied material.

5.3.5.1 Device fabrication

After studying the unique growth mechanism of nickel silicides, we decided to test a methodology with inverted fabrication steps. Following this approach, we first deposited the contacts on a pristine Si(111) substrate, then we created a narrow trench between the contacts using the FIB, and ultimately we performed ALD deposition and annealing to promote silicidation. To avoid introducing too many competing

[18] I/V measurements were performed by M. Suárez Rodríguez and G.Avedissian from nanodevices group at CIC nanoGUNE.

parameters, the ALD process of nickel oxide was fixed to 4 nm in thickness, optimal annealing conditions were 620 °C for 15 minutes. The variable parameter was the FIB dose used for the defect formation.

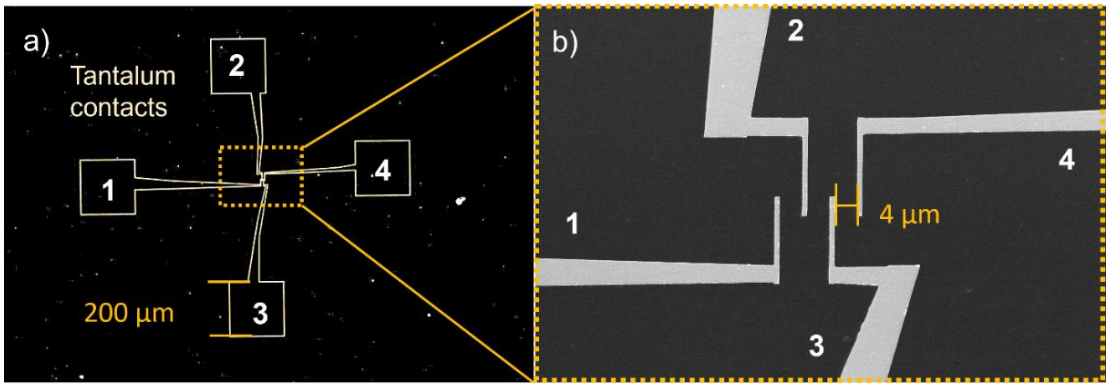

Figure 56: Tantalum contacts architecture and dimensions: a) Dark field optical micrograph of a complete device, b) SEM image of the contact arms that will be in contact with the silicide after AS-silicidation.

Four Tantalum contacts with a final thickness of 40 nm have been sputter-deposited (**Figure 56**). Tantalum was chosen for its high melting point of 2996°C, which enables thermal annealing of the substrate for the silicide formation without destroying the contacts. Each contact had on the probe side a 200 µm x 200 µm sized pad to facilitate the connection with the electrical probes (**Figure 56**, a). On the nickel silicide side, the contact has 1 µm sized legs with 4 µm inter-leg spacing, which were the interface with the silicide crystal (**Figure 56**, b). After fabricating the contacts, the growth of a nickel silicide rod between and below the contacts was enabled by creating a narrow trench with the FIB (**Figure 57**).

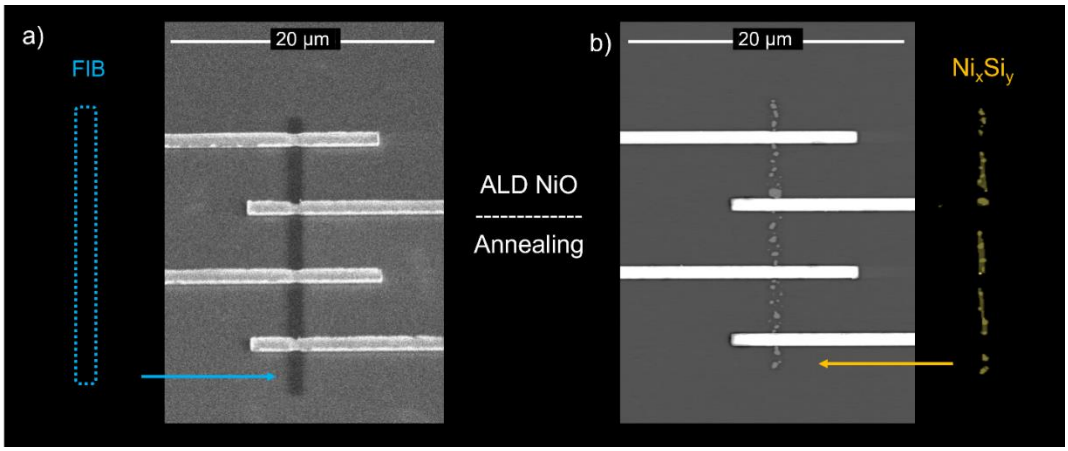

Figure 57: Two step of AS-silicidation a) FIB-exposed area between contacts before ALD and RTA. b) Silicide formation along the FIB-fabricated trench after ALD and RTA.

A test sample containing several tantalum rods was used to identify the ideal FIB conditions (ion dose) for creating the optimal defect and enable continuous silicide growth between the contacts. **Figure 57** shows an example of a test structure after FIB milling (a) and silicidation (b). In **Figure 57**-b, the non-optimized patterning parameters led to the formation of islands instead of a rod. [19]

The FIB-exposed area used for each sample is a trench of 20 µm x 0.2 µm in size. The dose was varied between different samples between 0.1 pC/µm^2 and 0.1 µC/µm^2.

Three characteristic test samples (**Figure 58**, a) show that small ion doses (0.1-1 pC/µm^2) are ideal for preserving the integrity of the contacts after patterning, but they are not sufficient to impose a preferential growth direction. For both 0.1 and 1 pC/µm^2, nickel silicide islands are formed between contacts at different nucleation sites. The nucleation sites have spacings of approximately 100 nm, which corresponds to the pitch between ion beam spots used to raster the desired trench. This means that for such small doses the irradiated area is composed of separated defects instead of a single uniform trench, that, consistently with previous results (**Figure 53**, a), favor silicide nucleation over silicide growth, thus leading to the formation of different islands.

In contrast, doses of 10-40 of pC/µm^2 produce well-defined trenches (**Figure 58**, a) and the formation of continuous polycrystalline nickel silicide rods that connect the four contacts. The chosen dose for the I/V measurement is 10 pC/µm^2 as higher doses caused excessive milling of the contact. The functioning device is shown in **Figure 58**-b.

[19] The two figures do not belong to the same sample, in fact figure a) represents optimal FIB conditions for defect fabrication of 20 pC/µm^2. Figure b) shows island formation due to low FIB dose of 0.1 pC/µm^2.

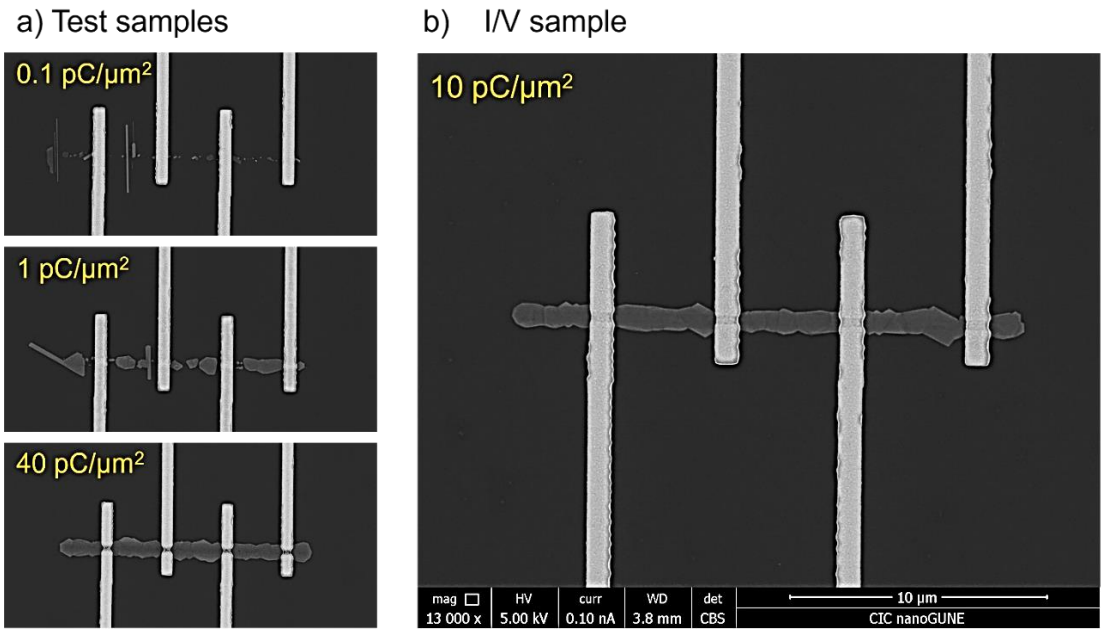

Figure 58: Nickel silicide formation in FIB-exposed trenches fabricated using different ion doses. a) Test samples showing effects of underdosing (0.1-1 pC/µm^2) and overdosing (40 pC/µm^2). b) Sample used for the I/V measurement showing optimal silicide formation without contact damaging (10 pC/µm^2).

5.3.5.2 Device characterization

The resistance was calculated by applying Ohm's law (R=V/I) to the measurement data. The measurements were repeated for different contacts couples (numbered 1,2,3,4, see **Figure 59**). To ensure that no current was leaking through the substrate due to semiconducting character of silicon or the gallium implantation during patterning, an electrical measurement was performed after FIB exposure of the growth-trench between contacts (before silicidation). The measurement (**Figure 59**, a), performed between two closest contacts (1-2 and 3-4), shows no detectable current flowing through the channel and confirms that the trench is non-conductive (>100 MΩ out of range). In the upper part of the figure, the SEM image shows a darker line, which is attributable to carbon contamination during ion bombardment and corresponding to the FIB-exposed area. It can be seen that the damage on the contacts is negligible. [20]

[20] The image of FIB exposed area prior silicidation was collected from a test sample where the same patterning parameters used for device fabrication where applied. This was done to avoid contamination of the device used for characterization. Also, the axis of 59-b are inverted because the measurement was performed by applying the current and reading the voltage

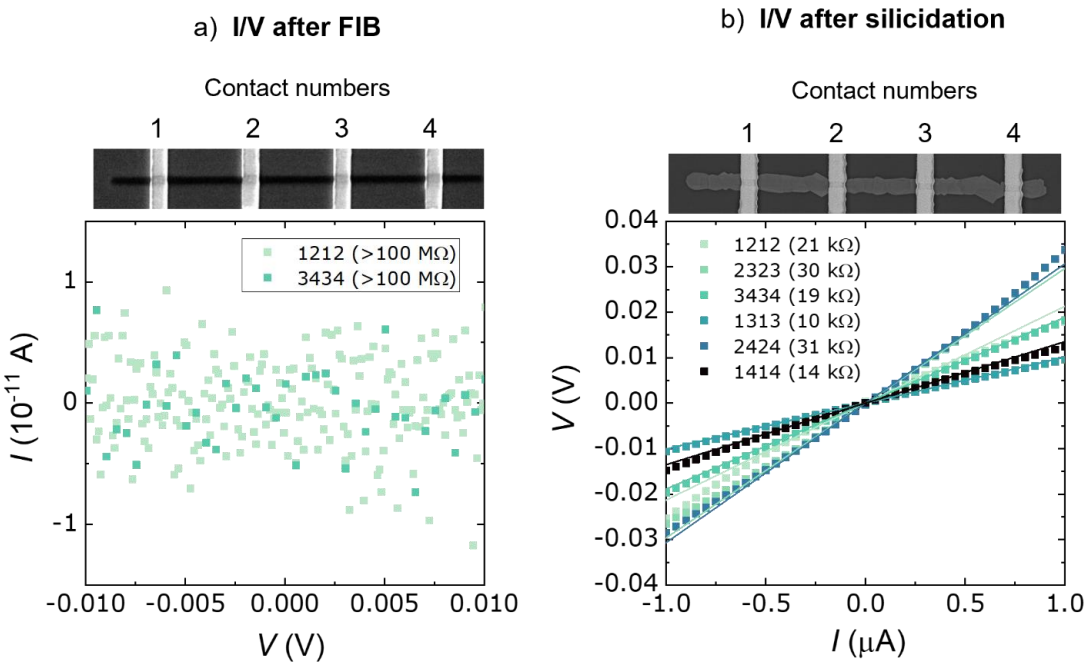

Figure 59: I/V characterization of the device at two different steps of the fabrication. a) I/V measurement after FIB patterning of the trench between contacts using 10 pC/µm². b) I/V measurement after silicidation.

The I/V measurement was repeated after annealing and performed between different combinations of contacts. Before contacting the probes, the four contact pads were milled using the FIB in the SEM to remove the insulating tantalum oxide layer that is rapidly formed upon exposure to air. With the native nominal tantalum oxide thickness being approximately 3 nm, [185] ion milling of 4 nm was performed. After removing the sample from the SEM/FIB system, the surface was capped under vacuum with 4 nm of Pt to avoid re-oxidation of the contacts.

As reported in **Figure 59**-b, each individual measurement shows an ohmic response that can only be attributed to the formation of nickel silicide below and between the contacts. However, the corresponding resistance for each pair of contacts does not scale with the material length (l). One possible reason is related to the high contact resistance at both the silicide/contact and the contact/probe interfaces. [186] Between nickel silicide and tantalum, the presence of tantalum oxide is likely hampering the electron flow through the silicide. Another probable source could be related to the interface between tantalum and the probes. However, the motivation behind performing this unconventional fabrication procedure was to test the methodology and to demonstrate that FIB patterning followed by AS-silicidation enables top-down fabrication strategies which have never been reported before.

To obtain reliable resistance measurements and exclude the mentioned sources of uncertainty, conventional device fabrication should be adopted, performing silicidation followed by contact deposition using either gold or platinum. Also, for future experiments, 4-point probe measurement will be applied for improved accuracy.

5.3.5.3 Structural and compositional characterization

A lamella of the I/V sample was fabricated (See 2.4.1.3) to further investigate the properties of the synthetized material (phase, composition) and its interfaces (between different silicide grains and between silicide and other interfaced materials). TEM characterization was performed in collaboration with the electron microscopy [21] group at CIC nanoGUNE.

The lamella was extracted from a region of the sample containing two contacts and cut along the (110) plane (See **Figure 60**).

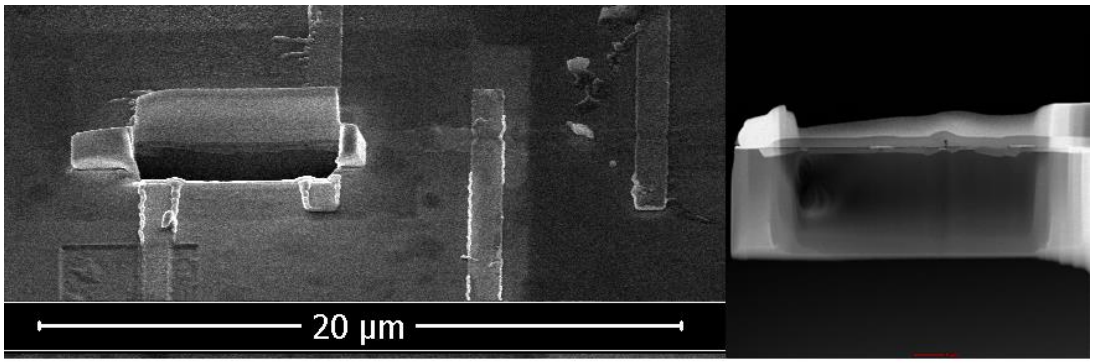

Figure 60: Lamella extraction location (left) and lamella (right) used for the cross-sectional TEM analysis.

The cross section of the sample reveals that Ni silicide growth occurs in an extended subsurface volume. Consistent with the electrical measurement, which showed conduction through different channels, it can be observed that the silicide is grown below the tantalum contacts and extends throughout the whole FIB-milled area. Under the adopted processing conditions silicidation leads to the formation of 2D nanosheets which grow planarly on Si(111). [174] Ultra-thin nickel silicides can be found on the silicon free surface, but in proximity of the trench the silicide is noticeably thicker and composed by different crystallites (**Figure 61**).

[21] TEM analysis was performed by Ch.Tollan, E.Modin and A. Chuvilin.

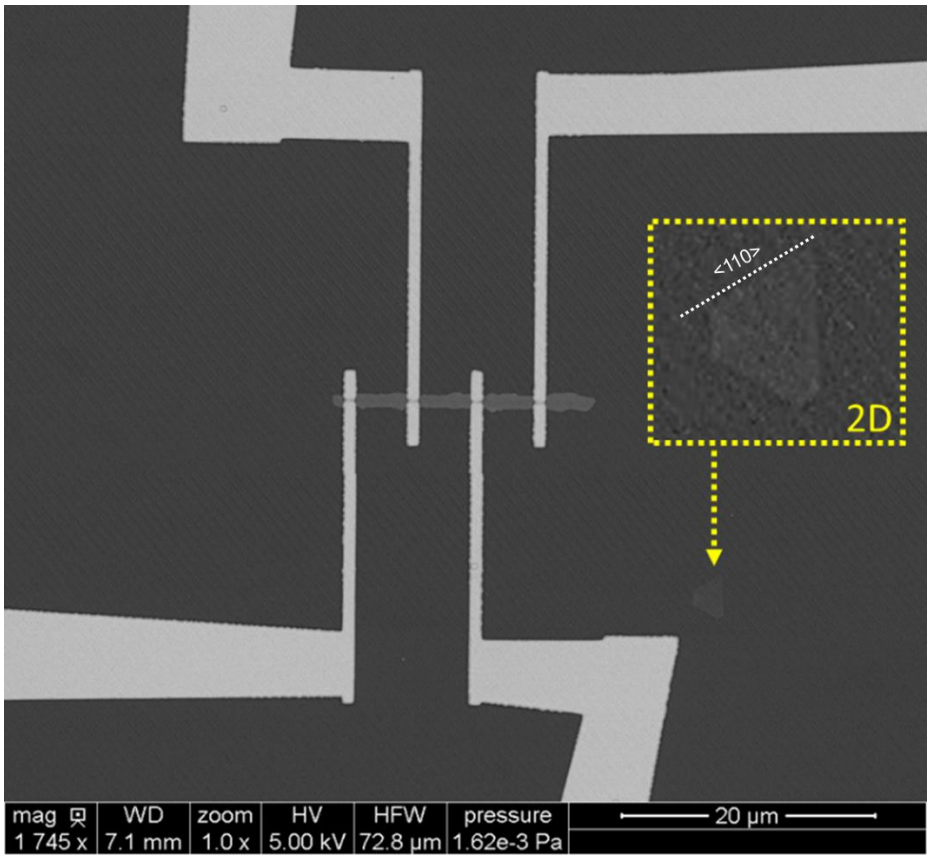

Figure 61: SEM image of the test sample used to check reproducibility of the method. It shows the formation of a single nickel silicide nanorod in the desired area. On the native silicon surface a 2D silicide crystal aligns epitaxially with the substrate, emphasizing the misalignment of the device with any relevant crystallographic axis of the substrate.

From the lamella analysis, the nickel silicide formed in the trench is a rod that extends hundreds of nanometers deep into the Si-bulk and is composed of grains (**Figure 62**, a). The silicide grows below the contacts where dark gaps or particles can be observed, confirming the poor quality of the interface with tantalum. From this cross-section, it can also be observed that two crystallites, composing the nickel silicide rods, are thin and aligned with the substrate orientation. These crystallites, that grow flat on the surface, are likely the first nucleation sites where the first silicide forms, consistent with its growth on pristine Si(111) ((**Figure 62**) as planar nanosheet.

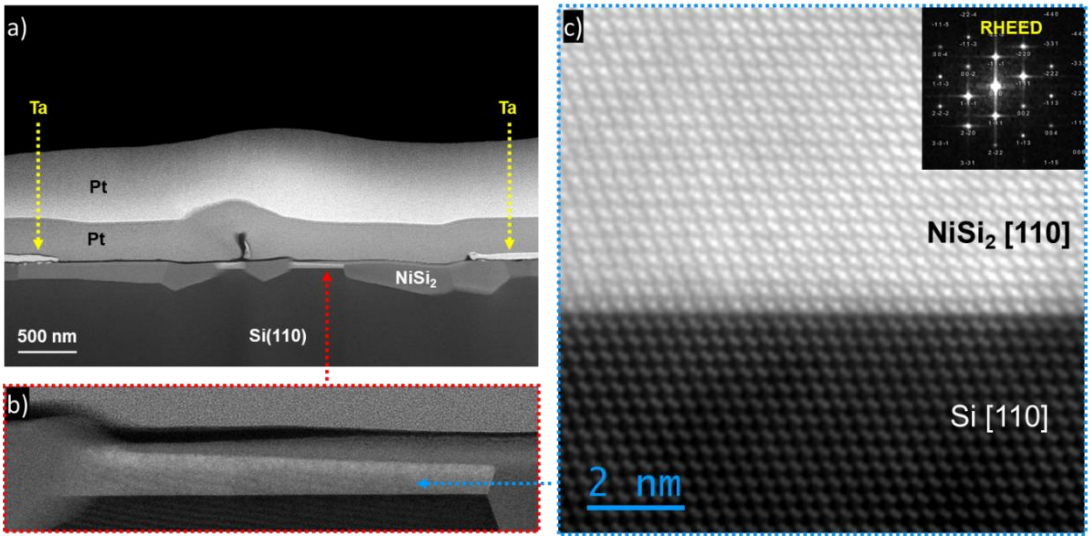

Figure 62: Cross-sectional (CS) TEM analysis of the device used for the I/V characterization. a) CS of $NiSi_2$ grown below the tantalum contacts. b) magnified image of the planar $NiSi_2$. c) High resolution image of the Si-$NiSi_2$ interface between planar silicide and substrate.

After the formation of the nanosheets (triangles, hexagons) aligned along the <111> directions, the enhanced diffusion to the trench gives rise to a rapid accumulation of nickel atoms. Cycles of nickel supersaturation will lead to rapid crystallites growth from the different nucleation sites, inducing lattice stress and favoring nickel diffusion into the bulk. [173] The development of grains is also related to the mis-orientation of the FIB exposed area with respect to the preferential growth axis of nickel silicide on Si(111). This mismatch can be clearly visualized in **Figure 61**, where the device orientation can be compared with the natural 2D crystal growth on pristine silicon. To promote crystal growth over nucleation on a rectangular trench on Si(111), the long axis of the FIB-exposed area should be placed along the <110> direction (**Figure 48**, b).

A thin silicide nanosheet (**Figure 62**, b) was studied in more detail to characterize its crystal structure. From high resolution TEM imaging and electron diffraction (RHEED) of its interface with silicon (**Figure 62**, c) the phase is identified as $NiSi_2$.

This result is in contrast with the previous identification of NiSi, based on the characteristic morphology of the nanosheets that are formed in the bulk of Si(100) or on the surface of Si(111). However, it is certain that the silicidation mechanism occurring on the pristine surface strongly differs from the silicidation mechanism on the FIB-modified trench (increased nickel load and disorder from defect formation).

5.4 Hypothesis for the growth mechanism

Based on the experimental results and the extended bibliographic research, we propose following interpretation.

Defective areas promote nickel silicide nucleation and epitaxial growth regardless of resulting from RTA [187] or being fabricated through direct-write patterning (ion-milling). This phenomenon is observed only if NiO is used instead of a pure metallic film as nickel supply for the silicidation reaction. In fact, if PVD-deposited metallic nickel is used as supply, the area selectivity of the process is lost.

We propose that the long-range surface diffusivity is necessarily related to two main factors: a) the chemical transformation of Ni^{2+} to Ni^{0} occurring during RTA in presence of forming gas and 2) the presence/absence of native silicon dioxide on the surface.

a) When NiO is used as supply, at the beginning of the annealing ramp, silicidation is hindered because the metal is mainly present in form of Ni^{2+}. As the reduction proceeds, newly formed Ni^{0} atoms are detached from NiO crystallites, agglomerating through ripening into clusters of metallic nickel. [117] This phenomenon involves displacement of atoms and explains the increase of surface diffusivity that is observed only if NiO is utilized.

b) Pristine silicon presents native silicon oxide on the surface. [188] Our initial results show that RTA of few nanometers of nickel oxide on pristine silicon surfaces leads to the formation of small nickel silicide crystals in correspondence of defective areas of the substrate. These bulk silicon defects are formed when the temperature is rapidly increased during RTA and create gaps in the silicon oxide [187] which enable the interdiffusion of nickel atoms into the lattice. [189]

When creating surface defects with FIB, the native silicon oxide is removed. Upon exposure of the substrates to air after patterning, this oxide layer can partially re-form. However, gallium implantation [190] (when Ga^{+} ion milling is used) or carbon sputtering are typical surface contamination produced by surface milling that can hinder native oxide formation. If the native oxide forms in the patterned area (Ar-ion milling) the topographic milling of the surface is still enough to enable preferential silicide growth along the edges of the defect.

This explanation is consistent with the evidence that silicide growth differs if gallium and argon beams are used. In the first case, gallium implantation prevents silicon dioxide formation, consequently favoring the growth of silicide crystals in the whole patterned area. When Ar-ion beams are used, the lower surface contamination enables the formation of silicon dioxide. However, upon annealing the edges of the milled areas favor nickel silicide formation.

The reason why nickel tends to accumulate where the oxide is could be linked the increased affinity between the newly formed metallic nickel and crystalline silicon compared to silicon dioxide. [191]

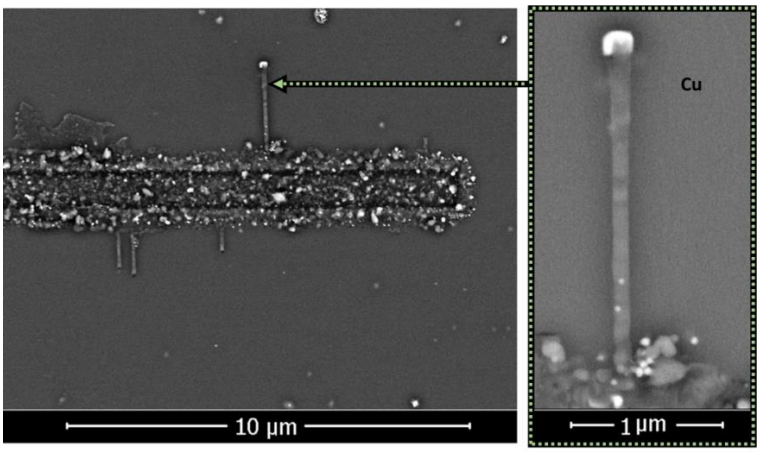

Figure 63: Copper nanorod growth on a FIB exposed area.

In parallel to surface diffusion, lattice diffusion also takes place. The presence of interstitial nickel leads to silicon lattice expansion and creates a strain gradient which guides nickel atoms to accumulate in preferential crystallographic planes (111 and 110), with increased lattice spacing (phenomena described in literature as supersaturation and uphill diffusion). [173]

A similar process, utilizing copper oxide as metal supply, led to similar nucleation of copper silicide rods, suggesting the applicability of this approach to other metal-silicon systems.

5.5 Conclusions

FIB surface milling is found to be a valid direct-write method for pre-patterning a silicon surface and promoting area-selective silicidation. The area selectivity is linked to the use of nickel oxide as metal supply but is not clear yet whether the deposition method ALD also plays a role. We recall that the first interaction between nickel and silicon can impact the phase diagram of the silicidation. In this sense it is reasonable to assume that ALD, being based on chemical reactions between precursor and surface, could trigger silicide formation. Considering that the activation energy required for Ni_2Si formation is very close to the thermal energy supplied during the ALD process,

such scenario is likely occurring. This hypothesis can explain why nickel silicides grow epitaxially only whenever ALD is performed after FIB milling (See **Figure 51**, b).

Future experiments will be addressed at better studying the direct formation of nickel silicide during ALD and further elucidating nucleation and growth mechanisms of nickel silicide nanocrystals.

6

AS-ALD of nickel

This chapter is dedicated to an inherently area-selective ALD process. It focuses on the development of a deposition process for metallic nickel (instead of NiO) using a nickel precursor from the class of Bis(1,4-di-t-butyl-1,3-diazabutadienyl)M(II) (M-(DAD)$_2$ with M=Mn, Cr, Fe, Co, Ni). These complexes have been extensively studied by the group of Charles Winter in the past years for application in area-selective ALD. [192] They were systematically characterized through thermogravimetric studies, sublimation and solid-state decomposition analysis and demonstrated good thermal stability which correlates with the reduction potential of the M(II) center. The higher the reduction potential of the cation, the higher is the molecule's thermal stability. The decomposition temperature scales in the order Mn-Cr-Fe-Co-Ni from highest to lowest, with nickel being the least stable complex of that series. For the case of cobalt and nickel-based complexes, their similar ALD processabilities and selective behavior have triggered studies which focused on their deposition in conjunction with reducing co-reagents (formic acid, hydrazine and tert-butylamine) to obtain selective metal deposition on metallic substrates. [30,29,193]

In this chapter, we focused on the deposition of nickel thin films using Ni(DAD)$_2$ (**Figure 3**, c) and tert-butylamine. This process is reported to lead to selective nickel growth on platinum and ruthenium substrates, island formation on copper substrates and no deposition on non-metallic substrates. [29] We apply this process to substrates of different nature to further elucidate the role of surface composition. Ultimately, we discuss the importance of ALD processing parameters on the area selectivity.

6.1 The process in literature

Literature reports that the ALD window of this process (Ni(DAD)$_2$ and tert-butylamine) is between 180 and 195 °C, where a stable and self-limiting growth of 0.6 Å/cy is obtained on platinum in a wide range of cycle numbers (0 to 1000 cycles). [29] After selecting 180°C as the optimal processing temperature, the authors extended the growth studies to other substrates. On ruthenium they also report selective growth, but it shows a nucleation delay of approximately 150 cycles. Between 150 cycles and 250 cycles the film slowly grows at 0.12 Å/cy and finally stabilizes to a value of 0.44 Å/cy when more than 500 cycles are applied. However, this value is lower than the GPC found on platinum (0.6 Å/cy). The nucleation delay is further increased when

copper substrates are used. In this case the authors report island growth of nickel for up to 1000 cycles. The authors attribute the delayed nucleation on ruthenium and copper to the presence of oxides on the surface, [194] an effect that they already observed in previous studies. [193,195]

M.Kerrigan et al. characterized the precursor $Co(DAD)_2$, [30] highlighting that using nitrogen with lower purity as carrier gas lowers the growth rate, likely because of the formation of cobalt oxides. In contrast to what they reported for $Ni(DAD)_2$, the presence of copper oxide on the surface of copper substrates (corroborated with XPS) leads to no nucleation delay when $Co(DAD)_2$ is used. Saturative growth of 0.98 Å/cy is found on both copper and platinum substrates. However, a small nucleation delay of metallic cobalt on ruthenium is reported.

6.2 Experimental section

Initial ALD runs were performed on conventional stainless steel ALD reactors (See 2.1.2.1, reactor 1) and yielded no deposition. This suggested poor delivery of the precursor due to extended manifold lengths and the use of low precursors loads.

Up to date, we can only refer to one single study related to the stability of $Ni(DAD)_2$. [192] In this work, the characterization is carried out by heating the precursor crystals inside a glass container (SiO_2) which is not the ideal reference for the thermal stability of the precursor when heated inside a metallic container during ALD. For $Ni(DAD)_2$, this statement is particularly valid knowing that the molecule preferentially chemisorbs/decomposes on metallic surfaces. We underline, that a systematic study of the molecule´s stability under various conditions should be provided by the product producers.

6.2.1 ALD processing

To limit a possible decomposition of the precursor and facilitate vapor delivery, reactor 2 (See 2.1.2.2) was constructed using solely quartz and Pyrex elements. Also, the Pyrex pipette, used as precursor sublimation container, is directly inserted into the reactor, thereby shortening the vapor traveling distance between source and the substrate to 20 cm only. The reactor was heated with a temperature gradient going from 77°C on the cold end (inlet; precursor location) to a maximum of 195 °C on the hot end of the quartz tube (**Figure 10**). The baseline pressure in the evacuated reactor with no carrier gas flow was 0.1 mbar. The nitrogen carrier gas purity was 99.99%, however, minor leaks in correspondence of the flanges positioned at the two sides of the quartz reactor could lead to minor atmospheric contaminations. To characterize the GPC in

entire temperature range of interest (145 °C - 195 °C) in one single experiment, substrates were specifically designed and positioned to cover different positions corresponding to different temperatures. Given the short distance between the ni-precursor source and substrates, the static mode was preferred to suppress any unwanted effect resulting from the vapors flow. Using the static mode, we ensured that the precursor concentration is uniform in the whole reactor volume. Also, as discussed in chapter III, the use of static dosing enables to significantly reduce the precursor loads required to achieve surface saturation. The co-precursor pulse was performed in flow mode (connected to vacuum) given the high vapor pressure of tert-butylamine.

The nitrogen flow was set to 200 sccm during the $Ni(DAD)_2$ pulse and 300 sccm during the purging step and pulsing step of tert-butylamine.

Bis(1,4-di-t-butyl-1,3-diazabutadienyl)nickel(II) $Ni(DAD)_2$, min. 98% (99.999%-Ni); CAS: 63576-87-4. was purchased from STREM. In each experiment 130 mg of $Ni(DAD)_2$ were loaded into the Pyrex vessel and heated at 77°C. Any manipulation was carried out in the glovebox. *Tert*-butylamine was purchased from Sigma-Aldrich and transferred into a cylinder using a syringe for a total volume of 20 ml.

6.2.2 Substrates design

Stripes (8x1 cm) of Si with 300 nm thermal oxide [100; P-doped (Boron) from Photon Export] were used to fabricate the samples reported in **Figure 64**; a,b. ***Sample a*** had a 5 mm wide, 50 nm thick Pt stripe deposited on half of the silicon dioxide substrate along the whole length. ***Sample b*** had 2 mm wide, 45 nm thick stripes of different metals/metal oxides deposited using tabletop sputtering machine as described in the general experimental section (See 2.3.2). Referring to **Figure 64**-b, the stripes are Au, Pt, FeO_x, SiO_2 (substrate) and CrO_x from left to right.

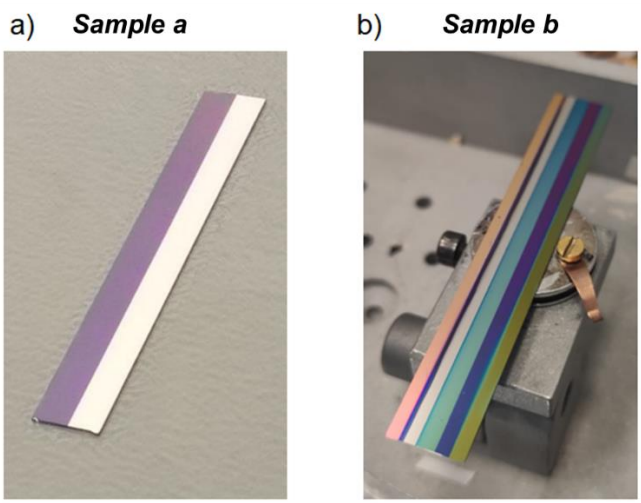

Figure 64: Si wafer with SiO_2, coated with different metals and metal oxides. a) left: SiO_2, right: Pt. b) From left to right; Au, Pt, FeOx, SiO_2, CrOx. Between the first two stripes of Au and Pt a small gap shows the SiO_2 substrate.

During the experiment, substrates a and b were positioned into the tube longitudinally in the flow direction with one side heated to 195 °C and the other side to 145 °C. The real temperature at these positions was measured in a calibration run using two k-type thermocouples in contact with the inner walls of the reactor.

A 10x10 cm fused quartz substrate [type GE124 from nanoandmoreQMBH] was used to fabricate ***Sample c*** (**Figure 65**). This sample was used for studying the selectivity on metallic nanostructures of Au, Pt, FeO_x, CrO_x. The structures were positioned in four different areas of the same substrate (**Figure 65** a) and fabricated using eBL+deposition (**Figure 16**, a) using the procedure described in 2.5.1. The optical image of the metal/metal-oxide nanostructures (**Figure 65**, b) and their detailed geometrical description (**Figure 65**, c) are also reported. Each of the metals/metal-oxides was deposited with a thickness of 45 nm using the tabletop sputtering machine described in the general experimental section (See 2.3.2).

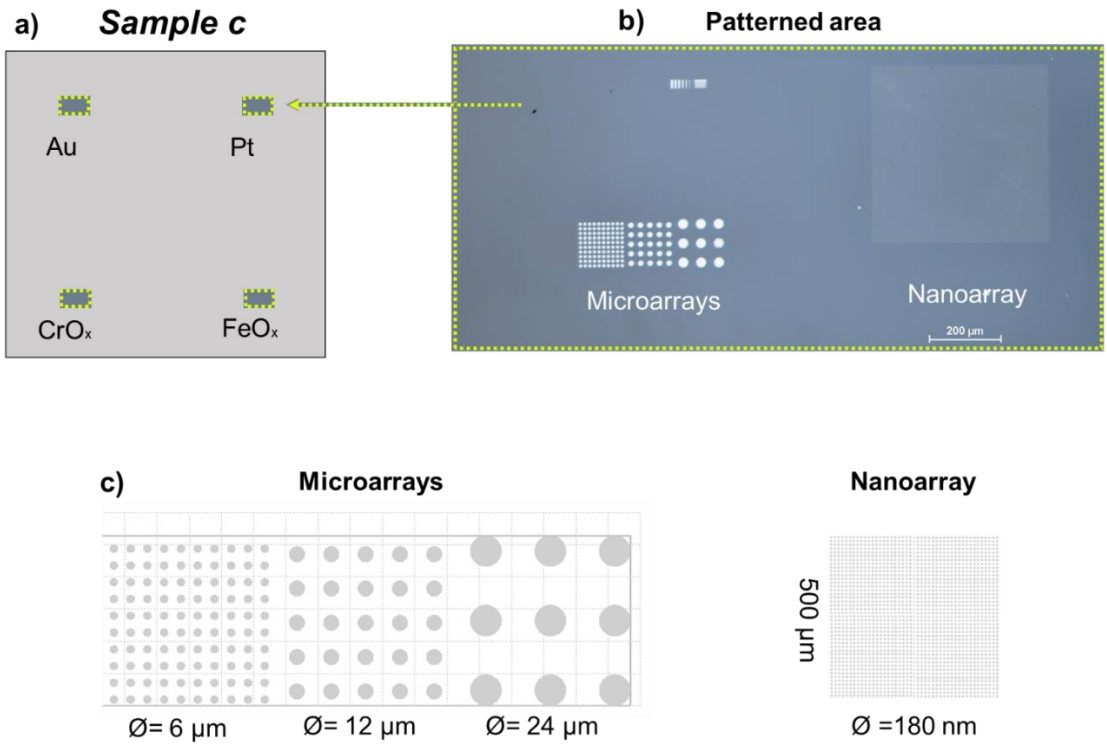

Figure 65: Sample-c. a) 10x10 mm quartz substrate decorated with b) 4 different metal-metal oxide nanostructures. c) eBl pattern used for fabricating the structures.

For the nickel deposition, the sample was placed into the reactor at a location corresponding to 185 -190 °C and processed with sample b (250 cycles AS-ALD).

6.2.3 Sample characterization

XRR analyses have been performed using tools and software as described in the general experimental section (See 2.6.1).

EDX spectra of the different surfaces were collected using 3kV accelerating voltage, and the current was adjusted to have approximately 5'000 CPS readout from the detector. The imaged area during EDX acquisition was 40x40 μm. Sample-c was coated with 10 nm sputtered carbon prior EDX analysis to prevent charge accumulation and image drifting during the spectra collection.

*The spectra analyses consisted of simple background correction smoothing (background: 2nd derivative to calculate anchor points on the curve, interpolate with a line and subtract; smoothing: 6 point-adjacent averaging). Finally, to have a visual quantification of the nickel amount on the surface, each spectrum was normalized to the counts of the substrate.

The XPS analysis was performed on a 10x8 mm portion of sample b that was accurately cleaved from the high temperature side of the wafer. The substrate temperature of the sample, analyzed with XPS, was assumed to be 190 ± 5 °C. Before data collection the samples were annealed under vacuum at 190°C for 5 minutes to reproduce the pre/post-ALD processing conditions and remove possible contamination due to exposure to air. The experiments were carried out at CFM as detailed in the general experimental section (See 2.6.2).

6.3 Results

6.3.1 Selectivity for low amounts of injected $Ni(DAD)_2$

The first experiment consisted of 300 ALD cycles composed of 1) a static pulsing step of 7s of $Ni(DAD)_2$, corresponding to an average mass injected of 0.26 mg/cycle, 2) purging step of 10 seconds, followed by 3) a tert-butylamine pulse of 0.5 s (25 ml load, 5 ml total consumption), followed by 4) a purging step of 10 s. The experiments were carried out using *sample a* (**Figure 65**, a).

Th first characterization of the nickel growth was performed by collecting the EDX signal at three different substrate positions corresponding to 145°C, 170°C and 195°C process temperature. The CPS of the spectra collected from different areas of the sample have been normalized to the intensity of the peaks related to the substrates, which are silicon on one side (**Figure 66**, a) and platinum on the other side (**Figure 66**, b). With this normalization, the nickel peak intensity becomes representative of the film thickness between different areas of the same substrate (either silicon or platinum). [196] From this analysis it can be observed that at low temperatures (145 °C) nickel is deposited on both silicon dioxide and platinum surfaces. At low temperatures the $Ni_{L\alpha}$ is associated to an increased $C_{k\alpha}$ and $N_{k\alpha}$ signal, presumably due to incomplete removal of the ligands, resulting in carbon and nitrogen incorporation into the thin film during growth. As we move to the central part of the substrate, where the deposition temperature was approximately 170 °C, it can be observed that, while the $Ni_{L\alpha}$ peak remains almost unvaried on the platinum side, it vanishes on SiO_2. Finally, as the temperature is increased to 195 °C, the $Ni_{L\alpha}$ signal is still absent on silicon, while it slightly decreases on platinum. From this preliminary characterization it can already be concluded that at low processing temperatures enhanced condensation leads to loss of the substrate selectivity. The nickel growth found on silicon at 145 °C is likely due to $Ni(DAD)_2$ molecules physisorbed on the surface. These molecules are partially decomposed as the co-reactant is pulsed, resulting in the formation of solid, nickel-containing residuals which are irreversibly accumulated on the surface as the process runs. For temperatures above 170 °C condensation is suppressed, resulting in

efficient removal of the precursor from the silicon dioxide surface and leading to AS-ALD on platinum.

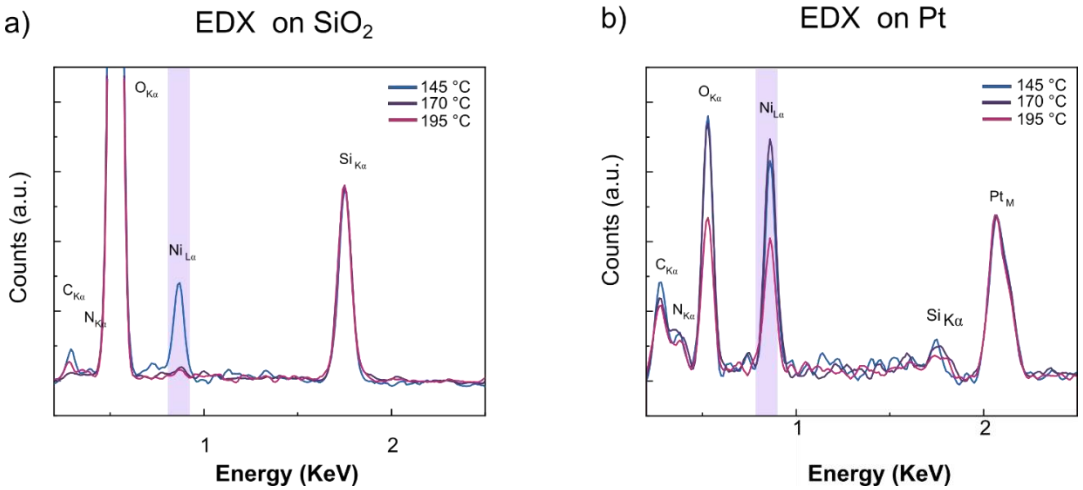

Figure 66: EDX spectra of sample a collected from a) SiO_2 region and b) Pt region between 145°C and 195°C.

6.3.1.1 Growth on SiO_2

XRR measurements at different locations of the SiO_2 stripe allowed to quantify the growth per cycle as function of substrate temperature. The XRR spectra showed interference between 145 °C and 170 °C, but at higher temperatures no thin film was detected. The XRR spectra (**Figure 67**, b) were collected from 4 different locations corresponding to approximately 145 °C, 153 °C, 161 °C and 170 °C. From the Fourier analysis of the XRR spectra (**Figure 67**, c), the thickness values of the thin films has been calculated (**Figure 67**, a), allowing to estimate the GPC of the CVD-like growth on silicon dioxide. The GPC at 145 °C was 0.34 Å and rapidly decreased as the temperature increases, reaching a value of approximately 0.1 Å at 170 °C. To corroborate the precision of this method for determining the film thickness, the XRR spectrum corresponding to the 151 °C substrate temperature was collected from a sample region close to the platinum stripe. In this way both SiO_2 and Pt interference patterns are collected simultaneously, enabling to use the Pt peak position as reference. This peak position (**Figure 67**, c), centered exactly at 50 nm, which is the known value for the Pt film thickness, shows that no shifts are present during Fourier analysis, confirming the reliability of this method for determining the nickel film thickness.

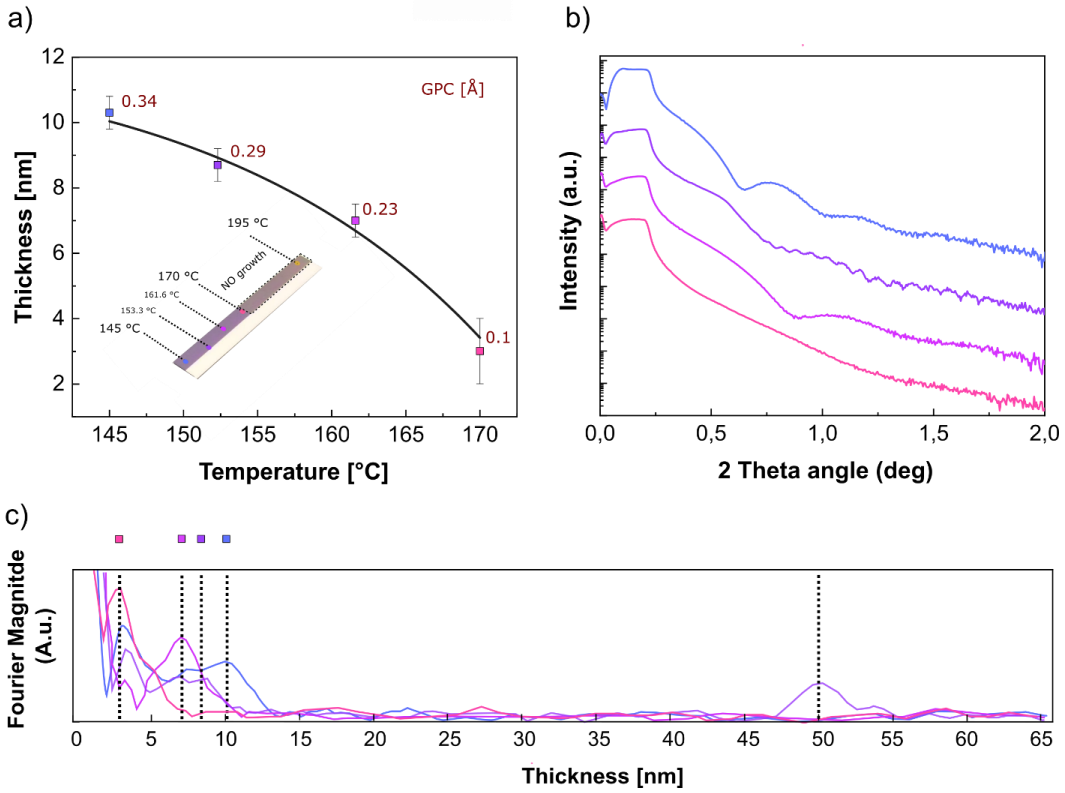

Figure 67: XRR analysis of the SiO_2 surface after ALD. a) Thickness values of the thin film as function of substrate temperature obtained by collecting b) XRR spectra at different temperature coordinates, and c) applying Fourier analysis of the XRR spectra.

6.3.1.2 Growth on platinum

To characterize the growth on the platinum stripe of sample a with more accuracy, TEM analysis of lamellae was preferred to XRR. Given the similarity between the EDX $Ni_{L\alpha}$ intensity relative to the 145 °C and 170 °C positions, cross-sections of the sample were extracted only from the 170°C and 195°C positions, revealing thicknesses of 8.5 nm and 5.5 nm, respectively (**Figure 68**). These cross-sections showed that the EDX measurement gives a reasonably good estimation (16.9% deviation) of the relative amount of nickel present on the surface. This value was obtained by first calculating the ratio between the nickel EDX peak integrals (170°C sample divided by 195°C sample), which resulted in 1.30, and comparison with the ratio between the film thicknesses at 170°C and 195°C, which was 1.54.

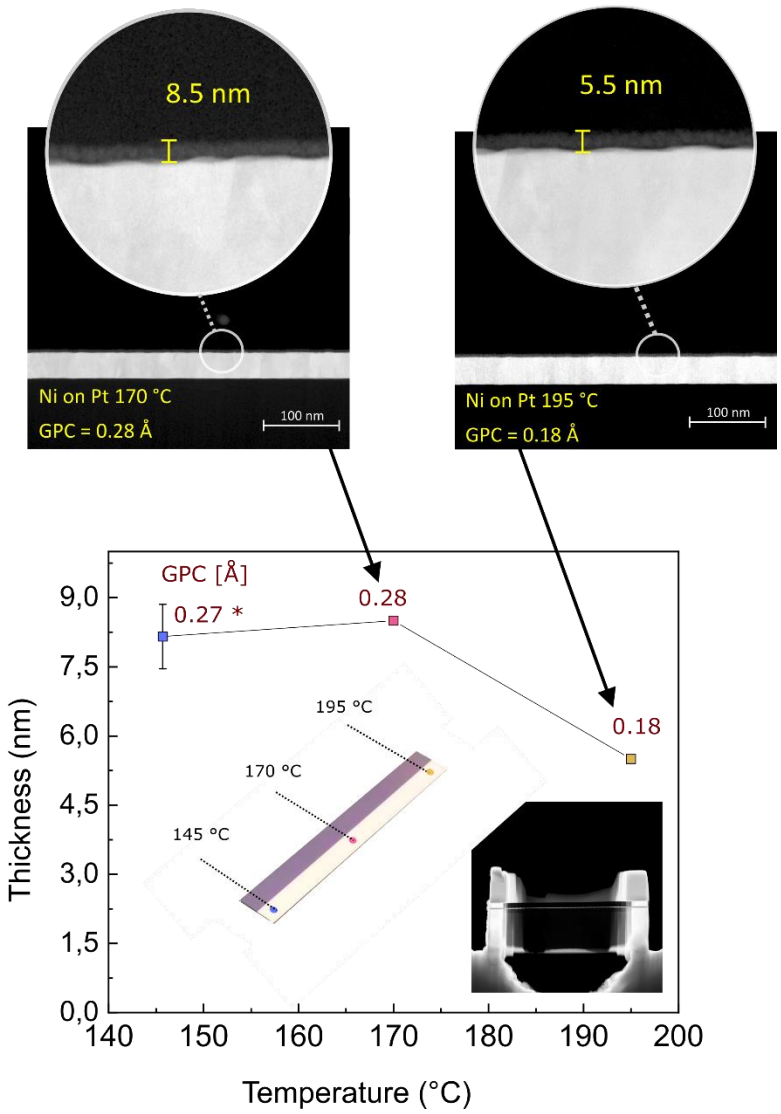

Figure 68: Thickness analysis of the Pt stripe of sample a through TEM imaging of the cross sections of the sample at different substrate temperature coordinates.

This first experiment showed area-selectivity on platinum at temperature values which agree with the ALD window reported in literature for this process. For platinum as substrate, we report approximately a third of the GPC value reported in previous studies. [29]

To exclude precursor undersaturation as a cause for the lower growth rates, in the following experiments the precursor exposure was increased.

6.3.2 Selectivity for increased amounts of injected $Ni(DAD)_2$

In this experiment, substrate b and substrate c were processed with 250 ALD cycles. Compared to the previous experiment, the pulsing time of $Ni(DAD)_2$ was increased to 10 s, while all remaining parameters were left unchanged. The increment of the pulsing time causes an increase of the average mass injected per pulse from 0.26 mg to 0.40 mg. The motivation behind increasing the exposure to $Ni(DAD)_2$ vapors is the study of the optimal precursor dose required to obtain saturation.

Considering the results of the previous experiment on sample a, which showed loss of area-selectivity at low temperatures, the section of the substrate with nominal processing temperatures below 165°C will not be further discussed.

EDX spectra were collected from 3 different sections of the specimen corresponding to the 165°C, 180°C and 195°C (blue lines in **Figure 69**, a), scanning horizontally from one material stripe to another. The elemental species attributed to each peak are demarked at the top of the plots.

6.3.2.1 Growth on SiO_2: the role of hydroxyl groups

On the non-growth area (SiO_2), at 165°C no nickel signal can be detected, at 180°C $Ni_{L\alpha}$ signal increases just above EDX detection limit (but still very low), while at 195 °C the signal is intense (**Figure 69**, b). From the previous experiment (**Figure 66**, a), no nickel growth on SiO_2 was expected to occur in this temperature range. The mechanism, which is responsible for the loss of selectivity, is most certainly related to the increased precursor dose as it is the only changed parameter. Also, it cannot be attributed to parasitic CVD (e.g., due to poor purging), because such contribution would lead to an enhanced deposition independent of the underlying substrate. Moreover, as it will be shown later in this chapter, the growth on metallic surfaces, such as gold and platinum, is not affected by the increased precursor dose.

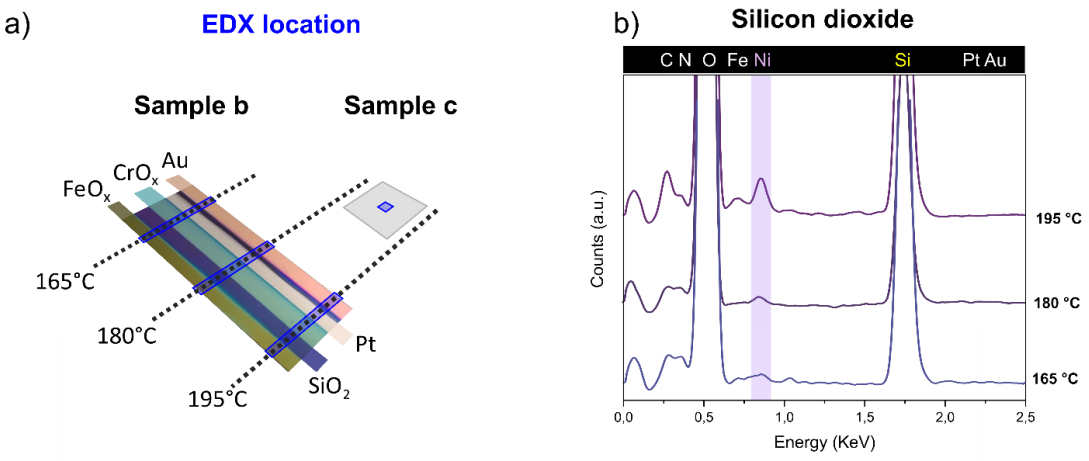

Figure 69: a) Image of sample b and sample c. The blue stripes and dotted lines indicate the locations on the substrate analyzed by EDX. b) EDX spectra collected at coordinates corresponding to 165 °C, 180 °C and 195 °C locations on silicon dioxide after 250 cycles ALD.

The mechanism which causes undesired growth on silicon dioxide is the surface diffusion of the physiosorbed precursor from growth to non-growth areas. [70] This mechanism has been recently studied for $Co(DAD)_2$ and here we found that is equally valid for $Ni(DAD)_2$. In agreement with the explanation proposed by M. Breeden et al, the increase of the precursor dose above surface saturation is the driving force for this undesired growth. When the growth-surface (metal) is already saturated, the excess precursor can weakly physisorb to the first molecular layer and consequently diffuse towards neighboring areas where it binds to hydroxyl groups. [70]

This mechanism, defined by the authors as "proximity affect", can be suppressed by either lowering the precursor doses or by utilizing substrates with lower concentrations of surface-OH groups.

6.3.2.2 Nickel growth on metals and metal oxides

The metallic nature of platinum and gold substrates was confirmed by performing XPS analysis of the surfaces prior to ALD. The $Pt4f_{7/2}$ (**Figure 70**, a) and $Au4f_{7/2}$ (**Figure 70**, b) peaks, positioned at 71.4 eV and 84.1 eV, respectively, are attributed to the Pt^0

and Au^0 states. [197] The XPS analysis of the same spectral regions was repeated after ALD, showing no changes in the oxidation states of both metallic surfaces.

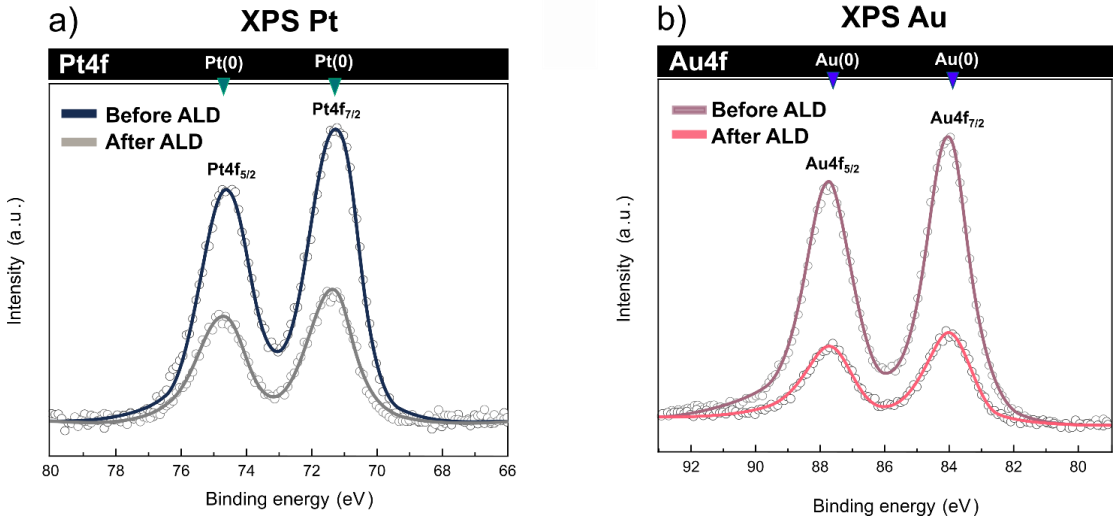

Figure 70: XPS spectra collected from a) platinum and b) gold substrates before and after 250 Ni ALD cycles at 195°C.

The two metal oxide surfaces were also characterized via XPS to determine surface composition before and after ALD.

The XPS analysis of the chromium stripe (**Figure 71**, a) shows two peaks at 576.6 eV and 586 eV, which stem from Cr $2p_{3/2}$ and Cr $2p_{1/2}$, respectively. These peaks stand in agreement with the typical binding energy of Cr(III). [198] Hence, we assume that the surface prior to ALD is entirely composed of Cr_2O_3. After nickel deposition, the composition of chromium oxide is left unaltered.

The composition of the iron stripe was also studied before and after ALD (**Figure 71**, b). From the deconvolution of the spectra collected between 700 and 730 eV, the pristine surface composition (**Figure 71**, c) presents a mixture of Fe(II) and Fe(III), where Fe^{2+} is the main component with approximately 80%. The surface is presumed to be composed in its majority of Hematite (α-Fe_2O_3), the most thermodynamically stable iron oxide, and a small amount of FeO. [199] After ALD processing, the Fe(II) component is slightly lowered in favor of Fe(III) (**Figure 71**, d). However, without using high purity iron standards and statistical XPS data sampling, this data alone cannot be used to prove any compositional change.

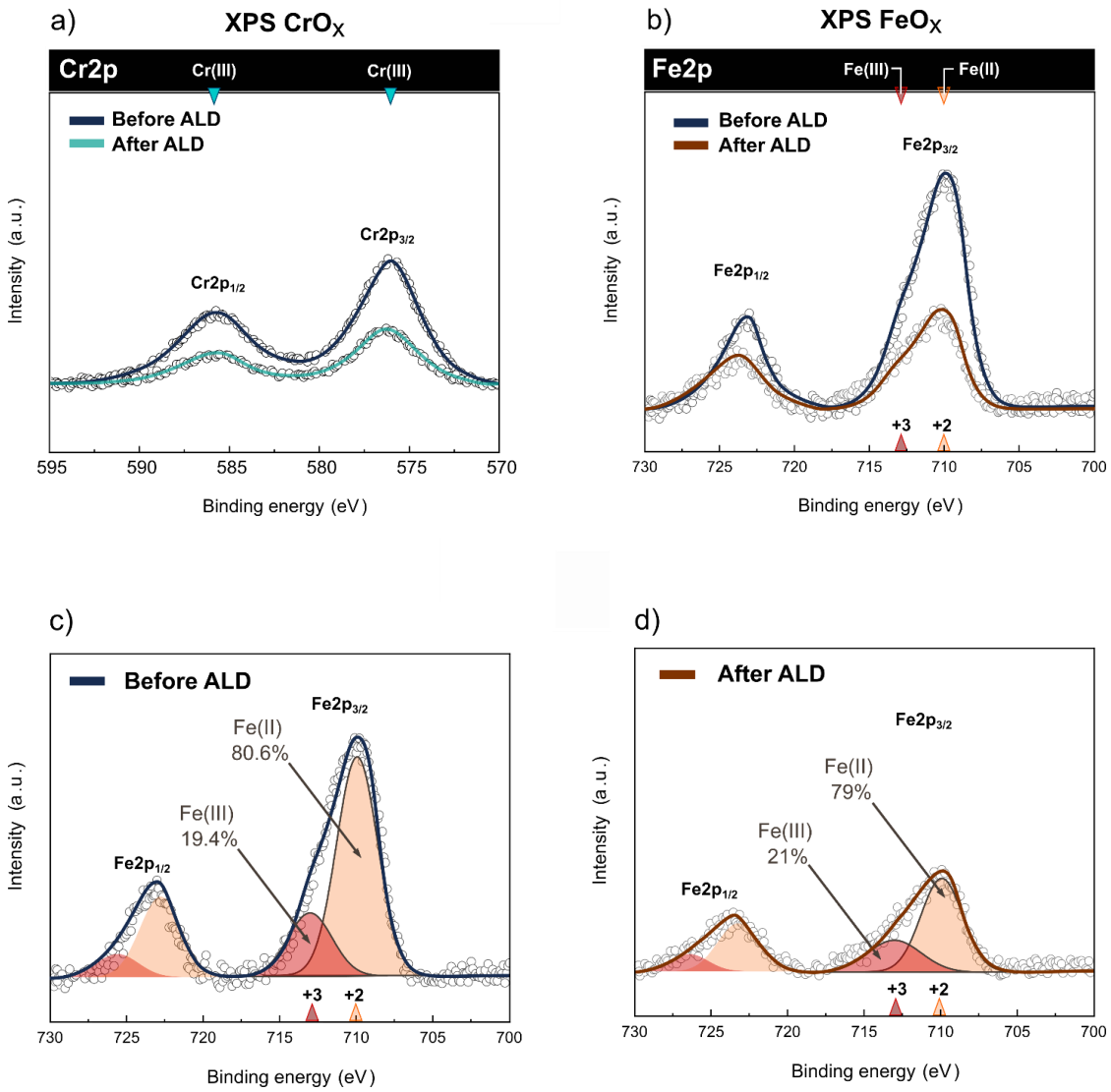

Figure 71: XPS spectra collected from a) chromium and b) iron substrates before and after 250 Ni ALD cycles at 195°C. c) Peak deconvolution of Fe2p peaks measured on the blank iron substrate. d) Peak deconvolution of Fe2p peaks measured on the iron substrate after 250 ALD cycles.

Analysis of the EDX signal on sample b and the decrease of the overall intensity of the XPS spectra observed after ALD processing revealed the presence of nickel on each metal/metal oxide stripe in the whole temperature range.

EDX spectra of the two metallic surfaces, Pt and Au, present a distinguishable $Ni_{L\alpha}$ peak in the whole temperature range.

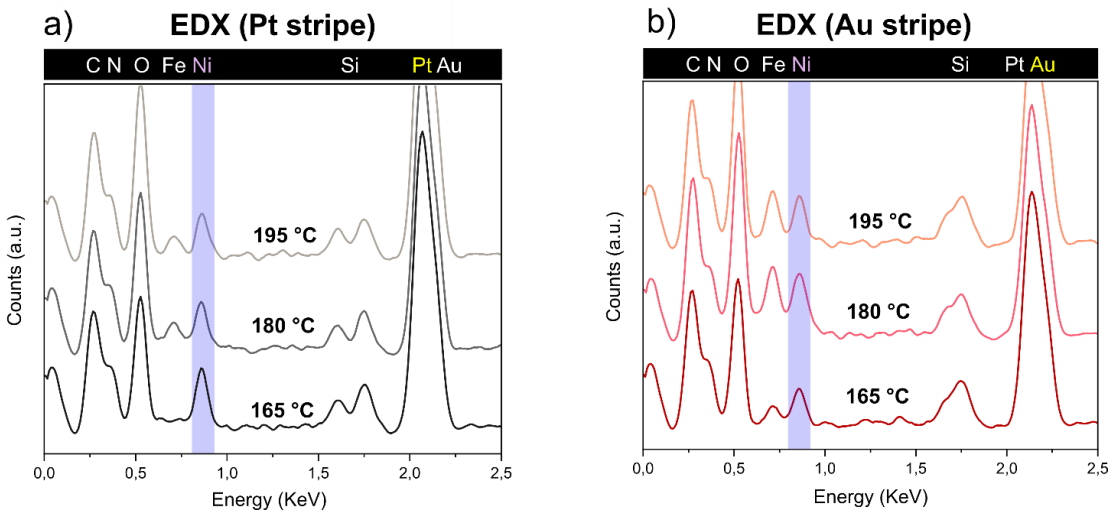

Figure 72: EDX spectra collected at the temperature coordinates of 165 °C, 180 °C, and 195 °C after 250 cycles ALD on a) platinum and b) gold substrates.

On the platinum surface (**Figure 72**, a), the $Ni_{L\alpha}$ signal is visually stronger at 165°C than at higher temperatures. This result is consistent with the previously shown reduction of the GPC (from 0.28 Å to 0.18 Å) observed on the platinum surface of sample a when temperature exceeds 170 °C (**Figure 68**).

In contrast to that, on the gold surface (**Figure 72**, b) the $Ni_{L\alpha}$ peak signal shows increased intensity with increasing temperature. A similar trend is found on chromium oxide (**Figure 73**, a) and iron oxide (**Figure 73**, b) surfaces, where the signal also increases when the substrate temperature is increased from 165 °C to 180 °C.

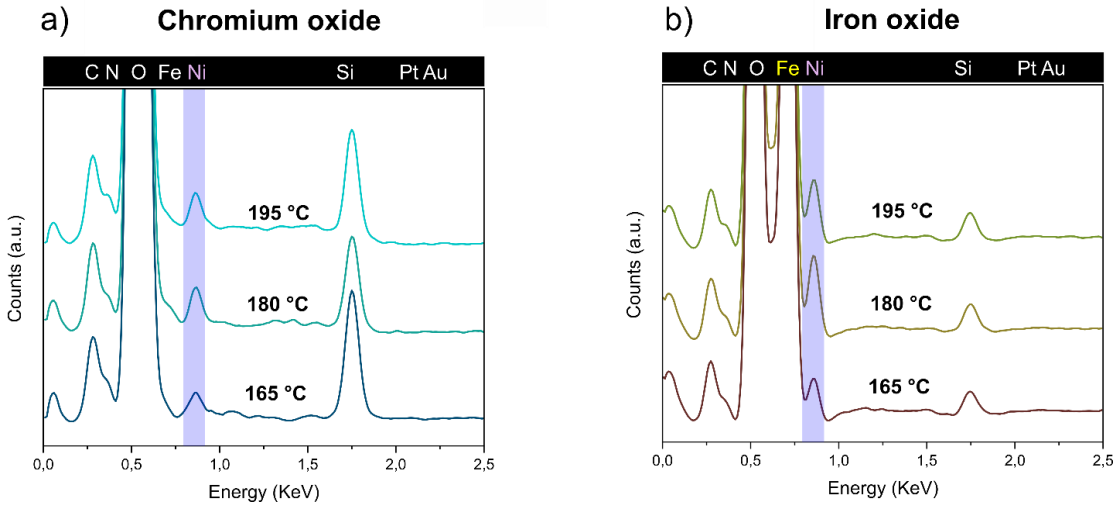

Figure 73: EDX spectra collected at the substrate locations corresponding to 165 °C, 180 °C and 195 °C after 250 cycles ALD on a) chromium oxide and b) iron oxide substrates.

This qualitative difference observed between platinum and the other surfaces could be due to different chemisorption energetics promoted by the different surfaces. By considering the low temperature curves (165 °C), the stronger EDX signal from Pt than from gold and the two oxides, could signify that indeed nucleation is more favorable on Pt surfaces. However, to prove this hypothesis further experiments are required.

The fact that nickel growth is not inhibited on the oxidized surfaces (FeO_x and CrO_x) differs from previous reports in which the presence of oxidized surfaces was proposed to compete to nickel growth inhibition. [29,193,195]

The presence of Iron

Another characteristic x-ray peak collected from each surface is the $Fe_{L\alpha}$ emission which is positioned at 0.705 eV. While on silicon dioxide the iron peak only appears at high substrate temperatures (**Figure 69**, b), on platinum and gold this peak can be clearly distinguished in the whole temperature range (**Figure 72**, a-b). On chromium oxide, the intensity of this peak is markedly increasing as the substrate temperature is increased but the peak is partially hidden from other contributions from oxygen and chromium emissions (**Figure 73**, a).

Iron contamination of the measured sites prior to the ALD process has been excluded by collecting EDX data from different surface points of the blank sample (substrate b, before ALD). One accreditable explanation is that the ALD process etches iron atoms from the surface and re-deposit them elsewhere.

The Fe signal is also detected on the Au stripe by XPS (**Figure 74**). By considering the geometrical distance between the FeO_x stripe (source of Fe atoms) and the Au stripe (re-deposition location), they are positioned at two opposite sides of the wafer (**Figure 69**, a). Any solid diffusion/dissolution mechanism of iron atoms into gold can be thus excluded. This lends credence to the hypothesis that the transport of iron atoms occurs through etching and redeposition.

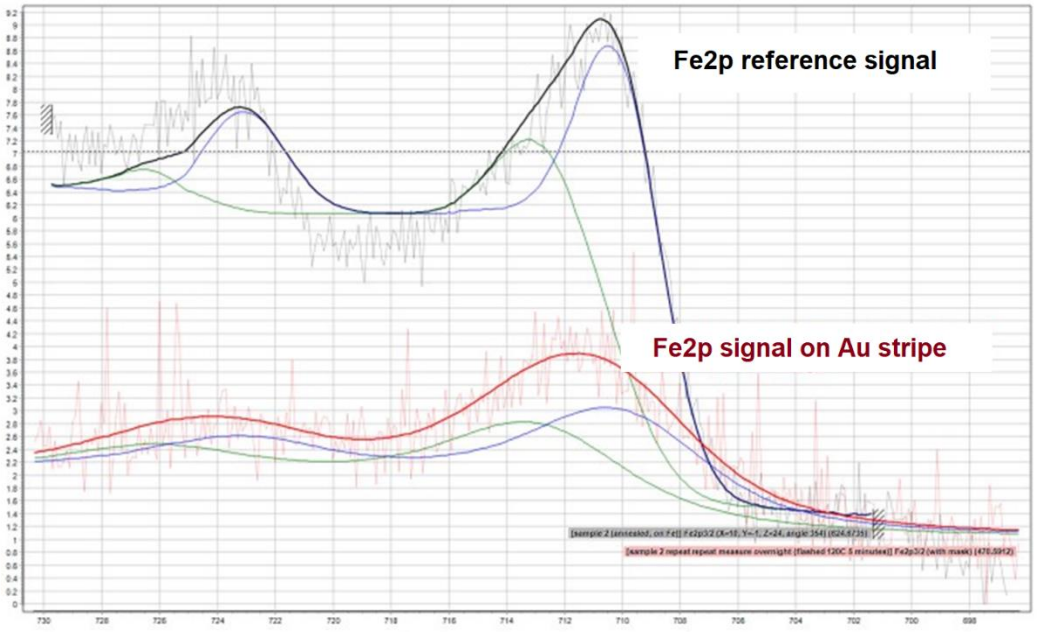

Figure 74: Fe2p signal collected from iron oxide stripe (black) and gold stripe (red) of sample b after 250 cy AS-ALD at 185-190°C.

We hypothesize that $Ni(DAD)_2$ chemisorption/decomposition on iron oxide substrates can lead to the coordination of DAD ligands with iron atoms available on the surface. This newly formed iron-containing complex can either desorb from the surface if it is volatile enough, or simply diffuse along the surface ultimately chemisorbing at higher substrate temperatures. Similar reaction mechanisms are employed in dry etching and atomic layer etching (ALE) techniques to remove metals and metal oxides from the surface. [200] In literature, β-diketones are excellent organic vapor etchants thanks to their high volatility and the formation of stable diketonates with metals such as cobalt, iron and nickel. [201] Similarly, DAD ligands can also be good candidates for etching transition metals given their good reactivity towards metal cations. Recently, thermal dry etching of iron has been achieved using acetylacetonate precursors. [202] Previous studies on cobalt etching with hexafluoroacetylacetone (hfacH) demonstrated that purely metallic cobalt surfaces cannot be etched and that surface Co(II) is necessary to initiate the etching. [203] If the surface is oxidized, hfacH ligands can bind to Co(II) to form volatile $Co(hfac)_2$ that can later desorb from the surface, otherwise, if the surface is purely metallic hfacH, ligand decomposition is favored.

Similar to those studies, we postulate that 1,4-diazadiene-derived ligands can bind to oxidized iron centers (II or III) forming $Fe(DAD)_2$ or similar DAD-based compounds. Given the increased thermal stability of $Fe(DAD)_2$ (decomposition temperature of 260 °C) compared to $Ni(DAD)_2$ (decomposition temperature of 230 °C), [192] the formation of the iron complex could be an energetically favorable pathway to stabilize the ligands. If this hypothesis holds true, we can expect this mechanism to be energetically

favorable for chromium and manganese oxide substrates as well. On platinum and gold surfaces instead, precursor decomposition is favored.

We thus provide experimental evidence of iron re-deposition/surface diffusion, and we propose a mechanism of etching by DAD-derived ligands, suggesting that this topic should be studied in more depth with further experimental and theoretical data. The role of the co-precursor as well as the on promoting such mechanism is not yet identified.

This interpretation would explain the failure in obtaining deposition on stainless steel ALD setups.

6.3.3 AS-ALD on nanostructures

The analysis of ***sample c*** (**Figure 65**) provides further insights into the selectivity mechanism of the deposition. This sample was processed together with *sample b* during the same ALD run. Thus, the processing parameters are the same. From the positioning of the substrate inside the reactor during the experiment, the substrate temperature is estimated to be between 185-190 °C (**Figure 69**, a), which is within the ALD window reported for this process. [29] The substrate of choice was quartz, due to its low concentration of silanol (Si-OH) groups which should suppress nickel growth. [70]

As predicted, XPS confirmed that the diminished hydroxyl concentration of quartz results in the hindering of nickel nucleation. As it can be observed in **Figure 75**, after AS-ALD, the quartz surface shows no nickel signal while SiO_2, (processed under the same conditions) shows instead Ni on the surface.

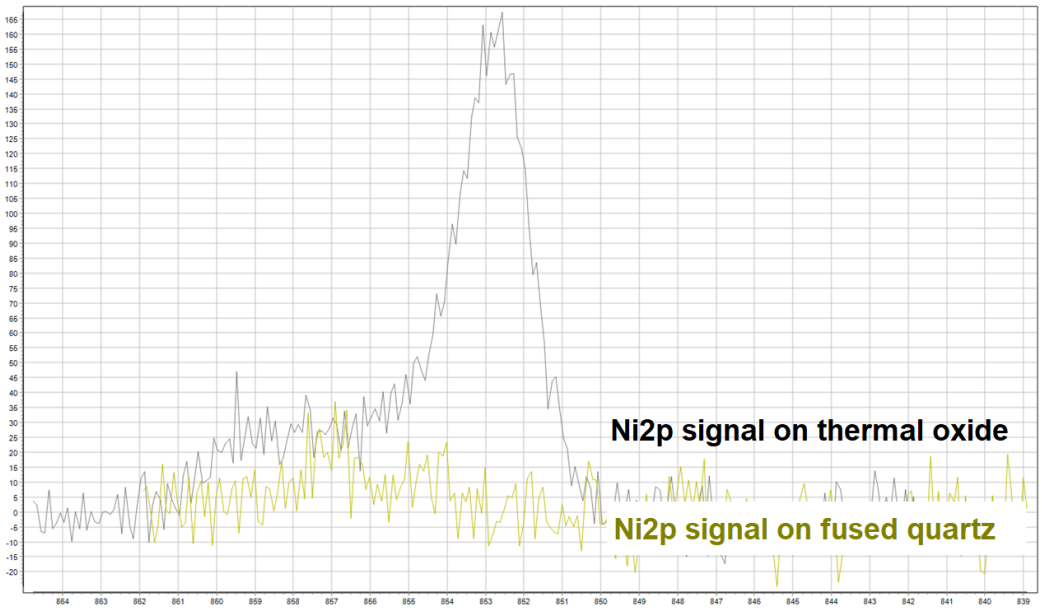

Figure 75: Ni2p region measured on Quartz (yellow) and SiO_2 (black) surface after being exposed to 250 cy AS-ALD at 185-190°C.

The selectivity of nickel deposition can be visualized through EDX mapping of the surface of sample c (**Figure 76**), where an increase of counts per second (CPS) is associated to brighter coloring (grey).

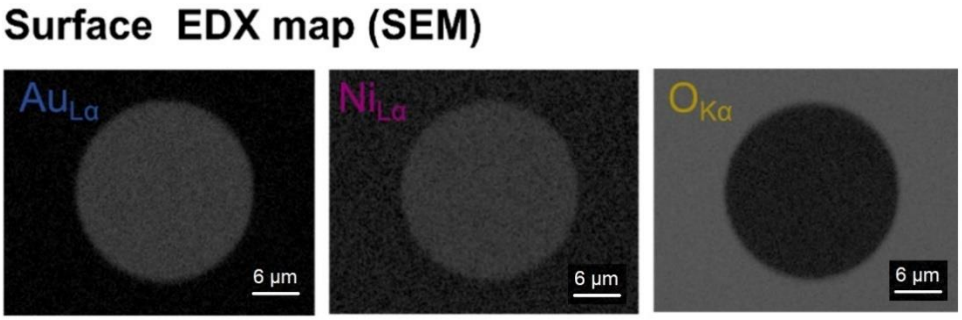

Figure 76: EDX map Au, Ni and O signal collected from the surface of a gold micro-disc. Increased CPS relative to the atomic species emission is associated to brighter color (grey).

The signal has been collected from the surface of gold micro-discs of 24 μm in diameter (**Figure 65**, a-b). An increased CPS of nickel is found to correlate with the signal of the features and not with the oxygen signal associated with the SiO_2 substrate. In **Figure 76**, we present the EDX map of a gold disc, but this behavior is observed for each of the materials used as growth-area, that is, platinum, chromium oxide and iron oxide. Based on this first analysis, the following characterization will focus on two of

the four materials, taking gold and iron oxide as representatives for metallic and oxidized surfaces, respectively. At this stage of the investigation and given the similarity between the materials chosen as non-oxidised and oxidised surfaces, the conclusions relative to growth on Au and FeO_x can be also extended to platinum and chromium oxide.

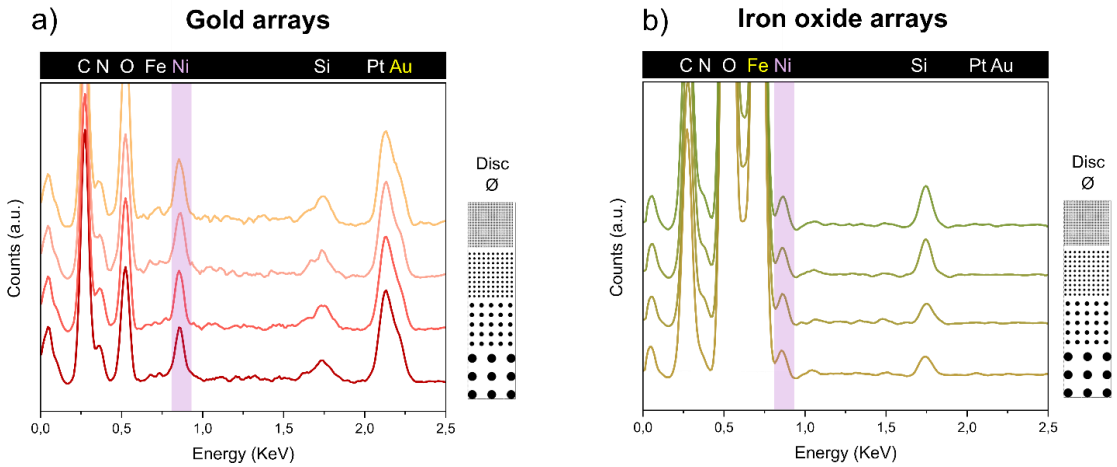

Figure 77: EDX spectra collected from a) gold arrays and b) Iron oxide arrays after 250 ALD cycles at 190°C.

From the EDX analysis, nickel growth is confirmed on each structure, for both gold and iron oxide and for all disc sizes from nano to micro-discs. Interestingly, the iron signal attributed to redeposition on gold, as observed from the gold stripe (*sample b,* **Figure 72**, b), was not present on the gold nanostructures (**Figure 77**, a). This result is consistent with the hypothesis that iron atoms are etched from the FeO_x surface, which in this case is drastically reduced, being iron only present in the nano/micro-arrays. In the previously discussed sample b (**Figure 69**, a) instead, the iron stripe covers approximately the 20% of the substrate surface accentuating this mechanism of iron etching and re-deposition.

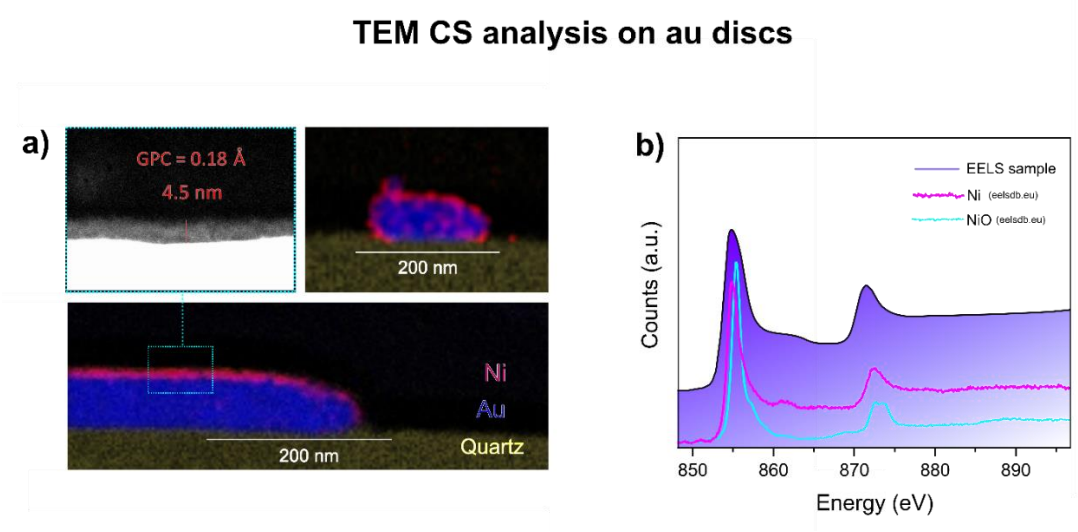

Figure 78: TEM analysis of lamellae of Au micro and nano-discs, showing a) area selective nickel deposition of 4.5 nm on gold nanostructures, and b) the metallic character of the ALD-deposited nickel.

TEM analysis of lamellae extracted from the Au and FeO_x discs was also performed. For the gold structures, two lamellae were fabricated: the first from a micro-disc of 24 μm in diameter and the second from a nano-disc (**Figure 78**, a). High resolution imaging of the nickel thin film on the micro-disc revealed a GPC of 0.18 Å, which matches the GPC obtained in previous studies on platinum in this temperature range [22]. Two conclusions can be drawn from this result: i) the growth on platinum and gold is indeed very similar, ii) lower doses of 0.26 mg/cycles, used for the initial experiments on sample a, were already sufficient for saturation of $Ni(DAD)_2$ and an increase to 0.4 mg/cycles only favors undesired nucleation on growth-inhibited areas. The EDX maps of the disc cross-sections (**Figure 78**, a) show AS-nickel growth (red) on gold discs (blue) and no deposition on the quartz substrate (yellow). EELS analysis further confirmed the metallic character of the nickel thin film (**Figure 78**, b).

[22] The GPC of 0.18 Å on platinum nanostructures was confirmed by cross-section TEM analysis of a platinum microdisc from sample c.

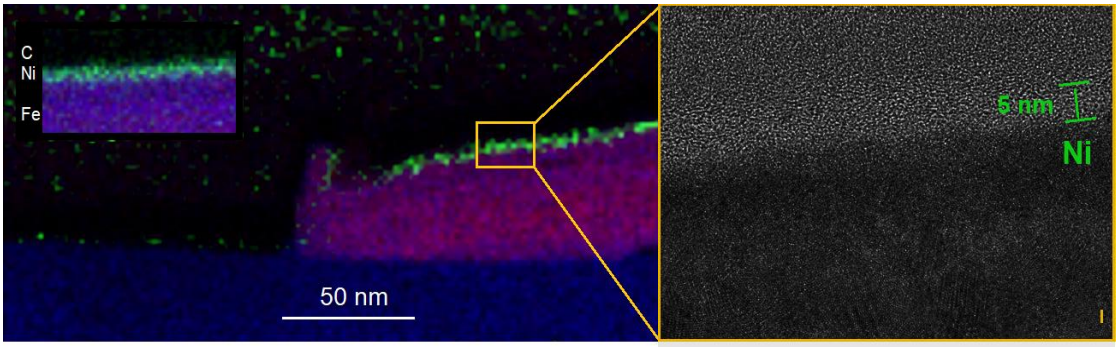

Figure 79: TEM analysis of a lamella of a FeO_x micro-disc showing area-selective nickel deposition (left). High resolution TEM image of the cross section reveals approximately 5 nm thick nickel on iron oxide (right).

Both EDX and high-resolution TEM micrographs of an iron oxide micro-disc confirm both area-selectivity and a GPC similar to that on metallic substrates (**Figure 79**). However, a clear visualization of the nickel thin film on the disc is compromised by the presence of sidewall artifacts at the edges of the structure that do not permit to clearly resolve the nickel signal at the interface with the substrate. The lower contrast deriving from the presence of lighter elements, such as oxygen, also limits the resolution impeding determination of the interface between thin film and the FeO_x substrate. Likewise, the nickel thin film and the carbon coating deposited on the surface during cross section fabrication present very similar contrast, and the nickel coating is only barely distinguishable (slightly brighter). This suggests that the carbon content of the nickel thin film is very high.

6.4 Conclusions

It is evident that the development of reliable AS-methodologies still requires extensive effort to unveil many of the mechanisms which affect the growth and that are yet not fully understood. In this context, we emphasize that the "proximity effect", that leads to undesired growth, is strongly affected by the concentration of defective sites of the growth-inhibited areas (demonstrated by switching from Si-OH rich silicon with thermal oxide to fused quartz). Another critical factor is the precursor dose. Undesired nucleation is triggered by the presence of molecularly adsorbed excess precursor on growth areas that can migrate to neighboring non-growth areas. The optimal precursor dose may vary depending on the relative size of the growth and non-growth areas.

Given that the nickel growth per cycle is almost identical on both noble substrates (Au, Pt) and oxidized metals (Fe,Cr), we state that it cannot be generalized that the growth inhibition results from the presence of oxide layers.

TEM/XPS analyses of the obtained nickel thin films showed that nickel is metallic, but likely intermixed with carbon. Future process optimization should involve the study of co-precursor saturation curves, together with the use of leak tested tools to exclude any oxygen contamination. These factors could be determining for increasing growth rate of this process.

A deeper study and understanding of the chemistry and physics of the M-$(DAD)_2$ precursors is required. In particular, the possible existence of an energetically favorable decomposition pathways for $Ni(DAD)_2$ when in contact with iron oxide would hinder the technological applications of this compound for ALD purposes and should thus be clarified.

Summary and Outlook

Tool engineering plays a crucial role for new approaches and discoveries in Atomic Layer Deposition (ALD), especially when it comes to ensuring reproducibility even with intricate chemistries. This becomes particularly evident when scaling up processes which involve sophisticated precursors with distinct chemisorption or decomposition properties. This reality was consistently observed throughout this thesis and demanded significant experimental attention, as illustrated in Chapter III and Chapter VI, focusing on nickel oxide deposition with $Ni(Cp)_2$ and $Ni(DAD)_2$.

Historically, ALD machine characteristics have led to the selection of chemical precursor with well-defined properties. We have now reached a point where this scheme is inverted. This, as mentioned at the beginning of this thesis, is not limited to ALD but is a global challenge. We shift into an era where new scientific discoveries need to define the design of future machines and not vice-versa.

In ALD, an important component that has remained largely unchanged since decades is the *hot source,* a heated assembly that evaporates chemical precursors. We propose that redesigning of these simple components could facilitate precursor delivery, reducing waste, and mitigate machine aging. This could be achieved by utilizing materials with smaller thermal inertia than stainless steel, allowing to heat the precursors only when needed rather than throughout the entire process, and by shortening the distance between precursor sources and substrates as illustrated in this work. For this, CFD has demonstrated to be a powerful tool for solving specific technical questions during the machine design. As it was shown throughout this thesis, CFD simulations can also be beneficial for explaining experimental data and should not only used for engineering purposes.

Another processing option studied in this thesis is sample post-processing through thermal annealing. Routines applied in ALD, such as vapor dosing through pulsing sequences and purging steps, have been applied to achieve better control in sample fabrication during rapid thermal annealing (RTA) processes. These studies led to the knowledge that RTA treatments can be used for top-down modification of already fabricated materials and, if combined with direct write patterning tools, can be used to produce functional structures (Chapter IV), or to promote area-selective reactions (Chapter V). The methodology was also used in for achieving local reduction of nickel oxide thin films to produce nickel domains embedded in nickel oxide. We propose to utilize laser writing or thermal lithography to produce localised heating and promote surface chemical reactions with the gaseous environment in the patterned areas only. As highlighted in the thesis, the fabrication of Ni/NiO composites is an interesting

platform for testing this method envisioning different technological applications. This methodology could be easily extended to many other materials.

Chapter V highlights the resurgence of silicides through studies on 2D structures with novel properties. This work underlines that solid-state reactions can become area-selective when combined with surface patterning methods involving focused ion beams. This approach, here demonstrated for nickel silicide, could likely be extended to other metal silicides from the first series of transition metals which are known to present similar interstitial diffusivity of nickel. The findings show that area-selectivity is based on a phenomenon of surface diffusion, which arises when ALD-deposited NiO is used as nickel supply instead of metallic nickel. The presence of native silicon dioxide is shown to play an important role for the selectivity between silicide growth and growth-inhibition. The growth areas are designed through selective removal of the surface oxide layer via ion milling, thereby defining energetically favourable locations for the nickel silicide formation.

AS-ALD, especially when combined with direct writing techniques, holds substantial potential for the future of micro/nano fabrication. Despite the concise study in this chapter, the significant experimental effort underscores the existing knowledge gap which requires future in-depth studies of the reaction mechanisms. For the case of $Ni(DAD)_2$, it is confirmed that the selectively results in chemisorption on noble metals and that hydroxylated surfaces can promote undesired growth. The observed nickel growth on metal oxides (iron and chromium oxide) suggests that this molecule can decompose also when in contact with metallic centres which can react with the complex ligands forming stable M-$(DAD)_2$ complexes. further experiments are planned for confirming this hypothesis.

Each of the sections of this thesis requires further in-depth investigation and analysis, which is foreseen for the future studies. The acquired new knowledge is expected to shed light into new strategies in AS-ALD under consideration of modelling, precursor chemistry, process engineering and solid-state physics.

The only certain conclusion is that science is a boundless mystery and, as such, it requires from us boundless curiosity.

Bibliography

[1] G. E. Moore, "Cramming more components onto integrated circuits, Reprinted from Electronics, volume 38, number 8, April 19, 1965, pp.114 ff.," *IEEE Solid-State Circuits Soc. Newsl.*, vol. 11, no. 3, pp. 33–35, 2009, doi: 10.1109/n-ssc.2006.4785860.

[2] W. M. Holt, "Moore's law: A path going forward," *Dig. Tech. Pap. - IEEE Int. Solid-State Circuits Conf.*, vol. 59, pp. 8–13, 2016, doi: 10.1109/ISSCC.2016.7417888.

[3] D. Bergeron, "More than Moore," *2008 IEEE Custom Integrated Circuits Conference*, San Jose, CA, USA, 2008, pp. xxv-xxvi, doi: 10.1109/CICC.2008.4672003.

[4] M. C. Lemme, D. Akinwande, C. Huyghebaert, and C. Stampfer, "2D materials for future heterogeneous electronics," *Nat. Commun.*, vol. 13, no. 1, pp. 2–6, 2022, doi: 10.1038/s41467-022-29001-4.

[5] L. Tong *et al.*, "2D materials-based homogeneous transistor-memory architecture for neuromorphic hardware," *Science (80-.).*, 2021, doi: 10.1126/science.abg3161.

[6] L. R. Harriott, "Limits of lithography," *Proc. IEEE*, vol. 89, no. 3, pp. 366–374, 2001, doi: 10.1109/5.915379.

[7] M. A. van de Kerkhof, J. P. H. Benschop, and V. Y. Banine, "Lithography for now and the future," *Solid. State. Electron.*, vol. 155, no. xxxx, pp. 20–26, 2019, doi: 10.1016/j.sse.2019.03.006.

[8] A. S. Gangnaik, Y. M. Georgiev, and J. D. Holmes, "New Generation Electron Beam Resists: A Review," *Chem. Mater.*, vol. 29, no. 5, pp. 1898–1917, 2017, doi: 10.1021/acs.chemmater.6b03483.

[9] V. R. Manfrinato *et al.*, "Determining the resolution limits of electron-beam lithography: Direct measurement of the point-spread function," *Nano Lett.*, vol. 14, no. 8, pp. 4406–4412, 2014, doi: 10.1021/nl5013773.

[10] S. Z. Butler *et al.*, "Progress, challenges, and opportunities in two-dimensional materials beyond graphene," *ACS Nano*, vol. 7, no. 4, pp. 2898–2926, 2013, doi: 10.1021/nn400280c.

[11] M. Weinhold and P. J. Klar, "Patterning 2D materials for devices by mild

lithography," *RSC Adv.*, vol. 11, no. 48, pp. 29887–29895, 2021, doi: 10.1039/d1ra04982h.

[12] E. Albisetti *et al.*, "Nanopatterning reconfigurable magnetic landscapes via thermally assisted scanning probe lithography," *Nat. Nanotechnol.*, vol. 11, no. 6, pp. 545–551, 2016, doi: 10.1038/nnano.2016.25.

[13] A. K. Yetisen *et al.*, "Art on the Nanoscale and beyond," *Advanced Materials*. 2016, doi: 10.1002/adma.201502382.

[14] M. Hentschel, J. Karst, and H. Giessen, "Tailored Optical Functionality by Combining Electron-Beam and Focused Gold-Ion Beam Lithography for Solid and Inverse Coupled Plasmonic Nanostructures," *Adv. Opt. Mater.*, vol. 8, no. 19, 2020, doi: 10.1002/adom.202000879.

[15] Q. Y. Lin *et al.*, "Building superlattices from individual nanoparticles via template-confined DNA-mediated assembly," *Science (80-.).*, vol. 359, no. 6376, pp. 669–672, 2018, doi: 10.1126/science.aaq0591.

[16] L. Bruchhaus, P. Mazarov, L. Bischoff, J. Gierak, A. D. Wieck, and H. Hövel, "Comparison of technologies for nano device prototyping with a special focus on ion beams: A review," *Applied Physics Reviews*. 2017, doi: 10.1063/1.4972262.

[17] M. F. J. Vos *et al.*, "Area-Selective Deposition of Ruthenium by Combining Atomic Layer Deposition and Selective Etching," *Chem. Mater.*, vol. 31, no. 11, pp. 3878–3882, 2019, doi: 10.1021/acs.chemmater.9b00193.

[18] S. T. Howell, A. Grushina, F. Holzner, and J. Brugger, "Thermal scanning probe lithography—a review," *Microsystems Nanoeng.*, vol. 6, no. 1, pp. 1–24, 2020, doi: 10.1038/s41378-019-0124-8.

[19] V. Levati *et al.*, "Phase Nanoengineering via Thermal Scanning Probe Lithography and Direct Laser Writing," *Adv. Mater. Technol.*, vol. 2300166, pp. 1–15, 2023, doi: 10.1002/admt.202300166.

[20] A. Nadzeyka *et al.*, "Ion beam lithography for direct patterning of high accuracy large area X-ray elements in gold on membranes," in *Microelectronic Engineering*, 2012, doi: 10.1016/j.mee.2012.07.036.

[21] F. Samad *et al.*, "Controlled and deterministic creation of synthetic antiferromagnetic domains by focused ion beam irradiation," *Appl. Phys. Lett.*, vol. 119, no. 2, pp. 1–5, 2021, doi: 10.1063/5.0049926.

[22] A. Enrico *et al.*, "Ultrafast and Resist-Free Nanopatterning of 2D Materials by Femtosecond Laser Irradiation," *ACS Nano*, 2023, doi:

10.1021/acsnano.2c09501.

[23] J. Lasseter, P. D. Rack, and S. J. Randolph, "Selected Area Deposition of High Purity Gold for Functional 3D Architectures," *Nanomaterials*, vol. 13, no. 4, 2023, doi: 10.3390/nano13040757.

[24] S. Lamb-camarena *et al.*, "3D Magnonic Conduits by Direct Write Nanofabrication," pp. 1–12, 2023.

[25] J. M. De Teresa, P. Orús, R. Córdoba, and P. Philipp, "Comparison between focused electron/ion beam-induced deposition at room temperature and under cryogenic conditions," *Micromachines*, vol. 10, no. 12, pp. 1–13, 2019, doi: 10.3390/mi10120799.

[26] G. N. Parsons and R. D. Clark, "Area-Selective Deposition: Fundamentals, Applications, and Future Outlook," *Chem. Mater.*, vol. 32, no. 12, pp. 4920–4953, 2020, doi: 10.1021/acs.chemmater.0c00722.

[27] A. J. M. Mackus, M. J. M. Merkx, and W. M. M. Kessels, "From the Bottom-Up: Toward Area-Selective Atomic Layer Deposition with High Selectivity †," *Chem. Mater.*, vol. 31, no. 1, pp. 2–12, 2019, doi: 10.1021/acs.chemmater.8b03454.

[28] P. C. Lemaire, M. King, G. N. Parsons, P. C. Lemaire, M. King, and G. N. Parsons, "Understanding inherent substrate selectivity during atomic layer deposition : Effect of surface preparation , hydroxyl density , and metal oxide composition on nucleation mechanisms during tungsten ALD Understanding inherent substrate selectivity during a," vol. 052811, 2017, doi: 10.1063/1.4967811.

[29] M. M. Kerrigan, J. P. Klesko, K. J. Blakeney, and C. H. Winter, "Low Temperature, Selective Atomic Layer Deposition of Nickel Metal Thin Films," *ACS Appl. Mater. Interfaces*, vol. 10, no. 16, pp. 14200–14208, 2018, doi: 10.1021/acsami.8b03074.

[30] M. M. Kerrigan, J. P. Klesko, and C. H. Winter, "Low Temperature, Selective Atomic Layer Deposition of Cobalt Metal Films Using Bis(1,4-di-tert-butyl-1,3-diazadienyl)cobalt and Alkylamine Precursors," *Chem. Mater.*, vol. 29, no. 17, pp. 7458–7466, 2017, doi: 10.1021/acs.chemmater.7b02456.

[31] J. A. Singh *et al.*, "Area-Selective Atomic Layer Deposition of Metal Oxides on Noble Metals through Catalytic Oxygen Activation," *Chem. Mater.*, vol. 30, no. 3, pp. 663–670, 2018, doi: 10.1021/acs.chemmater.7b03818.

[32] R. Chen *et al.*, "Achieving area-selective atomic layer deposition on patterned

substrates by selective surface modification Achieving area-selective atomic layer deposition on patterned substrates by selective surface modification," vol. 191910, no. 2005, pp. 6–9, 2014, doi: 10.1063/1.1922076.

[33] R. Khan *et al.*, "Area-Selective Atomic Layer Deposition Using Si Precursors as Inhibitors," *Chem. Mater.*, vol. 30, no. 21, pp. 7603–7610, 2018, doi: 10.1021/acs.chemmater.8b02774.

[34] J. Yarbrough *et al.*, "Tuning Molecular Inhibitors and Aluminum Precursors for the Area- Selective Atomic Layer Deposition of Al 2 O 3," 2022, doi: 10.1021/acs.chemmater.2c00513.

[35] K. Cao, J. Cai, and R. Chen, "Inherently Selective Atomic Layer Deposition and Applications," *Chem. Mater.*, vol. 32, no. 6, pp. 2195–2207, 2020, doi: 10.1021/acs.chemmater.9b04647.

[36] 3 Nick F W Thissen1, J.-W. W. , René H J Vervuurt1 , Adriaan J M Mackus1 , Johannes J L Mulders2, W. M. M. Kessels1, and and A. A. Bol1, "Graphene devices with bottom-up contacts by area-selective atomic layer deposition."

[37] W. M. M. Kessels, A. A. Bol, A. J. M. Mackus, N. F. W. Thissen, and J. J. L. Mulders, "layer-deposited platinum contacts Resist-free fabricated carbon nanotube field-effect transistors with high-quality atomic-layer-deposited platinum contacts," vol. 013101, 2017, doi: 10.1063/1.4973359.

[38] M. Kim *et al.*, "Atomic Layer Deposition of Nickel Using a Heteroleptic Ni Precursor with NH 3 and Selective Deposition on Defects of Graphene," 2019, doi: 10.1021/acsomega.9b01003.

[39] M. F. Mazza *et al.*, "Selective-Area, Water-Free Atomic Layer Deposition of Metal Oxides on Graphene Defects," pp. 1–5, 2022, doi: 10.1021/acsmaterialsau.1c00049.

[40] H. G. Kim and H. Lee, "Atomic Layer Deposition on 2D Materials †," 2017, doi: 10.1021/acs.chemmater.6b05103.

[41] C. B. Klein and M. Costa, "Nickel," in *Handbook on the Toxicology of Metals: Fifth Edition*, 2021.

[42] W. Ahmad, S. Chandra Bhatt, M. Verma, V. Kumar, and H. Kim, "A review on current trends in the green synthesis of nickel oxide nanoparticles, characterizations, and their applications," *Environmental Nanotechnology, Monitoring and Management*. 2022, doi: 10.1016/j.enmm.2022.100674.

[43] M. Utriainen, M. Kröger-Laukkanen, L. S. Johansson, and L. Niinistö, "Studies of metallic thin film growth in an atomic layer epitaxy reactor using M(acac)2

(M = Ni, Cu, Pt) precursors," *Appl. Surf. Sci.*, vol. 157, no. 3, pp. 151–158, 2000, doi: 10.1016/S0169-4332(99)00562-0.

[44] M. Utriainen, M. Kröger-Laukkanen, and L. Niinistö, "Studies of NiO thin film formation by atomic layer epitaxy," *Mater. Sci. Eng. B*, vol. B54, no. 1–2, pp. 98–103, 1998, doi: 10.1016/s0921-5107(98)00135-4.

[45] H. L. Lu *et al.*, "Atomic Layer Deposition of NiO Films on Si(100) Using Cyclopentadienyl-Type Compounds and Ozone as Precursors," *J. Electrochem. Soc.*, vol. 155, no. 10, p. H807, 2008, doi: 10.1149/1.2965456.

[46] H. B. R. Lee *et al.*, "Plasma-enhanced atomic layer deposition of Ni," *Jpn. J. Appl. Phys.*, 2010, doi: 10.1143/JJAP.49.05FA11.

[47] K. E. K. Holden, C. L. Dezelah, and J. F. Conley, "Atomic Layer Deposition of Transparent p-Type Semiconducting Nickel Oxide Using Ni(tBu2DAD)2 and Ozone," *ACS Appl. Mater. Interfaces*, vol. 11, no. 33, pp. 30437–30445, 2019, doi: 10.1021/acsami.9b08926.

[48] M. I. Pintor-Monroy, D. Barrera, B. L. Murillo-Borjas, F. J. Ochoa-Estrella, J. W. P. Hsu, and M. A. Quevedo-Lopez, "Tunable Electrical and Optical Properties of Nickel Oxide (NiO x) Thin Films for Fully Transparent NiO x - Ga 2 O 3 p-n Junction Diodes," *ACS Appl. Mater. Interfaces*, vol. 10, no. 44, pp. 38159–38165, 2018, doi: 10.1021/acsami.8b08095.

[49] G. Brunetti *et al.*, "Determination of γ-γ' lattice misfit in a single-crystal nickel-based superalloy using convergent beam electron diffraction aided by finite element calculations," *Micron*, vol. 43, no. 2–3, pp. 396–406, 2012, doi: 10.1016/j.micron.2011.10.009.

[50] X. Wang, M. Li, Y. Wang, C. Zhang, and Z. Wen, "Creep damage repair of a nickel-based single crystal superalloy based on heat treatment," *Metals (Basel).*, vol. 11, no. 4, 2021, doi: 10.3390/met11040623.

[51] A. Aslinjensipriya *et al.*, "Exploring the influence of tin in micro-structural, magneto-optical and antimicrobial traits of nickel oxide nanoparticles," *Surfaces and Interfaces*, 2022, doi: 10.1016/j.surfin.2021.101605.

[52] J. Kim *et al.*, "Tailoring Binding Abilities by Incorporating Oxophilic Transition Metals on 3D Nanostructured Ni Arrays for Accelerated Alkaline Hydrogen Evolution Reaction," *J. Am. Chem. Soc.*, vol. 143, no. 3, pp. 1399–1408, 2021, doi: 10.1021/jacs.0c10661.

[53] a M. Jerome W. F. Innocent, a Mari Napari, b‡ Andrew L. Johnson, a Thom R. Harris-Lee and E. Regue, c Timo Sajavaara, d Judith L. MacManus-Driscoll,

b Frank Marken, a and Feras Alkhalil, "Atomic Scale Surface Modification of TiO2 3D Nano-Arrays: Plasma Enhanced Atomic Layer Deposition of NiO for Photocatalysis.," *Mater. Adv.*, vol. 1, pp. 525–553, 2020, doi: 00.0000/00000000.

[54] Z. Zeng *et al.*, "Advances on Nickel-Based Electrode Materials for Secondary Battery Systems: A Review," *ACS Appl. Energy Mater.*, vol. 5, no. 7, pp. 9189–9213, 2022, doi: 10.1021/acsaem.2c01863.

[55] J. Joe, T. A. Ho, C. Bae, and H. Shin, "Role of Sulfur Incorporation in p-Type Nickel Oxide (p-NiO) on n-Type Silicon (n-Si) Photoelectrodes for Water Oxidation Reactions," *ACS Appl. Energy Mater.*, vol. 3, no. 5, pp. 4255–4264, 2020, doi: 10.1021/acsaem.9b02507.

[56] U. Farva and J. Kim, "Temperature optimization of NiO hole transport layer prepared by atomic layer deposition," *Vacuum*, 2023, doi: 10.1016/j.vacuum.2022.111674.

[57] N. Maccaferri *et al.*, "Ultrasensitive and label-free molecular-level detection enabled by light phase control in magnetoplasmonic nanoantennas," *Nat. Commun.*, vol. 6, 2015, doi: 10.1038/ncomms7150.

[58] N. Maccaferri *et al.*, "Tuning the magneto-optical response of nanosize ferromagnetic Ni disks using the phase of localized plasmons," *Phys. Rev. Lett.*, vol. 111, no. 16, pp. 1–5, 2013, doi: 10.1103/PhysRevLett.111.167401.

[59] G. Srinivasan and M. S. Seehra, "Magnetic susceptibilities, their temperature variation, and exchange constants of NiO," *Phys. Rev. B*, vol. 29, no. 11, pp. 6295–6298, 1984, doi: 10.1103/PhysRevB.29.6295.

[60] M. Tadic, D. Nikolic, M. Panjan, and G. R. Blake, "Magnetic properties of NiO (nickel oxide) nanoparticles : Blocking temperature and Neel temperature," *J. Alloys Compd.*, vol. 647, pp. 1061–1068, 2015, doi: 10.1016/j.jallcom.2015.06.027.

[61] T. Jungwirth, X. Marti, P. Wadley, and J. Wunderlich, "Antiferromagnetic spintronics," *Nat. Nanotechnol.*, vol. 11, no. 3, pp. 231–241, 2016, doi: 10.1038/nnano.2016.18.

[62] D. Y. Cho, S. J. Song, U. K. Kim, K. M. Kim, H. K. Lee, and C. S. Hwang, "Spectroscopic investigation of the hole states in Ni-deficient NiO films," *J. Mater. Chem. C*, vol. 1, no. 28, pp. 4334–4338, 2013, doi: 10.1039/c3tc30687a.

[63] J. Chae, H. S. Park, and S. W. Kang, "Atomic layer deposition of nickel by the reduction of preformed nickel oxide," *Electrochem. Solid-State Lett.*, vol. 5, no. 6, pp. 64–67, 2002, doi: 10.1149/1.1475199.

[64] A. Pereira, J. L. Palma, J. C. Denardin, and J. Escrig, "Temperature-dependent magnetic properties of Ni nanotubes synthesized by atomic layer deposition," *Nanotechnology*, vol. 27, no. 34, pp. 1–6, 2016, doi: 10.1088/0957-4484/27/34/345709.

[65] M. Napari *et al.*, "Antiferromagnetism and p-type conductivity of nonstoichiometric nickel oxide thin films," *InfoMat*, vol. 2, no. 4, pp. 769–774, 2020, doi: 10.1002/inf2.12076.

[66] J. Bachmann *et al.*, "Stoichiometry of nickel oxide films prepared by ALD," *Chem. Vap. Depos.*, vol. 17, no. 7–9, pp. 177–180, 2011, doi: 10.1002/cvde.201004300.

[67] N. Breil *et al.*, "Challenges of nickel silicidation in CMOS technologies," *Microelectron. Eng.*, vol. 137, no. 1, pp. 79–87, 2015, doi: 10.1016/j.mee.2014.12.013.

[68] I. Kounta *et al.*, "Competitive actions of MnSi in the epitaxial growth of Mn5Si3 thin films on Si(111)," *Phys. Rev. Mater.*, vol. 7, no. 2, pp. 1–13, 2023, doi: 10.1103/PhysRevMaterials.7.024416.

[69] N. G. Galkin *et al.*, "The Nature of Ferromagnetism in a System of Self-Ordered α-FeSi2 Nanorods on a Si(111)-4° Vicinal Surface: Experiment and Theory," *Nanomaterials*, vol. 12, no. 20, 2022, doi: 10.3390/nano12203707.

[70] M. Breeden *et al.*, "Proximity Effects of the Selective Atomic Layer Deposition of Cobalt on the Nanoscale: Implications for Interconnects," *ACS Appl. Nano Mater.*, vol. 4, no. 8, pp. 8447–8454, 2021, doi: 10.1021/acsanm.1c01639.

[71] R. L. Puurunen, "A short history of atomic layer deposition: Tuomo Suntola's atomic layer epitaxy," *Chem. Vap. Depos.*, vol. 20, no. 10–12, pp. 332–344, 2014, doi: 10.1002/cvde.201402012.

[72] N. Pinna and M. Knez, *Atomic Layer Deposition of Nanostructured Materials*. 2012.

[73] C. V. Deposition, "Thermodynamics and Kinetics of Chemical Vapour Deposition," pp. 129–164, 2010, doi: 10.1007/978-1-84882-894-0_4.

[74] S. M. George, "Atomic layer deposition: An overview," *Chem. Rev.*, 2010, doi: 10.1021/cr900056b.

[75] R. W. Johnson, A. Hultqvist, and S. F. Bent, "A brief review of atomic layer deposition: From fundamentals to applications," *Materials Today*. 2014, doi: 10.1016/j.mattod.2014.04.026.

[76] P. Maydannik, K. Lahtinen, T. Kääriäinen, and D. C. Cameron, "Continuous atomic layer deposition process development," *TAPPI Eur. PLACE Conf.*, vol. 1, p. 446, 2011.

[77] J. E. Maslar, W. A. Kimes, B. A. Sperling, and R. K. Kanjolia, "Characterization of vapor draw vessel performance for low-volatility solid precursor delivery," *J. Vac. Sci. Technol. A*, vol. 39, no. 1, p. 012403, 2021, doi: 10.1116/6.0000676.

[78] K. Ashurbekova, K. Ashurbekova, G. Botta, O. Yurkevich, M. Knez, and M. Knez, "Vapor phase processing: A novel approach for fabricating functional hybrid materials," *Nanotechnology*. 2020, doi: 10.1088/1361-6528/ab8edb.

[79] "COMSOLMultiphysics®v. 6.1;www.comsol.com.COMSOLAB:Stockholm,Sweden." .

[80] D. W. Pepper and J. C. Heinrich, *The finite element method: Basic concepts and applications with MATLAB®, MAPLE, and COMSOL*. 2017.

[81] V. Cremers, R. L. Puurunen, and J. Dendooven, "Conformality in atomic layer deposition: Current status overview of analysis and modelling," *Appl. Phys. Rev.*, vol. 6, no. 2, 2019, doi: 10.1063/1.5060967.

[82] A. Bashir, T. I. Awan, A. Tehseen, M. B. Tahir, and M. Ijaz, *Interfaces and surfaces*. INC, 2020.

[83] B. J. Inkson, "Scanning Electron Microscopy (SEM) and Transmission Electron Microscopy (TEM) for Materials Characterization," in *Materials Characterization Using Nondestructive Evaluation (NDE) Methods*, 2016.

[84] Y. Chen, "Nanofabrication by electron beam lithography and its applications: A review," *Microelectron. Eng.*, vol. 135, pp. 57–72, 2015, doi: 10.1016/j.mee.2015.02.042.

[85] A. A. Tseng, K. Chen, C. D. Chen, and K. J. Ma, "Electron beam lithography in nanoscale fabrication: Recent development," *IEEE Trans. Electron. Packag. Manuf.*, 2003, doi: 10.1109/TEPM.2003.817714.

[86] R. Schäfer, "Investigation of Domains and Dynamics of Domain Walls by the Magneto-optical Kerr-effect," *Handb. Magn. Adv. Magn. Mater.*, 2007, doi: 10.1002/9780470022184.hmm310.

[87] F. Pineider and C. Sangregorio, "Magneto-optical (MO) characterization tools for chemically prepared magnetic nanomaterials," in *Magnetic Characterization Techniques for Nanomaterials*, 2017.

[88] M. Weber *et al.*, "Assessing the Environmental Impact of Atomic Layer Deposition (ALD) Processes and Pathways to Lower It," *ACS Mater. Au*, vol. 3, no. 4, pp. 274–298, 2023, doi: 10.1021/acsmaterialsau.3c00002.

[89] G. P. Gakis, H. Vergnes, E. Scheid, C. Vahlas, B. Caussat, and A. G. Boudouvis, "Computational Fluid Dynamics simulation of the ALD of alumina from TMA and H2O in a commercial reactor," *Chem. Eng. Res. Des.*, vol. 132, no. March, pp. 795–811, 2018, doi: 10.1016/j.cherd.2018.02.031.

[90] G. Ersavas Isitman, D. Izbassarov, R. L. Puurunen, and V. Vuorinen, "Computational fluid dynamics study of the atomic layer deposition process around cylindrical and planar configurations," *Chem. Eng. Sci.*, 2023, doi: 10.1016/j.ces.2023.118862.

[91] D. Sibanda, S. T. Oyinbo, and T. C. Jen, "A review of atomic layer deposition modelling and simulation methodologies: Density functional theory and molecular dynamics," *Nanotechnology Reviews*. 2022, doi: 10.1515/ntrev-2022-0084.

[92] Z. Deng, W. He, C. Duan, B. Shan, and R. Chen, "Atomic layer deposition process optimization by computational fluid dynamics," *Vacuum*, 2016, doi: 10.1016/j.vacuum.2015.10.023.

[93] J. O. Wilkes, *Fluid mechanics for chemical engineers with Microfluidics and CFD*. 1991.

[94] J. Rourke, "Christoph Elschenbroich. Organometallics. Wiley-VCH, 2006, 3rd edn, 818 pp. ISBN 3-527-29390-6 (paperback)," *Appl. Organomet. Chem.*, 2006, doi: 10.1002/aoc.1136.

[95] J. W. Benzie, G. E. Harmon-Welch, J. C. Hoefler, V. I. Bakhmutov, and J. Blümel, "Molecular Dynamics and Surface Interactions of Nickelocene Adsorbed on Silica: A Paramagnetic Solid-State NMR Study," *Langmuir*, 2022, doi: 10.1021/acs.langmuir.2c00301.

[96] K. J. Cluff, M. Schnellbach, C. R. Hilliard, and J. Blümel, "The adsorption of chromocene and ferrocene on silica: A solid-state NMR study," *J. Organomet. Chem.*, 2013, doi: 10.1016/j.jorganchem.2013.05.037.

[97] L. Brissonneau, R. Sahnoun, C. Mijoule, and C. Vahlas, "Investigation of Nickelocene Decomposition during Chemical Vapor Deposition of Nickel," *J. Electrochem. Soc.*, vol. 147, no. 4, p. 1443, 2000, doi: 10.1149/1.1393375.

[98] D. Welipitiya *et al.*, "The adsorption of nickelocene Part 2: Decomposition and selective area deposition," *Surf. Sci.*, 1998, doi: 10.1016/S0039-6028(98)00742-

0.

[99] X. Zhong and J. W. Bozzelli, "Thermochemical and kinetic analysis of the H, OH, HO2, O, and O2 association reactions with cyclopentadienyl radical," *J. Phys. Chem. A*, 1998, doi: 10.1021/jp9804446.

[100] D. L. Pugmire, C. M. Woodbridge, N. M. Boag, and M. A. Langell, "Adsorption and decomposition of nickelocene on Ag(1 0 0): A high-resolution electron energy loss spectroscopy and temperature programmed desorption study," *Surf. Sci.*, vol. 472, no. 3, pp. 155–171, 2001, doi: 10.1016/S0039-6028(00)00939-0.

[101] M. D. Hoops and B. S. Ault, "Matrix isolation study of the early intermediates in the ozonolysis of cyclopentene and cyclopentadiene: Observation of two criegee intermediates," *J. Am. Chem. Soc.*, vol. 131, no. 8, pp. 2853–2863, 2009, doi: 10.1021/ja8065286.

[102] R. A. Siddiqui, "Experimental Investigations Of Thermodinamic Properties of Organometallic Compounds," *Thesis Diss.*

[103] K. Ashurbekova *et al.*, "Ultrathin Hybrid SiAlCOH Dielectric Films through Ring-Opening Molecular Layer Deposition of Cyclic Tetrasiloxane," *Chem. Mater.*, 2021, doi: 10.1021/acs.chemmater.0c04408.

[104] J. E. Maslar, W. A. Kimes, B. A. Sperling, and R. K. Kanjolia, "Nondispersive Infrared Gas Analyzer for Partial Pressure Measurements of a Tantalum Alkylamide During Vapor Deposition Processes," *Appl. Spectrosc.*, vol. 74, no. 10, pp. 1219–1229, 2020, doi: 10.1177/0003702819885182.

[105] Y. Koshtyal *et al.*, "Atomic Layer Deposition of NiO to Produce Active Material for Thin-Film Lithium-Ion Batteries," vol. 2, pp. 1–16, 2019.

[106] J. G. Baker, J. R. Schneider, J. A. Raiford, C. De Paula, and S. F. Bent, "Nucleation Effects in the Atomic Layer Deposition of Nickel-Aluminum Oxide Thin Films," *Chem. Mater.*, vol. 32, no. 5, pp. 1925–1936, 2020, doi: 10.1021/acs.chemmater.9b04630.

[107] J. K. Kang and S. W. Rhee, "Metalorganic chemical vapor deposition of nickel films from Ni(C5H5)2/H2," *J. Mater. Res.*, 2000, doi: 10.1557/JMR.2000.0264.

[108] P. Pourhakkak, A. Taghizadeh, M. Taghizadeh, M. Ghaedi, and S. Haghdoust, "Fundamentals of adsorption technology," in *Interface Science and Technology*, 2021.

[109] L. Y. Xie *et al.*, "Growth, physical and electrical characterization of nickel oxide thin films prepared by plasma-enhanced atomic layer deposition using nickelocene and oxygen precursors," *Mater. Res. Express*, vol. 7, no. 4, 2020,

doi: 10.1088/2053-1591/ab82c9.

[110] T. A. Utigard, M. Wu, G. Plascencia, and T. Marin, "Reduction kinetics of Goro nickel oxide using hydrogen," *Chem. Eng. Sci.*, vol. 60, no. 7, pp. 2061–2068, 2005, doi: 10.1016/j.ces.2004.11.024.

[111] V. E. Quiroz Cabascango and V. Yu Bazhin, "Nickel oxide reduction in CO/CO2 gas mixtures in reverberatory furnaces," *J. Phys. Conf. Ser.*, vol. 1515, no. 2, 2020, doi: 10.1088/1742-6596/1515/2/022028.

[112] S. L. Kharatyan, H. A. Chatilyan, and K. V. Manukyan, "Kinetics and Mechanism of Nickel Oxide Reduction by Methane," *J. Phys. Chem. C*, vol. 123, no. 35, pp. 21513–21521, 2019, doi: 10.1021/acs.jpcc.9b04506.

[113] M. Sokić *et al.*, "Kinetics of NiO and NiCl2 hydrogen reduction as precursors and properties of produced Ni/Al2O3 and Ni-Pd/Al2O3 catalysts," *Sci. World J.*, vol. 2015, 2015, doi: 10.1155/2015/601970.

[114] K. V. Manukyan *et al.*, "Nickel Oxide Reduction by Hydrogen: Kinetics and Structural Transformations," *J. Phys. Chem. C*, vol. 119, no. 28, pp. 16131–16138, 2015, doi: 10.1021/acs.jpcc.5b04313.

[115] I. K. Schuller, "Exchange bias," vol. 192, 1999.

[116] Y. Fujii, "Recent Developments in the X-ray Reflectivity Analysis," *Am. J. Phys. Appl.*, 2016, doi: 10.11648/j.ajpa.20160402.12.

[117] J. T. Richardson, R. Scates, and M. V. Twigg, "X-ray diffraction study of nickel oxide reduction by hydrogen," *Appl. Catal. A Gen.*, vol. 246, no. 1, pp. 137–150, 2003, doi: 10.1016/S0926-860X(02)00669-5.

[118] D. Maurya *et al.*, "Giant strain with ultra-low hysteresis and high temperature stability in grain oriented lead-free K 0.5 Bi 0.5 TiO3-BaTiO3-Na0.5 Bi0.5 TiO3 piezoelectric materials," *Sci. Rep.*, vol. 5, pp. 1–8, 2015, doi: 10.1038/srep08595.

[119] C. L. Prajapat and T. V. Chandrasekhar Rao, "Tailoring of magnetic properties of Co films by vacuum annealing upto 800 °C," *Mater. Sci. Energy Technol.*, vol. 2, no. 2, pp. 345–348, 2019, doi: 10.1016/j.mset.2019.03.001.

[120] J. Hu, S. Bandyopadhyay, Y. H. Liu, and L. Y. Shao, "A Review on Metasurface: From Principle to Smart Metadevices," *Front. Phys.*, vol. 8, no. January, pp. 1–20, 2021, doi: 10.3389/fphy.2020.586087.

[121] Y. Bi, L. Huang, X. Li, and Y. Wang, "Magnetically controllable metasurface and its application," *Front. Optoelectron.*, vol. 14, no. 2, pp. 154–169, 2021, doi: 10.1007/s12200-021-1125-4.

[122] V. G. Kravets, A. V. Kabashin, W. L. Barnes, and A. N. Grigorenko, "Plasmonic Surface Lattice Resonances: A Review of Properties and Applications," *Chem. Rev.*, vol. 118, no. 12, pp. 5912–5951, 2018, doi: 10.1021/acs.chemrev.8b00243.

[123] M. Kataja, T. K. Hakala, A. Julku, M. J. Huttunen, S. Van Dijken, and P. Törmä, "Surface lattice resonances and magneto-optical response in magnetic nanoparticle arrays," *Nat. Commun.*, vol. 6, no. May, 2015, doi: 10.1038/ncomms8072.

[124] R. Lee and M. L. Coote, "Mechanistic insights into ozone-initiated oxidative degradation of saturated hydrocarbons and polymers," *Phys. Chem. Chem. Phys.*, 2016, doi: 10.1039/c6cp05064f.

[125] Z. Yu and S. Fan, "Extraordinarily high spectral sensitivity in refractive index sensors using multiple optical modes," in *Optics InfoBase Conference Papers*, 2012, doi: 10.1364/oe.19.010029.

[126] A. D. Utyushev, V. I. Zakomirnyi, and I. L. Rasskazov, "Collective lattice resonances: Plasmonics and beyond," *Rev. Phys.*, vol. 6, no. November 2020, p. 100051, 2021, doi: 10.1016/j.revip.2021.100051.

[127] E. S. A. Goerlitzer *et al.*, "Molecular-Induced Chirality Transfer to Plasmonic Lattice Modes," *ACS Photonics*, 2023, doi: 10.1021/acsphotonics.3c00174.

[128] S. Nilsson *et al.*, "Probing the role of grain boundaries in single Cu nanoparticle oxidation by in situ plasmonic scattering," *Phys. Rev. Mater.*, 2022, doi: 10.1103/PhysRevMaterials.6.045201.

[129] M. J. Aus, B. Szpunar, U. Erb, A. M. El-Sherik, G. Palumbo, and K. T. Aust, "Electrical resistivity of bulk nanocrystalline nickel," *J. Appl. Phys.*, 1994, doi: 10.1063/1.356076.

[130] A. Vihervaara, T. Hatanpää, K. Mizohata, M. Chundak, G. Popov, and M. Ritala, "A low-temperature thermal ALD process for nickel utilizing dichlorobis(triethylphosphine)nickel(ii) and 1,4-bis(trimethylgermyl)-1,4-dihydropyrazine," *Dalt. Trans.*, 2022, doi: 10.1039/d2dt01347a.

[131] B. Hoex, S. B. S. Heil, E. Langereis, M. C. M. Van De Banden, and W. M. M. Kessels, "Ultralow surface recombination of c-Si substrates passivated by plasma-assisted atomic layer deposited Al2O3," *Appl. Phys. Lett.*, vol. 89, no. 4, pp. 5–8, 2006, doi: 10.1063/1.2240736.

[132] P. Saint-Cast, D. Kania, M. Hofmann, J. Benick, J. Rentsch, and R. Preu, "Very low surface recombination velocity on p -type c -Si by high-rate plasma-

deposited aluminum oxide," *Appl. Phys. Lett.*, 2009, doi: 10.1063/1.3250157.

[133] V. Nemanič, "Hydrogen permeation barriers: Basic requirements, materials selection, deposition methods, and quality evaluation," *Nuclear Materials and Energy*. 2019, doi: 10.1016/j.nme.2019.04.001.

[134] M. D. Groner, F. H. Fabreguette, J. W. Elam, and S. M. George, "Low-Temperature Al2O3 Atomic Layer Deposition," *Chem. Mater.*, 2004, doi: 10.1021/cm0304546.

[135] V. Kolkovsky and N. Lange, "Passivation and Electrical Properties of Alumina Layers Deposited by Atomic-Layer Deposition with Different Precursors," *Phys. Status Solidi Appl. Mater. Sci.*, 2022, doi: 10.1002/pssa.202200138.

[136] C. Guerra-Nuñez, M. Döbeli, J. Michler, and I. Utke, "Reaction and Growth Mechanisms in Al2O3 deposited via Atomic Layer Deposition: Elucidating the Hydrogen Source," *Chem. Mater.*, 2017, doi: 10.1021/acs.chemmater.7b02759.

[137] G. Dingemans, F. Einsele, W. Beyer, M. C. M. Van De Sanden, and W. M. M. Kessels, "Influence of annealing and Al 2O 3 properties on the hydrogen-induced passivation of the Si/SiO 2 interface," *J. Appl. Phys.*, vol. 111, no. 9, 2012, doi: 10.1063/1.4709729.

[138] G. Dingemans, M. C. Van de Sanden, W. M. Kessels, and W. Beyer, "Hydrogen induced passivation of Si interfaces by Al2O3 films and SiO2/ Al2O3 stacks," *Appl. Phys. Lett.*, 2010, doi: 10.1109/5.333744.

[139] Y. Lee *et al.*, "Hydrogen Barriers Based on Chemical Trapping Using Chemically Modulated Al2O3Grown by Atomic Layer Deposition for InGaZnO Thin-Film Transistors," *ACS Appl. Mater. Interfaces*, vol. 13, no. 17, pp. 20349–20360, 2021, doi: 10.1021/acsami.1c02597.

[140] G. Dingemans, F. Einsele, W. Beyer, M. C. M. Van De Sanden, and W. M. M. Kessels, "Influence of annealing and Al 2O 3 properties on the hydrogen-induced passivation of the Si/SiO 2 interface," *J. Appl. Phys.*, 2012, doi: 10.1063/1.4709729.

[141] O. Beldarrain, M. Duch, M. Zabala, J. M. Rafí, M. B. González, and F. Campabadal, "Blistering of atomic layer deposition Al2O3 layers grown on silicon and its effect on metal–insulator–semiconductor structures," *J. Vac. Sci. Technol. A Vacuum, Surfaces, Film.*, 2013, doi: 10.1116/1.4768170.

[142] J. R. Schneider, C. De Paula, N. E. Richey, J. G. Baker, S. T. Oyakhire, and S. F. Bent, "Understanding and Utilizing Reactive Oxygen Reservoirs in Atomic Layer Deposition of Metal Oxides with Ozone," *Chem. Mater.*, vol. 34, no. 12,

pp. 5584–5597, 2022, doi: 10.1021/acs.chemmater.2c00753.

[143] A. P. Grosvenor, M. C. Biesinger, R. S. C. Smart, and N. S. McIntyre, "New interpretations of XPS spectra of nickel metal and oxides," *Surf. Sci.*, 2006, doi: 10.1016/j.susc.2006.01.041.

[144] M. Qin *et al.*, "PDA modification and properties of α-AlH3," *Sci. Rep.*, 2022, doi: 10.1038/s41598-022-16424-8.

[145] P. J. Megia, A. J. Vizcaino, J. A. Calles, and A. Carrero, "Hydrogen Production Technologies: From Fossil Fuels toward Renewable Sources. A Mini Review," *Energy and Fuels*, vol. 35, no. 20, pp. 16403–16415, 2021, doi: 10.1021/acs.energyfuels.1c02501.

[146] M. R. Usman, "Hydrogen storage methods: Review and current status," *Renewable and Sustainable Energy Reviews*. 2022, doi: 10.1016/j.rser.2022.112743.

[147] T. Suguro, F. Kishimoto, and K. Takanabe, "Photocatalytic Hydrogen Production under Water Vapor Feeding-A Minireview," *Energy and Fuels*, vol. 36, no. 16, pp. 8978–8994, 2022, doi: 10.1021/acs.energyfuels.2c01478.

[148] K. Maeda *et al.*, "Preparation of core-shell-structured nanoparticles (with a noble-metal or metal oxide core and a chromia shell) and their application in water splitting by means of visible light," *Chem. - A Eur. J.*, vol. 16, no. 26, pp. 7750–7759, 2010, doi: 10.1002/chem.201000616.

[149] L. Huo, C. Jin, K. Jiang, Q. Bao, Z. Hu, and J. Chu, "Applications of Nickel-Based Electrocatalysts for Hydrogen Evolution Reaction," *Advanced Energy and Sustainability Research*. 2022, doi: 10.1002/aesr.202100189.

[150] S. Seo, G. A. Perez, K. Tewari, X. Comas, and M. Kim, "Catalytic activity of nickel nanoparticles stabilized by adsorbing polymers for enhanced carbon sequestration," *Sci. Rep.*, vol. 8, no. 1, pp. 1–11, 2018, doi: 10.1038/s41598-018-29605-1.

[151] S. Dey and N. S. Mehta, "Oxidation of carbon monoxide over various nickel oxide catalysts in different conditions: A review," *Chemical Engineering Journal Advances*. 2020, doi: 10.1016/j.ceja.2020.100008.

[152] J. Kim and W. A. Anderson, "Spontaneous nickel monosilicide nanowire formation by metal induced growth," *Thin Solid Films*, vol. 483, no. 1–2, pp. 60–65, 2005, doi: 10.1016/j.tsf.2004.12.025.

[153] A. L. Schmitt, M. J. Bierman, D. Schmeisser, F. J. Himpsel, and S. Jin, "Synthesis and properties of single-crystal FeSi nanowires," *Nano Lett.*, vol. 6,

no. 8, pp. 1617–1621, 2006, doi: 10.1021/nl060550g.

[154] J. M. Higgins, A. L. Schmitt, I. A. Guzei, and S. Jin, "Higher manganese silicide nanowires of nowotny chimney ladder phase," *J. Am. Chem. Soc.*, vol. 130, no. 47, pp. 16086–16094, 2008, doi: 10.1021/ja8065122.

[155] R. K. Pandey, G. Maity, S. Pathak, P. Kalita, and S. Dubey, "New insights on Ni-Si system for microelectronics applications," *Microelectronic Engineering*. 2022, doi: 10.1016/j.mee.2022.111871.

[156] Y. Chen, Y. C. Lin, X. Zhong, H. C. Cheng, X. Duan, and Y. Huang, "Kinetic manipulation of silicide phase formation in Si nanowire templates," *Nano Lett.*, vol. 13, no. 8, pp. 3703–3708, 2013, doi: 10.1021/nl401593f.

[157] C. L. Hsin, C. W. Huang, C. H. Cheng, H. S. Teng, and W. W. Wu, "Shape control of nickel silicide nanocrystals on stress-modified surface," *CrystEngComm*, vol. 16, no. 9, pp. 1611–1614, 2014, doi: 10.1039/c3ce41882k.

[158] M. Gharooni, M. Hosseini, S. Mohajerzadeh, M. Taghinejad, H. Taghinejad, and Y. Abdi, "Realization of highly crystallographic three-dimensional nanosheets by a stress-induced oriented-diffusion method," *Appl. Phys. Lett.*, vol. 105, no. 4, 2014, doi: 10.1063/1.4892091.

[159] M. Hosseini and S. Mohajerzadeh, "Evolution of Silicon-Nickel Nanosheets on (111) Silicon Substrates to Realize Reduced Graphene Oxide-Silicide Heterostructures," *IEEE Electron Device Lett.*, vol. 40, no. 10, pp. 1690–1693, 2019, doi: 10.1109/LED.2019.2936417.

[160] M. Gharooni *et al.*, "A novel method for realization of nickel silicide nanosheets with advanced morphology and photoemission," *NSTI Adv. Mater. - TechConnect Briefs 2015*, vol. 1, pp. 612–615, 2015.

[161] T. Liao *et al.*, "Magnetic iron-cobalt silicides discovered using machine-learning," *Phys. Rev. Mater.*, 2023, doi: 10.1103/PhysRevMaterials.7.034410.

[162] Y. Song *et al.*, "Heterostructured Cobalt Silicide Nanocrystals: Synthesis in Molten Salts, Ferromagnetism, and Electrocatalysis," *J. Am. Chem. Soc.*, 2023, doi: 10.1021/jacs.3c01110.

[163] K. Sekar, G. Kuri, P. V. Satyam, B. Sundaravel, D. P. Mahapatra, and B. N. Dev, "Growth and alignment of gold silicide islands on Br-passivated vicinal Si(111) surfaces," *Surf. Sci.*, 1995, doi: 10.1016/0039-6028(95)00606-0.

[164] K. Sekar, G. Kuri, P. V. Satyam, B. Sundaravel, D. P. Mahapatra, and B. N. Dev, "Shape transition in the epitaxial growth of gold silicide in Au thin films on Si(111)," *Phys. Rev. B*, 1995, doi: 10.1103/PhysRevB.51.14330.

[165] J. C. Mahato *et al.*, "Uniformity of epitaxial nanostructures of CoSi2 via defect control of the Si (111) surface," *Thin Solid Films*, vol. 534, pp. 296–300, 2013, doi: 10.1016/j.tsf.2013.01.092.

[166] D. Das, J. C. Mahato, B. Bisi, B. Satpati, and B. N. Dev, "Self-organized patterns along sidewalls of iron silicide nanowires on Si(110) and their origin," *Appl. Phys. Lett.*, vol. 105, no. 19, 2014, doi: 10.1063/1.4901815.

[167] P. Nürnberger, H. M. Reinhardt, D. Rhinow, R. Riedel, S. Werner, and N. A. Hampp, "Controlled growth of periodically aligned copper-silicide nanocrystal arrays on silicon directed by laser-induced periodic surface structures (LIPSS)," *Appl. Surf. Sci.*, vol. 420, pp. 70–76, 2017, doi: 10.1016/j.apsusc.2017.05.005.

[168] A. K. Das, S. K. Ghose, B. N. Dev, G. Kuri, and T. R. Yang, "Spontaneous nanostructural island formation and layer-to-island mass transport in Ge layers on Si(111) surfaces," *Appl. Surf. Sci.*, 2000, doi: 10.1016/S0169-4332(00)00357-3.

[169] K. Matsukawa, K. Shirai, H. Yamaguchi, and H. Katayama-Yoshida, "Diffusion of transition-metal impurities in silicon," *Phys. B Condens. Matter*, 2007, doi: 10.1016/j.physb.2007.08.134.

[170] Y. Kamon, H. Harima, A. Yanase, and H. Katayama-Yoshida, "Ultra-fast diffusion mechanism of the late 3d transition metal impurities in silicon," *Phys. B Condens. Matter*, 2001, doi: 10.1016/S0921-4526(01)00754-2.

[171] T. T. Tran, C. Lavoie, Z. Zhang, and D. Primetzhofer, "In-situ nanoscale characterization of composition and structure during formation of ultrathin nickel silicide," *Appl. Surf. Sci.*, vol. 536, no. September 2020, p. 147781, 2021, doi: 10.1016/j.apsusc.2020.147781.

[172] A. Hou, Y. Ting, K. Tai, C. Huang, and K. Lu, "Applied Surface Science Atomic-scale silicidation of low resistivity Ni-Si system through in-situ TEM investigation," *Appl. Surf. Sci.*, vol. 538, no. 1001, p. 148129, 2021, doi: 10.1016/j.apsusc.2020.148129.

[173] Y. C. Chou, L. J. Chen, and K. N. Tu, "Uphill Diffusion Induced Point Contact Reaction in Si Nanowires," *Nano Lett.*, 2022, doi: 10.1021/acs.nanolett.2c01265.

[174] R. T. Tung, J. M. Gibson, and J. M. Poate, "Formation of ultrathin single-crystal silicide films on Si: Surface and interfacial stabilization of Si-NiSi2 epitaxial structures," *Phys. Rev. Lett.*, 1983, doi: 10.1103/PhysRevLett.50.429.

[175] F. A. Geenen, E. Solano, J. Jordan-Sweet, C. Lavoie, C. Mocuta, and C. Detavernier, "The influence of alloying on the phase formation sequence of ultra-

thin nickel silicide films and on the inheritance of texture," *J. Appl. Phys.*, 2018, doi: 10.1063/1.5022070.

[176] A. Jay *et al.*, "A comprehensive atomistic picture of the as-deposited Ni-Si interface before thermal silicidation process," vol. 631, no. May, 2023, doi: 10.1016/j.apsusc.2023.157563.

[177] N. Ikarashi and K. Masuzaki, "Silicide formation process in ultra-thin Ni-silicide film for advanced semiconductor devices: Mechanism of NiSi2 formation at low temperature," in *Journal of Physics: Conference Series*, 2011, doi: 10.1088/1742-6596/326/1/012051.

[178] A. Y. Hou, Y. H. Ting, K. L. Tai, C. Y. Huang, K. C. Lu, and W. W. Wu, "Atomic-scale silicidation of low resistivity Ni-Si system through in-situ TEM investigation," *Appl. Surf. Sci.*, 2021, doi: 10.1016/j.apsusc.2020.148129.

[179] J. Foggiato, W. S. Yoo, M. Ouaknine, T. Murakami, and T. Fukada, "Optimizing the formation of nickel silicide," *Mater. Sci. Eng. B*, vol. 114–115, no. SPEC. ISS., pp. 56–60, 2004, doi: 10.1016/j.mseb.2004.07.033.

[180] R. T. Tung, J. M. Gibson, and J. M. Poate, "Growth of single crystal epitaxial silicides on silicon by the use of template layers," *Appl. Phys. Lett.*, 1983, doi: 10.1063/1.93776.

[181] S. Karthika, T. K. Radhakrishnan, and P. Kalaichelvi, "A Review of Classical and Nonclassical Nucleation Theories," *Cryst. Growth Des.*, 2016, doi: 10.1021/acs.cgd.6b00794.

[182] Y. Q. Wang, R. Smirani, G. G. Ross, Y. Q. Wang, R. Smirani, and G. G. Ross, "Stacking faults in Si nanocrystals," vol. 221920, pp. 86–89, 2005, doi: 10.1063/1.1943501.

[183] T. Y. Tan and U. M. Gösele, "Generation of Point and Extended Defects During Oxidation and Silicidation of Silicon," *Encycl. Mater. Sci. Technol.*, no. c, pp. 3497–3504, 2001, doi: 10.1016/b0-08-043152-6/00623-9.

[184] P. W. Voorhees, "The theory of Ostwald ripening," *J. Stat. Phys.*, 1985, doi: 10.1007/BF01017860.

[185] Y. Freeman *et al.*, "Low Voltage Specific Charge (CV/g) Loss in Tantalum Capacitors," *J. Electrochem. Soc.*, 2010, doi: 10.1149/1.3391671.

[186] J. Wang, Z. Wu, C. Mao, Y. Zhao, J. Yang, and Y. Chen, "Effect of electrical contact resistance on measurement of thermal conductivity and wiedemann-franz law for individual metallic nanowires," *Sci. Rep.*, 2018, doi: 10.1038/s41598-018-23291-9.

[187] J. G. Jung, K. Lee, B. Lee, and H. S. Lee, "Effect of rapid thermal annealing on bulk micro-defects and plastic deformation in silicon during high temperature processing," *Mater. Sci. Semicond. Process.*, 2018, doi: 10.1016/j.mssp.2018.06.003.

[188] S. Salimian and M. Delfino, "Removal of native silicon oxide with low-energy argon ions," *J. Appl. Phys.*, 1991, doi: 10.1063/1.349160.

[189] F. H. M. Spit, D. Gupta, and K. N. Tu, "Diffusivity and solubility of Ni (63Ni) in monocrystalline Si," *Phys. Rev. B*, 1989, doi: 10.1103/PhysRevB.39.1255.

[190] J. Huang, M. Loeffler, W. Moeller, and E. Zschech, "Ga contamination in silicon by Focused Ion Beam milling: Dynamic model simulation and Atom Probe Tomography experiment," *Microelectron. Reliab.*, 2016, doi: 10.1016/j.microrel.2016.07.087.

[191] A. Mondon, M. N. Jawaid, J. Bartsch, M. Glatthaar, and S. W. Glunz, "Microstructure analysis of the interface situation and adhesion of thermally formed nickel silicide for plated nickel-copper contacts on silicon solar cells," *Sol. Energy Mater. Sol. Cells*, 2013, doi: 10.1016/j.solmat.2013.06.005.

[192] T. J. Knisley, M. J. Saly, M. J. Heeg, J. L. Roberts, and C. H. Winter, "Volatility and high thermal stability in mid- to late-first-row transition-metal diazadienyl complexes," *Organometallics*, 2011, doi: 10.1021/om200626w.

[193] M. M. Kerrigan *et al.*, "Substrate selectivity in the low temperature atomic layer deposition of cobalt metal films from bis(1,4-di- tert -butyl-1,3-diazadienyl)cobalt and formic acid," *J. Chem. Phys.*, 2017, doi: 10.1063/1.4968848.

[194] J. A. Dean, *Lange's Handbook Of Chemistry, 15th ed.* 1999.

[195] J. P. Klesko, M. M. Kerrigan, and C. H. Winter, "Low Temperature Thermal Atomic Layer Deposition of Cobalt Metal Films," *Chem. Mater.*, 2016, doi: 10.1021/acs.chemmater.5b03504.

[196] P. V. Kamat, "Absolute, Arbitrary, Relative, or Normalized Scale? How to Get the Scale Right," *ACS Energy Letters*. 2019, doi: 10.1021/acsenergylett.9b01571.

[197] J. C. Dupin, D. Gonbeau, P. Vinatier, and A. Levasseur, "Systematic XPS studies of metal oxides, hydroxides and peroxides," *Phys. Chem. Chem. Phys.*, 2000, doi: 10.1039/a908800h.

[198] A. Bumajdad, S. Al-ghareeb, M. Madkour, and F. Al Sagheer, "Non-noble , efficient catalyst of unsupported α -Cr 2 O 3 nanoparticles for low temperature

CO Oxidation," *Sci. Rep.*, no. October, pp. 2–10, 2017, doi: 10.1038/s41598-017-14779-x.

[199] T. Yamashita and P. Hayes, "Analysis of XPS spectra of Fe 2+ and Fe 3+ ions in oxide materials," *Appl. Surf. Sci.*, 2008, doi: 10.1016/j.apsusc.2007.09.063.

[200] K. J. Kanarik, S. Tan, and R. A. Gottscho, "Atomic Layer Etching: Rethinking the Art of Etch," *Journal of Physical Chemistry Letters*. 2018, doi: 10.1021/acs.jpclett.8b00997.

[201] M. Rasadujjaman, Y. Nakamura, M. Watanabe, E. Kondoh, and M. R. Baklanov, "Supercritical carbon dioxide etching of transition metal (Cu, Ni, Co, Fe) thin films," *Microelectron. Eng.*, 2016, doi: 10.1016/j.mee.2015.12.018.

[202] X. Lin, M. Chen, A. Janotti, and R. Opila, " In situ XPS study on atomic layer etching of Fe thin film using Cl2 and acetylacetone ," *J. Vac. Sci. Technol. A Vacuum, Surfaces, Film.*, 2018, doi: 10.1116/1.5039517.

[203] J. Zhao, M. Konh, and A. Teplyakov, "Surface chemistry of thermal dry etching of cobalt thin films using hexafluoroacetylacetone (hfacH)," *Appl. Surf. Sci.*, 2018, doi: 10.1016/j.apsusc.2018.05.182.

List of abbreviations

AFM	Atomic Force Microscopy
ALD	Atomic Layer Deposition
AS-ALD	Area Selective Atomic Layer Deposition
BSE	Backscattered Electrons
CBS	Concentric Backscattered
CFD	Computational Fluid dynamics
CVD	Chemical Vapor Deposition
DFT	Density Functional Theory
eBL	Electron Beam Litography
EDX	Energy Dispersive X-ray spectroscopy
FEBID	Focused Electron Beam Induced Deposition
FEM	Finite Element Method
FIB	Focused Ion Beam
FIBID	Focused Ion Beam Induced Deposition
GIS	Gas Injection System
GPC	Growth Per Cycle
HER	Hydrogen Evolution Reaction

IR	Infra Red
LPM	Litres Per Minute
MD	Molecular Dynamics
MFM	Magnetic Force Microscopy
MO	Magneto Optical
MOKE	Magneto Optical Kerr Effect
PVD	Physical Vapor Deposition
RTA	Rapid Thermal Annealing
SCCM	Standard Cubic Centimetre per Minute
SE	Secondary Electron
SEM	Scanning Electron Microscopy
SLR	Surface Lattice Resonances
SPR	Surface Plasmon Resonance
TEM	Transmission Electron Microscopy
XPS	X-ray Photoelectron Spectroscopy
XRD	X-Ray Diffraction
XRR	X-Ray Reflectivity

List of publications

[1] Azpitarte, I., Botta, G. A., Tollan, C., & Knez, M. (2020). SCIP: A New Simultaneous Vapor Phase Coating and Infiltration Process for Tougher and UV-Resistant Polymer Fibers. *RSC advances*, *10*(27), 15976-15982

[2] Ashurbekova, K., Ashurbekova, K., Botta, G., Yurkevich, O., & Knez, M. (2020). Vapor Phase Processing: a Novel Approach for Fabricating Functional Hybrid Materials. *Nanotechnology*, *31*(34), 342001.

Acknowledgements

If I can be honest, I would have never thought to become a doctor. The simple idea of adding the title of "Dr." before my name it is quite hilarious.

In any case, it is clear that this is not only a personal achievement but a clear reminder that as a collective, unthinkable things can be done.

In fact, this whole thing would not have been possible without the help of an impressive number of people that supported me. I will surely forget somebody so please don't get mad.

For the shared effort behind the realization of this thesis I need to start by thanking my supervisor Mato Knez. Your support during these crazy last months of writing literally saved me digesting myself in the throes of an anxiety attack. During this PhD, you shared your knowledge without imposing it and you gave me trust and freedom to fully build my identity as a scientist.

The scientific collaborators that I need to acknowledge are surely Celia, Maxim and Jed for the XPS analysis. Thanks to Mario Zapata from CFM for the simulation and nice talks. I would like to also thank James Maslar and Berc Kalanyan from the NIST of Gaithserburg and Charles Dezelah for sharing their knowledge about DAD_2 precursor, Chapter V would probably be empty without their help.

I also want to thank the many members of my group that made this PhD fun and gave me never-ending support. I would like to thank Momo, Marina, Susan and Ana for the fun coffee breaks and the mental and technical support during this thesis. Kari for the sweet final help with paperwork and Kris for trusting in my disastrous experiments. I want to tank Andoni for helping me with though paperwork and thrilling near death experiences in the water. I would like to thank Oksana for the help in the lab and your sweet words when needed. Thanks to Raydel for the huge effort in keeping the lab functioning. I also would like to tank Hazal for the inspiring stories and WenWen for showing me the best dance-moves.

Then the list of friends and colleagues that collaborated with me during this thesis requires some words. First, some scientists from the "high tower" that

supported me are Paolo Vavassori and Andrey Chuvilin. Meetings with Paolo have always been scientifically useful and somehow funny. I have really appreciated the cynical sense of humor that you are gifted with and its functionality, when coupled to your knowledge, to quickly get to the point of the discussion. Andrey, well he knows how many times he helped me with technical problems or weird experiments on the SEM, I thank you for the trust and the support during these years.

Remaining in the microscopy group there is a lot of people to thank starting from Chris and Zhenya (haha nice spelling). You guys have really no idea, of how much did your support meant to me. I could cry right now thinking about it, I'm serious. If I had to pay back the hours that you dedicated to me, I would have to move to live with you for a couple of years each. Mucho mucho love

Thanks to the one and only hawaiian sun for the crazy time on the island and the patient support with the CFD simulations and paperwork.

A big hug to Schermatone, Charlie y Cesar for helping me with the "meccanica di precisione" and absorbing the emotional damage del culatone!

Love to the two sweetest polpettoni di grafenea, Nerea (tutora de espanol) y Juanma for the cleanroom technical support, funny lunchbreaks and spicy gossips. Bueno, now I cannot avoid forgetting the two Japan-adopted former colleagues that I was too cool to spend enough time together when they were there and that I miss so bad. Thanks, Inge, for trusting in my hidden talent and printing my sketches on her thesis cover. Thanks Fra for the mille pause paglia traboccanti di sana blasfemia delirante, quando ti vedo ti raddrizzo il dentino a suon di baci.

A huge thanks also to Ralph, for never stepping back when I needed help. Thanks for showing how to work in the cleanroom, I wish one day I will start working a bit more like you and stop doing "chapuzas".

From the current group of people from nanogune I send my love to Manu and Garen for helping me with some measurement. Thanks Garen for the best fitting motivational speech I ever received, that will not be forgotten. Thanks, Kat, for being there listening to my never-ending delirious talks and for setting the fire at the zoo. Thanks also for helping me to format my scientific thoughts, chapter 6 would be a mess without you. Thanks to Eli for the helping me navigate in the messy bureaucracy of the PhD life and giving me funny

conversations. Thanks to my flatmates, the old and the new ones; great people to share my daily life with. Thanks to my many friends that supported me during these years starting from the gang secan@s to my dear friends Richi, Gio e I due "Tarantini", that constantly supported me despite the distance. Thanks to my beautiful parents for the unconditional support from day one, you gave me a peaceful harbour for the stormy nights. (wow that's cheeeesy).

I surely forgot some people, in that case please don't take it personally! LOVE